Flow in Multistage Transonic Compressors

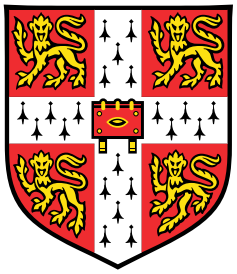

Anthony Dent

Whittle Laboratory
Department of Engineering
University of Cambridge

This dissertation is submitted for the degree of
Doctor of Philosophy

King's College

September 2017

Flow in Multistage Transonic Compressors

Anthony Dent

Abstract

Transonic compressors are regularly used as part of the compression system in industrial gas turbines because their high operating speeds make them capable of producing high stage pressure ratios and they have a high efficiency. The flow inside these compressors is inherently unsteady due to rotor-stator interactions. The flow in transonic compressors is also subject to shock waves leading to further unsteady interactions such as the interaction between the inlet guide vanes and the rotor leading edge shock waves. Despite the presence of unsteady flow, CFD simulations regularly assume the flow to be steady relative to each blade row in order to reduce the cost and time to perform simulations, however, this introduces more assumptions into the simulations compared to unsteady CFD simulations.

The first aim of this thesis is to investigate the causes of the differences in predicted efficiency observed between steady and unsteady simulations in order to show the operating conditions at which the steady flow assumptions break down. It is shown that the efficiency in the rotor blade row is over predicted in the steady simulations due to a weaker shock wave. The efficiency in the IGV is also over predicted while the efficiency in the stator blade row is under predicted. The unsteady simulations are also used to show that the stage efficiency characteristic is not affected by the unsteady effects from the downstream blade rows, when the stage is embedded in a multistage machine.

In the next part of the thesis, the effect of the IGV-Rotor axial gap on the compressor efficiency, and the dynamic blade loading, is investigated in multistage unsteady simulations. This shows that a reduced IGV-Rotor axial spacing gives an improvement in the efficiency but leads to an increase in the dynamic loading which may prove detrimental to the blade life. It is also shown that altering the IGV-Rotor spacing has an effect on the loadings of the blade rows in the downstream stages.

The final part of the thesis investigates vane rescheduling in a multistage transonic compressor using steady CFD simulations. Vane rescheduling is important in multistage compressors in order to prevent the compressor stalling and to maximise the efficiency when operating at off-design speeds. Vane schedules are optimised for a range of design and off-design speeds and the effect of rescheduling on the radial flow distribution is analysed. It is shown that the flow can be affected far downstream of the rescheduled blade row and that this can affect the location of the separation in downstream blade rows.

Declaration

I hereby declare that except where specific reference is made to the work of others, the contents of this dissertation are original and have not been submitted in whole or in part for consideration for any other degree or qualification in this, or any other university. This dissertation is my own work and contains nothing which is the outcome of work done in collaboration with others, except as specified in the text and acknowledgements. This dissertation contains approximately 44,000 words and has 120 figures.

Anthony Dent
September 2017

Acknowledgements

I would like to thank my supervisor, Dr Liping Xu, for all his help throughout the course of my PhD, and for all of the guidance and knowledge he has provided to facilitate this project. I'd also like to thank all of the staff and students whose assistance and company made the Whittle Lab an enjoyable place to work.

The project has been funded by the Engineering and Physical Sciences Research Council (EPSRC) and Siemens Industrial Turbomachinery Ltd, and all of the experimental data in this thesis has been collected by Siemens. I am grateful to Roger Wells and Dr Senthil Krishnababu for all of their input, providing an industrial point of view and for their part in collecting the experimental data. In addition, I'm also thankful to Senthil for kindly providing the relevant data and methods for the rotor model force analysis.

Finally I would like to thank my wife, Connie, and the rest of my family for their support and encouragement.

Table of contents

Nomenclature

Roman Symbols

C_p	Stage pressure coefficient
c_p	Specific heat capacity at constant pressure
$\bar{h}$	Mass and time averaged static enthalpy
h_0	Stagnation enthalpy
M	Mach number
P	Static pressure
P_0	Stagnation pressure
P_{atm}	Atmospheric pressure
r	Radial coordinate
$\bar{s}$	Mass and time averaged specific entropy
$\bar{T}$	Mass and time averaged static temperature
T_0	Stagnation temperature
U	Blade speed
U_{tip}	Blade tip speed
V_r	Radial component of velocity
V_x	Axial component of velocity
x	Axial coordinate

y^+	Non-dimensional wall distance

Greek Symbols

$\Delta\eta_p$	Difference in polytropic efficiency between steady and unsteady simulation
δ^*	Boundary layer displacement thickness
θ	Boundary layer momentum thickness
η_{isent}	Isentropic efficiency
η_p	Polytropic efficiency
γ	Ratio of specific heats
ω	Blade pressure loss coefficient
ψ	Stage loading coefficient
ρ	Density

Subscripts

design	Design Operating Point
nwl	Nominal Working Line

Acronyms / Abbreviations

CFD	Computational Fluid Dynamics
EO	Engine Order
GPU	Graphics Processing Unit
IGV	Inlet Guide Vane
ND	Nodal Diameter
RANS	Reynolds-Averaged Navier-Stokes
URANS	Unsteady Reynolds-Averaged Navier-Stokes
VGV	Variable Guide Vane

Chapter 1

Introduction

Industrial gas turbines are widely used for power generation and mechanical drive due to their high efficiency and reliability. When used for power generation, simple cycle gas turbines provide a power source that can react to changes in demand in a matter of minutes making them ideal for use as standby generators or peaking power plants. The fast start up time for simple cycle gas turbines makes them very useful for balancing renewable sources of electricity generation that have an unpredictable electricity output. As renewable energy sources make up an increasing proportion of the total grid capacity it is necessary to have more sources of electricity that are able to balance this output as needed. In a simple cycle configuration the thermal efficiency of gas turbines is around 30%–40%. In order to improve the thermal efficiency to around 60%, larger gas turbines are typically used in a combined cycle configuration where the waste heat from the gas turbine is used to power a steam cycle. Alternatively, the waste heat can be used for space or water heating or used to drive an absorption refrigeration cycle for chilling purposes. In mechanical drive applications, the turbine shaft power can be used directly, thereby eliminating the efficiency losses associated with generating electricity. This configuration is typically used in the oil and gas industry for driving compressors and pumps.

There is a continual pressure to improve the efficiency and reliability of gas turbines in order to reduce operation and maintenance costs and also in order to reduce emissions of carbon dioxide. For some applications there is the additional desire to reduce the overall package size and weight. This has led to the development of higher and higher stage pressure ratios in order to achieve higher overall pressure ratios or in order to reduce the number of stages required and hence reducing the overall size, weight and complexity of the compressor. In order to achieve higher pressure ratios it is necessary to use transonic compressors. It can be shown that this is necessary with a basic understanding of compressor theory. Using the definitions of polytropic efficiency (Eqn. (1.1)) and stage loading coefficient (Eqn. (1.2)) it is

possible to acquire an expression for the stage stagnation pressure ratio as a function of stage loading coefficient and blade speed (Eqn. (1.3)). This has been plotted in Fig. 1.1 for a range of stage loading coefficients, and a realistic polytropic efficiency of 0.9, with the blade tip speed expressed as a Mach number. It is clear from the graph that in order to achieve high pressure ratios it is necessary to use compressors operating at transonic speeds.

$$\frac{P_{02}}{P_{01}} = \left(\frac{T_{02}}{T_{01}}\right)^{\frac{\gamma\eta_p}{\gamma-1}} \tag{1.1}$$

$$\psi = \frac{\Delta h_0}{U_{tip}^2} = \frac{c_p(T_{02} - T_{01})}{U_{tip}^2} \tag{1.2}$$

$$\frac{P_{02}}{P_{01}} = \left(\psi\frac{U_{tip}^2}{c_p T_{01}} + 1\right)^{\frac{\gamma\eta_p}{\gamma-1}} \tag{1.3}$$

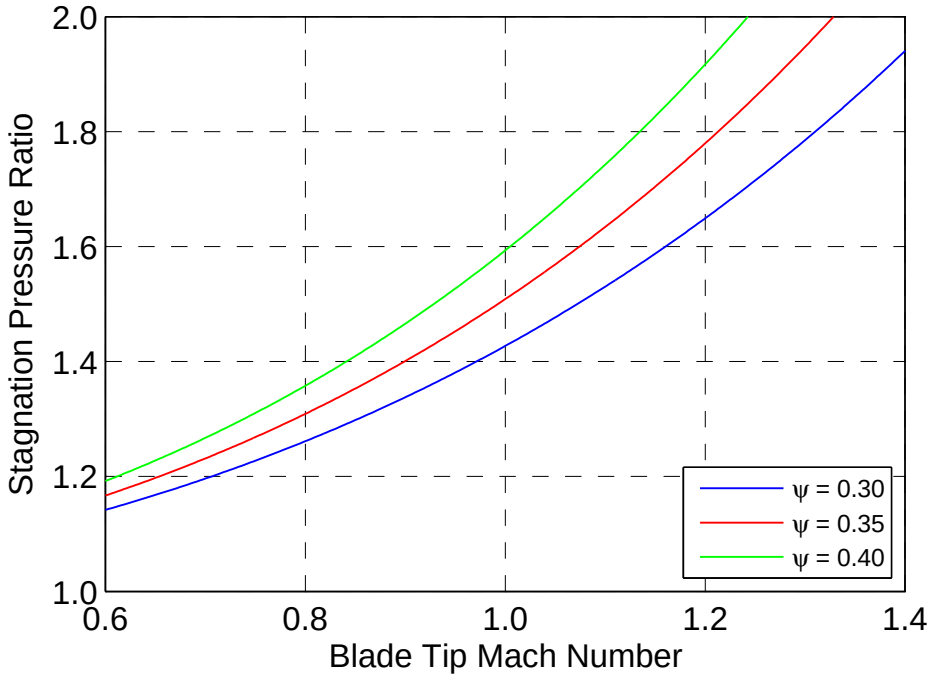

Fig. 1.1 Theoretical compressor pressure ratio

Transonic compressors have high relative Mach numbers at the rotor inlet in the upper parts of the span, while the flow remains subsonic near the hub. The supersonic flow gives rise to a shock system that aids the compression process, helping transonic compressors to achieve a higher pressure ratio per stage with greater efficiency than fully subsonic or supersonic compressors. The compression system is one of the fundamental components of a gas turbine so the use of transonic compressors has helped drive improvements in the overall performance of gas turbines and transonic compressors are now commonly used in jet engines and industrial gas turbines, typically making up the first few stages of the compression system.

Transonic compressors have very complex internal flow features because shock waves are present, in addition to all the other flow features found in subsonic machines, which leads to a large amount of interaction between the shock waves and the viscous flow features such as the boundary layers. In order to develop new compressor designs with improved performance it is desirable to model the flow using numerical methods such as Computational Fluid Dynamics (CFD). In a multi-blade row compressor the flow is inherently unsteady, due to rotor-stator interactions, which makes simulation of the unsteady flow very expensive and time-consuming. In order to reduce the cost of simulations, the flow may be modelled in a steady simulation by making certain assumptions, for example, one could assume the flow to be steady relative to each blade row and use a mixing plane between the blade rows to transfer mixed out flow properties across the blade row interface [26]. This means that physical flow features, such as the unsteady rotor-stator interactions, are not being modelled, leading to less accurate predictions of the losses and less accurate predictions of the compressor performance.

Despite this, steady simulations are far more common in compressor design cycles than unsteady simulations. This is due to unsteady simulations typically costing 1–3 orders of magnitude more to perform than steady simulations. This means that while it may be feasible to perform unsteady simulations at the nominal design point, it is often not possible to perform unsteady simulations at a great number of off-design conditions to cover the full range of the operation of interest to the designers.

Gas turbines are frequently required to operate at a wide variety of operating conditions in order to match the power output with the demand. This requires the compressor to be able to operate at a range of speeds with as high an efficiency as possible. In multistage compressors variable guide vanes can be used to improve the stage matching at off-design conditions.

In this thesis, steady and unsteady CFD are used to investigate the flow within a transonic compressor. The aim is to aid physical understanding about the flow so that this can provide

information for compressor designers to help them make the best decisions during the design cycle. The work in this thesis will focus on unsteady flows and vane rescheduling in transonic multistage compressors. The investigation into unsteady flows seeks to gain a better understanding of the limitations of the assumptions made when using steady flow design tools in the design process to calculate the overall compressor performance. A particular focus is given to investigating the unsteady interaction between the IGV and the rotor in order to gain further understanding about the effect this interaction has on the compressor and particularly on the downstream blade rows. In addition the effect of varying the IGV-Rotor axial spacing is examined to assess the impact that this has on the aerodynamic performance as well as investigating the mechanical implications for the blades. Vane rescheduling is investigated as it is an important way of achieving off-design performance, however despite this, little is known about the effect this has on the flow field in a transonic compressor. This is due in part to the majority of current vane scheduling prediction methods being based on low fidelity modelling codes that are not capable of predicting the internal 3D flow field. They are therefore unable to predict the compressor performance accurately enough. There is a desire to test the ability of 3D CFD to accurately predict vane schedules at low speeds where large regions of separated flow exist. The work in this thesis makes a step towards achieving this by analysing vane rescheduling at speeds close to the design speed. The work presented in this thesis seeks to predict what efficiency gains are achievable and provide new insights into the flow field which is affected by the varying vane settings.

This thesis will continue in Chapter 2 with a review of some of the previous research on axial flow compressors, with a particular focus on unsteady flow and vane rescheduling in transonic compressors which are relevant to the current study. The numerical methods used in this thesis will be described in Chapter 3 along with a validation of the numerical results against experimental data. Chapter 4 contains a presentation of work investigating the effect that unsteady flow has on the simulated compressor performance by comparing results from steady and unsteady simulations. This provides important information to a compressor designer for when steady simulations may not be appropriate to accurately predict compressor characteristics. Unsteady flow interactions will continue to be investigated in Chapter 5 by analysing the IGV-Rotor interactions that are present in transonic compressors. In Chapter 6, the effects of vane rescheduling in transonic compressors will be investigated by using steady CFD simulations to improve the overall efficiency and operating range at off-design speeds. In addition it will be shown how rescheduling can affect the radial redistribution of the flow, leading to changes in the stator separation location. Finally Chapter 7 contains a summary of all the main conclusions and provides recommendations for future work.

Chapter 2

Literature Review

2.1 Introduction

Over the last 60 years there has been an extensive amount of research into transonic axial flow compressors and some of this research will be reviewed in this chapter in order to provide a technical background to the studies performed in this thesis.

The main difference in the aerodynamics between transonic and sub-sonic compressors is the presence of the shock system in the rotor blade row. This shock system changes depending on the operating conditions. Figure. 2.1 shows an over-simplified, yet not atypical shock configuration for 3 different operating points, in a 2D section of a transonic compressor rotor. At low pressure ratios the rotor is choked as in Fig. 2.1a and a normal passage shock wave forms across the rotor passage. In addition to the passage shock wave there is a shock wave formed from the leading edge of the rotor. As the pressure ratio increases towards the peak efficiency operating point in Fig. 2.1b, the passage shock wave is pushed upstream and it merges with the rotor leading edge shock wave. When the pressure ratio increases further towards stall in Fig. 2.1c the shock wave is pushed upstream and out of the front of the rotor passage before flow becomes unstable and ultimately the blade stalls.

Over the years a large number of models have been developed to analyse the flow inside transonic compressors. Most of the models focus on the loss due to the shock waves themselves which is relatively manageable to predict as it is directly correlated to the Mach number and the shock orientation. However, a significant proportion of the loss is associated with the shock wave/viscous layer interactions which are very difficult to generalise and to quantify. Despite this, the shock waves remain a significant source of loss and many attempts have been made to develop analytical models to predict the loss [60, 73, 9, 74]. In addition early attempts to quantify the losses were carried out by cascade experiments [59, 75]. The details of the shock structure are directly affected by the rotor blade profiles so

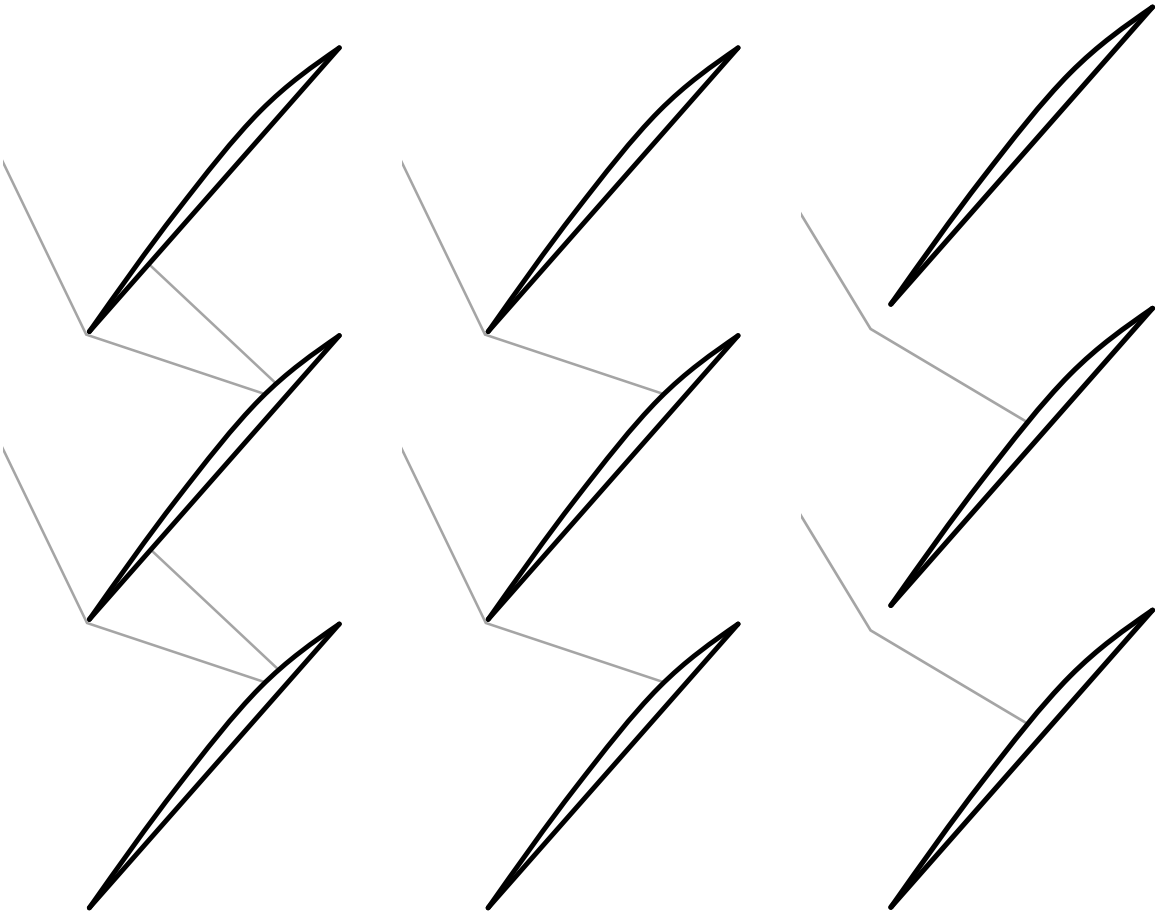

(a) Choked (b) Peak efficiency (c) Near stall

Fig. 2.1 Sketch of rotor shock system for different operating conditions

it is no surprise that a large research effort has been spent understanding this and developing new ways to design blade profiles. At a fundamental level this has included research on specific features such as the blade throat area ratio [86] and the blade thickness distribution [87]. More recently, optimisation algorithms have been developed to optimise blade profiles using CFD. A number of pieces of work have performed optimisations of NASA rotor 67 [15, 64, 90]. Despite using different techniques they all managed to achieve an improvement in efficiency of 1.8 percentage points. A common theme for all these blade optimisations is the reduction in the peak suction surface Mach number in order to reduce the shock losses. This has led to increasingly more complex blade definitions in a move away from Double Circular Arc (DCA) blade designs. Wang [90] also performed an optimisation of the 3-stage compressor modelled by the current author and the thesis presents results from simulations on both the original [56] and optimised geometries.

In a transonic blade row, the performance is significantly affected by the 3D flow field which has led to changes in the 3D design in order to control the secondary flow and improve the interaction between the secondary flows and the shock waves. A large amount of research has investigated the effect of applying sweep [40, 88, 65, 5] and lean [4, 61] to rotor blades. Incorporating this into the design has led to improvements in the efficiency and stall margin of transonic compressors. Forward sweep in particular has proved to provide significant performance gains. When forward sweep is used, the position of the shock wave near the casing must move backwards in order that the shock is normal to the casing, and this reduces the shock-boundary layer interaction. One of the most important secondary flow features is the radial migration of flow in the blade passage and forward sweep reduces the radial migration of low momentum fluid to the tip region. This further reduces the shock-boundary layer interaction and improves the efficiency. The reduced low momentum fluid at the tip also reduces the blockage which keeps the tip region stable at lower flow rates and improves the operating range. The interaction of the tip leakage flow with the shock waves is another source of complex flow interaction in transonic compressors. This interaction can affect the stalling point and the efficiency of the compressor by creating a large blockage [81, 95, 41]. The effect of the tip leakage is, to some extent, determined by the size of the tip gap (e.g. Copenhaver [20]) as well as the local aerodynamic loading distributions.

The previous pieces of research, mentioned above, represent only a very small portion of the work carried out on transonic compressors and a much more detailed summary has been provided by others [48, 17, 12, 8]. The rest of this chapter will focus on the previous research that has been performed in the areas of particular interest for the work in this thesis. The following sections will cover work on unsteady flow in compressors, IGV-Rotor interaction (including the effect of varying the axial spacing between the IGV and rotor) and vane rescheduling in multistage machines. This chapter concludes with the research objectives that are addressed in the remainder of this thesis.

2.2 Unsteady Flow in Compressors

The largest sources of unsteady flow in a compressor are caused by the relative motion between the rotor and the stator blade rows. This causes a potential pressure field to be exerted on neighbouring blades. In addition the convection of wakes downstream creates an unsteady inlet condition to the downstream blade row. In this section, sources of unsteady flow generic to all compressors are considered before going on to explore research into the unsteady flows in transonic compressors.

As mentioned above, each blade exerts a potential pressure field on the flow that propagates upstream and downstream, and, as the blade rows move relative to each other, these potential pressure fields interact with each other and with the blades in other blade rows. In subsonic blade rows, these pressure fluctuations are shown to affect loading of the adjacent blade rows. Kemp [46] took a theoretical approach to understanding this for incompressible, inviscid, 2D flow of two thin aerofoils in relative motion and verified his work with numerical analysis. The unsteady variation is relatively small in comparison to the steady state loading and is strongly dependent on the axial spacing between the blade rows, however, unsteady variations of up to 18% of the steady state loading were observed by Kemp. Osborne [62] extended the theory further in order to consider compressible flow and found the unsteady loading varies by up to 10% of the steady state loading for the cases considered. It has also been shown that the potential fields can affect the flow of the wakes from the upstream blade row (e.g. Key [49]). This can lead to unsteady changes in the flow angle of the wakes which in turn affect the flow in the downstream blade row.

The interaction between wakes and the blade rows downstream, shown in Fig. 2.2, is another source of unsteady flow that affects all compressors. As a wake travels downstream it is chopped up by the downstream blade row and continues to convect through the blade passage. After exiting the downstream blade passage, the wake continues to travel downstream and will be further chopped and convected through subsequent downstream blade rows. Figure 2.2 shows the blade row wakes propagating downstream and being chopped up by the downstream blade rows. This process has been investigated by many people for subsonic flow (e.g. [77, 47, 34]). As the wake passes through the downstream blade row, the velocity deficit in the wake creates a negative jet perturbation travelling from the suction surface to the pressure surface.

The action of wakes passing through a downstream blade row also has an effect on the mixing loss of the wakes. Adamczyk [1] performed an analysis to investigate if it was beneficial for wakes to pass through a downstream blade row before mixing out. Adamczyk shows that the unsteady nature of passing wakes through a downstream blade row leads to a stagnation pressure recovery which can reduce the overall wake mixing loss by up to 70%. It is therefore beneficial for wakes not to be mixed out before passing through the downstream blade row. In practice, this can be aided by reducing the axial spacing between blade rows. This process of wake recovery has also been investigated for transonic compressors and more detail of this research is given in later sections.

The interaction between the wake and the boundary layers of the downstream blade row is another source of losses generated unsteadily. The negative jet effect of the wake transports fluid from the suction surface to the pressure surface of the blades across the blade

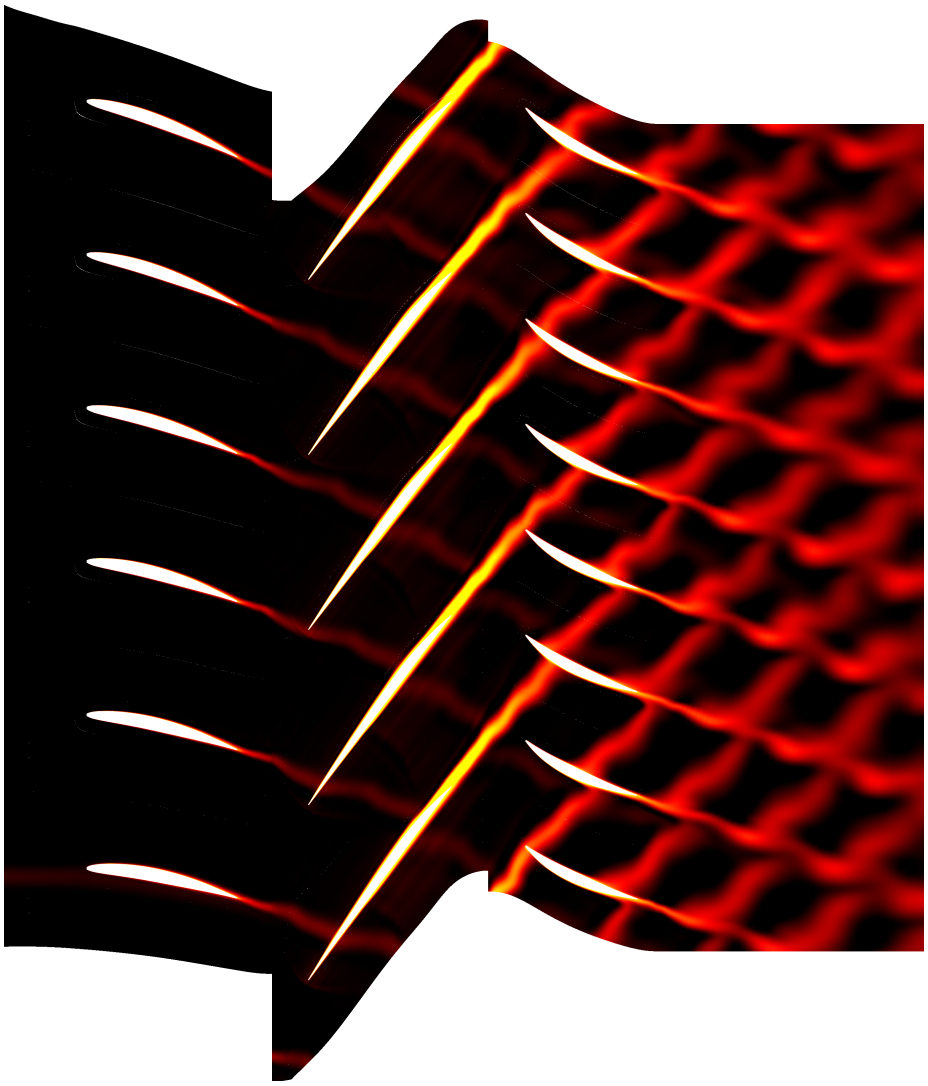

Fig. 2.2 Plot of entropy showing convection of wakes and chopping of wakes by downstream blade rows

passage. The extent of the unsteadiness can be determined by the reduced frequency (reduced frequency is the blade passing frequency normalised by the time taken for the flow to travel the length of the blade). Perkins and Henderson [66] performed experiments on a compressor cascade with a moving wake generator to investigate the effect that the reduced frequency had on the wake-stator interaction. Perkins and Henderson found that the blade pressure loss coefficient, ω (Eqn. (2.1)), decreased for the pressure surface by 0.0009 as the reduced frequency increased from 0 to 1.88. However, the blade pressure loss coefficient increased for the suction surface by 0.0019 resulting in an overall increase of 0.001, or about 4% of the total loss.

$$\omega = \frac{P_{01} - P_{02}}{P_{01} - P_1} \tag{2.1}$$

Unsteady Effects in Transonic Compressors

In transonic compressors there are other sources of unsteady flow that are present in addition to the source of unsteady flow already reviewed. This is mainly due to the existence of the shock system that provides a source of unsteadiness in itself as well as further interactions between it and other flow features. Previous research has been carried out on these types of flow and some of this work is reviewed here.

The presence of shock waves in themselves is a source of unsteadiness in transonic compressors. McDevitt [58] observed this unsteady characteristic of a shock wave on an aerofoil when performing 2D experimental work with a single aerofoil. McDevitt observed the unsteadiness to occur as a result of the shock wave interaction with the boundary layer which led to an oscillation between two different flow separation mechanisms that occurred when the peak Mach number over the aerofoil was around 1.25. At this speed, the location of the boundary layer separation oscillated between the trailing edge region of the aerofoil and near the base of the shock wave. As the separation position changed, it effectively altered the shape of the aerofoil (due to the blockage) and forced the change in the flow back to the previous state and thus made the oscillation of the shock wave self-sustaining. Similar experiments were performed by Lee [52] who measured the frequency of the shock oscillations. These experiments gave support to the theory that the shock waves oscillation is caused by pressure waves travelling between the shock location and the trailing edge inside the separated flow downstream of the shock position. This shock-boundary layer interaction is a source of loss and this interaction is affected when the shock wave strength varies. As the shock wave Mach number increases, the strength of the interaction with the boundary layer increases and this leads to greater loss [24, 13].

In a real compressor setting, the shock wave is never in isolation nor on a 2D aerofoil. In practice, pressure waves and wakes from other blade rows contribute to the movement of the shock waves in the rotor. Perturbations in the shock pressure ratio mean that the shock strength changes and this is achieved by the position of the shock moving. Copenhaver et al. [21] showed for a compressor rotor (with no upstream wakes) that the shock wave could oscillate up to 2% of the rotor chord. This work also showed that the additional unsteady loss associated with this shock oscillation amplitude was only 1% for the rotor studied.

Copenhaver et al. show that the additional loss as a fraction of the steady loss is greater for higher shock oscillations that occur at lower Mach numbers (although the absolute loss at higher Mach numbers will still be higher).

Transonic rotor blades also have a leading edge shock wave. Given that this shock rotates with the rotor blades it is a further source of unsteady flow. In addition, as this shock wave travels upstream it will interact with the upstream vane. This is a highly unsteady and significant interaction and is discussed in greater detail later in this chapter.

Predicting Transonic Compressor performance with CFD

Having presented a review into the causes of unsteady flow in compressors (with an additional focus on unsteady sources in transonic compressors), a review of the studies that have attempted to predict overall transonic compressor performance is now presented. Predicting the performance of transonic compressors accurately is very important for developing the designs of new compressors in order to reduce the time and cost of development. Given that it has been shown that the flow inside compressors (and particularly transonic compressors) is highly unsteady, the preferred option for predicting the operating performance would be to perform unsteady simulations. This would allow the unsteady flow features to be captured and provide the best possible prediction of the flow, losses and therefore the performance. In practice, unsteady simulations are very expensive and time consuming which has led to engineers developing alternative ways to simulate the 3D flow field. One option is to assume that the flow relative to each blade row is steady and to transfer the mixed out flow properties between blade rows through a mixing plane as originally developed by Denton [26]. This allows for much quicker and cheaper CFD simulations to be performed but it has introduced significant additional assumptions about the physical flow. It is important to know if the steady flow assumptions led to a difference in the performance predictions between steady and unsteady simulations so that it can be known whether steady CFD simulations are appropriate or if unsteady CFD simulations should be performed.

In recent years computational times for numerical simulations have decreased due to a number of factors. Single core processing speeds have increased but numerical codes have also been developed to take advantage of multiple processors. This allows simulations to be highly parallelised, taking advantage of a large numbers of affordable processing units simultaneously in a computer cluster. As well as taking advantage of a large number of Central Processing Units (CPUs) some codes are now able to use Graphical Processing Units (GPUs) to parallelise the simulation even further and gain a greater reduction in computational time.

These advances in computation have led to unsteady CFD simulations becoming more affordable and therefore the use of unsteady CFD, in order to capture the unsteady flow features discussed in this section, has become increasingly common. Despite this, steady CFD is still much more likely to be used than unsteady CFD as a design and analysis tool in industry. Steady CFD is not capable of capturing the unsteady flow features so it is useful to know how the performance predictions vary between steady and unsteady CFD simulations. Given that a number of unsteady transonic compressor simulations have been published, the rest of this section will contain a review of these unsteady simulations. A particular focus is given to work comparing results from steady and unsteady simulations.

Biesinger et al. [7] provide a good comparison between steady and unsteady CFD results for a single stage transonic compressor at design speed in addition to comparing the numerical results to experimental results. As well as not being able to simulate the unsteady variations in the flow, the additional modelling assumptions in the steady simulation are shown to lead to differences between the unsteady time averaged flow properties and the steady solution flow properties. The study uses two unsteady codes, ANSYS CFX Time-Inclining Method and NUMECA Non-Linear Harmonic Method, with steady simulations also run in both software packages. In both cases the steady simulations over predict the mass flow rate and stagnation pressure ratio when compared to their respective unsteady simulations. Further discrepancies exist in the radial flow profiles and blade loading distributions between the steady and unsteady time-averaged results.

Results by Arnone and Pacciani [2] show clearly that the steady simulations over predict the efficiency of a single stage transonic compressor (IGV-Rotor only) when compared to unsteady simulation results. This analysis is performed at a range of operating conditions but only at the design speed. Reising [69] also compares the variation in efficiency of a compressor stage, with two different stator geometries, between steady and unsteady simulations at design speed. His work shows good agreement in efficiency between steady and unsteady predicted efficiency at design and near choke, but steady simulations under predict efficiency at near stall conditions.

Further single stage unsteady simulations have been presented for part speed calculations [18, 82, 68] and at design speed [31, 43, 39, 53, 57, 35], including Large Eddy Simulations (LES) [38]. All of these give good information about the unsteady flow, however, none of them compare the unsteady simulations to steady simulations in detail in order to provide an insight or information about the cause of the differences observed.

The work on single stage compressors above has shown that discrepancies in overall performance metrics exist between steady and unsteady simulations when predicting single stage performance. This is important to know when attempting to use steady CFD to

accurately predict compressor performance. However, it would be of further use to know how these discrepancies change at off-design speeds and more importantly to gain an understanding of the root causes of the discrepancies.

Some research has been performed that makes useful comparisons between steady and unsteady performance predictions for multistage transonic compressors, although the number of studies is quite limited. Similar to single stage investigations, differences have also been reported between steady and unsteady simulations for multistage compressor simulations. Gourdain et al. [37] show the difference in predicted axial velocities between steady and unsteady simulations for a multistage compressor at design speed. This shows significant variations in the velocity of around 30% in the wake regions. These findings give additional weight to the knowledge that the steady flow assumptions prevent accurate modelling of the flow because the blade row interactions are not captured, but the work does not give any details for how this affects the overall performance predictions.

Yamagami et al. [97, 96] also show significant differences between steady and unsteady simulations for a multistage transonic compressor but do not clearly present the impact this has on the efficiency. Yamagami et al. do conclude that the wake mixing in the downstream blade passage in the unsteady simulations leads to a reduction in the mixing loss compared to the steady simulations. This is comparable to the results observed by others (and discussed above) for subsonic compressors where the chopping of wakes and their travel through the blade passage reduces the stagnation pressure loss due to mixing.

Steady and unsteady simulations are performed by Ottavy et al. [63] on a 3.5-stage compressor. However, the main focus of their work compares the unsteady simulation results with experimental results so there are limited steady simulation results provided. In the data that is provided, steady simulations are found to over predict the overall pressure ratio and efficiency when compared to unsteady simulations and this is particularly the case near stall. It is not possible to gain any further understanding as to why this is the case because only overall performance metrics are shown.

A review of transonic compressor simulations has been performed, focusing on work that makes comparisons between steady and unsteady simulations because having a better understanding of the discrepancies that exist between steady and unsteady simulations, and the cause of these discrepancies, gives the designer a better understanding of whether or not is is appropriate to use the steady flow assumptions of steady simulations in order to predict transonic compressor performance. Reviewing the work on single stage transonic compressors has shown that sometimes steady CFD under predicts efficiency and sometimes it over predicts efficiency when compared to unsteady CFD simulations. No previous research has been found to show how these discrepancies change at off-design speeds. In addition

there is no attempt to break down the losses between individual blade rows within the stage. This lack of research means it is hard to gain a detailed understanding as to why the discrepancies exist.

For multistage transonic compressors, the previous work suggests that similar discrepancies between steady and unsteady simulations exist when predicting the overall performance metrics. Again, it has not been possible to find any work that explores how these discrepancies change at off-design speeds and this would be useful to know as off-design speed operation is important in many applications. Investigating this would provide a better understanding of when it is and is not appropriate to make the steady flow simulation assumptions. Furthermore, for a multistage machine, it would be very useful to know how the presence of additional downstream blade rows affects the performance of the upstream stage. This is important to know because it determines how much consideration must be given to the unsteady pressure perturbation travelling upstream (from the downstream stage) when designing the upstream stage.

2.3 IGV-Rotor Interaction

The axial gap between the IGV trailing edge and the rotor leading edge is a region of very unsteady flow due to a number of interactions between the two blade rows, such as the potential pressure fields of each blade row, the IGV wakes and, in a transonic compressor, the rotor leading edge shock wave. Furthermore, in order to reduce the overall size and weight of axial compressors, it is desirable to make the axial spacing between blade rows smaller and smaller which leads to even greater interaction between the blade rows. Another driver for reducing the IGV-Rotor spacing is that it has been shown that reducing the axial spacing in low speed compressors improves the compressor efficiency, and that this is, in part, due to the effects of wake recovery discussed in the previous section. When the wakes pass through a downstream blade row the mixing losses can be reduced by up to 70% which equates to about a point increase in stage efficiency as argued by Adamczyk [1]. Further work by van de Wall et al. [85] suggest that the smallest possible axial spacing between blade rows will give the greatest benefit from increased wake recovery in subsonic compressors. The fact that this is an unsteady effect, that can only be captured with unsteady analysis, is also highlighted by Valkov and Tan [84] who point out that the increased efficiency that results from closer axial spacing cannot be captured by steady flow approximations. They find that the steady flow calculation would therefore lead to under prediction in the stage efficiency of between 0.3–0.5 percentage points for typical compressor stages, rising to a 0.6–1.0 percentage point under prediction for closely spaced subsonic compressors.

The work reviewed above shows that the axial spacing is an important factor in the stage efficiency. It has also been stated that reducing the axial spacing leads to greater unsteady interaction between the two blade rows. This is particularly true for transonic compressors where the presence of shock waves is an additional source of unsteady interaction. In the rest of this section the mechanisms of the unsteady interaction will be reviewed with a particular focus on studies in transonic compressors. In addition, research on varying the IGV-Rotor spacing in transonic compressors is presented in order to make a comparison between results from transonic and subsonic compressors.

One source of unsteadiness is the wakes from the IGVs travelling downstream and interacting with the rotor blades. This creates an unsteady inlet condition to the rotors as the rotors rotate and pass through the IGV wakes. This interaction induces a variation in the loading of the rotor and this unsteady loading occurs primarily at multiples of the frequency of the wake passing relative to the rotor. Simulations on an IGV and rotor by Arnone and Pacciani [2], show that the fundamental frequency is the strongest component of the unsteady loading and that the higher harmonic frequencies have a reducing magnitude. The extent to which the magnitudes of the higher harmonics roll off depends on the operating conditions of the compressor. Their work shows that the higher frequencies roll off fastest at peak efficiency, although the fundamental frequency is highest at this operating condition when compared to choke and near stall. This analysis has been performed without the presence of a downstream stator which is unfortunate as it is expected that the potential field from the stators would also influence the unsteady rotor loading.

At the same time as the IGV wakes are travelling downstream, the bow shock from the rotor is propagating upstream. In the absence of IGVs, the bow shock has been found to propagate at least 4 rotor chord lengths upstream of the rotor leading edge [67] meaning the bow shock will certainly interact with the IGV wakes and the IGV themselves when IGVs are present. The interaction between the IGV wakes and the bow shock is strongly determined by the operating condition as this determines the location of the bow shock. Estevadeordal et al. [32] investigated this using particle-image velocimetry (PIV) on a 1.5 stage compressor. As well as the frequency of the shedding vortex from the wake generator being locked to the rotor passing frequency, they also found that when the compressor was operating close to stall, and the rotor shock wave was pushed fully out of the rotor passage, the interaction of the shock and the wake from the wake generator caused the wake to have a significantly reduced velocity.

As well as the rotor shock affecting the IGV wake, the IGV wake also affects the rotor shock wave. Biela et al. [6] investigated this experimentally by comparing two cases with aerodynamically similar rotor inlet conditions but with different IGV loadings, thus varying

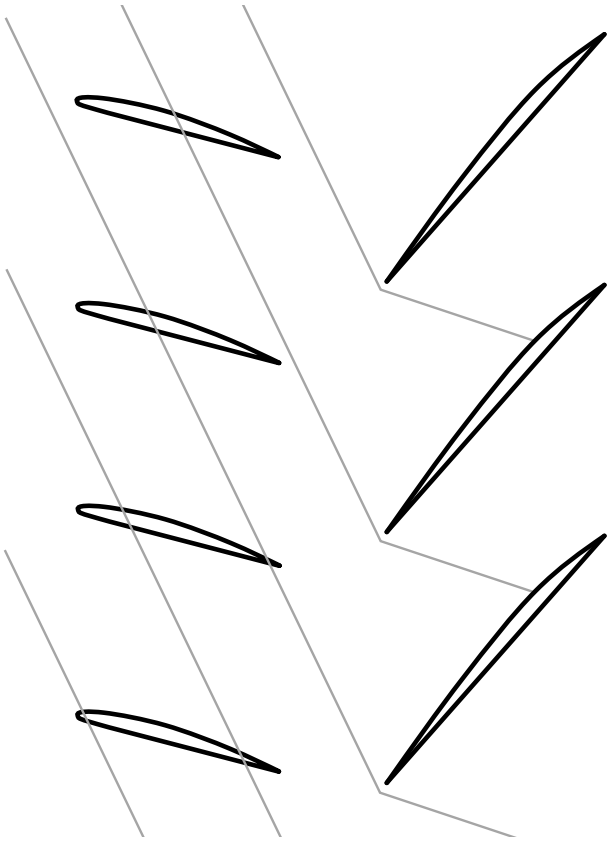

Fig. 2.3 Rotor leading edge shock interacting with IGVs

the intensity of the IGV wake entering the rotor blade row. Biela et al. found that the strength of the IGV wake affected the structure of the bow shock and that this affected the operating range of the compressor with the greater IGV loading case leading to increased range. Changing the axial gap between the IGVs and the rotor directly affects the point at which the IGV wakes and rotor bow shock interact. This was investigated by Gorrell et al.[36, 35] who found that, at smaller axial gaps, the increased strength of the shock (at the point of interaction with the IGV wakes) led to larger and stronger vortex shedding from the IGV. These studies have provided good insights into the physical flow features, but have not investigated the unsteady blade loading.

As the rotor leading edge shock travels upstream it interacts with the IGVs, in addition to the interaction with the IGV wakes, as shown in Fig. 2.3. The shock wave causes a variation in the loading of the IGV blades which is much greater than would exist in a subsonic compressor. The shock wave interaction with the IGV leads to vortex shedding from the IGV and this occurs at the rotor passing frequency [32]. The dynamic loading of the IGV increases as the stage pressure ratio increases because the bow shock is pushed further upstream [68]. The loading variation is also affected by the size of the axial gap between the IGV and the

rotor. As the axial spacing reduces the rotor bow shock is stronger at the point that it interacts with the IGVs and therefore the IGV loading has greater variation. This was investigated in a 1.5 stage compressor by Sanders and Fleeter [72]. The loading variation is an important mechanical consideration because the magnitude of the forcing will be a significant factor in determining the life of the blade when in operation. The interaction between the rotor leading edge shock waves and the IGVs has also been found to affect the flow field in the downstream stator blade row such as in work by Walker et al. [89]. This means that altering the axial spacing between the IGV and the Rotor could lead to changes in performance for downstream blade rows and it would be of interest to know if the effect of the IGV-Rotor interaction can be detected in these downstream stages.

Previous researchers have shown that changing the IGV-Rotor spacing can affect the strength of the interaction between the IGV and the Rotor. Changing the spacing (and therefore the interaction) can also affect the efficiency of the compressor. Some researchers have investigated the effect of axial spacing on efficiency by using steady CFD simulations, although this is not capable of capturing the blade row interactions [42, 19]. Despite this, the work showed that an optimal axial spacing exists with a peak efficiency that reduces at higher and lower axial spacings. This trend is verified by experimental work and unsteady CFD simulations. Sadek [71] has shown that an optimum axial spacing exists (which is neither the smallest nor largest possible) that gives the highest efficiency in unsteady CFD simulations with the axial spacing affecting the stage efficiency by up to 0.3 percentage points. Sadek found that peak efficiency was achieved with an axial spacing of 40% of the rotor mid-span chord. Computational work by List et al. [57], and supported by experimental results, has shown similar trends with a peak efficiency occurring at "mid" spacing.

The review of previous studies presented in this section has shown that a large amount of work has been undertaken in order to understand some of the physical flow features in the region between the IGV and the rotor. All of this work has been performed in machines with 3 blade rows or fewer which has provided good information on the local flow features but does not consider the effect of having addition blade rows present or the effect on the downstream blade rows from the IGV-Rotor interaction.

2.4 Vane Rescheduling

In a multistage compressor, it is necessary for all the individual stages to be matched to each other so that all of the stages operate within their own operating range. In addition, this usually involves designing the compressor stages so that, at the design point, each stage is operating close to its peak efficiency in order that the overall efficiency is maximised. At

off-design conditions the individual stages will start to operate far from design conditions because stages are impacted in different ways as the overall operating conditions change.

A summary of the effect of different operating conditions is shown in Fig. 2.4. As the overall pressure ratio increases while maintaining a constant speed, (points a $\rightarrow$ d) the stages at the rear of the machine pick up the additional pressure rise before the front stages pick up any additional pressure rise. This results in the last stage operating close to stall, with a lower efficiency, while the first stage is still operating close to design. At part speed, the differences in operating conditions between individual stages is even greater. When the compressor operates at lower speeds along the working line (a $\rightarrow$ b $\rightarrow$ c), the front stage operates close to stall while the rear stage operates fully choked. This leads to a large mismatch between the stages which reduces the operating range and the overall efficiency as individual stages are no longer operating at peak efficiency.

In order to improve the stage matching and operate the compressor at part speed, Variable Guide Vanes (VGVs) and/or compressor bleed are typically used to achieve better range and efficiency. Bleed allows the front stages to pass more mass flow than the rear stages which brings the front stages away from stall. VGVs can be used to alter the matching between stages in order to improve the overall efficiency or range of a compressor at a given speed. In some cases, particularly at very low compressor speeds, vane rescheduling is required in order for the compressor to operate at all and is therefore essential for starting up the compressor or operating at part speed.

As described above, the uses of vane rescheduling can broadly be classified into two categories. One use is at part speed, such as during start up or in order to operate at part load, where VGVs can be used to redistribute the loading between the stages and enable the compressor to operate. At these low speeds, large angle changes are required. This may cause large areas of separated flow that is hard to predict with simulations. Another use of VGVs is to make small adjustments to the stage matching in order to improve the efficiency or the operating range. This could be to correct stage mismatching at design speed or to improve performance at speeds close to the design speed. This requires relatively small vane angle settings up to around 10 degrees. In the rest of this section, a review of work on vane rescheduling is presented. First, a review of some work on subsonic vane rescheduling is presented, as this is still applicable to transonic compressors (particularly when operating at part speed). Following this, a review of vane rescheduling studies in transonic compressors is presented.

A lot of work on VGV scheduling has been experimental however various prediction methods have been used as well, including, 1D stage stacking, 2D streamline curvature and 3D CFD methods. An example of using the stage stacking method to investigate vane

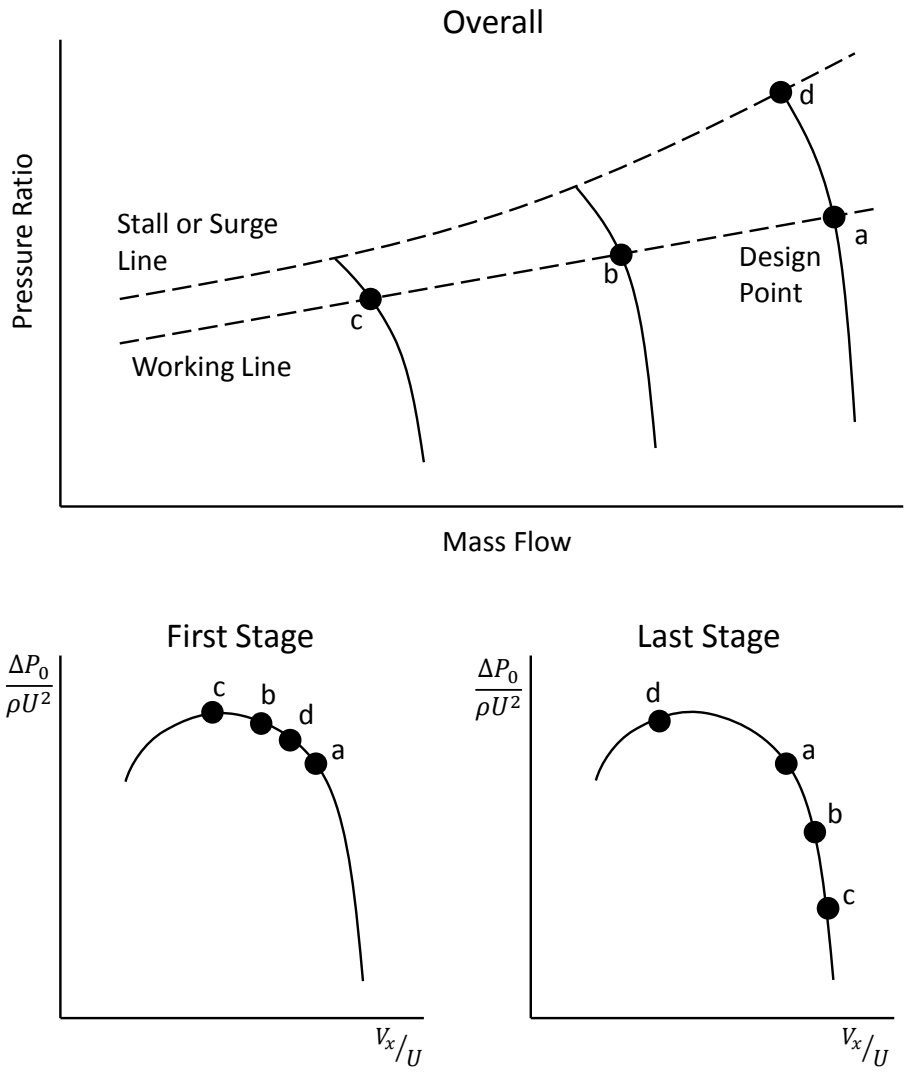

Fig. 2.4 Multistage compressor behaviour at different operating points (Adapted from [22])

rescheduling is provided by Tomita and Barbosa [83]. Their investigation on an 8.5 stage compressor with 9 variable blade rows gives a systematic presentation of the effects of varying individual blade rows and shows how rescheduling can be used to increased range and efficiency at off-design speeds. Unfortunately, only overall machine data is presented so it is not possible to gain any understanding of how the individual stages respond to rescheduling.

Wu et al. [94] sought to improve the off-design speed range and efficiency of a 10-stage subsonic compressor by rescheduling 4 rows of VGVs. In order to do this they used a stage stacking model to predict the correct vane schedules which they then verified with experimental results and found fairly good agreement between the two. This allowed them to

improve part speed efficiency by up to 12.7% and improve the overall operating range of the compressor. A limitation of 1D prediction methods is that no understanding of how the flow field varies across the span can be gained and any attempt to measure this experimentally was beyond the scope of the study. Understanding the changes to the flow field is important in order to be able to improve blade designs so that they can perform well when rescheduled. Cyrus [23] did attempt to measure the variation in the flow across the span for a single stage subsonic compressor and found that the flow variations are not uniform across the span as the stator is rescheduled due to changes in the radial flow field. This behaviour is anticipated but not much is known about it and it highlights the need to understand the changes to the 3D flow field as blade rows are rescheduled.

Rescheduling VGVs in a transonic compressor brings additional factors into consideration because of the effects that choked blade rows have on the matching of the stages. This means that it is important to review work that has been performed on VGVs in transonic compressors. In the rest of this section, a review of studies that include rescheduling in transonic compressors is presented. Experimental work is reviewed first, followed by a review of studies using low fidelity models and then studies that make use of 3D CFD.

Examples of experimental work on VGV scheduling in transonic compressors is limited. Calvert et al. [16] presented an experimental study of a 1-stage transonic military fan. Although rescheduling was not the focus of this study, it did show that opening the stator by 5 degrees gave an improvement in part speed efficiency. The work also investigated the benefit of using a variable IGV blade row in a 2-stage fan using a stage stacking model which also showed an improvement in part speed efficiency. Burger and Keenan [14] performed a VGV investigation on a 2-stage fan with 2 variable stators. They were able to achieve a 2 percentage point increase in stall margin at design speed and a 1.8 percentage point increase in efficiency at 105% speed, however this was at the expense of efficiency and stall margin respectively. This trade-off between efficiency and stall margin is a common trend for VGV rescheduling. For the VGV schedules tested, no improvement in stall margin or efficiency was achieved for part speed operation of 70%. The lack of a variable IGV significantly limits the possible impact of rescheduling to relieve the front stage loading at part speed. A 2-stage transonic compressor with variable IGV, stator 1 and stator 2 blade rows was investigated by Broichhausen and Harster [11] concluding that: the vane settings mainly influence the downstream stage; the upstream stage is only significantly influenced if the rescheduled vane is choked; and the IGV and stator 1 rows are both almost equally able to influence the overall compressor characteristics. Further analysis of the flow is also conducted but there is no back to back comparison of the radial flow field.

Another study on a transonic compressor is presented by Dodds and Vahdati [28, 29] using experimental and numerical techniques to investigate an 8-stage compressor with variable IGV, stator 1 and stator 2 blade rows. A total of 26 VGV schedules were tested with 7 chosen for detailed analysis, suggesting that a large amount of data was gathered with rescheduled VGVs in a transonic compressor. However, the focus of the study was rotating stall and therefore the main use of the VGVs was to deliberately initiate rotating stall in different blade rows so that the rotating stall could be studied. As such, there is no attempt to present the effect that the VGVs schedule has on the compressor's efficiency or show the effect of rescheduling on the 3D flow field.

Other researchers have focused on using low fidelity models to predict optimum vane schedules. Shadaram et al. [76] compare stream line curvature model predictions and experimental data of a 10-stage compressor with reasonable accuracy. Some [54, 33] have placed their modelling techniques inside novel optimisation algorithms in order to find the optimal schedules for compressors with many VGV rows, however, the accuracy of the result is still reliant on the underlining compressor simulations—in these cases, low fidelity mean line codes. Attempts have also been made to optimise the compressor VGVs in the context of a full engine analysis in order to improve the overall thermodynamic cycle [70, 50]. This is taken one step further by Kim [51] by also attempting to optimise the bleed mass flow rate in tandem with the VGV settings. This model still relies on the underlying modelling of the compressor which uses low fidelity models and as such provides no information about how the 3D flow inside the compressor changes as a result of rescheduling.

Some work has used 3D CFD in order to investigate VGV scheduling in compressors. As well as using higher fidelity modelling to predict optimal VGV schedules, 3D CFD is also able to provide details of how the rescheduling affects the internal flow field. Detailed steady and unsteady CFD results are presented by Li and Sayma [55] for a 3.5 stage compressor with a maximum relative inlet Mach number of 0.89. Significant discussion of the flow is given but the focus of the work is to investigate the implications for the compressor should the VGV system fail and the compressor has to operate with a VGV schedule designed for a different operating point. As such, the focus is on rotating stall and there is little to be learnt about how the flow field changes when trying to optimise the VGV settings for a given operating condition.

Dong et al. [30] use CFD simulations to look at a 4-stage compressor with a transonic first stage. Rescheduling is not the main focus of the work but closing the first stage stator is investigated as an option to improve the matching at design, which it does, and the efficiency is improved. No further details of the flow are provided. One other piece of CFD research on rescheduling, this time in a 5-stage transonic compressor, has been performed by Barbosa

et al. [3]. The work investigates the rescheduling of the IGV in order to improve the stall margin at part speed and uses this information to develop better control of the compressor and prevent surge as it accelerates and decelerates through different operating conditions. In this compressor, the IGV is the only variable blade row so investigations are limited to rescheduling this row only and the results focus on overall performance with no details of the internal flow field.

Generally, the aim of most previous studies into vane rescheduling in transonic compressors has been to seek improvements to the overall efficiency and/or operating range of a compressor by proposing new vane schedules. The majority of studies provide little or no details of the effect on the 3D flow field that rescheduling imposes, either because the studies have used low fidelity models (and therefore the information does not exist), the experimental data has not been collected or results from 3D dimensional CFD have not been presented. This leaves a significant gap in the understanding of the effect that rescheduling has on the flow field which makes it impossible to design VGVs that are able to perform better in rescheduled conditions.

2.5 Summary and Research Objectives

A review of previous compressor research has been presented with a particular focus on unsteady flow and vane rescheduling in transonic machines. The existing work has included many studies using steady CFD and low order models to fairly successfully predict compressor performance at design. While these methods can and are used at off-design conditions, interpretation of the results relies a lot on experience in order to not have unrealised expectations for the off-design performance. Unsteady simulations can make use of more physical models and fewer correlations thereby removing some of the unknown factors in order to obtain the best possible results. In the rest of this section, 3 areas are identified where there is a gap in the existing research and this will form the basis for the work presented in the rest of this thesis.

2.5.1 Steady Versus Unsteady Simulations

Previous research has identified and explained a number of unsteady flow features that exist within transonic compressors, however despite this, it is very rare to use any unsteady modelling predictions until very near the end of the design cycle. Instead it is a common approach, when performing 3D CFD simulations of multiple blade rows, to assume that the flow is steady relative to each blade row and to mix out the flow properties at a mixing

plane located between the blade rows [26]. Steady simulations are performed in preference to unsteady simulations because unsteady simulations cost much more to perform. It is important for designers to have an appreciation of how the steady flow assumptions affect the predictions over the whole compressor operational range so that they are able to make more informed decisions earlier in the design process and know when it may be necessary to perform unsteady simulations.

The majority of the research reported in the literature that compares steady and unsteady CFD simulations for transonic compressors has been performed on single stage machines and the efficiency is almost always considered only for an entire stage (or an entire machine) rather than breaking down the losses between individual blade rows. This provides a lack of clarity and gives no understanding for why some researchers find steady simulations to over predict efficiency (e.g. Arnone and Pacciani [2], Ottavy et al. [63]) while others have found it to under predict efficiency (e.g. Reising [69]). Therefore, there is a lack of information in the literature about how the differences in the overall efficiency break down between the individual blade rows. In a multistage machine the implication of unsteady effects propagating from downstream stages to upstream stages is also unknown. Furthermore, there is a lack of understanding as to how these discrepancies (between steady and unsteady simulations) change at different operating speeds and whether the unsteady effects from other blade rows significantly affect the performance of a blade row that is under design.

The first results chapter in this thesis contains an investigation into these issues in order to provide information to designers that can be used to better understand the implications of the steady flow assumptions in a multistage transonic compressor environment. This is done by breaking down the differences between steady and unsteady simulations to the individual blade rows and assessing the differences in the flow. In addition to performing an analysis at design speed the compressor is also analysed at part speed and at over speed in order to show how the effects of the steady state assumptions change at a range of operating conditions. Finally, the multistage effects are compared by investigating the differences between single stage and multistage simulations.

2.5.2 IGV-Rotor Spacing

In the review of previous research, a particular focus has been given to previous work that investigated the interaction between the IGV and the rotor because this is a region of significant unsteady flow for transonic compressors. A lot of research effort has gone into understanding this interaction, however there is no work investigating this for a multistage machine. It is not known how the interaction will affect the downstream stages when in a

multistage environment and what affect this has on the overall performance. In addition the mechanical implications for other stages has not been investigated.

The effect of the IGV-Rotor interaction in a multistage transonic compressor is investigated in the second results chapter by performing unsteady simulations with two different axial spacings between the IGV and the rotor. Changing the axial spacing changes the strength of the IGV-Rotor interaction which allows the effect of this to be analysed. Performing this analysis in a multistage transonic compressor has not previously been reported and will allow an understanding of how the IGV-Rotor interactions affect downstream stages to be gained. The investigation analyses the unsteady blade loadings of the blade rows with the different axial spacings. This gives an understanding of the mechanical implications that must be considered when the IGV-Rotor axial spacing is altered. In addition, the study investigates how the losses generated (and the mechanisms by which they are generated), inside the individual blade rows, change as the IGV-Rotor axial spacing is altered.

2.5.3 Vane Rescheduling

Reviewing the previous work on VGV rescheduling has shown the important role that VGVs play in multistage transonic compressors in order to improve the efficiency and the operating range. Despite this, the majority of studies rely on low fidelity models to predict the best vane schedules for a given operating condition. It is known that low fidelity models are not able to capture the details of the internal flow field and therefore they are very unlikely to be able to produce accurate predictions of the compressor performance, and therefore optimal vane schedules (particularly when operating at low speeds when large regions of separated flow exist). In order to improve the prediction of compressor performance and therefore predict more accurate vane schedules, it is thought that using 3D CFD would be beneficial.

Despite this, very little investigation has been performed using 3D CFD for VGV rescheduling and optimisation in transonic compressors. Of the previous work that does exist, none of it has investigated multistage transonic compressors with more than one variable blade row while presenting the effect that varying the VGVs has on the compressor efficiency. In addition, an opportunity has been missed in that 3D CFD has not been used to provide any details about the changes to the internal flow with different VGV schedules which would be useful in order to provide a better understanding that could lead to improved vane designs that would perform better when they have been rescheduled.

The final results chapter of this thesis will focus on VGV rescheduling a multistage transonic compressor in order to address some of the gaps in the literature. Results from 3D steady CFD are used to gain a better understanding of how individual stages respond to stator rescheduling and to gain a better understanding of the changes that occur in the flow

field. CFD is used to produce optimal VGV schedules for different operation speeds close to the design speed. The intention is to investigate the ability of CFD to accurately predict the changes in performance when VGVs are rescheduled. If CFD is shown to be successful at speeds close to the design speed, where only small adjustment angles are required, then it is believed that the ability of CFD to be used at speeds further from design should be investigated in order to assess the ability of CFD to predict optimal vane schedules when there are large regions of separated flow.

Having predicted the optimised vane schedules for speeds close to the design speed, the internal flow is analysed for some key operating conditions in order to gain insights into how rescheduling VGV affects the flow field. This will provide designers with new knowledge that can be fed into the design cycle in order to design VGVs that can perform better at a range of operating conditions.

Chapter 3

Numerical Methods and Validation

3.1 Introduction

The focus of this work is to use Computational Fluid Dynamics (CFD) to investigate the flow in transonic compressors, and quantify the uncertainties introduced due to modelling issues. CFD allows the work to be accomplished much quicker and at less cost than experimental investigations. In addition CFD allows the flow field to be examined in more detail than is possible with an experimental rig. To be able to have confidence in the results it is however necessary to validate the CFD simulations by comparing the CFD results to experimental results in order to make sure that CFD captures the important physics that governs the flow.

The compressor that has been analysed for this work is a 3-stage transonic test compressor designed by Siemens Industrial Turbomachinery Ltd [56]. The compressor has a design pressure ratio of 3 with a design mass flow rate of 26.32kg/s at 18650rpm with a relative inlet Mach number of 1.33 near the rotor 1 tip. There is a good amount of test data available which allows comparisons to be made to CFD simulations. Since its original design, the compressor blading has been re-designed with an optimisation process that led to new blade geometries [90]. The optimisation process targeted the same design mass flow rate and pressure ratio as the original design and gave an increase in efficiency of 2.47 percentage points. Test data is also available from the optimised geometry and both the original and optimised geometries will be used in the CFD simulations in this thesis.

In this chapter the computational method for the CFD simulations will be explained and the differences in the set up between steady and unsteady simulations will be outlined. A mesh independence study is presented to show that the computational mesh used for the studies in this thesis is adequate and sufficient. The CFD simulations are then validated by comparing the CFD results to the experimental data that is available. Also explained in this chapter are the methods used to modify the geometry for some of the studies in this thesis.

3.2 Flow Solver

All the CFD simulations have been performed using the Turbostream solver [10]. Turbostream is a Reynolds-Averaged Navier-Stokes (RANS), finite volume solver based on Denton's solver TBLOCK [25]. The solver allows for complex geometries to be easily meshed by using multiple structured blocks. The solver runs on Graphics Processing Units (GPUs) which allow for faster calculations and in addition the code can be highly parallelised by solving different blocks on different processors.

All simulations assumed fully turbulent boundary layers and used the Spalart-Allmaras turbulence model [80] with a source term scaling factor equal to 1. The Spalart-Allmaras turbulence model for analysis of transonic compressors has been used many times before and has been shown to give good results (e.g. [7, 44, 97]). The flow at the walls is allowed to slip and a wall function is used to approximate the wall shear stresses. The first grid point from the wall should therefore lie either in the viscous sub-layer or in the logarithmic region of the turbulent boundary layer and the solver will automatically switch between a wall function for each region in order to use the most appropriate wall function for each cell.

Steady simulations of multiple blade rows made use of a mixing plane [26] between adjacent blade rows in order to transfer information between adjacent blade rows with different rotational speeds. At a mixing plane the flow is mixed out in the pitch-wise direction while the spanwise profile is conserved.

Unsteady (URANS) simulations used the dual time-stepping method [45] where inner time steps converge the flow to a solution, similar to the steady state solution, within each outer step for which the geometry, and the flow, is advanced in steps of real time. In unsteady simulations the flow is interpolated between adjacent blade rows through a sliding plane. This technique is investigated thoroughly, using the Turbostream solver, by Sohoni et al. [79] and is shown to transfer the flow field between blade rows well, provided a suitable mesh is used.

3.3 Computational Domain and Meshing

3.3.1 Steady Simulations

The CFD domain for the 3-stage steady simulations is shown in Fig. 3.1 and includes an inlet duct, with two rows of support struts, followed by an Inlet Guide Vane (IGV) row and three rotor-stator stages. The inlet duct is included in the CFD simulations in order to have accurate endwall boundary layers at entrance to the IGV row and to account for any losses from the support struts as well as simulating the effect of meridional streamline curvature

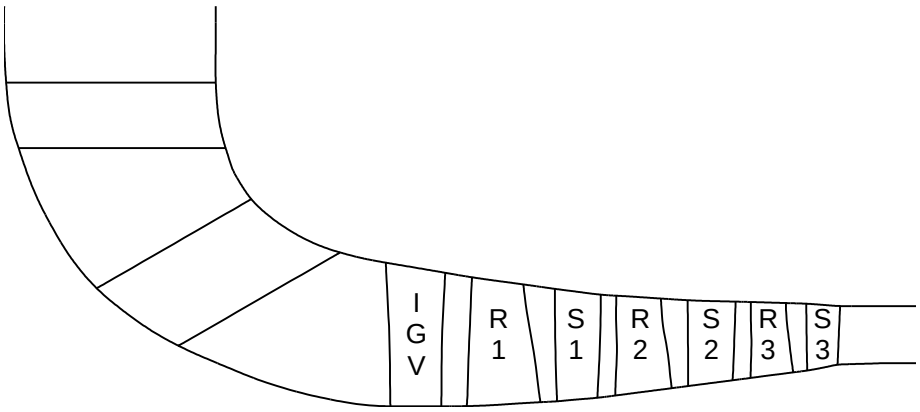

Fig. 3.1 CFD domain

which leads to spanwise pressure variations at the rotor inlet. The 2 inlet struts are attached to the endwalls at both the hub and casing while the remaining blade rows are cantilevered meaning the IGVs and stators have hub tip gaps and the rotors have casing tip gaps.

The mesh is generated using NUMECA Autogrid with "O" meshes around the blades and "H" meshes upstream, downstream and in the blade passage. Tip gaps are meshed by an "O" mesh with an "H" mesh in the centre. The domain for the single stage calculations removes the middle and downstream stages (R2, S2, R3, S3) and a parallel exit duct is added downstream of stator 1.

3.3.2 Boundary Conditions

The inlet boundary conditions are set upstream of the inlet duct and a uniform profile is given for stagnation temperature, stagnation pressure and flow angle. This allows the endwall boundary layer to develop in the same manner as the experimental rig. The flow angle is set to match the radial direction while the stagnation temperature and stagnation pressure are set to 288.15 K and 101325 Pa respectively. The inlet boundary condition is the same for all simulations.

The outlet boundary condition is set as a static pressure on the casing and the variation along the span is set by simple radial equilibrium. This exit back pressure is varied for different simulations in order to achieve operating points at different pressure ratios.

3.3.3 Mesh Independence

In order to have confidence that the results are not affected by the quality of the mesh it is necessary to make sure that the mesh is fine enough so that the calculated results

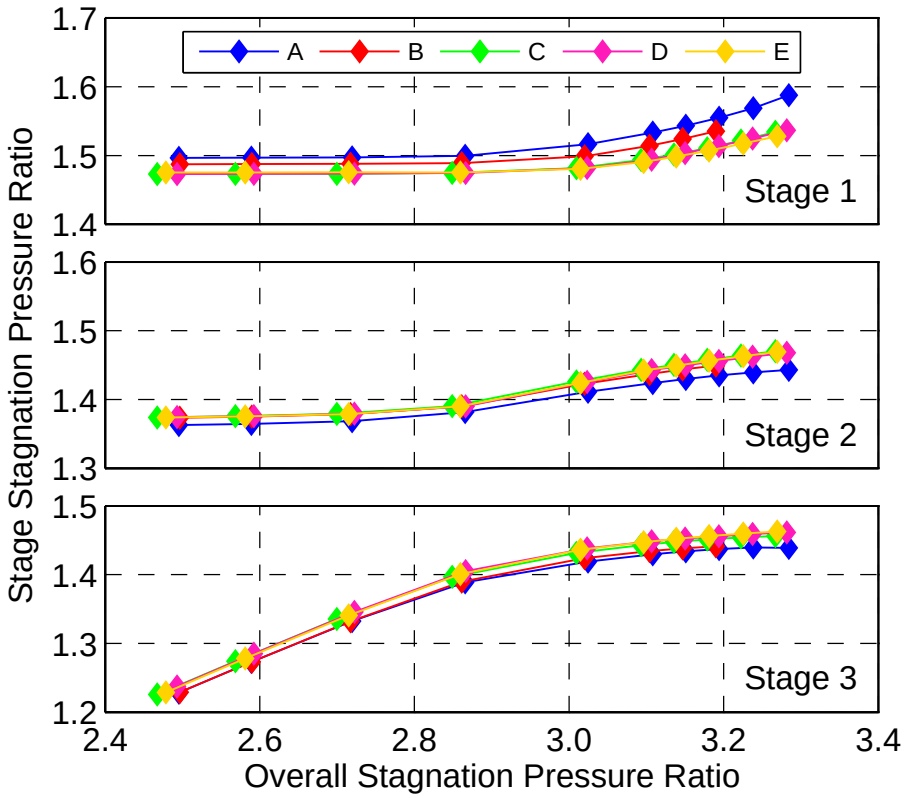

Fig. 3.2 Individual stage pressure ratios for meshes A to E

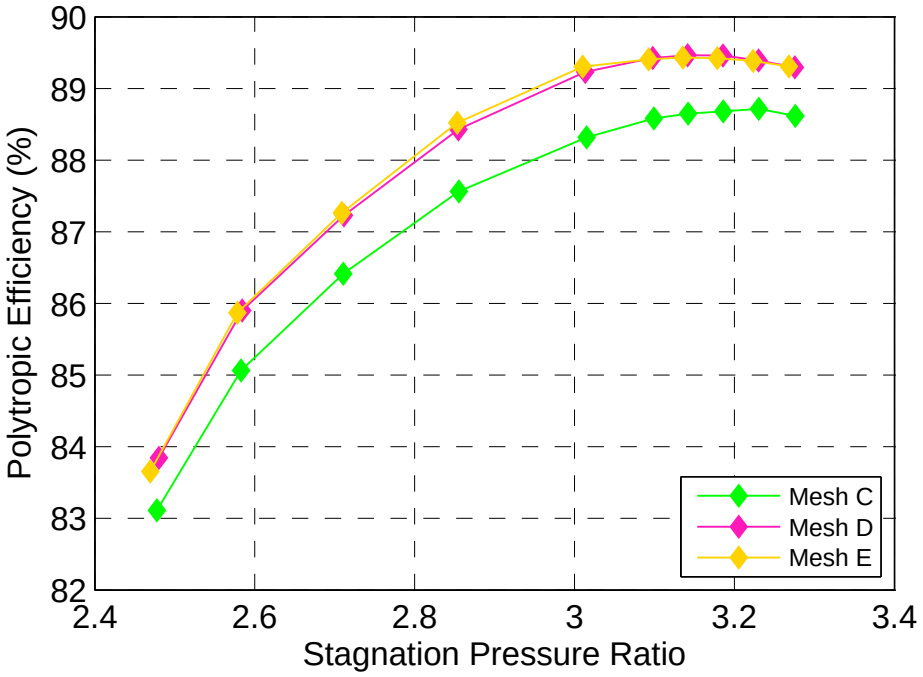

Fig. 3.3 Overall efficiencies for meshes C to E

Table 3.1 Mesh parameters

Mesh	y^+	Nodes per Rotor 1 Passage	Total Nodes
A	>30	0.5×10^6	4.5×10^6
B	5–15	0.6×10^6	5.3×10^6
C	≤5	1.2×10^6	9.7×10^6
D	≤5	1.6×10^6	11.1×10^6
E	≤5	6.4×10^6	52.8×10^6

are sufficiently independent of the density of the mesh. The mesh density required was established by calculating the 3-stage design speed characteristics on five different meshes ranging from 4.5 million nodes to 52.8 million nodes. Mesh details for each mesh are given in Table 3.1. In a multistage calculation the most fundamental feature to correctly predict is the stage matching. Figure 3.2 shows the individual stage stagnation pressure ratios plotted against the overall stagnation pressure ratio on the design speed line for each of the five meshes. It can be seen that Meshes A and B predict a different stage matching from the finer meshes, particularly for stage 1. From this it can be stated that it is important to have the first grid point in the laminar sub layer of the boundary layer by ensuring the first grid point is at a y^+ of less than five.

Having established mesh independence to the stage matching between meshes C, D and E, the predicted overall efficiency is compared in Fig. 3.3. Mesh C is seen to predict a lower efficiency while Meshes D and E give similar efficiency predictions. It has been demonstrated that the results are adequately mesh independent between Meshes D and E so the rest of the work will present results from simulations based on Mesh D.

3.3.4 Unsteady Simulations

In order to perform unsteady simulations of multiple blade rows with different blade counts, it is necessary to model multiple blade passages in each blade row. While some calculations have been performed of the whole annulus, it was decided to model one quarter of the annulus for the majority of unsteady simulations in order to make them quicker and more affordable. In order to be able to simulate one quarter of the annulus the blade counts of some blade rows had to be adjusted, as detailed in Table 3.2, so that the domain was periodic. In order to minimise the effect of adjusting the blade count on the performance predictions it is necessary to minimise any effect on the stage matching so the blade sections were scaled to maintain a constant pitch-to-chord ratio. In addition the axial position of each blade row was moved so that the upstream inter-blade-row spacing to chord ratio was maintained constant. The

Table 3.2 Individual row blade counts

Blade Row	Real Blade Counts	Adjusted Blade Counts	% Change
IGV	26	24	8%
Rotor 1	21	20	5%
Stator 1	32	32	0%
Rotor 2	23	24	4%
Stator 2	32	32	0%
Rotor 3	29	28	4%
Stator 3	44	44	0%

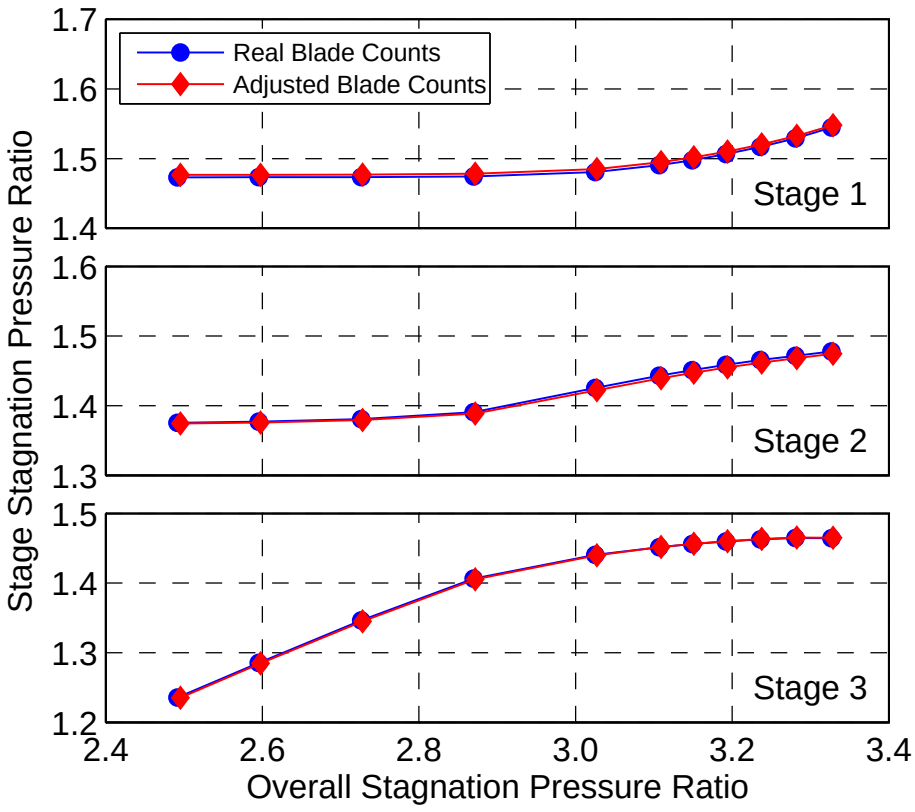

Fig. 3.4 Individual stage pressure ratios for real and adjusted blade counts

outcome of these adjustments is that the differences in the stage matching, between the real blade counts and the quarter annulus adjusted blade counts, are minimal as shown in Fig. 3.4.

In order to further verify the method of adjusting the blade count a full annulus unsteady simulation performed at the design point using the real (unadjusted) blade counts is compared to results from quarter annulus unsteady simulations with the adjusted blade count. When performing full annulus calculations the exit duct is extended so that its length is as long as the circumference of the compressor. This is done to give enough space in the domain to allow large scale waves to establish themselves. The full annulus simulation is performed on the optimised blade geometry and it is compared to the results from the quarter annulus simulations, also of the optimised geometry, in Figs. 3.5 and 3.6. These plots show that both the overall efficiency and the stage matching agree very well between the full and quarter annulus simulations. In order to be able to make fair comparisons, any analysis that requires comparison of results between steady and quarter annulus unsteady simulations have been performed using results that have been calculated from steady and unsteady simulations that both used the adjusted blade counts.

As previously mentioned the unsteady simulations use the dual time stepping method and sliding planes are placed between the plane rows. Physical time in the unsteady simulations was incremented at a rate of 72 outer time steps per rotor 3 blade passing (2088 steps per full revolution). The total number of outer time steps performed is large enough to ensure that the significant flow parameters have become periodic, in particular the overall efficiency and mass flow rate are monitored. Results are calculated using mass averaged properties and unsteady results are then time averaged over at least one full revolution of the CFD domain.

Other than comparing time averaged unsteady simulation predictions with steady simulation predictions, the investigation of the unsteady effects in this thesis is restricted to the interaction of the pressure waves from one blade row to another. This means that the most important frequencies to capture are those corresponding to the number of blades in each blade row, and as such there is a particular need to capture frequencies up to Engine Order (EO) 44 - corresponding to the number of blades in the stator 3 blade row. The number of time steps used in the unsteady simulation corresponds to EO 1944 so is easily enough to capture the fundamental frequencies and the first few harmonics of all the blade rows. At the other end of the scale, by using full annulus simulations and having extended the exit duct domain, it is possible to capture frequencies as low as EO1. The unsteady analysis in this thesis focuses on the unsteady interactions between blade rows which are on a much larger length scale that the unsteady effects found within the boundary layers. Therefore we can say that the quasi-steady boundary layer models used in the URANS solver will be adequate.

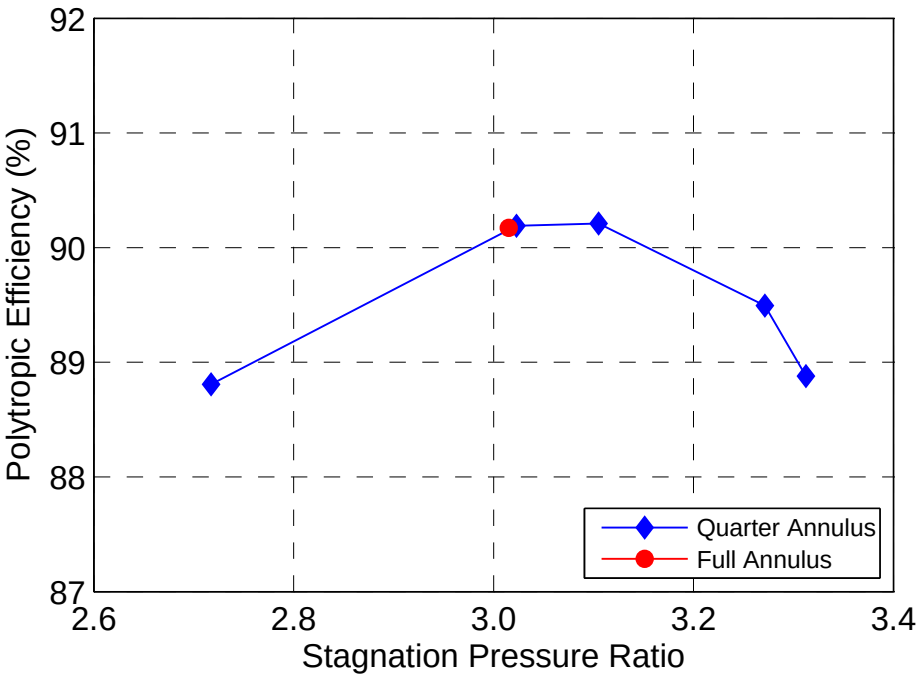

Fig. 3.5 Overall efficiency for unsteady simulations of the optimised blade geometry

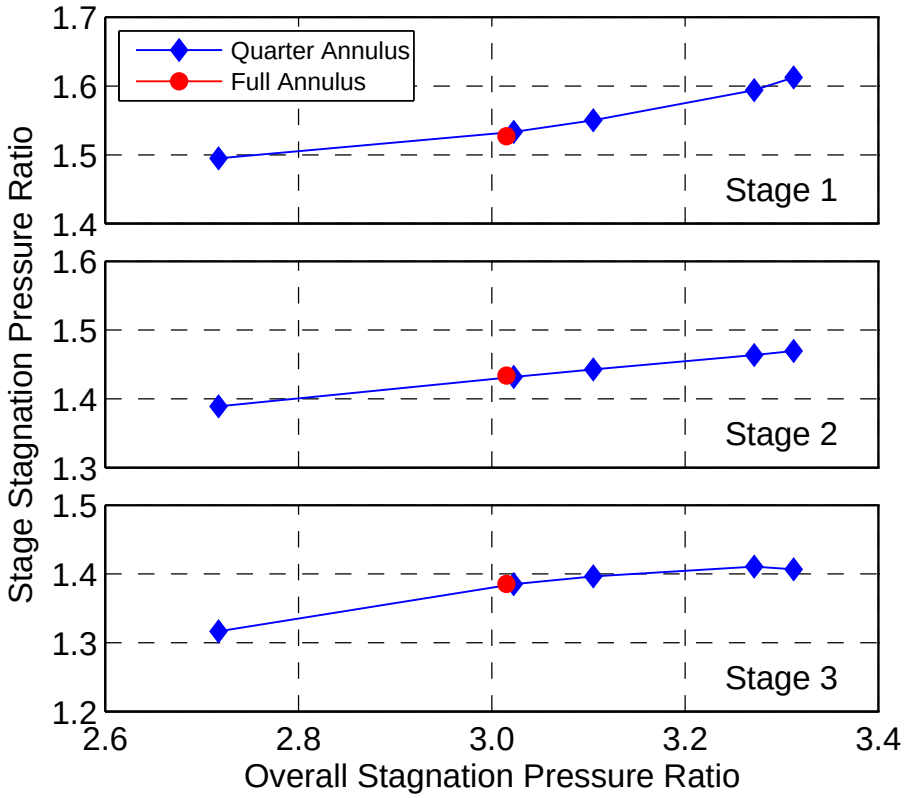

Fig. 3.6 Individual stage pressure ratios for unsteady simulations of the optimised blade geometry

3.3.5 Computational Resources

All the simulations were performed on Nvidia K20c Tesla GPUs operated by the University of Cambridge Research Computing Services. Typical computational resources for different types of simulations are given in Table 3.3.

Table 3.3 Computational Resources

Simulation	No. GPUs	Run Time (hours)	GPU Time (hours)
Steady Simulation - 1 Stage	2	1.5	3
Steady Simulation - 3 Stage	2	3.5	7
Unsteady Quarter Annulus Simulation - 1 Stage	48	11	528
Unsteady Quarter Annulus Simulation - 3 Stage	36	29	1044
Unsteady Full Annulus Simulation - 3 Stage	96	99	9504

3.4 Comparisons to Experimental Data

3.4.1 Experimental Set-up

All the experimental results have been obtained by Siemens Industrial Turbomachinery Ltd using the 3-stage transonic compressor test rig [56] in Lincoln. The test rig contains a working section the same as the CFD domain shown in Fig. 3.1 with the addition of an exit diffuser which leads to an exit plenum. The test rig is well instrumented, however, only the relevant instrumentation is outlined here.

Temperature and pressure measurements are obtained at the compressor inlet (upstream of the IGVs but downstream of the support vanes) and compressor exit (downstream of stator 3 but upstream of the exit diffuser). Total pressure rakes are located at these inlet and exit planes and a total temperature rake is located at the exit plane. In addition the temperature is measured in the inlet volute and the exit plenum. These measurements are used to calculate the overall pressure ratios and polytropic efficiency. When calculating the polytropic efficiency the exit temperature rake measurements are used in preference to the exit plenum temperature as the measurements differ and it is thought that the flow is not fully mixed out at the location of the measurement points in the plenum so the extra profile data provided by the rakes is required.

The inlet and exit rakes measure at 5 points across the span for 7 locations around the circumference. When comparing CFD and experimental results the CFD results are calculated

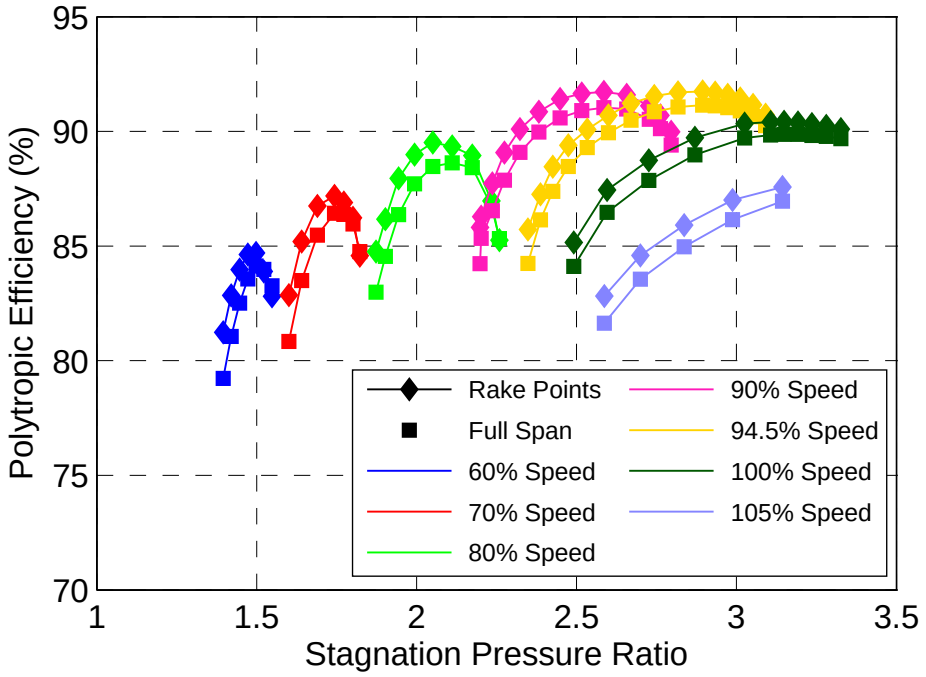

Fig. 3.7 Difference in predicted compressor efficiency when calculated using values integrated across whole span and values taken from spanwise locations of rake probes

from data extracted from the same spanwise positions in order to make fair comparisons. This is important because, due to the radial position of the probes in the inlet and exit ducts, the majority of the boundary layer is not captured by the experimental data. The difference in the efficiency predicted by the CFD simulations when using values integrated across the whole span and values taken from the same positions as the experimental rake data is shown in Fig. 3.7. Calculating the efficiency from values integrated over the whole span always leads to a lower predicted efficiency because a portion of the loss in the boundary layers at the exit is not captured by the experimental rakes (and hence the CFD data extracted from the same positions).

Mass flow rate is measured by an orifice plate downstream of the exit plenum and is corrected to the same inlet temperature and pressure as the CFD. Similarly the rotational speed is corrected to the inlet temperature. Additional measurements of total pressure and temperature are taken from probes mounted on the leading edges of some of the blades in the stationary blade rows (IGV and stators). This provides data for individual stages and allows calculation of pseudo stage pressure ratios where a pseudo stage is defined as a stator-rotor pair (instead of a rotor-stator pair). When making comparisons of stage pressure ratios between the CFD results and the rig leading edge instrumentation, it is important

(as discussed above for efficiency comparisons) to use CFD data from the same spanwise locations as the probes on the IGV and stator leading edges.

3.4.2 Comparisons Between Experimental and CFD Results

The overall performance of the compressor with the original blade geometries is compared with steady CFD simulations in Figs. 3.8, 3.9 and 3.10 for a range of operating speeds. Figure 3.8 shows that the mass flow rate and pressure ratio is well predicted by the CFD at 60% and 70% speeds. At higher speeds, the mass flow rate is over predicted by the CFD with the largest discrepancies occurring between 90% and 100% speed. It is however noteworthy that the experimental data points at these speeds also have a large amount of variation between them. While some points give a mass flow rate significantly lower than the CFD result, other data points are very close to the CFD prediction. Part of the reason for the low repeatability of the experimental results is that the tests were performed over a period of many years and on different builds of the test rig. The efficiencies from the experimental data in Figs. 3.9 and 3.10 show better repeatability apart from a couple of clear outliers at low speed. Again there is better agreement between the CFD and experimental results at low speeds however at high speeds the trends are still well matched, particularly at design speed and 105% speed where the CFD and experimental results are very similar but just offset slightly.

$$C_p = \frac{(P_{02} - P_{01})}{\rho_1 U_{tip}^2} \tag{3.1}$$

It has already been stated that it is very important to correctly simulate the stage matching in a multistage compressor so the CFD stage pressure rises will now be compared to the experimental results. Figure 3.11 shows the pseudo stage pressure coefficient (Eqn. (3.1)), for each stage, plotted against the flow coefficient of the stage. The stage pressure coefficient plotted is the pseudo stage pressure coefficient because it is calculated from pressures taken from the leading edge of the stationary blade rows and represents an IGV-rotor or stator-rotor pair. This allows direct comparison of the CFD results and the experimental results by using measurements from the IGV and stator leading edge instrumentation in the test rig. There is a good match between the CFD and experimental data for stage 3, however, there is a discrepancy in the flow coefficient between the CFD and experimental results for stages 1 and 2. This is partly due to the variation in the mass flow rate from the experimental results, as discussed above. When the throttle is closed, Fig. 3.11 shows that the majority of the extra

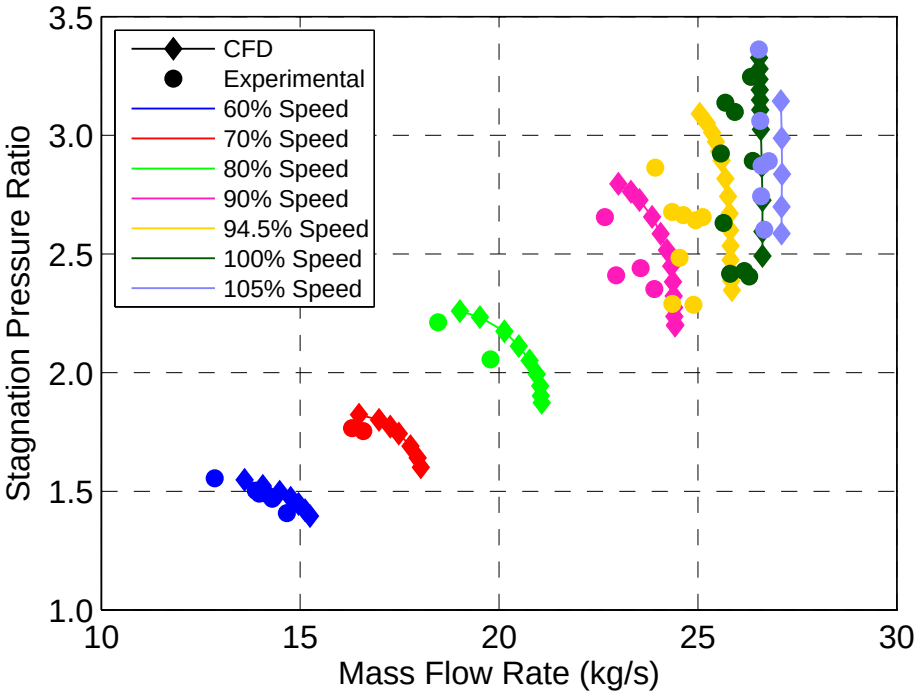

Fig. 3.8 Compressor performance for original geometry

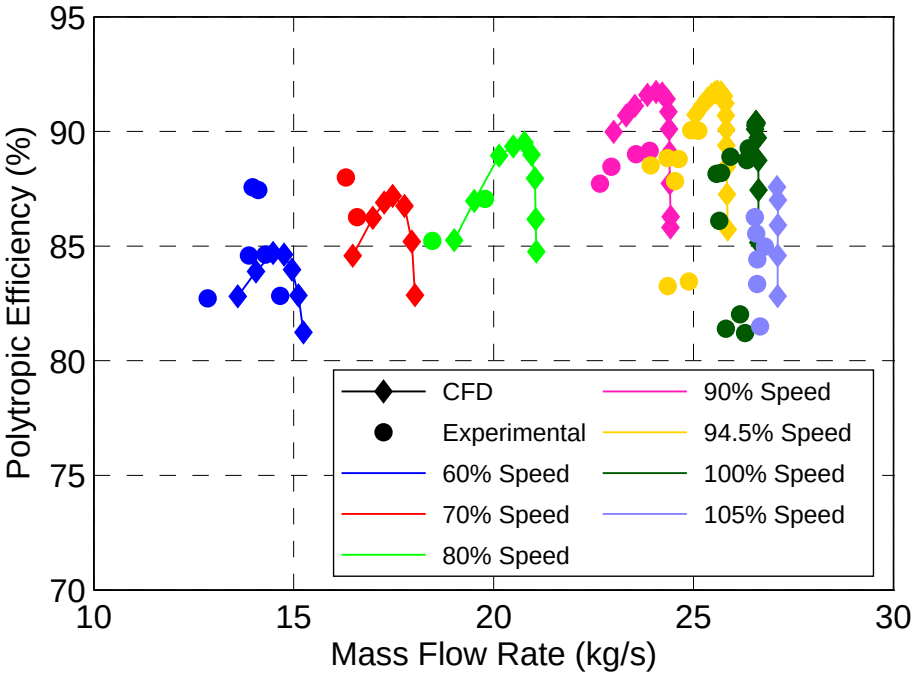

Fig. 3.9 Compressor efficiency for original geometry

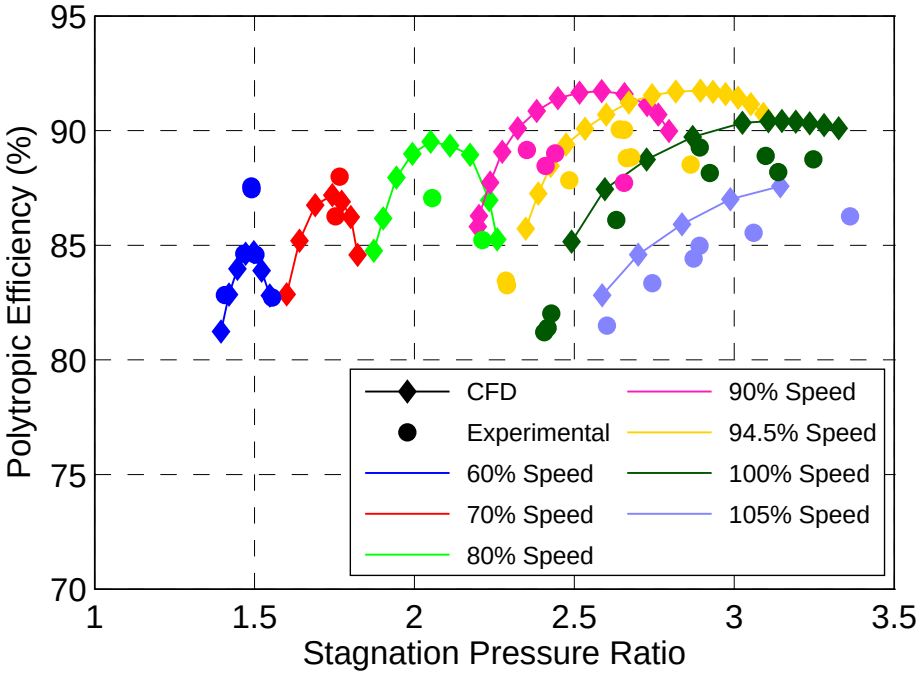

Fig. 3.10 Compressor efficiency for original geometry

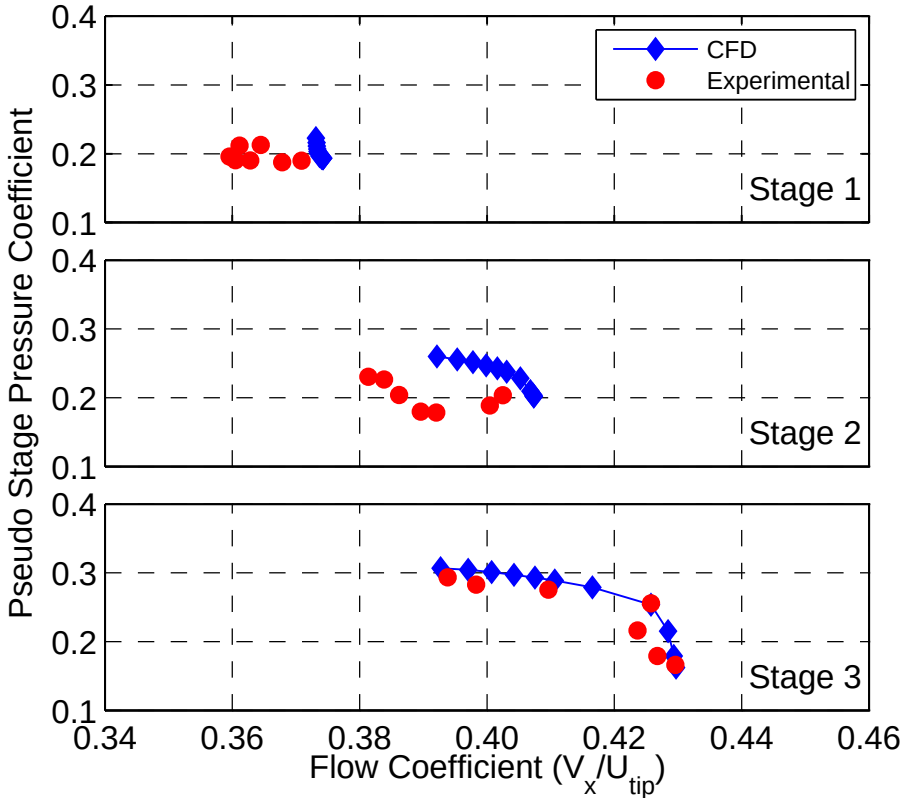

Fig. 3.11 Pseudo stage pressure coefficients for original geometry at design speed

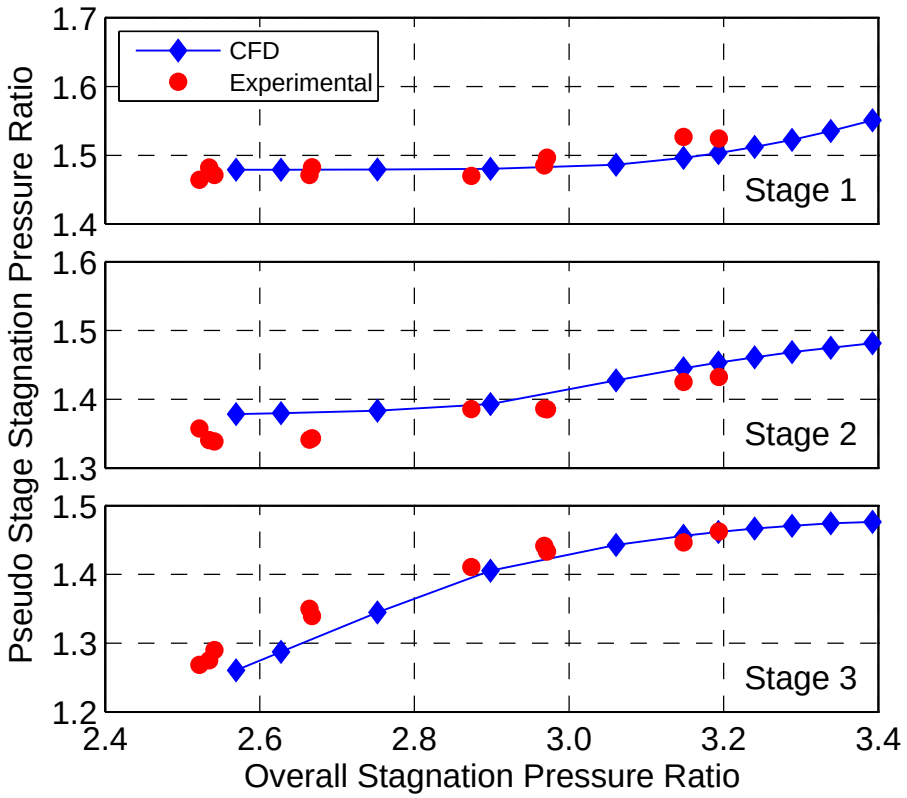

Fig. 3.12 Pseudo stage pressure ratios for original geometry at design speed

pressure rise is picked up by stage 3 with stage 2 picking up some of the additional pressure rise. However, due to each stage operating with different flow coefficients it is hard to see how the individual stage pressure rises vary as the operating point of the machine is changed. This, and the discrepancy in the flow coefficients between the CFD and experimental results makes comparing the CFD and experimental results difficult.

In order to overcome this, the individual stage pressure ratios are plotted against the overall pressure ratio for the design speed in Fig. 3.12, and also for 90% speed in Fig. 3.13. This allows the variation of the stage pressure ratios to be seen for the whole operating range of the compressor more clearly and allows better comparison between CFD and experimental data. The pressure ratios presented are pseudo stage pressure ratios in order to use the experimental results taken from the IGV and stator leading edge instrumentation in the test rig as described above. Generally the CFD results show very good agreement with the experimental results. For the design speed, shown in Fig. 3.12, stage one is well characterised by the CFD simulations across the whole range and stages 2 and 3 are also well predicted at and above the design pressure ratio of 3. At lower pressure ratios there is a small mismatch between the CFD and experimental results although the general trends are still well captured.

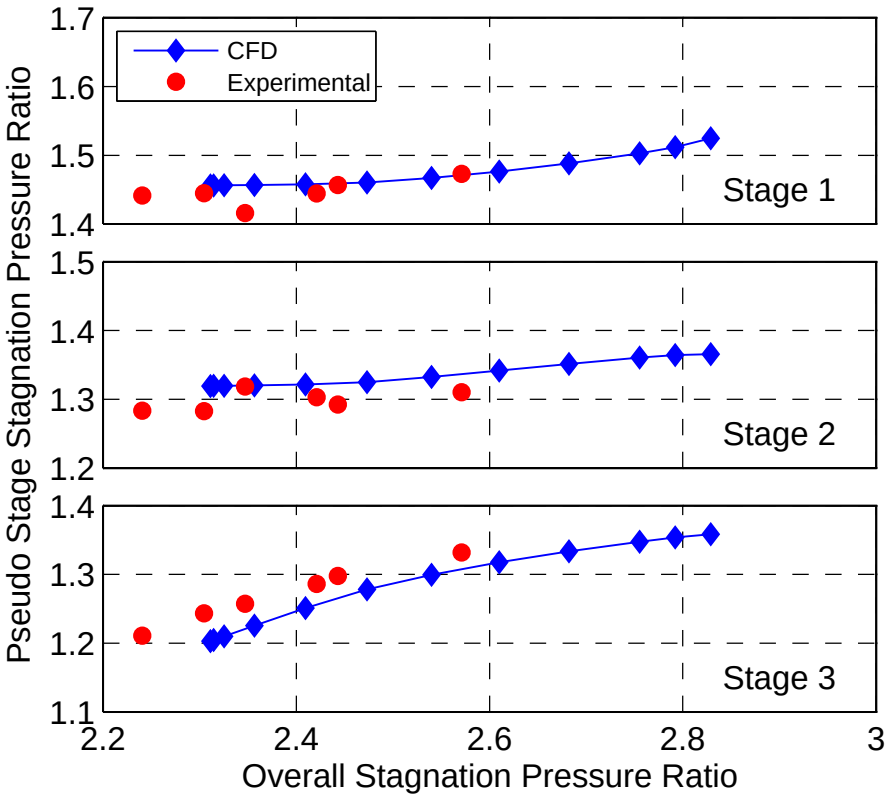

Fig. 3.13 Pseudo stage pressure ratios for original geometry at 90% speed

Figure 3.13 shows that the stage 1 pressure ratio is also accurately predicted by the CFD at 90% speed. The results for stage 2 and 3 are very similar to the results at design speed, with stage 2 slightly over predicted and stage 3 slightly under predicted, but again there is a very good correlation between the CFD and experimental results. At 90% speed it was found that the CFD efficiencies did not match with the experimental results very well but having shown that the stage matching is correct means that the fundamental flow characteristics have been correctly captured and this gives a greater chance of accurately predicting the changes in the overall performance even if the absolute magnitudes are not correct.

It is possible to compare the CFD results to the experimental data in even more detail by looking at the spanwise profiles measured by the vane leading edge probes. Figure 3.14 shows the results from the leading edge pressure measurements from a design speed operating point with a pressure ratio of 2.89—just below the design pressure ratio. The steady CFD results are also plotted in Fig. 3.14 and show values for the entire span at the same locations. Both the CFD and experimental data is plotted as a ratio to the inlet stagnation pressure. The profiles at all 4 locations are predicted very well by the CFD simulations. Similarly the temperature results are shown in Fig. 3.15 for the same locations and again as a ratio

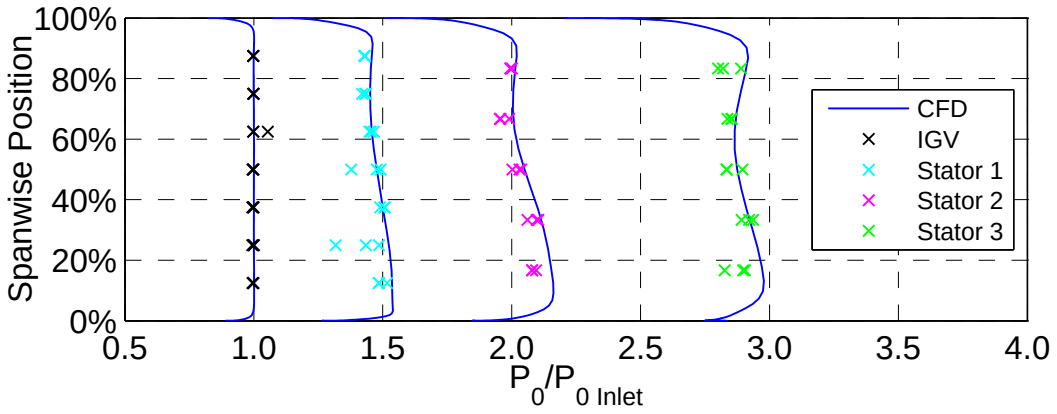

Fig. 3.14 Vane leading edge pressure measurements

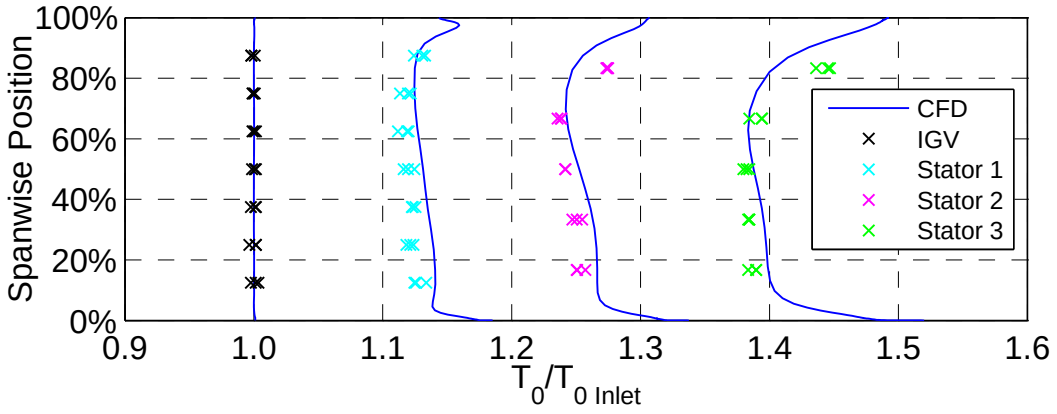

Fig. 3.15 Vane leading edge temperature measurements

to the inlet stagnation temperature. The profiles are captured well in the CFD results but not as well as the pressure profiles. Discrepancies appear particularly near the casing where the CFD under predicts the temperature rise. This is likely due to an under prediction of the downstream mixing of the tip region flow in the CFD or an under estimation of the tip clearance effects. Given that this is the region of the span that has the greatest mass flow this lower temperature prediction would contribute to a higher efficiency prediction in the CFD. Both the pressure and temperature profiles have a significant variation across the span which means a small shift in the shape of the CFD profiles could lead to different values being extracted when picking out the discrete spanwise points for comparison to the experimental results. This is another potential source of error for the difference seen between the CFD and experimental overall efficiency results.

The CFD and experimental results are compared again in Figs. 3.16 and 3.17, this time for the optimised blade geometry. Figure 3.16 shows experimental results for 94.5% speed and 100% speed and it can be seen that the data is much more consistent and repeatable

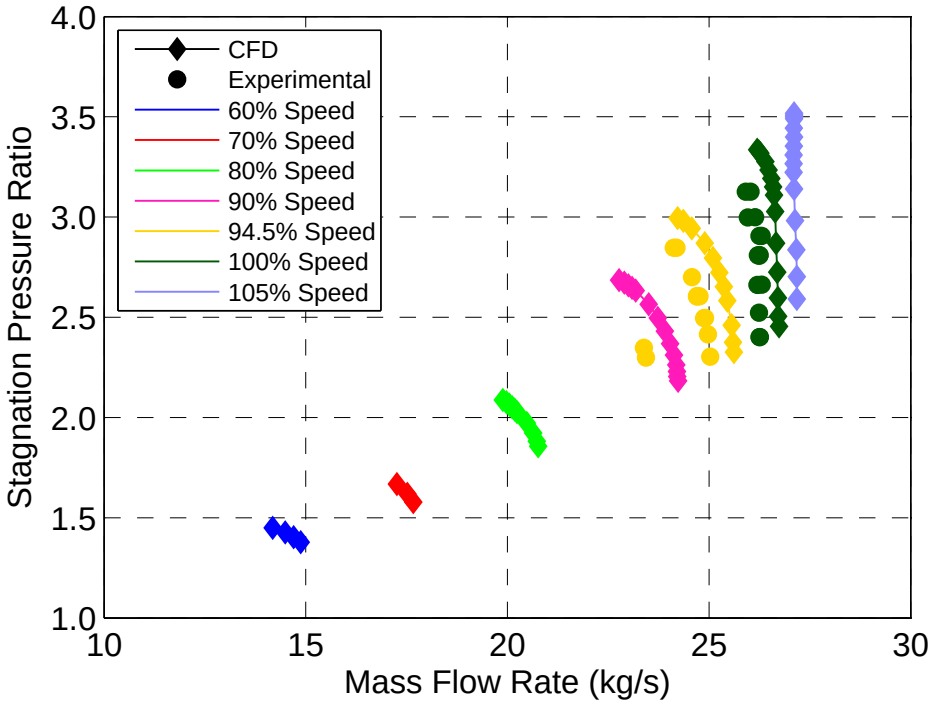

Fig. 3.16 Compressor performance for optimised geometry

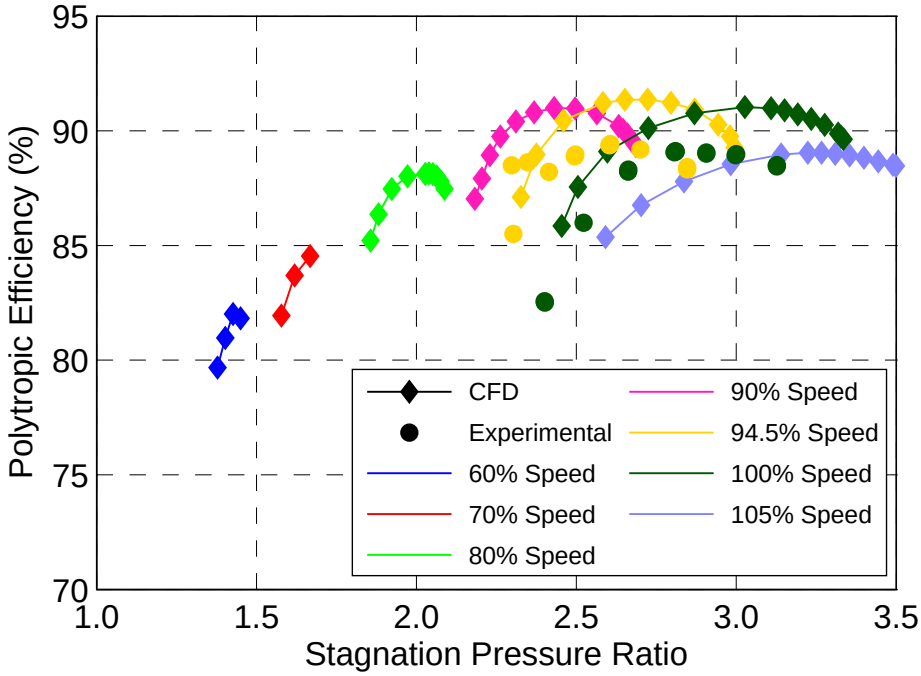

Fig. 3.17 Compressor efficiency for optimised geometry

than the results from the original geometry (except for 2 points at 94.5% speed with a very low mass flow rate). For both speeds the CFD captures the shape of the curve but the CFD still gives a higher mass flow rate than the experiments. The curves for the efficiencies in Fig. 3.17 show similar discrepancies as the original geometry. The CFD results give a higher efficiency than the experimental results and peak efficiency occurs at a lower pressure ratio however the general shape of the curve is still predicted correctly.

3.5 Geometry Modifications

3.5.1 Vane Rescheduling

The experimental rig contains four rows of variable guide vanes (IGV and 3 stator blade rows) which can be independently set to a range of stagger angles. A number of the CFD simulation results that will be shown have been performed with these blade rows having been rescheduled. The rescheduling was performed in NUMECA Autogrid as part of the meshing process. Blades were rescheduled by rotating them around the radial line at 50% of the blade's chord. The mesh was then regenerated using the same configuration.

3.5.2 Axial Spacing

In order to investigate the effect of the IGV-Rotor interactions on the compressor performance it was necessary to alter the size of the axial gap between the IGV trailing edge and the rotor leading edge by modifying the compressor geometry. In order to make the gap smaller the rotor and all the downstream blade rows were shifted axially in order to make the gap 40% the size of the original gap, as measured at mid span. Given that the radii of the hub and casing are not constant it was also necessary to adjust the hub and casing lines so that they remain continuous. Figure. 3.18 shows two different methods for achieving this. Figures. 3.18a and 3.18b show the original geometry of the hub and casing lines in black and the modified geometry, with 40% gap spacing, in red. The leading and trailing edges of the IGV and Rotor 1 are also shown. In Fig. 3.18a the casing radius at the IGV trailing edge has been kept constant. This has created a sudden change in the casing line. In Fig. 3.18b the casing radius at the IGV trailing edge has been allowed to change in order to reflect the smaller casing radius at the rotor leading edge that is now closer to the IGV trailing edge. This has given a much smoother radius variation and it is chosen to use this method for varying the axial spacing so that the impact of the changed casing shape on the flow is minimal. The impact of the change in the casing line is presented later in this thesis along with the investigation into the effects of the IGV-Rotor axial spacing.

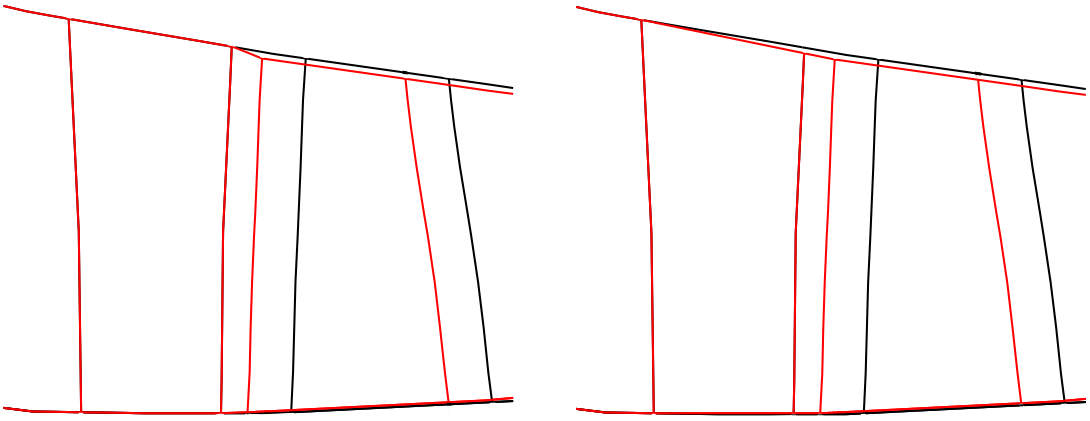

(a) IGV casing line fixed (b) IGV casing line adjusted

Fig. 3.18 Meridional views of IGV and rotor 1 at design spacing (black) and 40% spacing (red)

3.6 Conclusions

This chapter has set out to explain how the CFD simulations have been performed and validate the CFD results to experimental results. Confidence in the CFD method has been gained by showing that the mesh used is sufficient, so that the results obtained are regarded as independent of the mesh used. It has also been shown that the method of performing unsteady simulations by modelling a quarter of the annulus and adjusting the blade counts doesn't affect the results as the stage matching remains the same and the results match the full annulus simulation.

The CFD data has been compared to experimental results and has been shown to produce very similar trends despite an offset in the mass flow rate and a difficulty in predicting the efficiency exactly. Some of the experimental data has a large variation and it is believed to be hard to match temperature measurements between CFD and experiments without performing a full span traverse because large variations in temperature are predicted for small changes in spanwise position. In addition it is acknowledged that a weakness of CFD is the ability to accurately predict the flow in the rotor tip region due to the complex and intense turbulence in this area.

Overall the consistency of the comparisons between CFD and experimental results, and the accuracy with which the stage matching is predicted, gives good confidence in the ability of the CFD to accurately predict trends in the data but without the ability to predict absolute values of efficiency.

Chapter 4

Analysis of Unsteady Effects in Transonic Compressors

4.1 Introduction

Steady and unsteady CFD simulations are important design tools for a compressor designer. Steady simulations are generally able to predict the performance of a compressor reasonably well, however, various assumptions are made about the flow, most significantly that the flow in each blade row is steady with constant inlet conditions which are time independent. Unsteady simulations are able to model more of the physical flow features such as the interaction between downstream blades and the wakes from the upstream blade row and the propagation of the unsteady pressure potential between blade rows. In a steady simulation the transfer of this unsteady information and the wakes between blade rows is prevented when the flow passes through a mixing plane between adjacent blade rows. Modelling more of the physical flow, and therefore making fewer assumptions, should lead to a better prediction of the losses and a more accurate prediction of the compressor performance as well as giving better insight into the unsteady flow features.

In an ideal situation, unsteady simulations would always be chosen in preference to steady simulations, however, an unsteady simulation typically costs 1–3 orders of magnitude more to perform than a steady simulation. While it may be feasible to perform unsteady simulations at the nominal design operating condition, it is often not possible to perform unsteady simulations at a great number of off-design conditions within the time or budget available. Therefore it is useful for the designer to have an understanding of which operating conditions are likely to have a significant variation in the overall performance predictions

between steady and unsteady simulations so that the designer knows where on the operating map to target unsteady simulations during the design cycle.

The results from steady and unsteady simulations are presented in this chapter and compared in order to gain an insight into how the unsteady flow affects the predicted compressor performance. All the unsteady calculations presented in this chapter have been performed using a quarter annulus model with the blade counts adjusted in order to make the domain periodic while the steady calculations have been performed modelling a single passage but with the same blade counts as the unsteady simulations. The overall efficiency is broken down into individual blade row efficiencies so that it can be determined where the efficiency predictions for steady and unsteady simulations differ.

Initially the analysis is performed on the original design geometry for the compressor. Results from isolated simulations of the front 1.5 stages of the compressor are presented with an analysis of each blade row individually for the design speed. It is found that the steady simulations always give a higher efficiency prediction than the unsteady simulations of the 1.5 stages. This is due to the steady simulations predicting higher IGV and rotor blade efficiencies than the unsteady simulations. The higher IGV efficiency is a result of not capturing the interaction between the IGV and the rotor leading edge shock. The higher rotor efficiency is due to a lower shock Mach number in the rotor passage. For the stator, the steady simulations are found to predict a lower efficiency than the unsteady simulations. This is partly due to attributing the fully mixed out rotor wake loss to the stator blade row but also because some of the stagnation pressure loss in the wake may be recovered as it passes through the stator blade passage.

Results for off-design speeds are presented next in order to show how the difference between steady and unsteady simulations changes at 90% and 110% speed. Next, results are presented from multistage simulations in order to assess the impact of the unsteady effects from the downstream blade rows on the front stage efficiency predictions and it is found that the presence of the downstream stage does not affect the unsteady characteristics of the front stage. This is an important finding as it means that the designer can analyse and design the front stage without needing to consider how the propagation of unsteady flow from the downstream stages will affect its characteristics. Finally a similar analysis is presented for simulations of the newer, optimised compressor geometry [90]. The conclusions remain the same for the different geometry suggesting that the findings can be applied to wider range of transonic compressor geometries.

Table 4.1 Difference in polytropic efficiency between steady and unsteady calculations at design speed

Pressure Ratio	$\Delta\eta_p$
1.41	0.05
1.46	0.06
1.55	0.16
1.62	0.74
1.63	1.05

4.2 Front Stage Design Speed Analysis

Figure 4.1 shows the polytropic efficiency calculated from steady and unsteady simulations of the front stage (including the IGV blade row) at the design speed. The unsteady simulations predict a lower efficiency across the whole characteristic and the difference between the predicted efficiency of the steady and unsteady simulations increases with the pressure ratio, as shown in Table 4.1. In order to understand this variation it is helpful to look at the efficiency of the individual blade rows. The isentropic efficiencies for individual blade rows is shown in Fig. 4.2 where the isentropic efficiency for single blades is approximated by the definition in Eqn. (4.1) as shown by Denton [27].

$$\eta_{isent} \approx 1 - \frac{\bar{T}_{stage\ outlet}\left(\bar{s}_{blade\ outlet} - \bar{s}_{blade\ inlet}\right)}{\Delta\bar{h}_{stage}} \tag{4.1}$$

For steady simulations the entropy is measured upstream of the location of the mixing planes at both blade inlet and outlet. This means that the mixing loss associated with the wakes from the upstream blade row is included in the calculation of the blade row isentropic efficiency. This is an appropriate treatment of the mixing loss because in reality (with no mixing plane treatment) the wakes from the upstream blade row would indeed be mixing out in the blade row that is being analysed.

It can be seen that the variation in the single stage efficiency between steady and unsteady simulations is due to a variation in the efficiency within different blade rows. Despite the single stage results having a small efficiency delta (defined in Eqn. (4.2) and shown in Table 4.1) between steady and unsteady simulations at lower pressure ratios, it is seen in Fig. 4.2 that this is only because the efficiency deltas within the rotor and stator blade rows cancel each other out. At higher pressure ratios the steady and unsteady stator efficiencies start to converge while the rotor efficiency prediction is still lower for the unsteady simulation

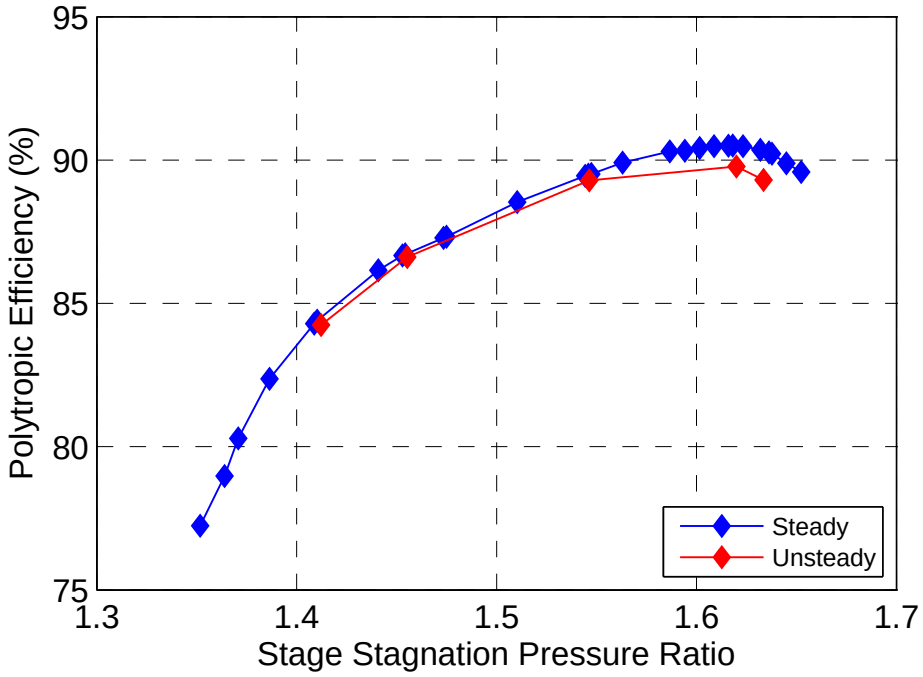

Fig. 4.1 Steady and unsteady polytropic efficiency predictions for 1.5 stage simulations at design speed

than for the steady simulation. This, combined with the slight increase of IGV efficiency in the steady simulations, leads to a greater single stage efficiency delta at higher pressure ratios.

$$\Delta\eta = \eta_{steady} - \eta_{unsteady} \tag{4.2}$$

4.2.1 Rotor Efficiency

The rotor predictions vary from a positive efficiency delta (steady simulation has a higher efficiency as defined in Eqn. (4.2)) of 1.3% at the lowest pressure ratio, to 0.6% near design. As the stage approaches stall, the efficiency delta increases again to 1.0%. In order to investigate the greatest efficiency delta for the rotor, which occurs at a pressure ratio of 1.41, the spanwise distribution of entropy increase through the rotor (including the mixing loss generated across the IGV-Rotor mixing plane) is plotted in Fig. 4.3. Results are plotted across the span and show a steady and unsteady simulation of the same pressure ratio. The unsteady simulation shows a higher entropy increase across the majority of the span which is to be

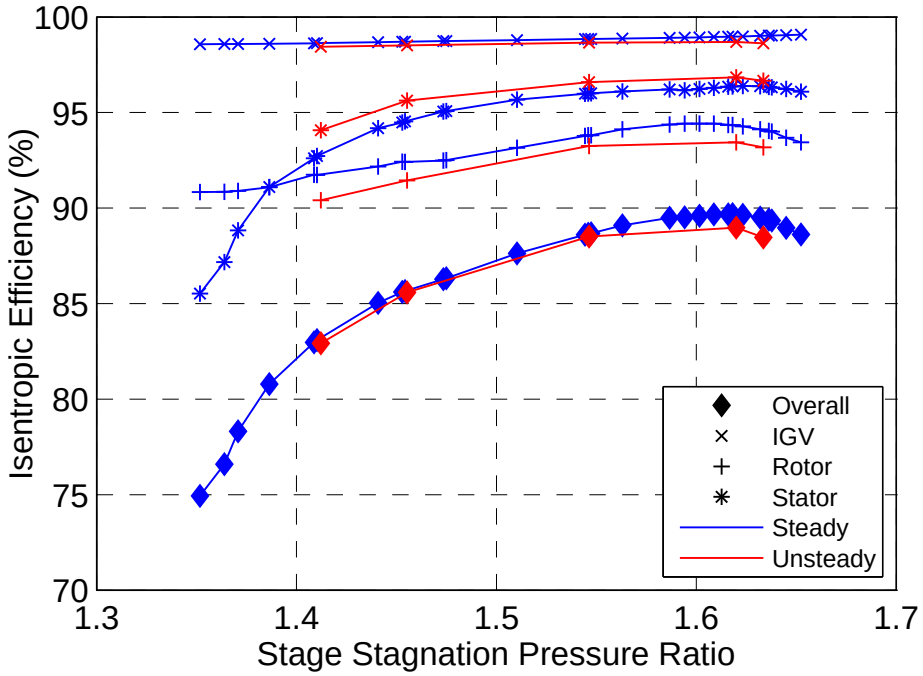

Fig. 4.2 Steady and unsteady isentropic efficiencies for 1.5 stage simulations at design speed

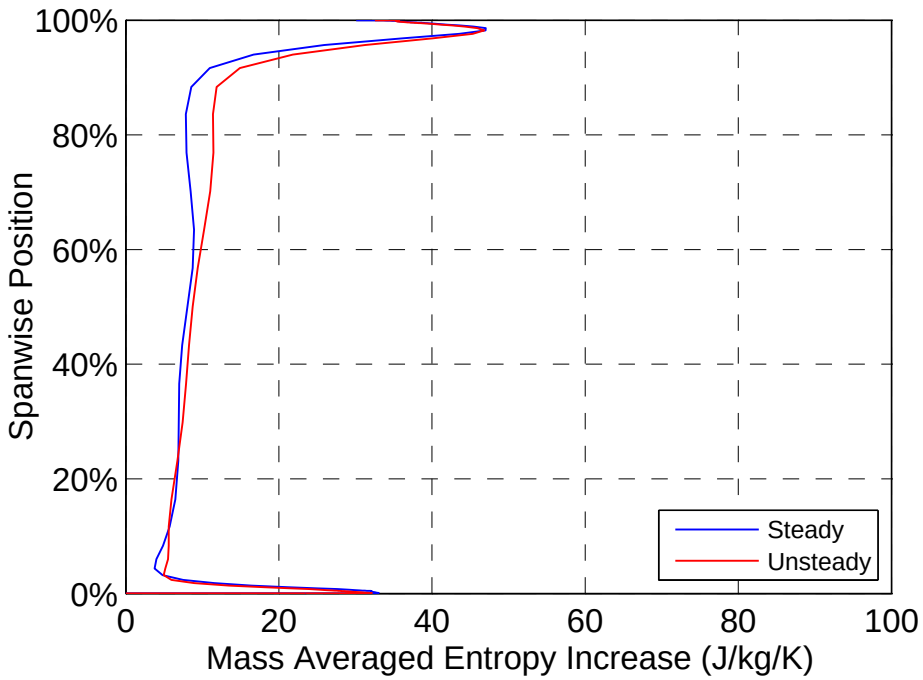

Fig. 4.3 Entropy increase across rotor near choke (including IGV-Rotor mixing plane entropy generation) at design speed for a pressure ratio of 1.41

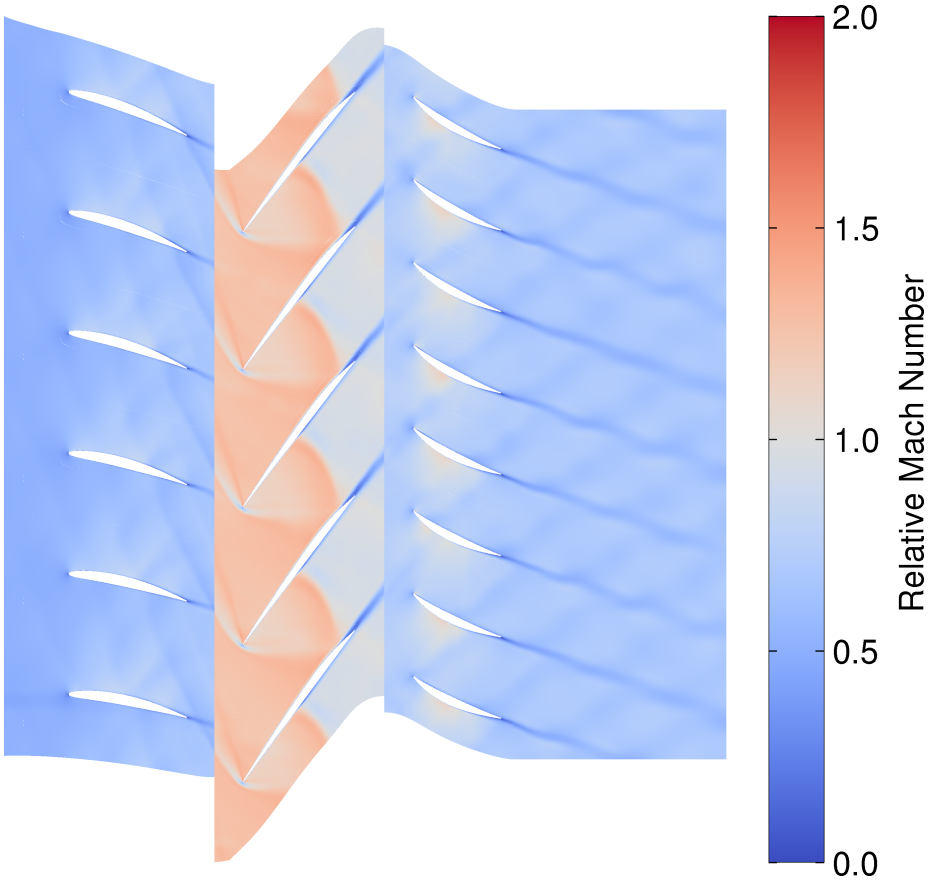

Fig. 4.4 Instantaneous unsteady relative Mach number at 80% span for pressure ratio of 1.41

expected as the unsteady simulation predicts a lower efficiency. The only exception to this is a small region just below 20% of span. The greatest discrepancy between the steady and unsteady results can be seen to occur in the upper half of the span with the greatest difference occurring at around 80% of span with a difference in specific entropy increase of 3.7 J/kg/K.

The greatest discrepancy, at 80% span is investigated further to explore the differences in the flow. Figure 4.4 shows the instantaneous relative Mach number for the unsteady simulation at a span of 80%. At this operating condition the rotor has a leading edge shock and a passage shock. The passage shock is located quite far into the rotor passage as the operating pressure ratio is low and the rotor is choked. It can be shown that the strength of the rotor passage shock is attributing to the greater entropy increase in the unsteady calculation. This is seen in Fig. 4.5 which shows the isentropic Mach number on the blade surface for the rotor at 80% span. The unsteady results at multiple instantaneous points, from throughout a complete cycle, are plotted in order to show the variation of the results over time. The passage shock can be clearly seen as a sudden drop in Mach number on the pressure surface at around 50% chord. The shock can be seen to move throughout the cycle in the unsteady

simulation although the movement is less than 1% of chord. It can be seen that the steady simulation predicts a lower Mach number (1.11) immediately upstream of the shock wave compared to the unsteady simulation Mach number (1.16). This gives a weaker shock which has less loss and contributes to the higher rotor isentropic efficiency.

Using the Mach number relations for static pressure and static temperature rise across a normal shock it can be calculated that the change in specific entropy between the steady and unsteady simulations across the shock wave is 1.0 J/kg/K when calculated using the maximum isentropic Mach number on the blade surface (given above). In the centre of the passage an entropy analysis also shows that the shock Mach number is lower in the steady simulation. To do this it is assumed that all the entropy generation in the centre of the passage is as a result of the passage shock and the specific entropy is calculated upstream and downstream of the shock. From the change in entropy across the shock, and by again using the Mach number relations for static pressure and static temperature ratios across a normal shock, it is possible to calculate the Mach number normal to the shock. Using this method, the Mach number normal to the shock, is calculated to be 1.11 in the steady simulation and 1.18 in the unsteady simulation. (The Mach number calculated from the entropy analysis is lower than the real Mach number because it represents only the portion of the Mach number normal to the shock wave.) Using these results for the shock Mach number, the theoretical difference in the specific entropy rise across the shock wave (due to the change in Mach number) between the steady and unsteady simulations is found to be 1.2 J/kg/K. It has been calculated that the weaker shock wave in the steady simulation leads to a decrease in the loss created by the shock wave. The decreased loss corresponds to a decrease in the specific entropy rise across the shock of between 1.0 J/kg/K (calculated using the blade surface Mach number) and 1.2 J/kg/K (calculated using the Mach number in the centre of the passage). This represents about one third of the 3.7 J/kg/K difference in the specific entropy increase seen between the steady and unsteady simulation through the rotor at 80% span shown in Fig. 4.3. The remaining reduction in the steady simulation loss must come from weaker shock wave - boundary layer interactions (caused by the weaker shock wave) and other regions of the flow but investigation into these is beyond the scope of the present study.

Figure 4.5 also shows that the location of the shock wave in the steady simulation is further downstream than in the unsteady simulation. To investigate the cause of this the flow is analysed in the centre of the passage (still at 80% span) through the rotor. The static pressure and radial velocity along this line are plotted in Fig. 4.6. The static pressure plot shows that the steady simulation has a higher pressure than the unsteady simulation upstream of the shock, at around 70% chord. In addition the steady simulation has a lower pressure downstream of the shock than the unsteady simulation as can be seen at around 80% chord.

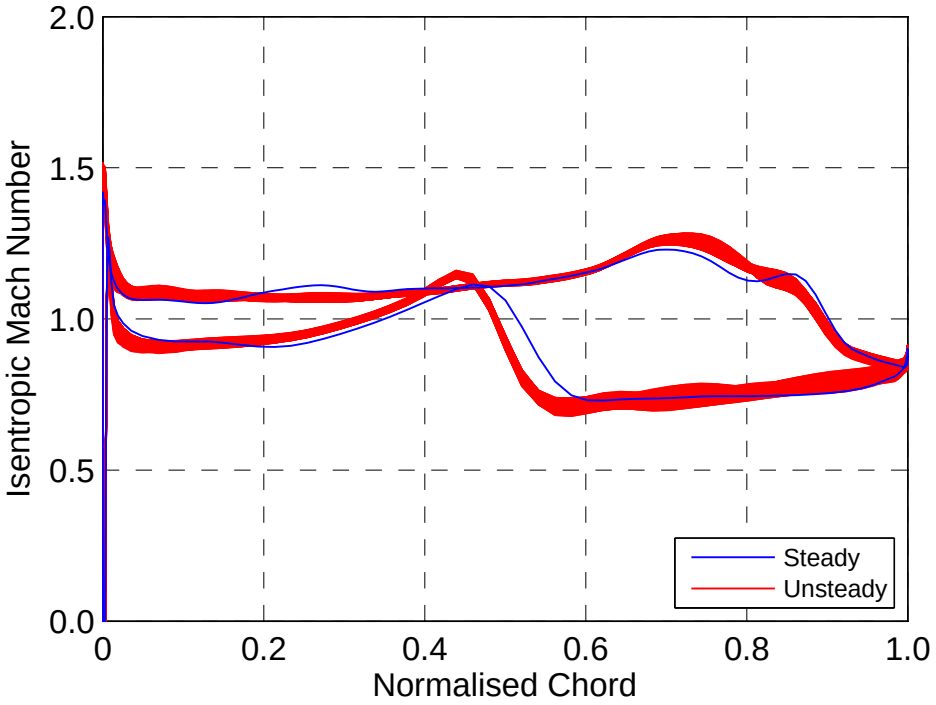

Fig. 4.5 Rotor surface isentropic Mach number near choke at 80% span

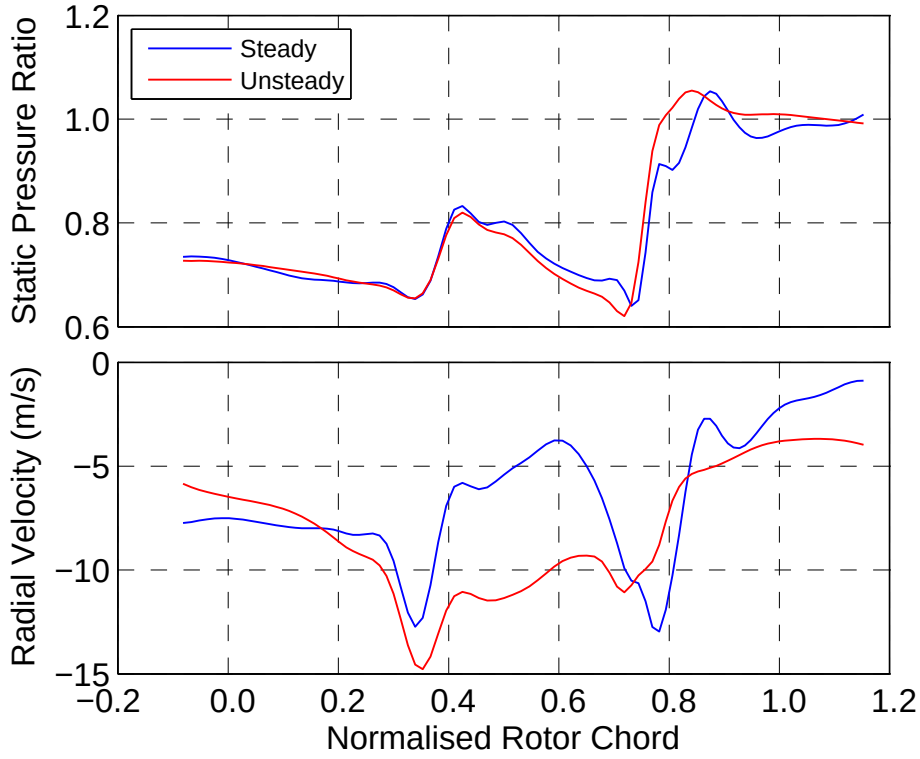

Fig. 4.6 Static pressure ratio (P/P_{atm}) and radial velocity through rotor mid passage at 80% span where radial velocity is as defined in Eqn. (4.3)

Given that the position of the shock in the steady simulation has moved downstream, from its position in the unsteady simulation, it is to be expected that the static pressure is higher upstream and lower downstream as the static pressure sets the position of the shock wave.

An explanation for the differences in the static pressure can be given by examining the radial velocity. The radial velocity plotted in Fig. 4.6 is defined in Eqn. (4.3). This is in order to subtract, from the absolute radial velocity, the proportion of the radial velocity that is primarily attributed to the contraction of the annulus as the flow travels through the rotor. The radial velocity plotted is therefore a measure of the redistribution of the flow in the rotor passage. It is clear that the magnitude of the radial velocity for the unsteady simulation is about twice that of the steady simulation just upstream of the passage shock wave (60% chord). This redistribution of flow away from the rotor tip suggests that the unsteady simulation has a higher level of blockage near the rotor tip than the steady simulation. The additional blockage leads to a higher back pressure which drives the change in shock wave location. This blockage also leads to the greater rate of acceleration upstream of the shock on the pressure surface of the rotor for the unsteady simulation seen in Fig. 4.5. Another indication that the unsteady simulation has a higher level of blockage than the steady simulation is that the mass flow rate predicted by the unsteady simulation is 0.3% lower than that predicted by the steady simulation.

$$\Delta V_r = V_r - V_{x\ (rotor\ inlet)} \tan^{-1}\left(\frac{\Delta r_{through\ rotor\ at\ 80\%\ span}}{\Delta x_{through\ rotor\ at\ 80\%\ span}}\right) \tag{4.3}$$

When the rotor is operating close to stall, at a stage pressure ratio of 1.63, Fig. 4.7 shows that the passage shock has been pushed out of the rotor passage and has merged with the rotor leading edge shock. Once again looking at the entropy increase through the rotor across the span (and still including the IGV-Rotor mixing plane loss), it can be seen in Fig. 4.8 that the main area of discrepancy between the steady and unsteady simulation is in the lower half of the span. Figure 4.9 shows the isentropic Mach number for the rotor blade surface at 30% span and reveals that the steady simulation has a lower shock Mach number again, accounting for the lower loss. Figure 4.9 also shows the passage shock is located nearer the leading edge of the rotor (than when operating near choke) and a greater variation in the unsteady loading across the cycle can be seen near the trailing edge.

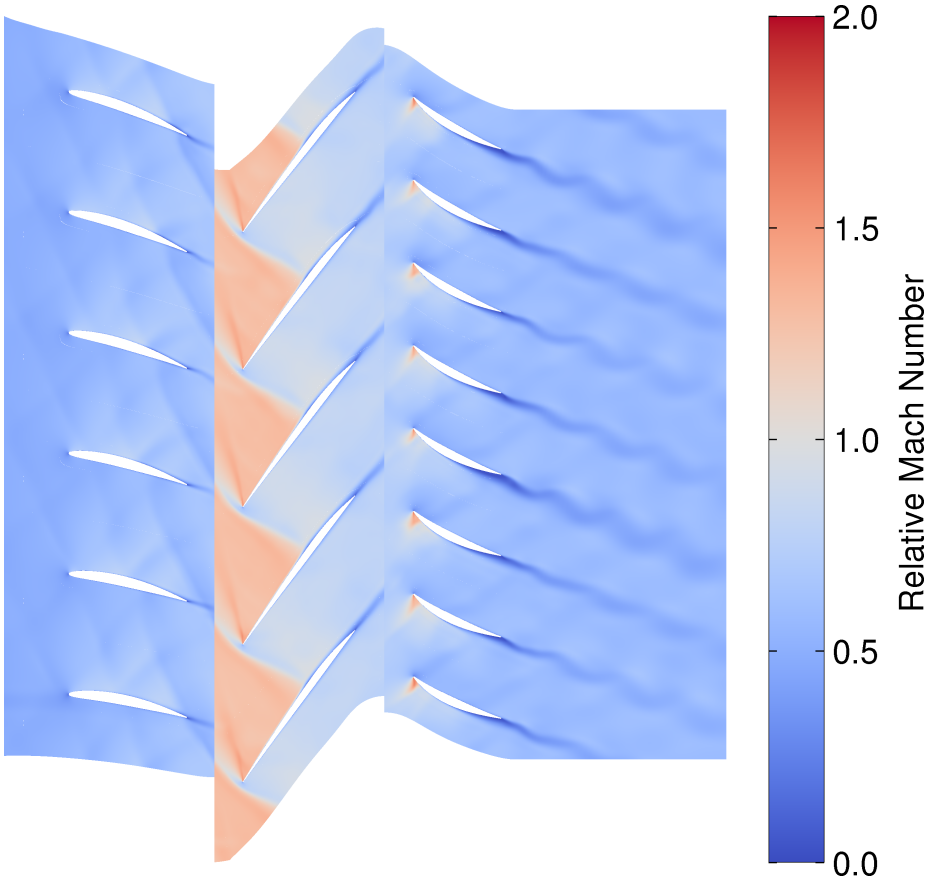

Fig. 4.7 Instantaneous unsteady relative Mach number at 80% span for pressure ratio of 1.63

4.2.2 Stator Efficiency

The stator efficiency in Fig. 4.2 is seen to drop off quickly at low pressure ratios. Comparing the flow field around the stator at high pressure ratios, shown in Fig. 4.7, and at low pressure ratios, shown in Fig. 4.4, it can be seen that the Mach number around the stator suction surface increases significantly at low pressure ratios and causes the drop off in efficiency. It is also at low pressure ratios that the stator efficiency delta increases to a magnitude of 1.3%, from 0.3% near stall (this delta is negative due to the steady efficiency being less than the unsteady efficiency). At choke this is a similar size of efficiency delta as for the rotor, however, as the stage approaches stall the stator efficiency delta is much smaller than seen in the rotor. To understand why the efficiency delta is present in the stator it is necessary to consider both the mixing losses from the mixing of the rotor wakes and how the unsteady inlet conditions to the stator affects the losses in the stator. The unsteady inlet conditions are caused by the rotor wakes and they have a large effect on the instantaneous loss generation in the stator.

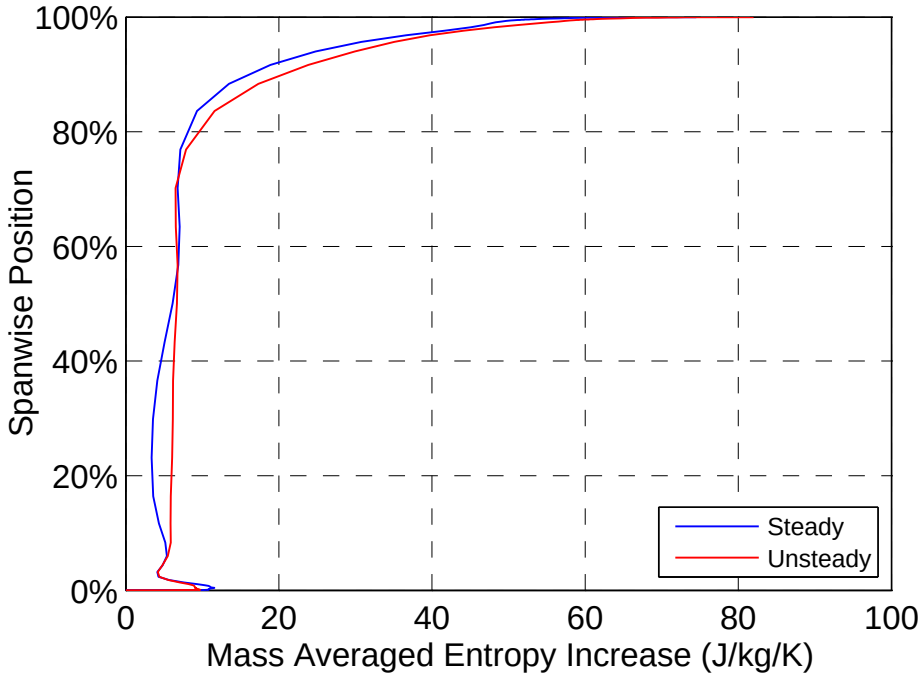

Fig. 4.8 Entropy increase across rotor near stall (including IGV-Rotor mixing plane entropy generation)

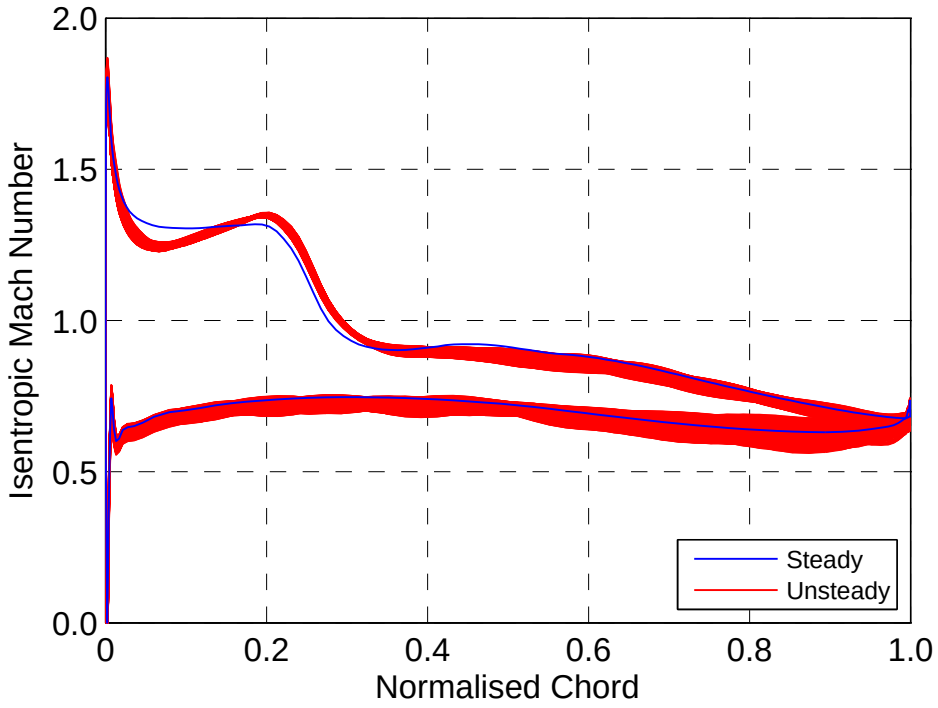

Fig. 4.9 Rotor surface isentropic Mach number near stall at 30% span

The mixing loss caused by the rotor wakes mixing out will be considered first. In the unsteady simulations the mixing loss occurs when the rotor wakes interact with the surrounding fluid as the wakes travel downstream through the stator blade row and beyond. In the steady simulations the mixing loss is generated when the rotor wakes are mixed out at the rotor-stator mixing plane. The stator isentropic efficiency in Fig. 4.2 includes the mixing loss at the rotor-stator mixing plane because the stator efficiency is calculated from the flow conditions measured upstream of this mixing plane. The isentropic efficiency can also be calculated using the flow conditions downstream of the rotor-stator mixing plane as the stator blade inlet conditions. Doing this excludes the rotor wake mixing loss from the stator blade efficiency in the steady efficiency calculations. The stator blade isentropic efficiency using inlet conditions upstream and downstream of the rotor-stator mixing plane has been calculated as is shown in Fig. 4.10 for the steady and unsteady simulations. The plots including the mixing loss are the same as the plot for the stator blade in Fig. 4.2. The steady efficiency prediction for the stator blade excluding the mixing loss is much higher than the efficiency including the mixing loss. The unsteady efficiency also increases slightly (even though most of the mixing loss is still captured in the blade passage) because the inlet measurement plane has moved slightly downstream (to downstream of the mixing plane location) and some of the rotor wake mixing has occurred before the measurement location so this loss is not included. Looking at the effect including the mixing loss has on the efficiency for the steady simulations, it can be said that the mixing loss accounts for a change in stator blade efficiency of between 1.3 and 3.3 percentage points, depending on the stage pressure ratio.

The other main difference to consider between the steady and unsteady simulations is that the steady simulation does not model the unsteady inlet conditions to the stator which means that the interaction between the rotor wake and the stator blade is not captured. The interaction between the rotor wakes and the stator blade is a source of loss. This is analysed by investigating the flow at 80% span. 80% span is chosen as there is a significant difference in the entropy generation through the stator between the steady and unsteady simulation at this location as shown in Fig. 4.11. The instantaneous rate of entropy generation on the surface at 80% span of a single stator blade is analysed for the steady and unsteady simulations at the peak efficiency pressure ratio. The total rate of entropy generation on this surface is shown, coloured blue, in Fig. 4.12 for 5 rotor blade passings. The entropy generation rate clearly varies at the rotor passing frequency. The equivalent value for the steady simulation is also plotted as the dashed blue line and shows a much lower value than the mean unsteady value. This is consistent with the higher stator blade efficiency calculated in the steady simulations when the rotor-stator mixing plane loss is excluded. To understand

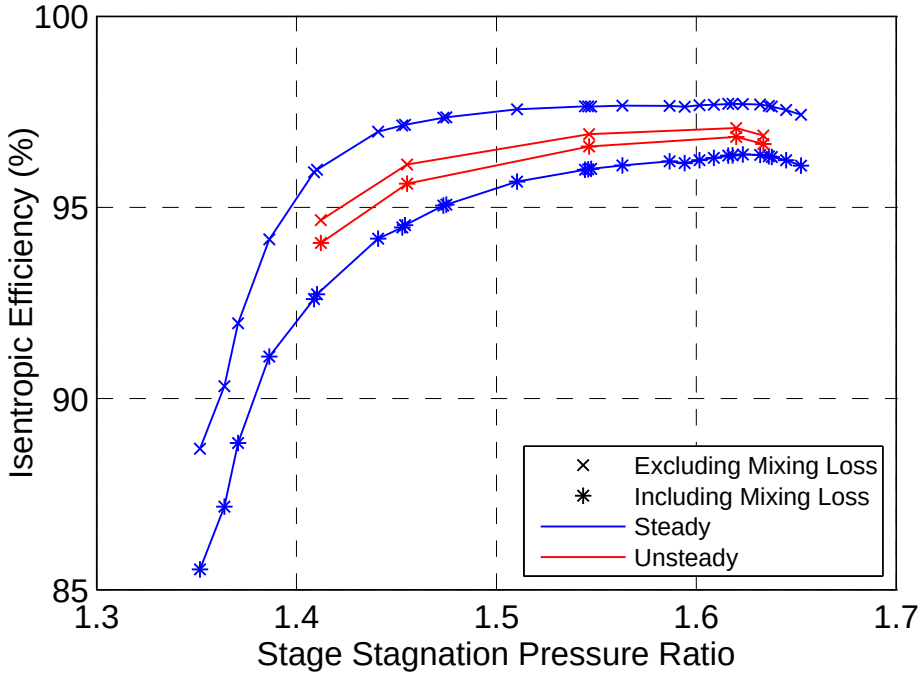

Fig. 4.10 Stator blade isentropic efficiency calculated upstream (including mixing loss) and downstream (excluding mixing loss) of rotor-stator mixing plane location

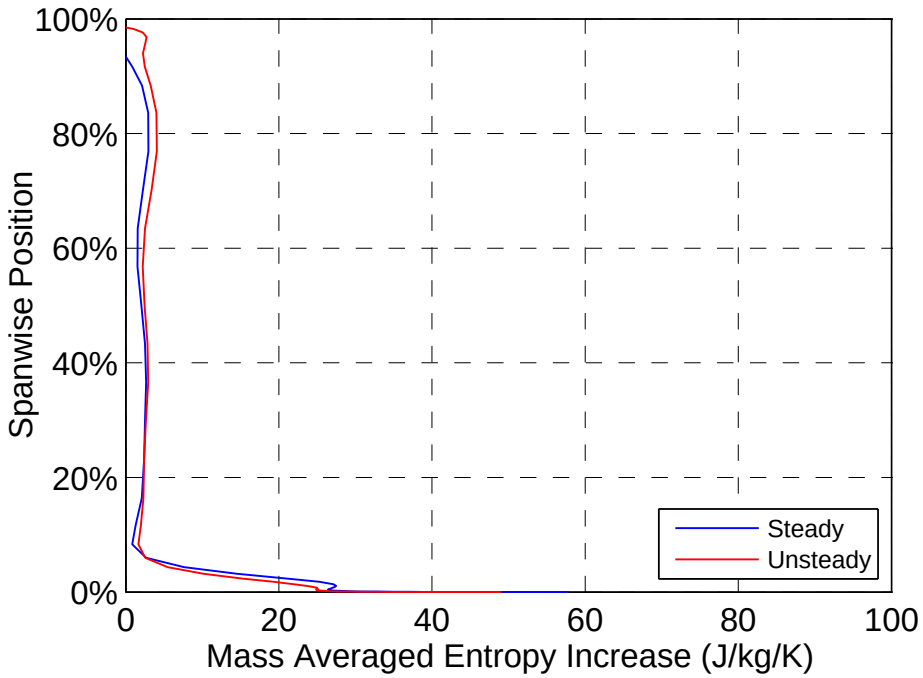

Fig. 4.11 Entropy increase across stator at peak stage efficiency (excluding rotor-stator mixing plane entropy generation)

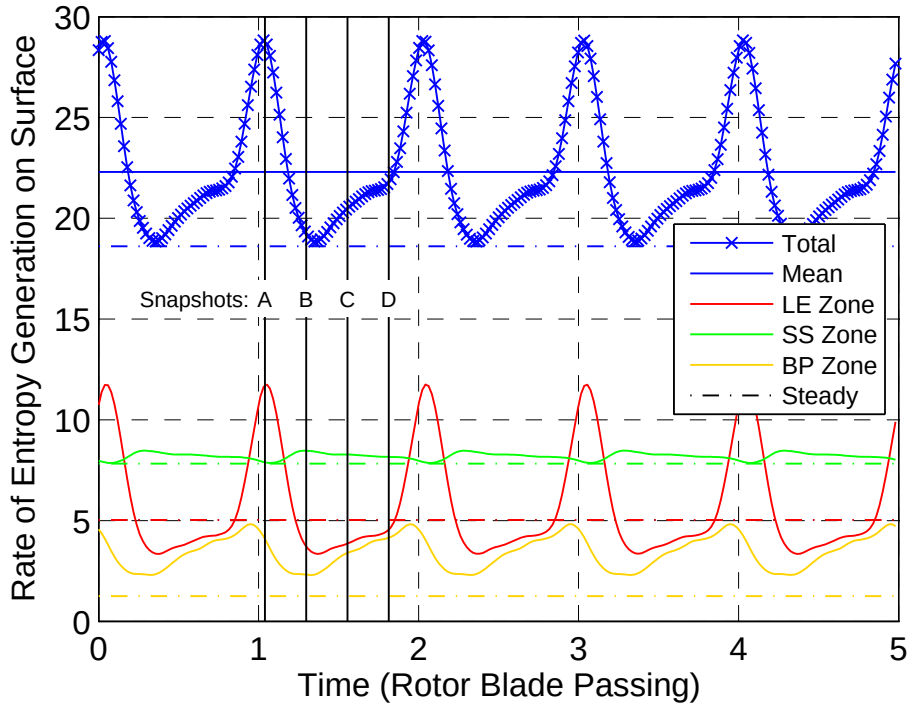

Fig. 4.12 Instantaneous rate of entropy generation for the stator at 80% span shown for the total surface as well as the leading edge (LE), suction surface(SS) and blade passage (BP) summation zones

the wake-stator interaction in more detail the instantaneous entropy generation rate at 80% span has been plotted in Fig. 4.13 for 4 points in time across one rotor passing (snapshots A to D) showing the entropy generated by the stator boundary layers and the rotor wakes interacting with the surrounding fluid. In addition the entropy generation rate on this surface has been broken down into 5 summation zones covering the leading edge (LE), trailing edge (TE), suction surface (SS), pressure surface (PS) and the rest of the blade passage (BP). These zones are marked on the plots in Fig. 4.13 and the sum of entropy generation rate for the LE, SS, and BP zones is plotted in Fig. 4.12. The values for the PP and TE zones have very little variation across the cycle and so are excluded for clarity.

The results in Fig. 4.12 show that the LE zone is the greatest contributor to the spikes in the total entropy generation rate. The peak occurs at Time A (Fig. 4.13a) when the rotor wake interacts with the stator leading edge. When the wake is not interacting with the LE (Fig. 4.13b, 4.13c & 4.13d) the entropy generation in the LE zone for the unsteady simulation is lower than the value in the LE zone for the steady simulation due to the difference in the inlet flow incidence, however the steady value remains lower than the unsteady mean. At Time B (Fig. 4.13b) the rotor wake has moved downstream of the leading edge and has a significant interaction with the suction surface. The wake causes a negative jet effect on the

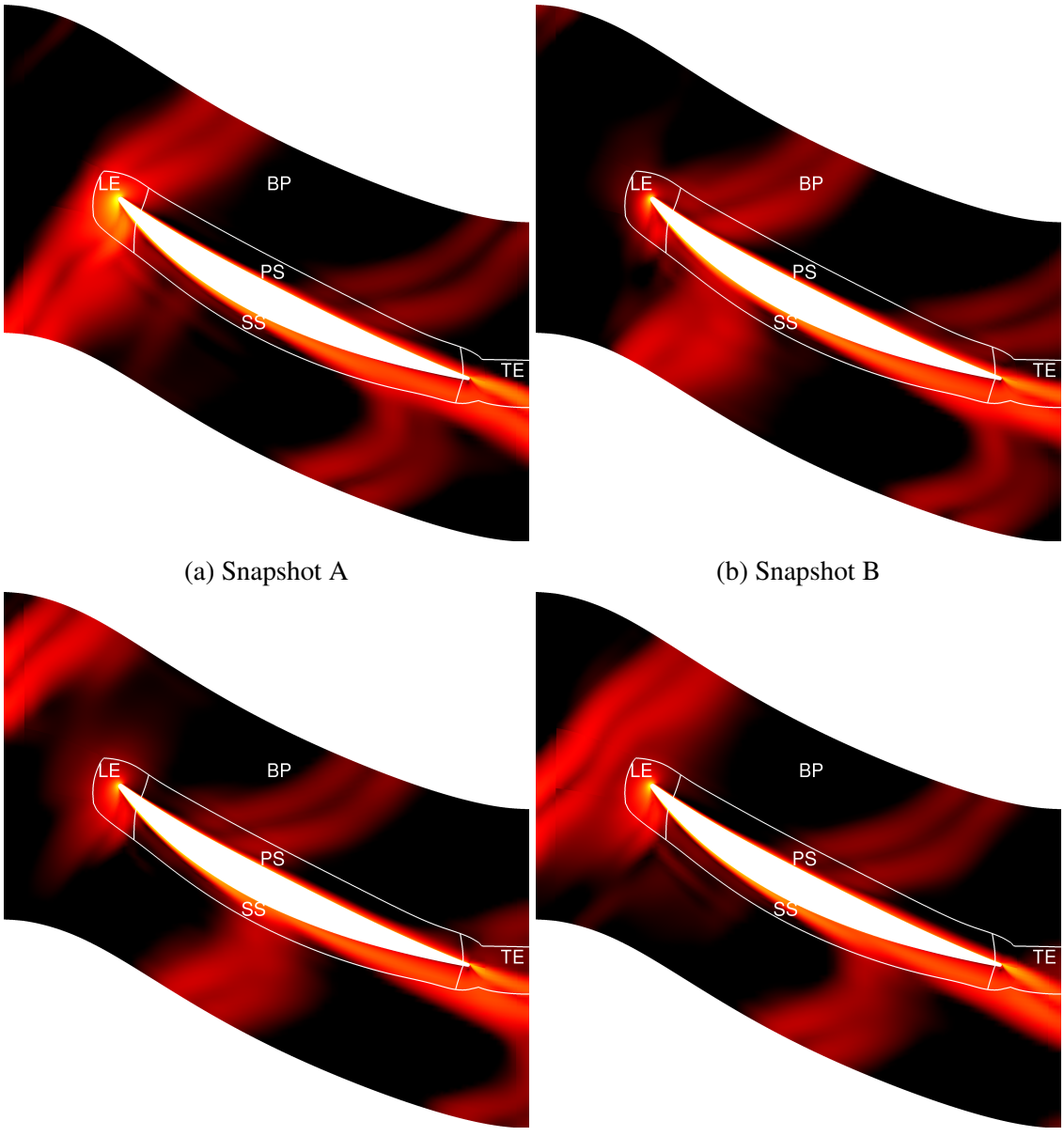

(a) Snapshot A

(b) Snapshot B

(c) Snapshot C

(d) Snapshot D

Fig. 4.13 Logarithm of the instantaneous entropy generation rate in the stator at 80% span for snapshots A to D with summation zones

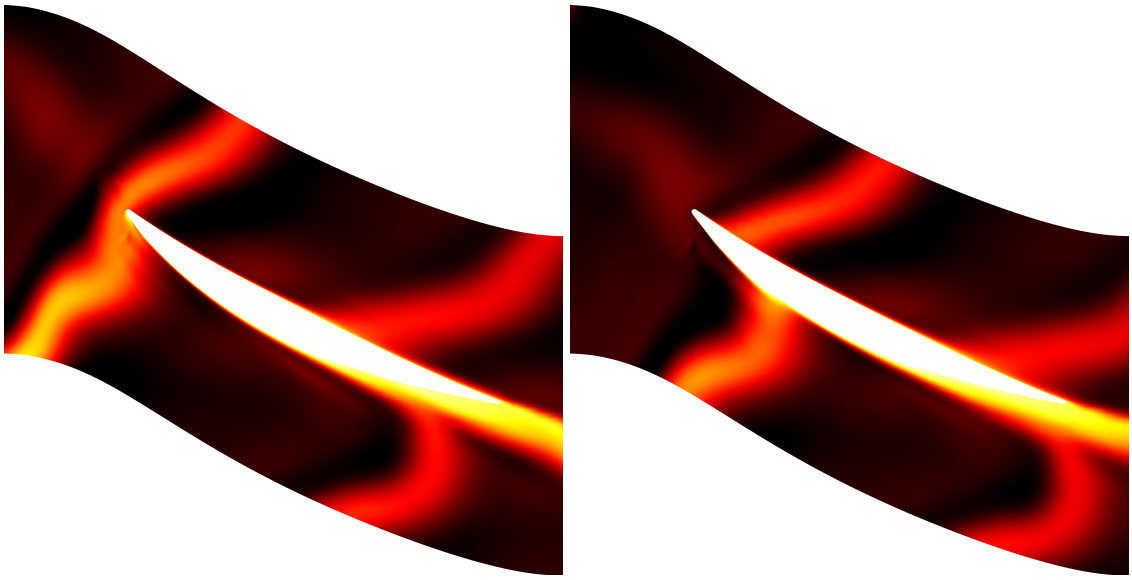

(a) Snapshot A

(b) Snapshot B

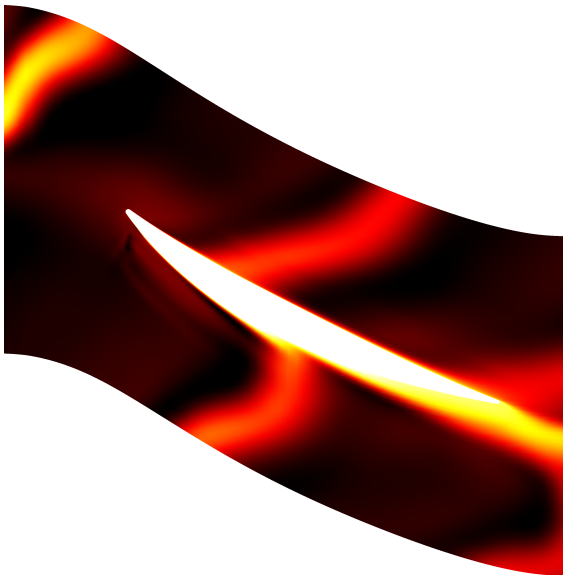

(c) Snapshot C

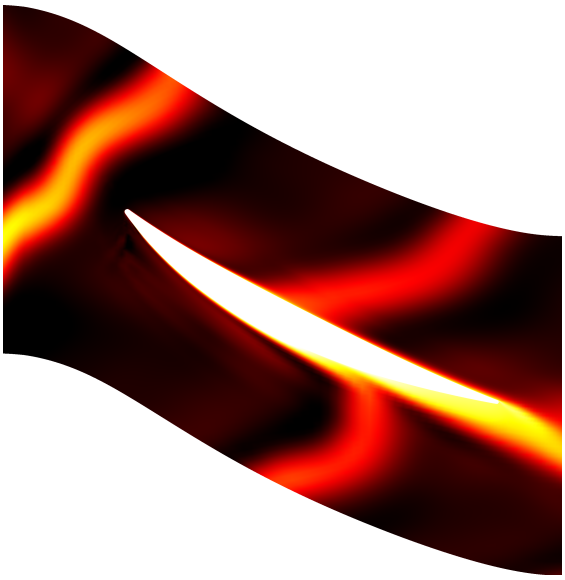

(d) Snapshot D

Fig. 4.14 Plots of entropy function in the stator at 80% span for snapshots A to D

suction surface that extends the suction surface boundary layer away from the blade and increases the entropy generation. This can be seen in Fig. 4.13b and as an increase in the SS zone entropy generation rate in Fig. 4.12 at Time B. The steady value for the SS zone is equal to the minimum value for the unsteady SS zone as this corresponds to no wake interaction on the suction surface. The BP zone has the highest entropy generation rate when the maximum rotor wake mixing is captured in this zone and occurs between Time D and A. The entropy generation rate for the BP zone is lower in the steady simulation because there is no rotor wake mixing occurring in the stator passage in the steady simulation as this mixing has already happened at the rotor-stator mixing plane. On the pressure surface the rotor wake is stretched as it passes through the stator passage. This can be mostly easily seen by looking at the entropy plots shown in Fig. 4.14. As the wake passes through, the area of the wake close to the pressure surface can be seen to stretch which causes an increase in the entropy generation for this region.

Interactions between wakes and downstream blade rows have been studied by others and similar observations have been made by Wheeler et al. [91–93]. Although Wheeler's work was performed in a low speed machine, it is notable that similar observations are made for both the low speed and transonic compressor designs. In particular, interaction of the wakes with the stator suction surface gives a similar thickening of the boundary layer leading to increased loss. It is useful to know that the flow features are similar between low speed and high speed compressors as it indicates that similar techniques for reducing loss in low speed designs could be used in high speed designs.

Figure 4.12, and the explanations above, show that the lack of interaction between the rotor wakes and the stator blades in the steady simulation leads to a lower rate of entropy generation than the unsteady simulations, particularly in the leading edge region. It is therefore expected that the stator efficiency for the steady simulation should be higher than for the unsteady simulation if the steady mixing plane loss is not included and this is what is seen in Fig. 4.10. It is also expected (if the steady mixing plane accurately calculates the mixing loss of the rotor wakes through the stator and therefore the steady and unsteady mixing losses are equal) that the steady stator efficiency should remain higher than the unsteady stator efficiency even when the steady mixing plane loss is included because it has been seen that the unsteady wake-stator interaction leads to addition loss, however, this is not seen in Fig. 4.10 as the steady stator efficiency is lower than the unsteady stator efficiency when the mixing plane loss is included. There are two contributing factors that lead to this. Firstly, the rotor wakes in the unsteady simulations have not fully mixed out by the time they exit the stator passage so they will continue to mix out further downstream, meaning that the mixing plane over predicts this loss for the domain considered. Another factor is that

the wakes may be recovering some of their stagnation pressure loss as they interact with the stator blades in the unsteady simulations. This process of wake recovery has been reported by other researchers [78, 1] who investigated closely spaced blades.

4.2.3 IGV Efficiency

The IGV blade efficiency in Fig. 4.2 is very similar between the steady and unsteady simulations for the whole pressure range except near stall where the steady simulation starts to give a slightly higher IGV efficiency. The increase in IGV efficiency at high pressure ratios is due to the reduction in the inlet Mach number as the stage approaches stall and the mass flow rate decreases.

In the unsteady simulation this effect is counteracted by the effect of the stronger interaction between the rotor leading edge shock wave and the IGV which causes the IGV efficiency to stay almost unchanged. One way to see this increased interaction is to look at the boundary layer displacement thickness and momentum thickness on the suction surface of the IGV. Figure 4.15 shows the IGV suction surface boundary layer displacement and momentum thicknesses for a choked simulation and a simulation near stall. The time averaged results are plotted as the solid line while the dash line marks the limits of the variation across the cycle.

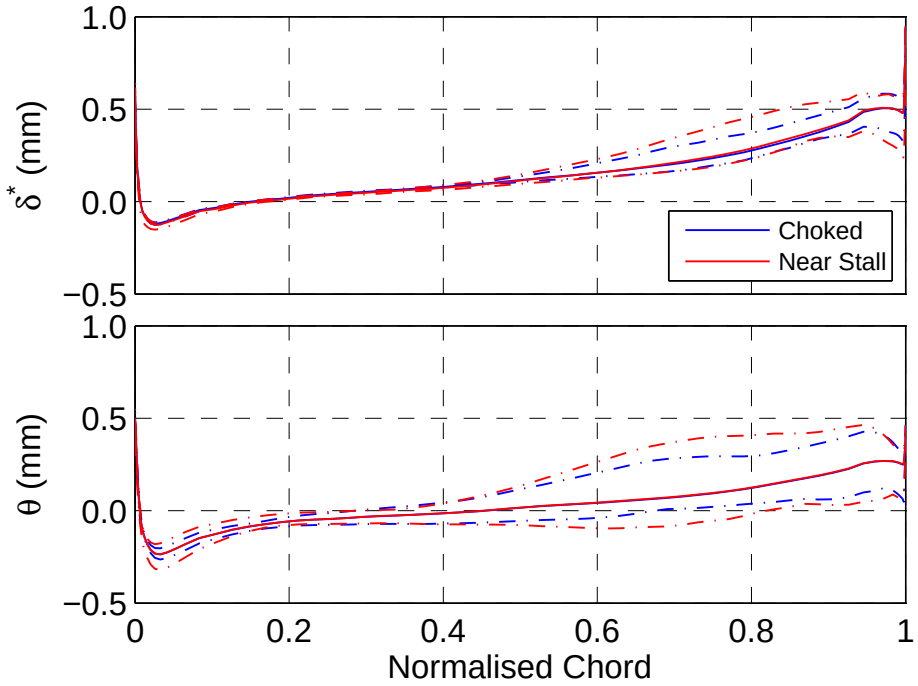

Fig. 4.15 IGV suction surface boundary layer displacement and momentum thicknesses at 80% span (solid line shows the time averaged results and the dash line shows the limits of the variation across the cycle)

Although the time averaged results do not change much, it can be seen that the variation in the displacement thickness and the momentum thickness is much greater near stall than when the stage is choked, showing that there is increased interaction with the rotor leading edge shock wave.

4.3 Front Stage Off-Design Speed Analysis

The analysis of the front stage is continued by investigating the performance of the compressor stage at off-design speeds in order to determine whether the trends seen at design speed stay the same or change. Figure 4.16 shows the stage efficiency for the compressor operating at 90%, 100% and 110% of design speed with results from steady and unsteady simulations. As with the calculations at design speed it can be seen that the steady simulations give a higher predicted polytropic efficiency for all pressure ratios. The efficiency delta increases as the operating point moves from low pressure ratios to peak efficiency in the same way as at the design speed. At part speed and over speed the efficiency delta reduces as the operating point moves from peak efficiency to near stall. This is in contrast to the case at design speed where the efficiency delta continues to increase. The efficiency delta at peak efficiency for each operating speed increases as the operating speed increases.

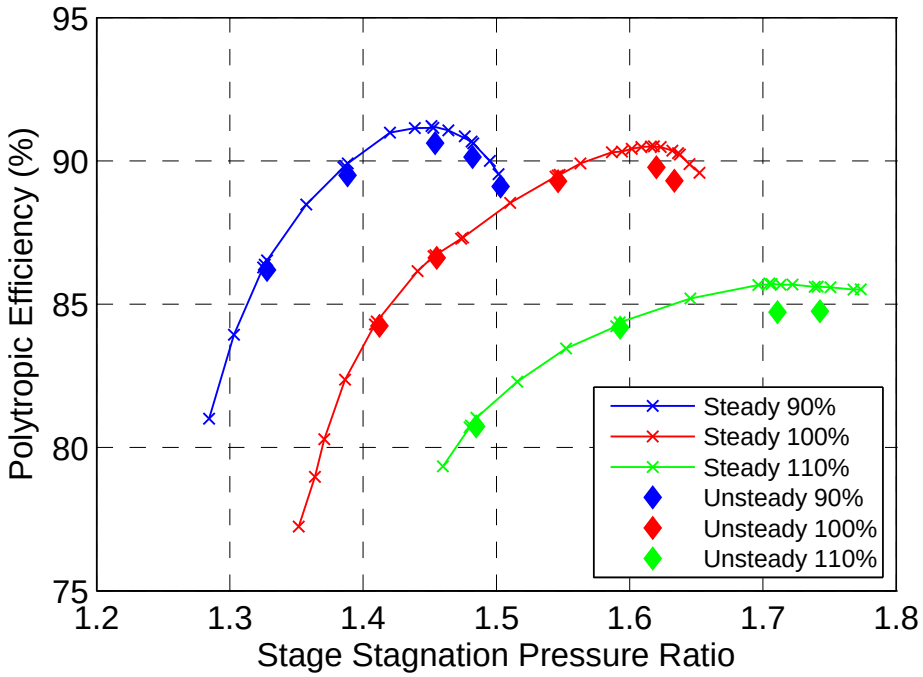

Fig. 4.16 Off-design speed polytropic efficiency predictions for 1.5 stage simulations

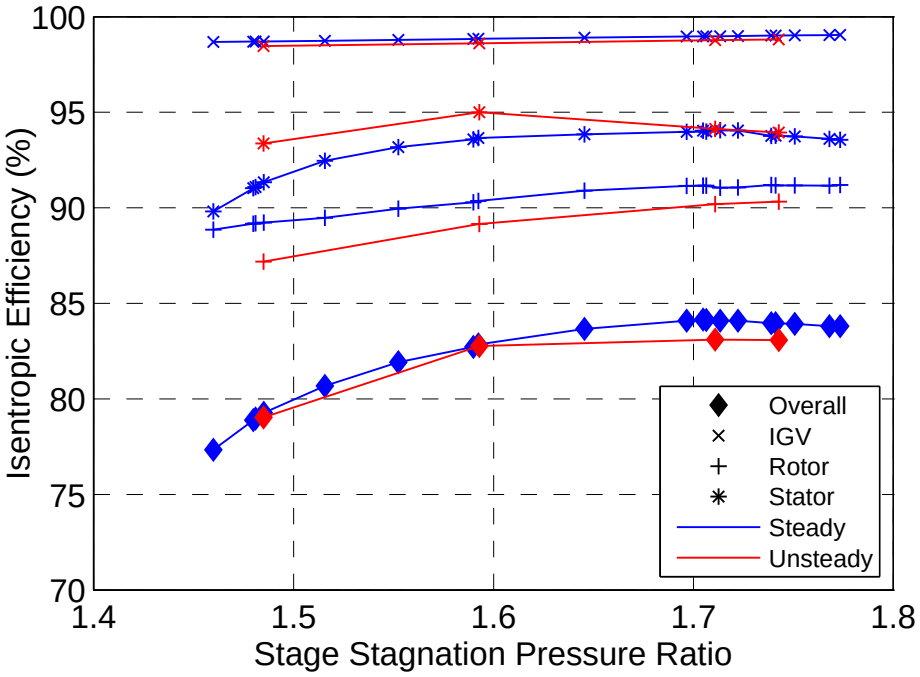

Fig. 4.17 Steady and unsteady isentropic efficiencies for 110% speed

The individual blade row isentropic efficiencies for 110% speed are plotted in Fig. 4.17. The main trends that exist at design speed are still present. The rotor and stator efficiency deltas continue to cancel each other out at low pressure ratios and the stator efficiency delta reduces faster than the rotor efficiency delta at high pressure ratios leading to an increase in the stage efficiency delta. The IGV efficiency does not vary significantly between the steady and unsteady simulations, even at high pressure ratios. This is because, at the higher axial Mach number, the compressor is pulling the shock structure further downstream and preventing it from fully exiting the rotor passage, even at high pressure ratios. This is also indicated by the fact that the rotor efficiency is still increasing at the highest simulated pressure ratio and has not yet reached the peak, suggesting that the shock structure will not be at its peak efficiency location and therefore not pushed out of the front of the rotor passage. The location of the shock wave at near stall operating conditions can be seen in Fig. 4.18.

Figure 4.19 shows the blade row isentropic efficiencies for the compressor when operating at 90% speed. At high pressure ratios the stator efficiency delta starts to increase again leading to a smaller stage efficiency delta. At these pressure ratios, combined with the lower axial Mach number, the rotor passage shock has been forced out of the front of the passage, as shown in Fig. 4.20. The shock waves, having being pushed out so far in front of the rotor, have much greater interaction with the IGVs than was seen at design speed.

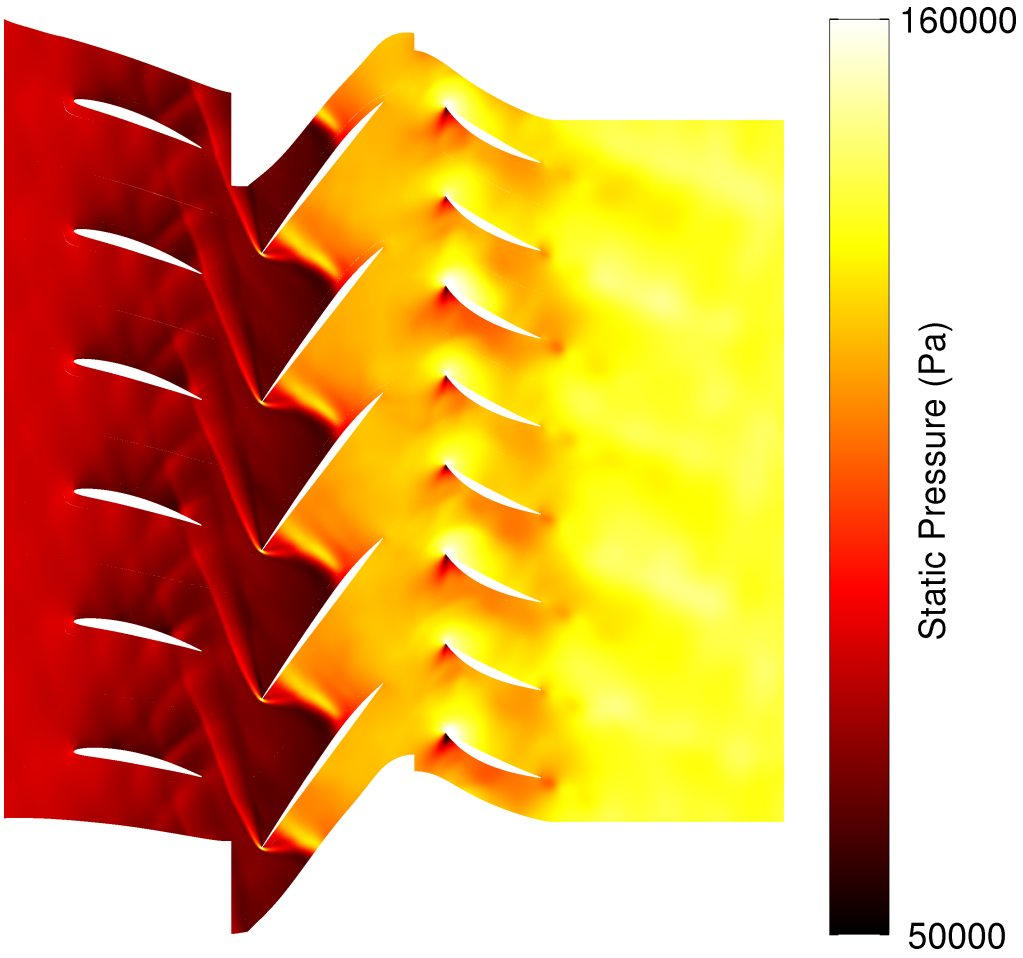

Fig. 4.18 Instantaneous static pressure field at 80% span for near stall at 110% speed showing choked rotor passage shock waves

This can be seen by looking at the variation in the IGV suction surface boundary layer displacement thickness and momentum thickness shown in Fig. 4.21. The time averaged displacement and momentum thicknesses are plotted along with the limits of the instantaneous variation across the cycle for choked and near stall operating conditions. There is a significant increase in the variation of the IGV suction surface boundary layer displacement thickness and momentum thickness from near choke to near stall showing increased IGV-Rotor shock wave interaction at near stall operation. The variation that is present near stall at 90% speed is much greater than the variation seen near stall at design speed in Fig. 4.15. This increased interaction is what causes the increased efficiency delta in the IGV efficiency between steady and unsteady simulations at high pressure ratios.

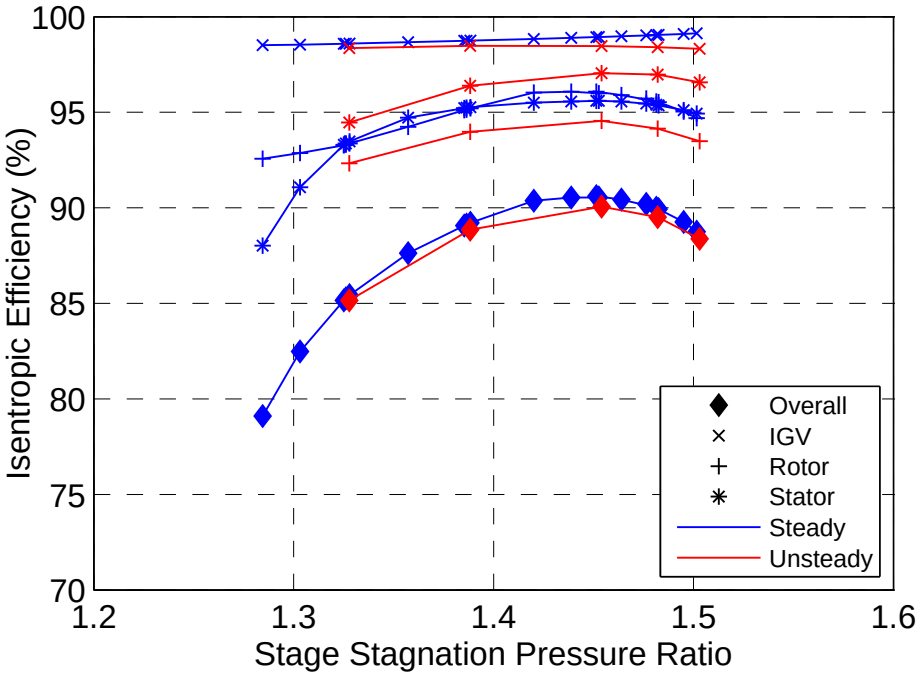

Fig. 4.19 Steady and unsteady isentropic efficiencies for 90% speed

4.4 Single Stage Performance in Embedded Environment

In a multistage environment the pressure potential from the blades in the downstream stages will propagate upstream and interact with the front stage. It is important to know if this interaction will affect the performance of the front stage or not. In order to investigate this, the whole 3-stage rig was simulated at once and the first stage efficiency was extracted and compared to the stage efficiency from the isolated stage simulations.

In the 3-stage environment the operating range of the first stage is limited to a small portion of its range due to the matching with the downstream stages. At 90% speed the first stage is always operating near stall and at 110% speed the first stage is always very close to fully choked. These operating points are shown in Fig. 4.22. At design speed the operating point of the first stage does change as the 3-stage operating point changes however the first stage only has a pressure ratio of 1.545 when the multistage simulation approaches stall which is significantly below the pressure ratios it can achieve when in isolation. In order to increase the pressure ratio across the first stage, stator 2 was re-staggered by 10 degrees. Re-staggering is discussed in greater detail later in this thesis but here it allows the embedded stage 1 to be simulated at a high pressure ratio without affecting its characteristics. It can be seen from the results in Fig. 4.22 that the presence of the downstream stages has virtually no effect on the polytropic efficiency characteristic for the first stage of the compressor.

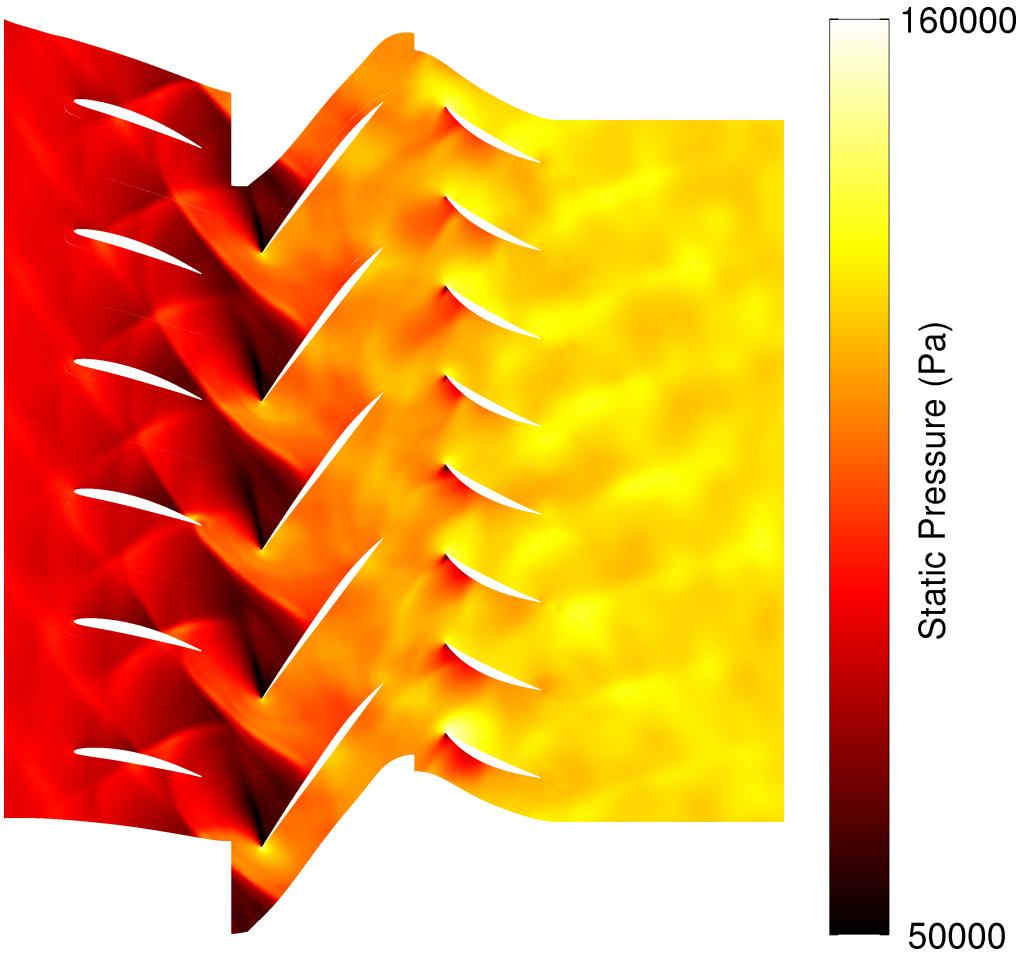

Fig. 4.20 Instantaneous static pressure field at 80% span for near stall at 90% speed showing strong interaction between the rotor leading edge shock waves and the IGVs

This is very important for the designer to know as it means that the stage can be designed without needing to be concerned that the unsteady pressure potential propagation from the downstream stages will significantly affect its performance. The downstream stage will still determine the operating point for the first stage but the front stage characteristic will not be significantly changed.

The individual blade efficiencies for the design speed line in Fig. 4.23 show that the IGV and rotor blade efficiencies remain virtually unchanged between the isolated and embedded simulations however there is a small decrease in the stator efficiency for the embedded stage at medium and high pressure ratios. This efficiency drop is caused by the increased interaction between the stator and the downstream rotor (rotor 2) as the downstream stage is pushed to stall. The Rotor 2 tip Mach number is 1.07 and has a similar leading edge shock wave to rotor 1. Although the Mach number is lower and the shock is weaker, the cause of

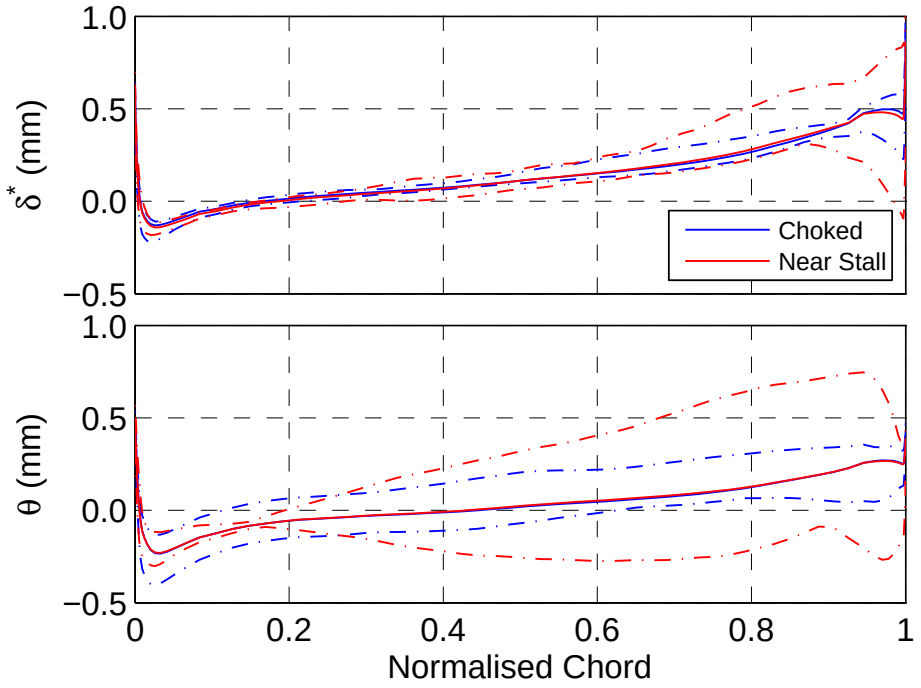

Fig. 4.21 IGV suction surface boundary layer displacement and momentum thicknesses at 80% span for 90% speed (solid line shows the time averaged results and the dash line shows the limits of the variation across the cycle)

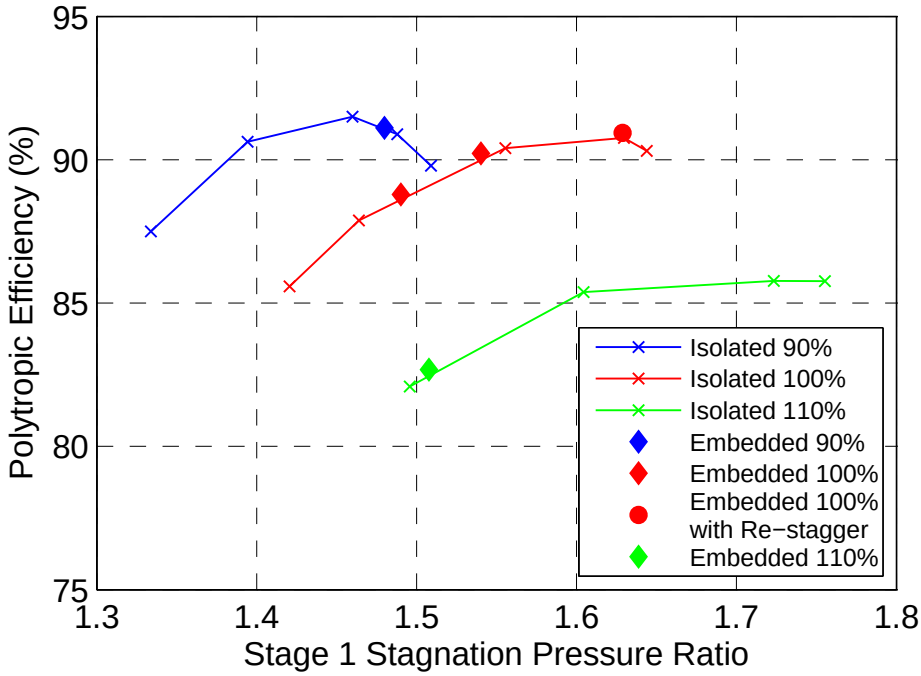

Fig. 4.22 First stage polytropic efficiency predictions for isolated and embedded simulations

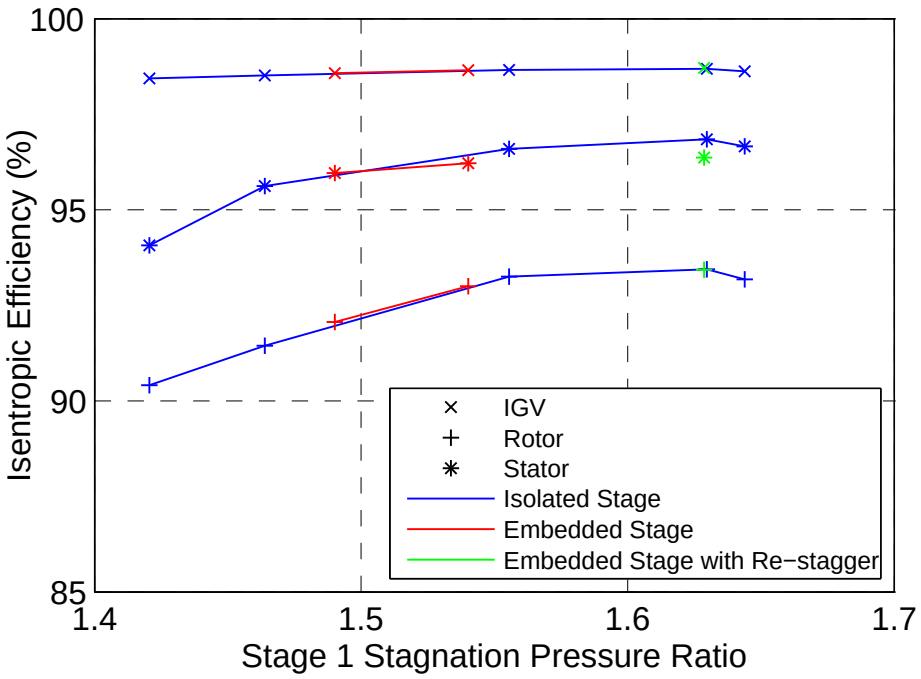

Fig. 4.23 Blade isentropic efficiencies for isolated and embedded unsteady simulations at design speed

the stator efficiency drop seen here is similar to the effect seen with the IGV and rotor 1 at high pressure ratios in the isolated simulations (Fig. 4.2).

4.5 Unsteady Effects in Optimised Blade Geometry

All of the findings presented so far in this chapter have been based on simulations of the original compressor blade geometry design of the 3-stage compressor [56]. In order to determine if the findings can be applied more widely to different transonic compressors a similar analysis is presented for the same compressor but with the newer blade designs that were developed during an optimisation by Wang [90]. A comparison of steady and unsteady simulations is made for the optimised blade geometry at the design speed. Once again the first stage of the compressor was simulated in isolation and the results for individual blade efficiencies at the design speed are shown in Fig. 4.24. This shows very similar results to the analysis of the baseline geometry shown in Fig. 4.2.

The optimised geometry was also simulated in the 3-stage compressor for which the isolated and embedded results are shown in Fig. 4.25. The optimised blade geometry has changed the stage matching so there is no longer any need to re-stagger stator 2 in order to operate stage 1 at high pressure ratios. Fig. 4.25 shows that there is no change in the blade

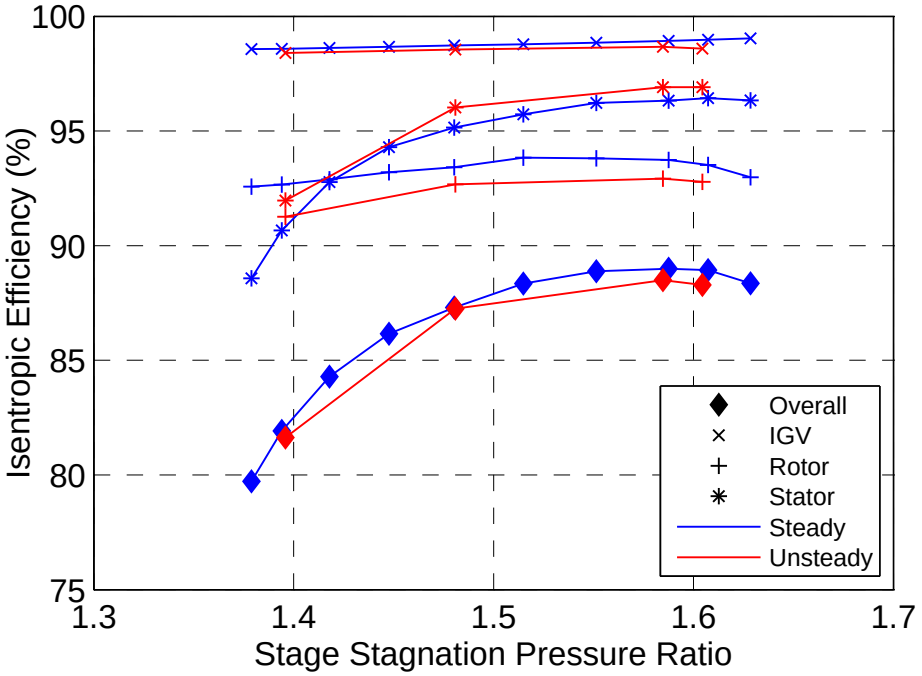

Fig. 4.24 Steady and unsteady blade isentropic efficiencies for 1.5 stage simulations of optimised geometry

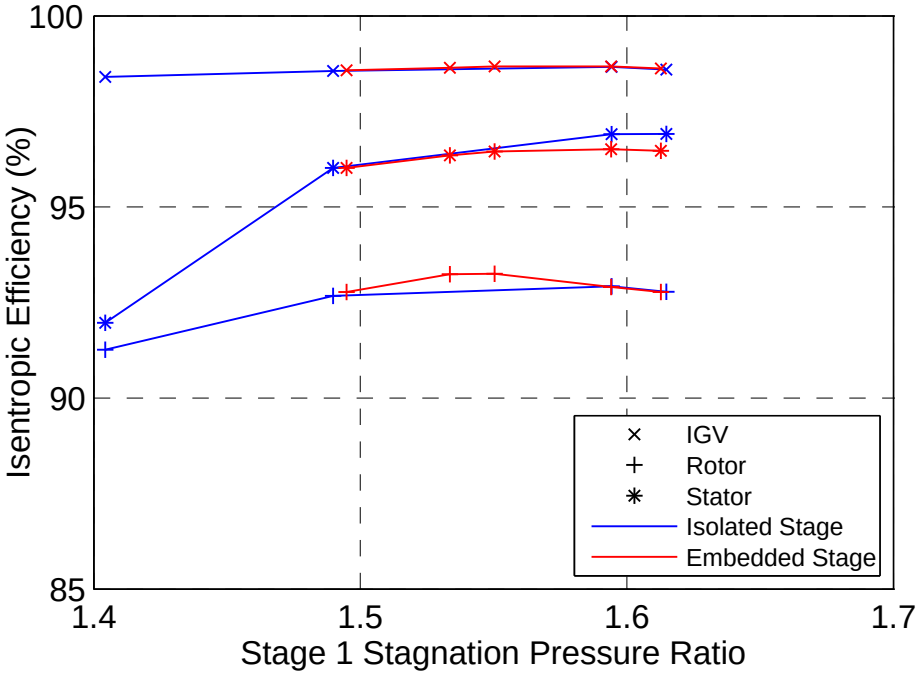

Fig. 4.25 Blade isentropic efficiencies for isolated and embedded unsteady simulations of optimised geometry

efficiencies between the isolated and embedded stages except for the stator at high pressure ratios. This is consistent with what was found for the baseline geometry in Fig. 4.23 and can again be attributed to the interaction that occurs between the rotor 2 leading edge shock wave and stator 1 when the downstream stages are present in the simulation.

4.6 Conclusions

Efficiency predictions in the baseline geometry for steady and unsteady simulations have been compared for a range of operating conditions at different speeds and it has been found that steady simulations always give a higher predicted efficiency with a maximum polytropic efficiency delta of 1.05 percentage points. The polytropic efficiency delta at peak efficiency for a given speed is larger at faster speeds varying from 0.54 percentage points at 90% speed to 0.98 percentage points at 110% speed. The small efficiency delta at low pressure ratios (<0.2 percentage points) is found to be because the efficiency deltas in the rotor and stator blade rows show opposite trends and cancel each other out. The steady simulations always give a higher rotor isentropic efficiency due to a weaker shock wave. It is also found that the unsteady shock wave position does not vary much throughout the cycle and that the oscillation is less than 1% of the rotor chord. In addition the steady shock wave is located further downstream than the unsteady shock wave position due to less blockage near the rotor tip in the steady simulation. The stator efficiency is always lower due to the full mixing out of the rotor wakes, at the rotor-stator mixing plane, being included when calculating the stator isentropic efficiency. It is known from the unsteady calculation that the rotor wakes are not fully mixed out by the time they exit the stator passage, in addition the rotor wakes may recover some of their loss as they travel through the stator passage. The interaction between the rotor wakes and the stator blade is an additional source of loss that is not modelled by the steady simulations. The steady simulation has a higher IGV efficiency than the unsteady simulations because the steady simulations do not capture the rotor leading edge shock wave interacting with the IGV that lowers the efficiency.

The smallest stage efficiency deltas occur at choke and are caused when the rotor and stator efficiency deltas counteract each other. This means there is a significant possibility that a shift in either the rotor or stator efficiency curves would lead to a much greater stage efficiency delta. This could make steady simulations more uncertain at these operating conditions when seeking to predict the overall stage efficiency. Given also that the largest efficiency delta occurs near stall it would seem desirable to perform unsteady simulations both at choke and near stall in order to more accurately predict the stage performance.

When the first stage is embedded within the 3-stage compressor the downstream stages do not significantly affect the efficiency characteristic prediction of the first stage which means the designer does not need to give great consideration to the unsteady interaction effects of the downstream stages when designing the first compressor stage, at least for the rotor speeds examined in this study. In addition these results have shown to be consistent for both the baseline and optimised geometries suggesting that the results presented here can be applied to further transonic compressors geometries.

Chapter 5

IGV-Rotor Unsteady Interaction - The Effect of Axial Spacing

5.1 Introduction

For a transonic compressor, the space between the trailing edge of the IGV and the leading edge of the rotor is an area of very complex flow interaction between the IGV wakes and the rotor leading edge shock waves. The axial spacing between these blade rows is also a design parameter that must be chosen within the constraints of the allowable minimum, set by safety margins for physical blade interference, and the maximum, set by structural constraints. The flow interactions mentioned above provide scope for improving the efficiency by changing the axial spacing between the blade rows, and the designer will always wish to seek this potential improvement. Gaining an increased knowledge of the flow in this region, in order to maximise the efficiency, is the main motivation for the majority of the previous research however all of the research into the axial spacing, for transonic compressors, has been conducted only on rotor blade rows with IGVs or single stage compressors. The current work has been performed in a multistage environment, comprising 3 stages, in order to allow the effect that changing the IGV-Rotor axial spacing has on the downstream stages to be analysed.

Another consideration when varying the blade row axial spacing is the effect that this has on the dynamic pressure loading experienced by the blades. This will be affected because the size of the axial space determines how much distance there is for the IGV wakes and rotor leading edge shock waves to decay before interacting with the adjacent blade row. The strength of this oscillating aerodynamic loading will in turn affect the mechanical integrity of

the blades and their lifespan, so the aero-mechanical implication of varying the axial spacing is another important aspect to understand.

The work in this chapter will focus on the Siemens' test rig with the optimised blade geometry [90] and will compare two different IGV-Rotor axial spacings: the design axial spacing and a reduced axial spacing measuring 40% of the original mid-span axial distance. It was chosen to vary the IGV-Rotor spacing, as opposed to any other blade row spacing, because rotor 1 has the highest Mach number and therefore any transonic effects will be strongest for this blade row.

Dynamic loading results from an unsteady simulation with the design spacing are presented first in order to show the dynamic forces present on the blades. In the following sections, results from the design and 40% axial spacing simulations are compared. The time averaged results are analysed in order to show the effect that the axial spacing has on the flow and the efficiency predictions. Time dependent results are then analysed in order to show the effect that the axial spacing has on the dynamic blade loading. The final section of results in this chapter contains the results from a modal force analysis in order to gain a better understanding of the mechanical implications of varying the axial spacing between the IGV and Rotor blade rows. Most of the analysis in this chapter is performed at design speed and pressure ratio using full annulus unsteady simulations. Full annulus simulations with the correct blade counts are used in order to obtain the correct frequencies of the blade forcing, so that the blade forcing can be attributed to the effect of the other blade rows by using Fourier transforms. The time averaged analysis is presented using results from steady, single passage simulations and unsteady quarter annulus simulations. Quarter annulus simulations were used in order to make it possible to simulate a range of operating points in a reasonable time frame and because it has already been shown that the time averaged results do not vary significantly between the quarter and full annulus unsteady simulations.

The findings in this chapter show that the stage 1 efficiency increases 0.2% when the IGV-Rotor gap is reduced, from the design axial spacing to 40% of the design spacing, and that this is due to a weaker shock wave in the rotor passage. Results from unsteady simulations have been compared to results from steady simulations to show that the reduction in endwall loss (due to the reduction in wetted surface area from reducing the axial spacing) is insignificant compared to the reduction in loss due to unsteady flow effects. In addition to affecting the loss, it is also found that the reduced axial gap leads to a significant increase in the dynamic loading on the IGVs and rotor 1 blades. Although the increase in dynamic loading is significant, the absolute magnitudes of the dynamic forces remain a lot less than the static pressure loading on the blades, so further study is needed to understand the effect of the increased dynamic loading on the blade life. Varying the IGV-Rotor axial spacing has

also affected the dynamic loading of the downstream stages, in particular causing a reduction in the dynamic loading in the rotor 2 and rotor 3 blades.

5.2 Dynamic Loading at Design Point

The aim of this section is to analyse the dynamic loading that is present, at the design point, on the first 3 blade rows (IGV, rotor 1 and stator 1) and to introduce the way that the data will be presented, before going on to compare the different IGV-Rotor axial spacings in the following sections. The dynamic loading is primarily compared by analysing the tangential and axial forces acting on the blades. This provides a clear comparison between different load cases and while it does not analyse the stresses in the blade directly, it is known that relative changes in the blade forces are directly proportional to the maximum blade stresses (because the blade forces are directly proportional to the root bending moment which, in turn, is directly proportional to the maximum blade stress).

The loading on the IGVs is analysed first and the instantaneous force acting on one IGV blade is shown in Fig. 5.1. The force plotted is the tangential force acting across the whole blade and it is plotted for one revolution of the rotor disc—21 rotor 1 blade passings (blade counts for each row are shown in Tab. 5.1 for reference). Only the tangential force is considered for the IGV because the tangential force (and the dynamic range) is much greater than the axial force. The tangential force varies over time around a mean value of 43.8 N and has a simple profile which is periodic for every rotor passing. While it can be seen by inspection of Fig. 5.1 that the IGV loading is strongly dependant on the rotor passing frequency, it is possible to show this more clearly by plotting the Fourier transform of the loading, as shown in Fig. 5.2. As expected, from inspection of Fig. 5.1, there is a clear spike in the frequency at Engine Order (EO) 21 corresponding to the blade passing frequency of the 21 (stage 1) rotor blades. The Fourier transform also reveals the higher harmonics that are present in the loading signal and clear spikes can be seen at the 2nd to 5th harmonics, all with reducing amplitudes.

This analysis has so far only considered a single IGV blade. In a simple unsteady stage simulation of a single rotor and single stator blade row with circumferential uniformity, it would be fair to assume that all the blades, in a given blade row, experienced the same loading variation (albeit with a phase lag). However, in a multistage simulation, the presence of other blade rows in the same relative frame of rotation, and with different blade counts, means that the compressor no longer has a repeating period of a single blade passage. Considering the blade counts for all the stationary blade rows in Tab. 5.1, the compressor, in the stationary frame of reference, has a period equal to half an annulus. In light of this, it is

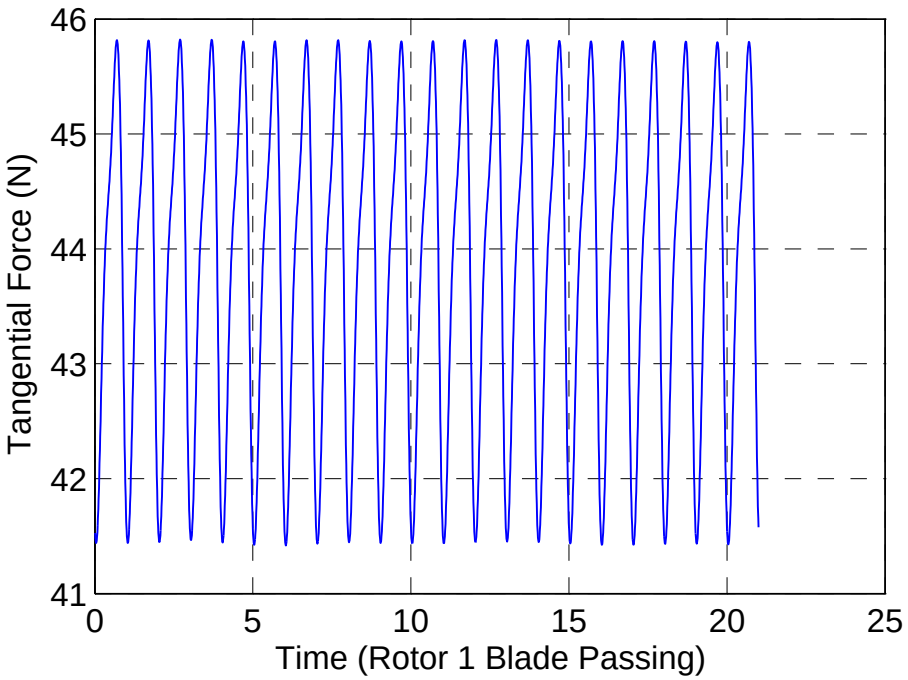

Fig. 5.1 Blade loading variation over time for a single IGV

Table 5.1 Number of blades in each blade row

Blade Row	Blade Count
IGV	26
Rotor 1	21
Stator 1	32
Rotor 2	23
Stator 2	32
Rotor 3	27
Stator 3	44

Table 5.2 IGV time averaged blade loadings

	Minimum	Mean	Maximum
Tangential blade loading	42.1 N	43.5 N	44.7 N
Difference from mean	-3.3%	0.0%	2.8%
Axial blade loading	13.0 N	13.1 N	13.4 N
Difference from mean	-1.5%	0.0%	3.0%

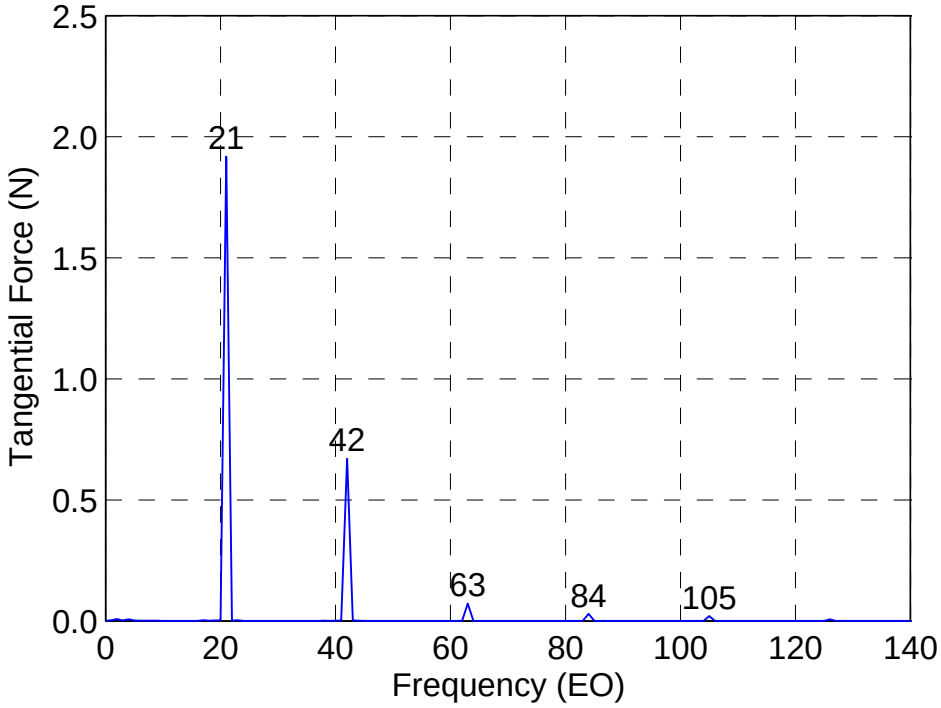

Fig. 5.2 Fourier transform of the loading for a single IGV

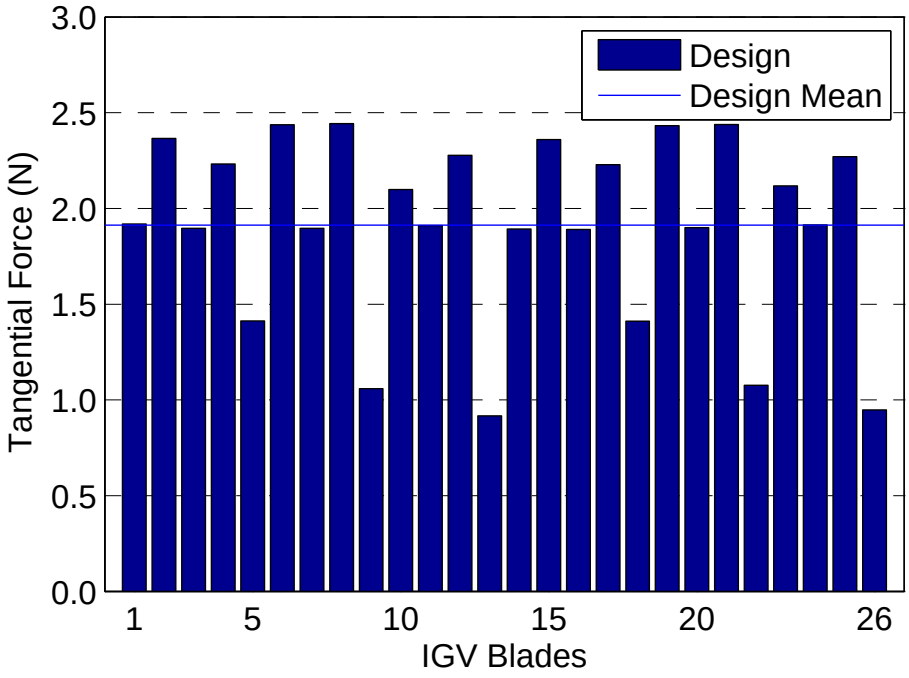

Fig. 5.3 Values of EO21 peaks from Fourier transform of each IGV loading

necessary to consider the dynamic loading of each IGV blade individually. This has been done in Fig. 5.3 by taking the peak value, from the Fourier transform of each individual IGV tangential loading signal, at the frequency of interest—in this case EO21. This gives a good measure of how the dynamic loading varies between blades. The mean dynamic loading, measured as the amplitude of the strongest frequency response (EO21), is 1.9 N but the peak values for the individual blades range from 48% to 128% of the mean. This variation in the magnitude of the dynamic loading is significantly greater than the variation in the time averaged loading between the blades for which the data is shown in Tab. 5.2. The mean time averaged tangential loading is found to be 43.5 N with a variation between individual blades of -3.3%/+2.8%. The magnitude and variation between blades is less for the time averaged axial loading. Inspection of Fig. 5.3 also reveals a periodic pattern of peaks every 13 blades, which corresponds to the compressor half annulus periodicity.

The same analysis is now applied to the first stage rotor and stator blade rows. The tangential loading for a single rotor 1 blade is plotted in Fig. 5.4 for one full revolution. The axial loading of the rotor is also considered and plotted in Fig. 5.5 because the magnitude and dynamic range is similar between the tangential and axial forces. These 2 plots show a much more complex signal than the plot for the IGV in Fig. 5.1, because the rotor loading is influenced by the upstream and downstream blade rows, whereas the IGV dynamic loading is only significantly influenced by a single rotor blade row. It is hard to gain any insight into the dynamic loadings from Figs. 5.4 & 5.5, however, the Fourier transforms of the two loading signals, shown in Figs. 5.6 & 5.7 reveal the component frequencies and therefore which blade rows are impacting the rotor loading. The strongest frequency present in both loading signals is at EO32 which corresponds to the downstream stator 1 blade row. (It is also possible that some of the loading variation could be driven by stator 2, which has the same blade count as stator 1, but separating this out is not possible with this analysis.) Harmonics of this can also be seen at EO64 and EO96. The effect of the wakes from the IGVs can be seen in the spikes at EO26, EO52, EO78 and EO104. Unusually the higher harmonics have a similar amplitude to the fundamental frequency meaning that although the fundamental frequency is not that strong the combined effect of IGVs on the rotor loading is still as significant as the effect of the stators. Peaks at EO6 (and harmonics at EO12 & EO18 for the axial loading) are evidence of the wakes from the inlet struts of which there are 2 rows of 6 vanes co-located around the circumference. The EO6 peaks may also occur as a result of the beat frequency between the IGV (EO26) and stator 1 (EO32) blade rows. The compositions of the tangential and axial loadings signals are very similar with only small changes in the amplitudes, reflecting the different strengths of the overall signals. The only

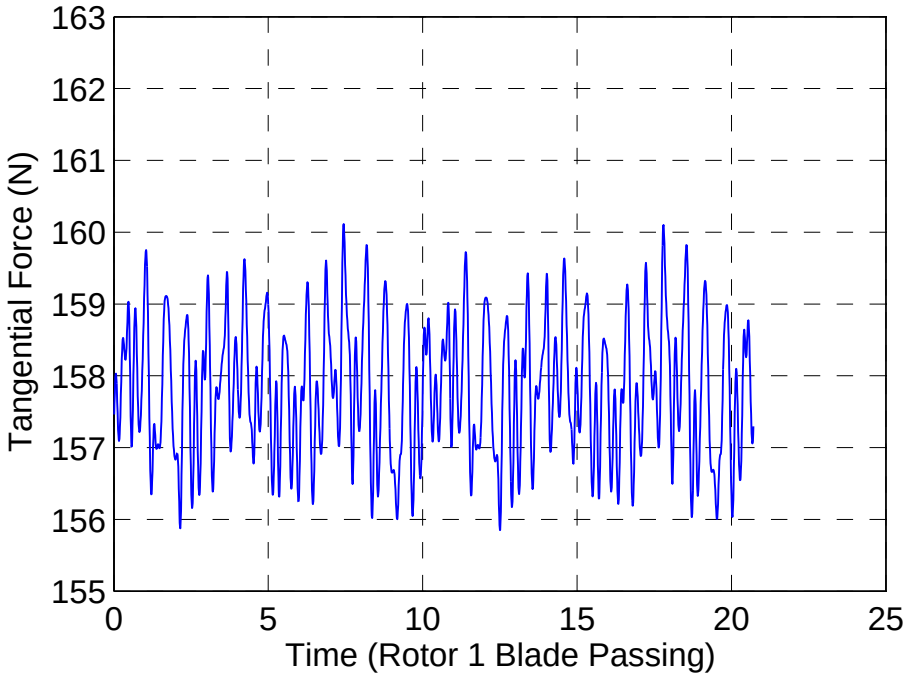

Fig. 5.4 Blade tangential loading variation over time for a single rotor 1 blade

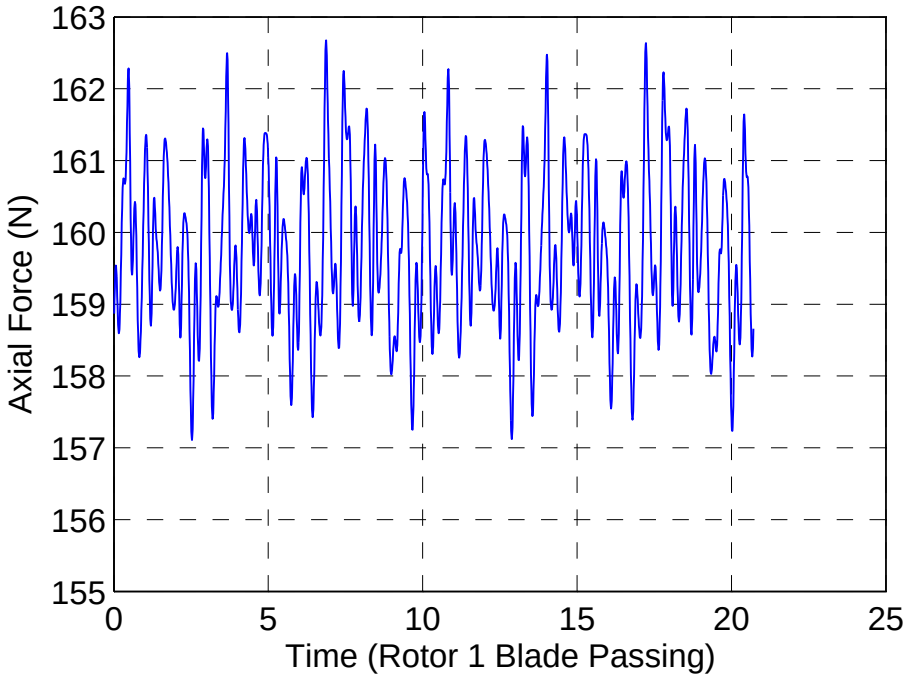

Fig. 5.5 Blade axial loading variation over time for a single rotor 1 blade

exception to this is that the dynamic axial loading is more influenced by the upstream blades (IGV at EO26 and inlet struts at EO6, EO12 & EO18) than the dynamic tangential loading.

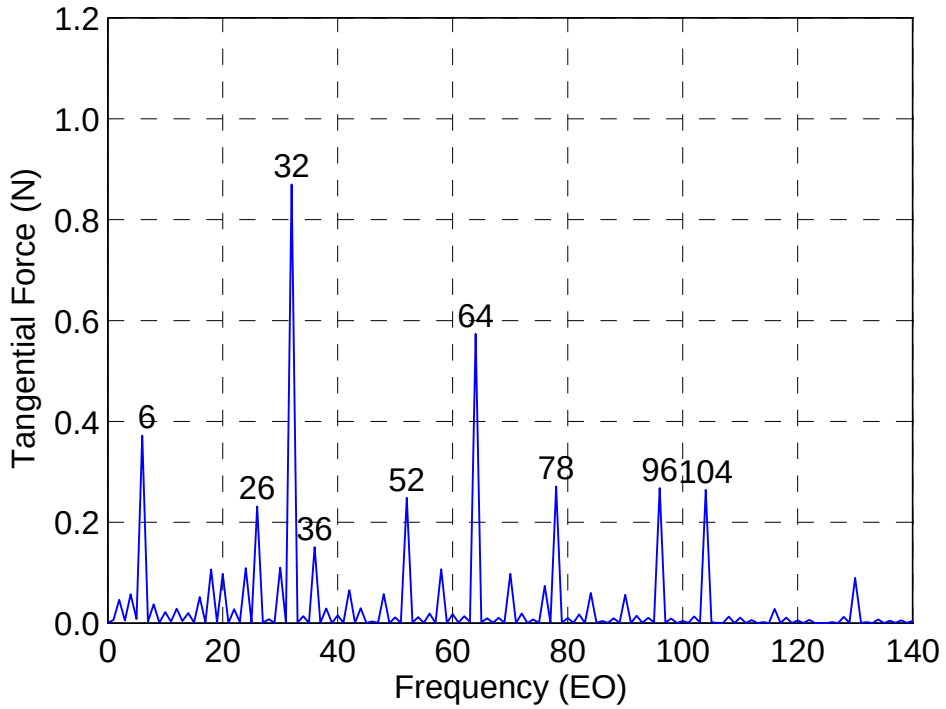

Fig. 5.6 Fourier transform of the tangential loading for a single rotor 1 blade

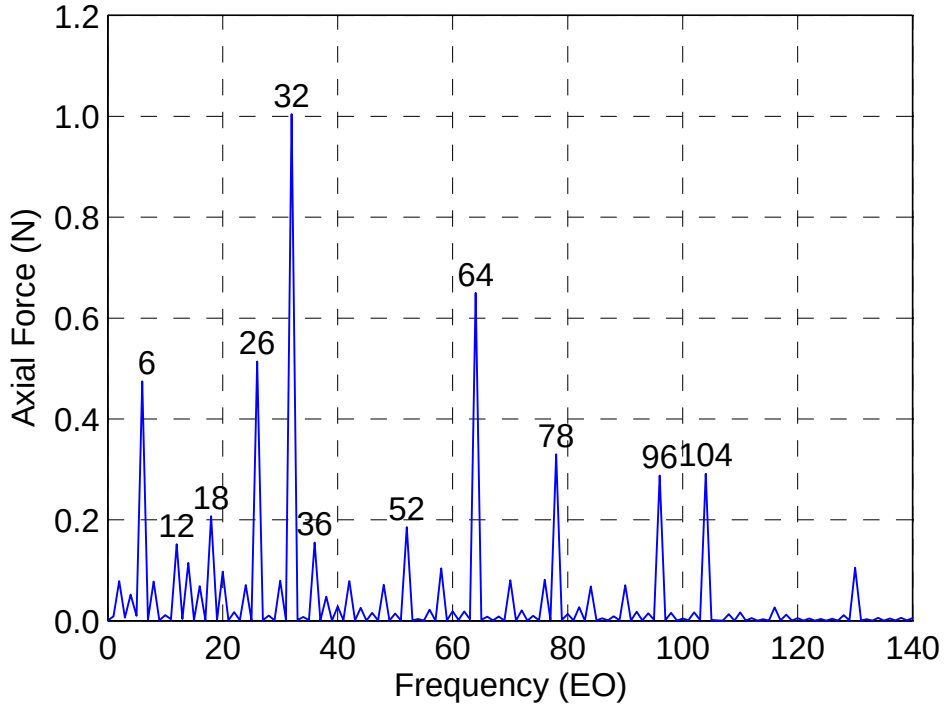

Fig. 5.7 Fourier transform of the axial loading for a single rotor 1 blade

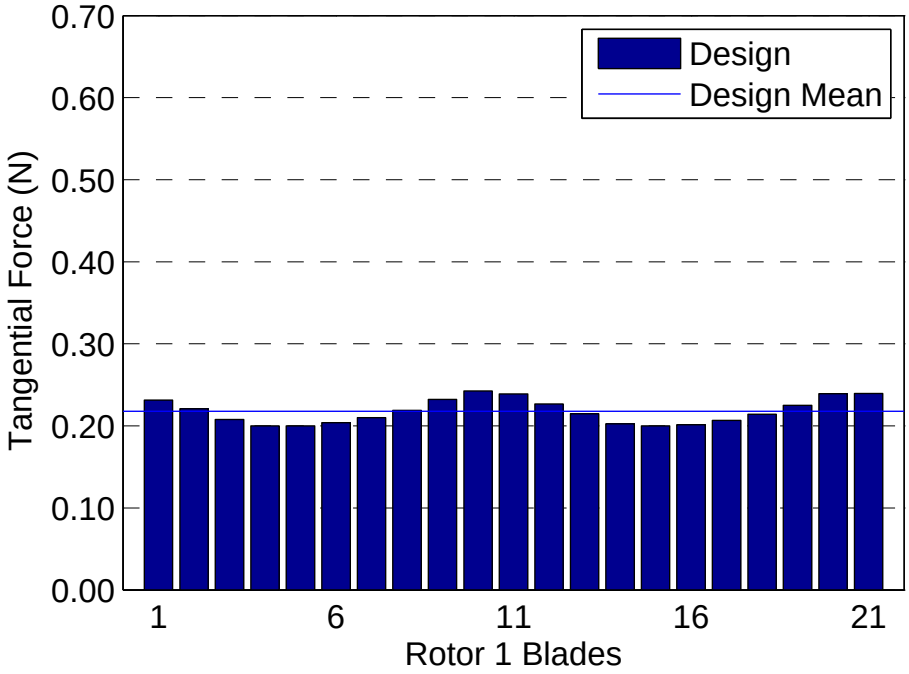

Fig. 5.8 Values of EO26 peaks from Fourier transform of each rotor 1 tangential blade loading

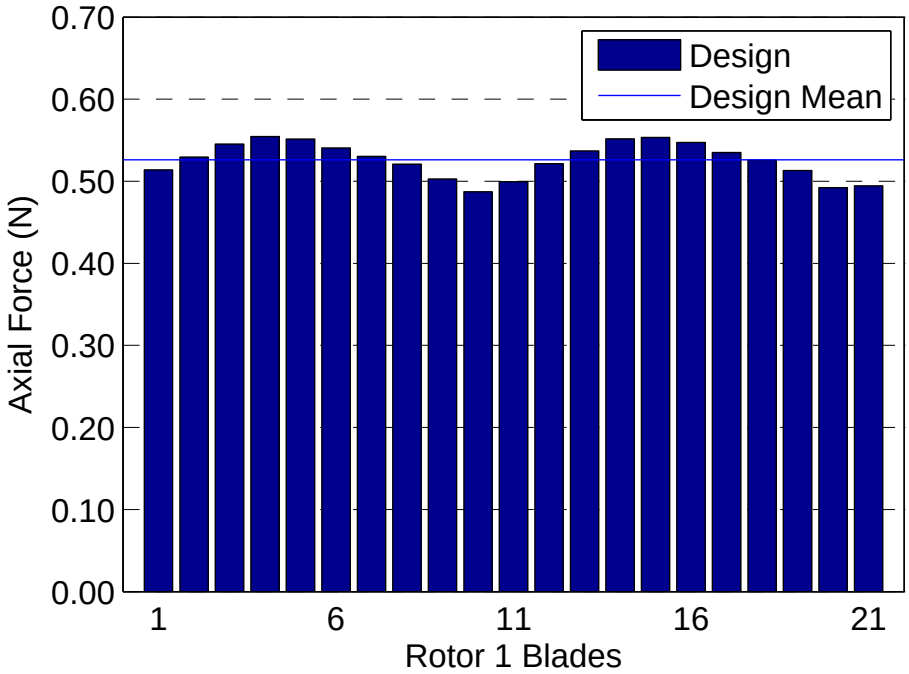

Fig. 5.9 Values of EO26 peaks from Fourier transform of each rotor 1 axial blade loading

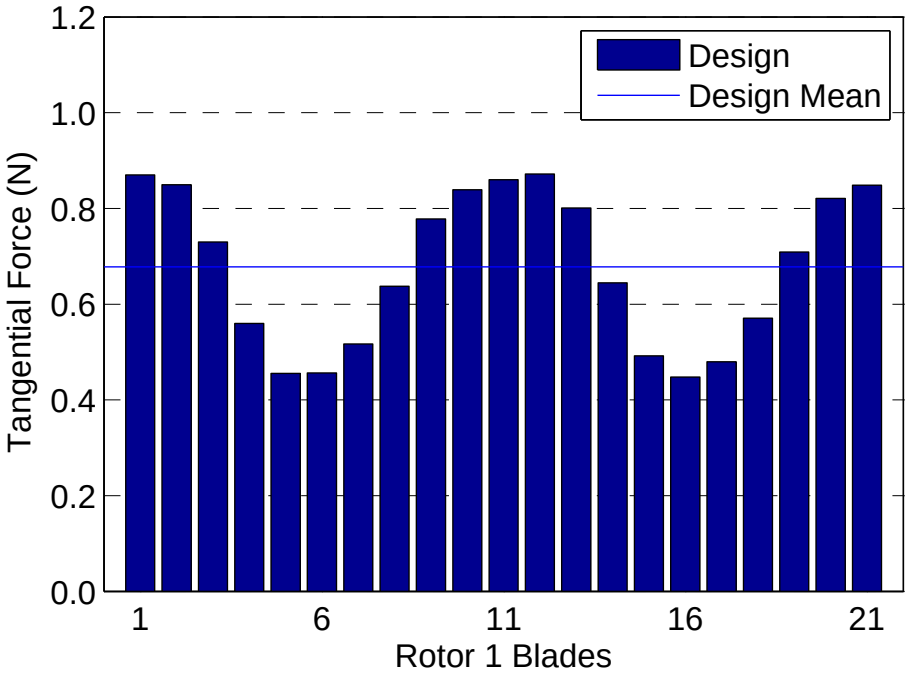

Fig. 5.10 Values of EO32 peaks from Fourier transform of each rotor 1 tangential blade loading

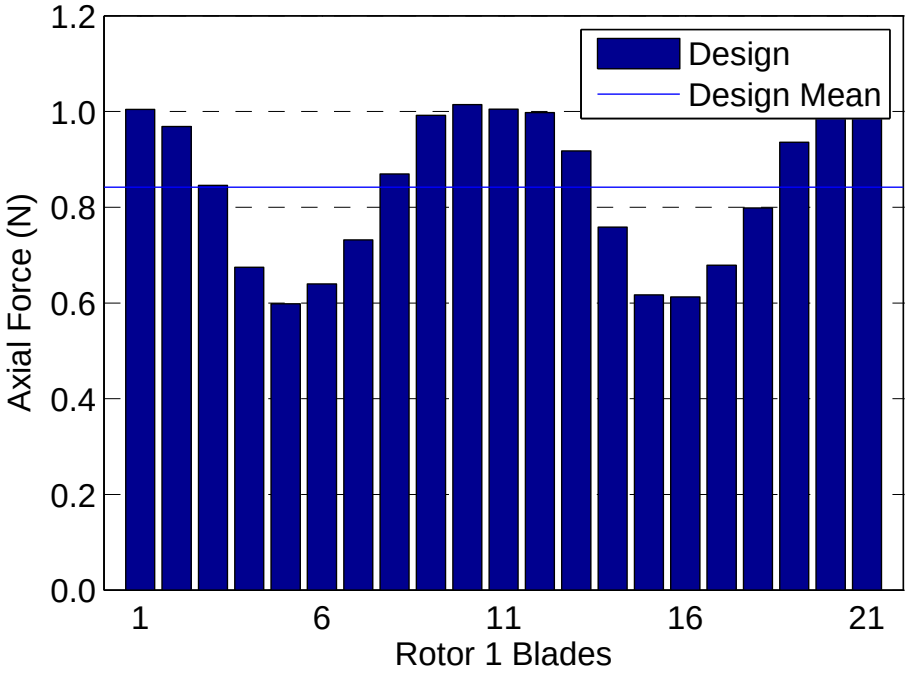

Fig. 5.11 Values of EO32 peaks from Fourier transform of each rotor 1 axial blade loading

Table 5.3 Rotor 1 time averaged blade loadings

	Minimum	Mean	Maximum
Tangential blade loading	157.6 N	157.8 N	158.1 N
Difference from mean	-0.1%	0.0%	0.1%
Axial blade loading	159.6 N	159.8 N	160.0 N
Difference from mean	-0.1%	0.0%	0.1%

To examine the variation in dynamic loading between the individual rotor blades, the peaks of the individual blade Fourier transforms (tangential and axial forces) have been plotted for EO26 (Figs. 5.8 & 5.10) and EO32 (Figs. 5.9 & 5.11). The variation between rotor blades is less than the variation seen between IGVs. The variation of the EO26 peaks between the rotors for the tangential loading is about $\pm 30\%$ and about $\pm 10\%$ for the axial loading (although this is due to the higher mean magnitude of the peaks as the absolute variation is similar). The differences between the tangential and axial force dynamic variations are very similar but are in anti-phase with each other. At EO32 the variation is about $\pm 10\%$ for both the tangential and axial forces. The variation in dynamic loadings between the rotor blades is much greater than the variation between the time averaged loadings for the individual blade rows, shown in Tab. 5.3, which is only $\pm 0.1\%$. The variation between rotor time averaged loadings is very small because the blade rotation means that they all experience the same flow variations that are present around the circumference of the compressor. This is in contrast to the IGVs for which the wakes from the inlet struts affect the time averaged loading of individual blades.

The tangential loading history for a stator 1 blade is plotted in Fig. 5.12 and the axial loading history in Fig. 5.13. For the stator, the tangential force is about twice the strength of the axial force. Both signals show a low frequency shape as well as the high frequency oscillation caused by blade interaction from adjacent rotor blade rows. The Fourier transforms of both signals in Figs. 5.14 & 5.15 show the frequency components at EO21 and EO23 from the upstream and downstream rotor blade rows respectively. These two blade counts create a beat frequency at EO2. The Fourier transforms only show a small peak at EO2, however the shape of the signals in Fig. 5.12 & 5.13 clearly reveal this beat frequency as the pattern repeats every 16 blades. Figures 5.16 & 5.17 show a comparison of all the stator 1 blades by examining the strength of the EO21 frequency component for each blade in the tangential and axial loading signals. There is a periodic pattern to the dynamic loadings that is similar in both the tangential and axial forces (although the magnitudes of the dynamic axial force are lower than the dynamic tangential forces) and it repeats half way around the circumference of the compressor, in the same manner as the loading variation between the IGV blades. The

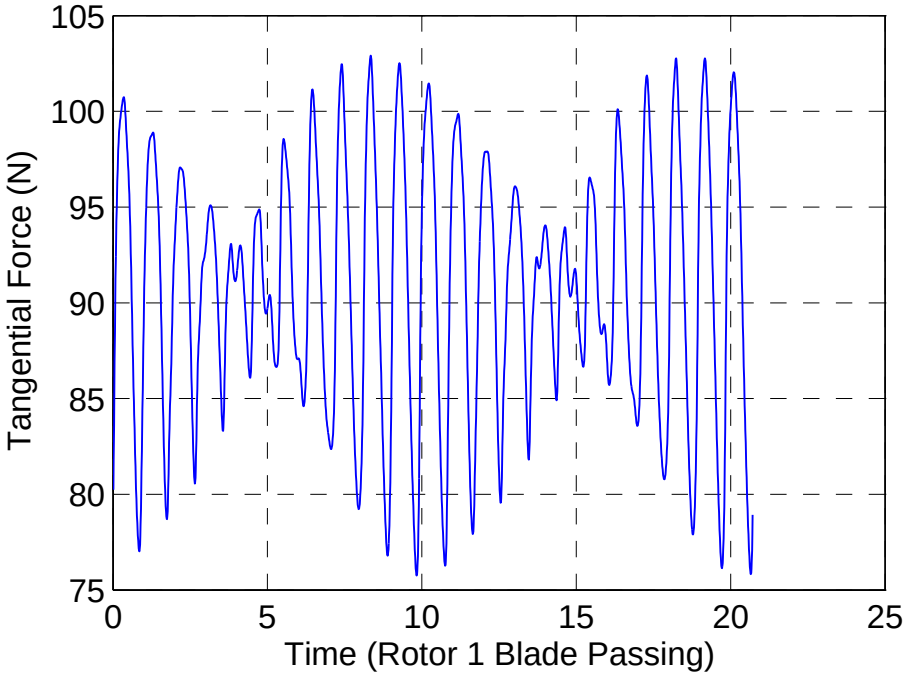

Fig. 5.12 Blade tangential loading variation over time for a single stator 1 blade

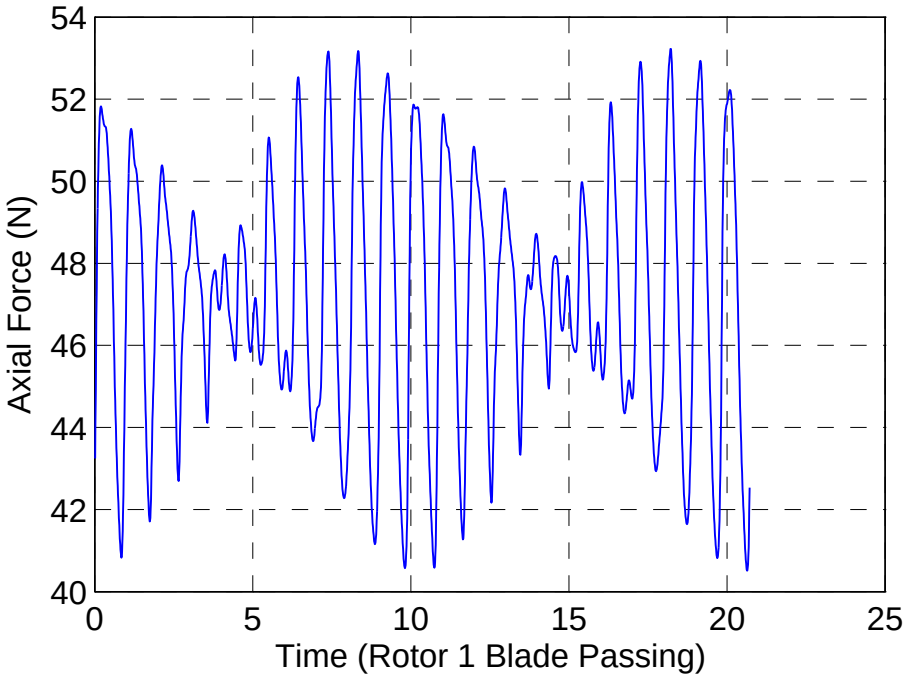

Fig. 5.13 Blade axial loading variation over time for a single stator 1 blade

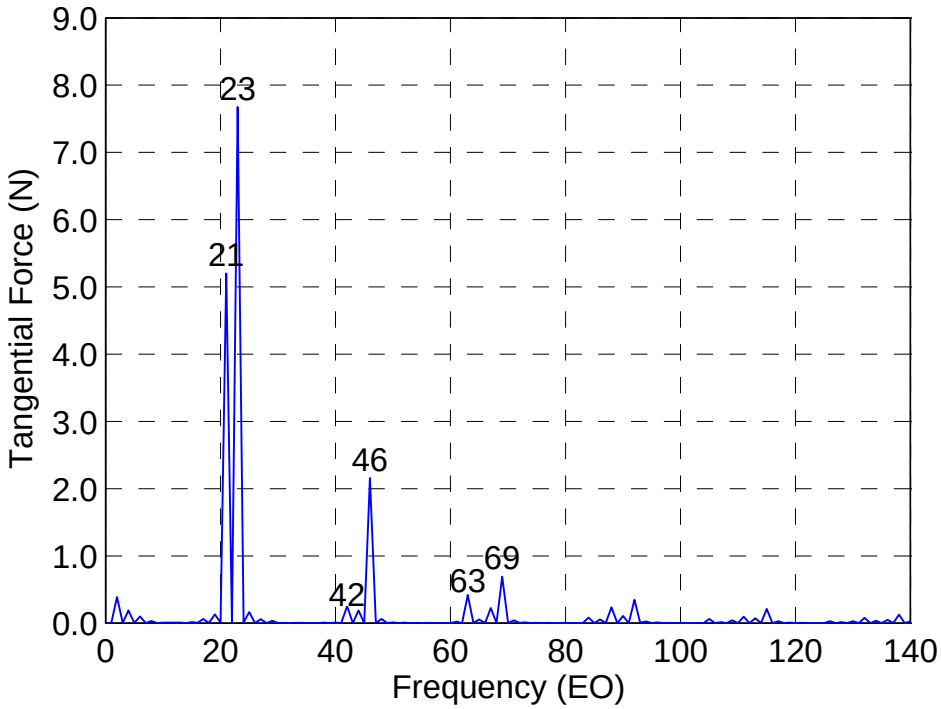

Fig. 5.14 Fourier transform of the tangential loading for a single stator 1 blade

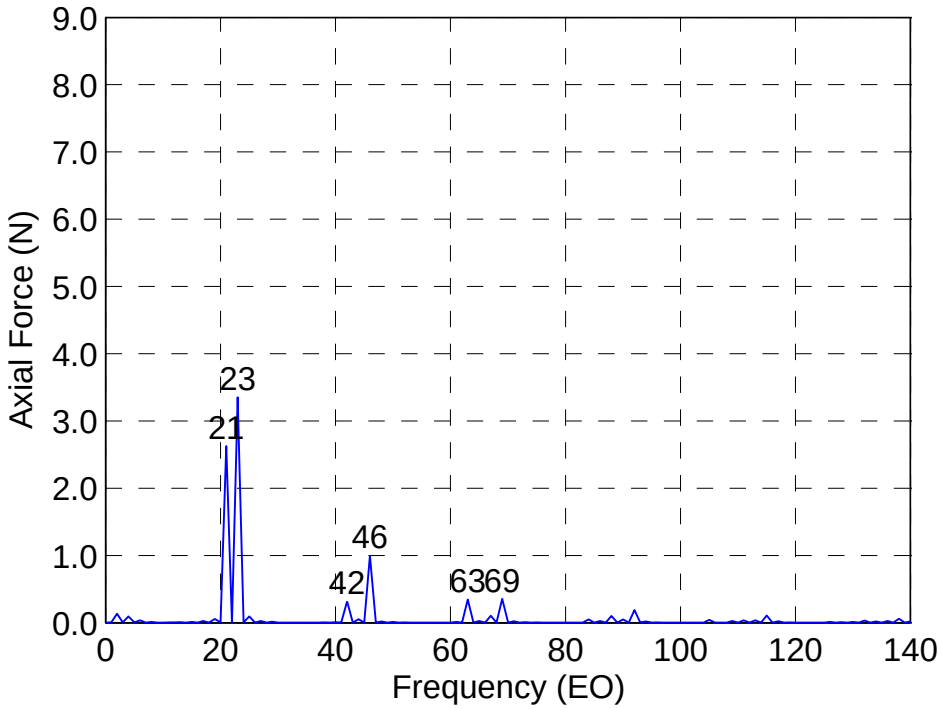

Fig. 5.15 Fourier transform of the axial loading for a single stator 1 blade

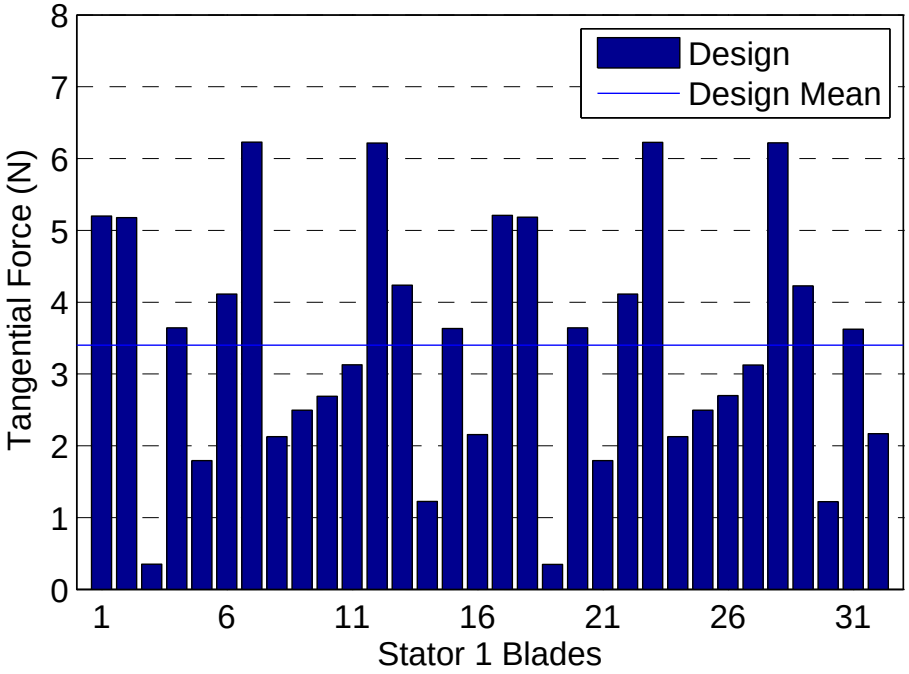

Fig. 5.16 Values of EO21 peaks from Fourier transform of each stator 1 tangential blade loading

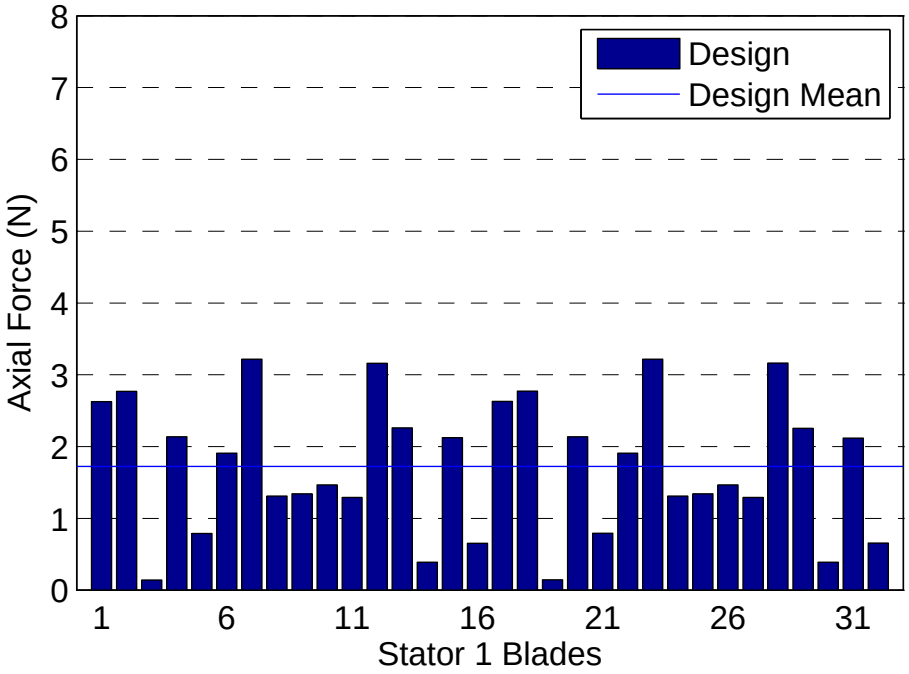

Fig. 5.17 Values of EO21 peaks from Fourier transform of each stator 1 axial blade loading

Table 5.4 Stator 1 time averaged blade loadings

	Minimum	Mean	Maximum
Tangential blade loading	88.0 N	90.1 N	91.2 N
Difference from mean	-2.4%	0.0%	1.2%
Axial blade loading	45.6 N	46.8 N	47.3 N
Difference from mean	-2.6%	0.0%	1.2%

stators, on average, experience a much greater dynamic tangential loading than either the IGVs or the rotor blades. The amplitude of the EO21 frequency component of the dynamic tangential loading has a mean value of 3.4 N across all the stators but there is a large blade to blade variation with values for individual blade varying between 10% and 184% of the mean. Data for the time averaged loadings is shown in Tab. 5.4. The mean time averaged loading for the stators is more than double that of the IGVs so although the absolute variation of the time averaged variation between blades has increased, compared to the IGVs, the percentage differences have reduced. The main cause of the difference in the time averaged loadings between stator 1 blades is the convection downstream of the inlet strut wakes that have a more significant effect on the IGVs.

5.3 Efficiency Analysis of Smaller Axial Spacing

In this section, a comparison of simulations performed with design axial spacing and 40% IGV-Rotor axial spacing is presented. In this section, the focus is on the efficiency differences between the two configurations. The initial investigation into the axial spacing used steady, single blade passage simulations and the 3-stage efficiency calculated from these simulations is shown in Fig.5.18. The 40% gap efficiency characteristic follows the design axial spacing efficiency characteristic very well from low pressure ratios up to around the design pressure ratio of 3. However, at higher pressure ratios the efficiency predictions start to diverge and the 40% gap simulation predicts a 0.3% lower efficiency at a pressure ratio of 3.3.

In order to change the axial spacing between the IGV and Rotor 1, the annulus line was altered as detailed in the methods chapter. Doing this has had an effect on the relative flow angle upstream of the rotor. The radial relative flow angle distribution upstream of the rotor 1 blade row is plotted in Fig. 5.19 for the design pressure ratio of 3. Near the tip there is a change in the flow angle of around 1 Degree. As has already been seen in Fig.5.18, there is no significant change in the efficiency at the design pressure ratio and therefore this change in flow angle is not significant for the current study.

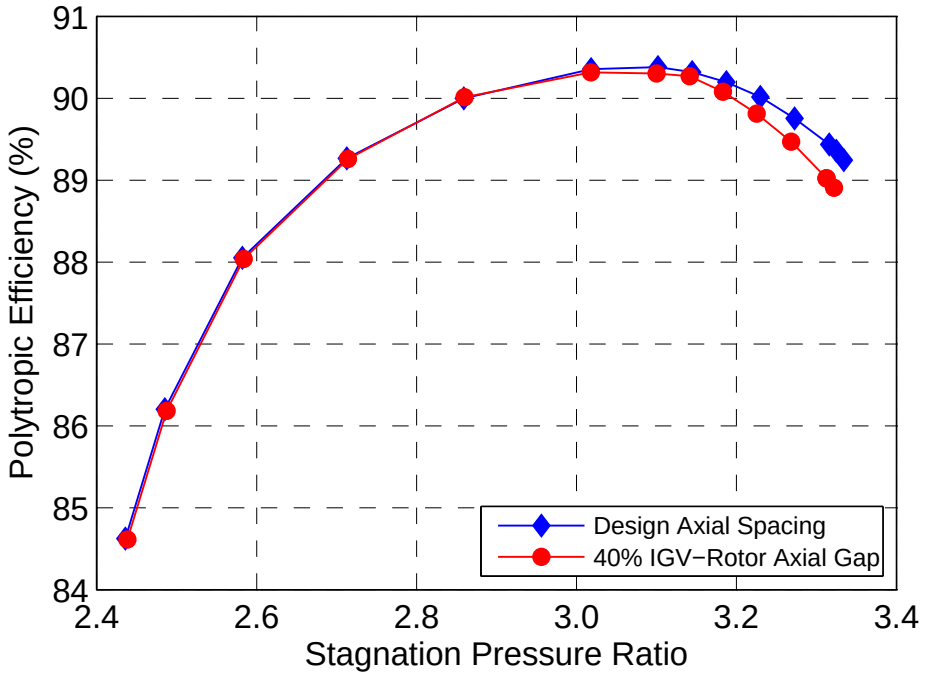

Fig. 5.18 3-stage efficiency for design and 40% IGV-Rotor axial spacing from steady simulations

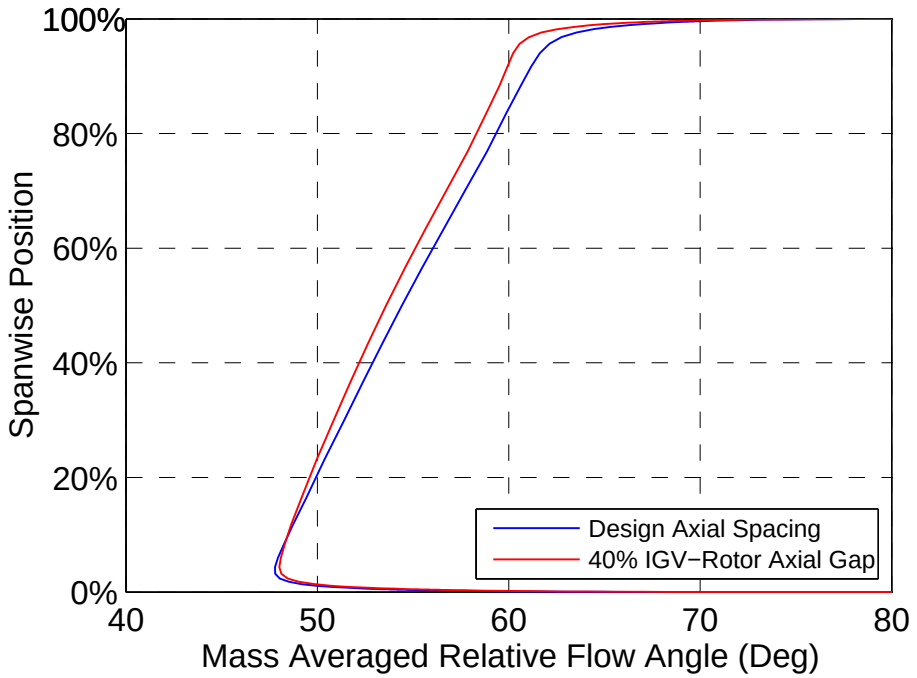

Fig. 5.19 Relative inlet flow angle to rotor 1 for design and 40% IGV-Rotor axial spacing from steady simulations at design pressure ratio

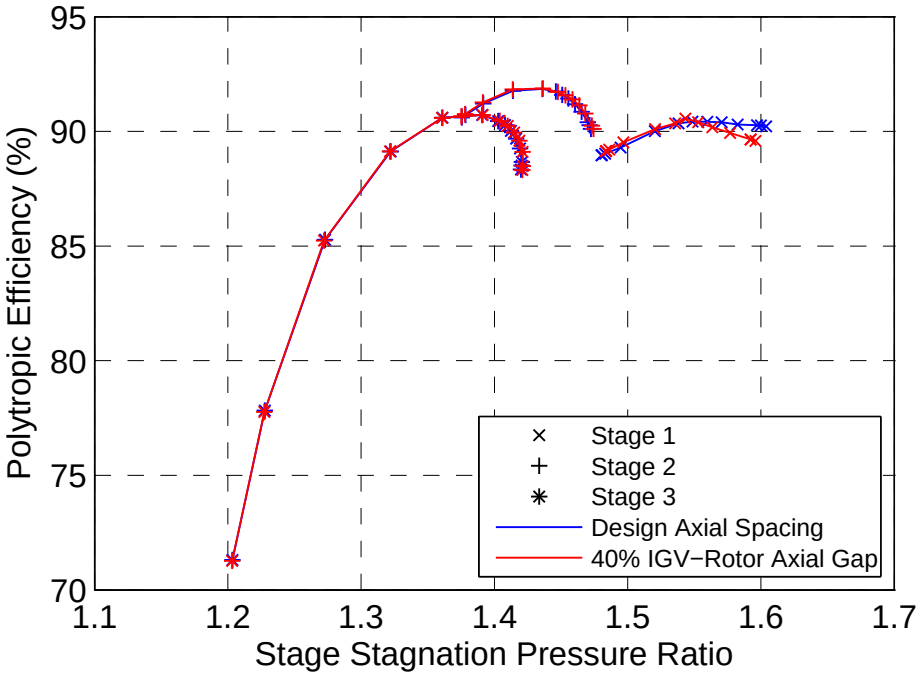

Fig. 5.20 Individual stage efficiencies for design and 40% IGV-Rotor axial spacing from steady simulations

A more detailed examination of the individual stage efficiencies, shown in Fig. 5.20, reveals that it is the stage 1 efficiency predictions, for the two configurations, that diverge at high pressure ratios. Reducing the size of the gap between the IGV and the rotor has meant that the mixing plane in the steady simulation is located closer to the IGV trailing edge and the rotor leading edge. The mixing plane loss has been analysed separately in order to check if the close proximity of the mixing plane to the blades has created an excessive loss across the mixing plane. The mixing plane loss is defined in Eqn. (5.1) and plotted in Fig. 5.21 for 3 different mixing planes in both the design axial spacing and 40% design axial spacing simulations at a stage 1 pressure ratio of just under 1.6. It can be seen that reducing the axial spacing has led to an 8 fold increase in the loss across the mixing plane between the IGV and the rotor. This loss is significantly greater than the changes in mixing plane loss for mixing planes between other blade rows. The close proximity of the mixing plane to the IGV trailing edge and rotor leading edge has possibly led to an artificial increase in the mixing loss. This has led to the conclusion that steady simulations with this mixing plane model may not be suitable for analysing this geometry with the very small axial spacing.

$$Mixing\ Plane\ Loss\ (\%) = 100\ \times\ \frac{\bar{T}_{stage\ outlet}(\Delta\bar{s}_{mixing\ plane})}{\Delta\bar{h}_{stage}} \tag{5.1}$$

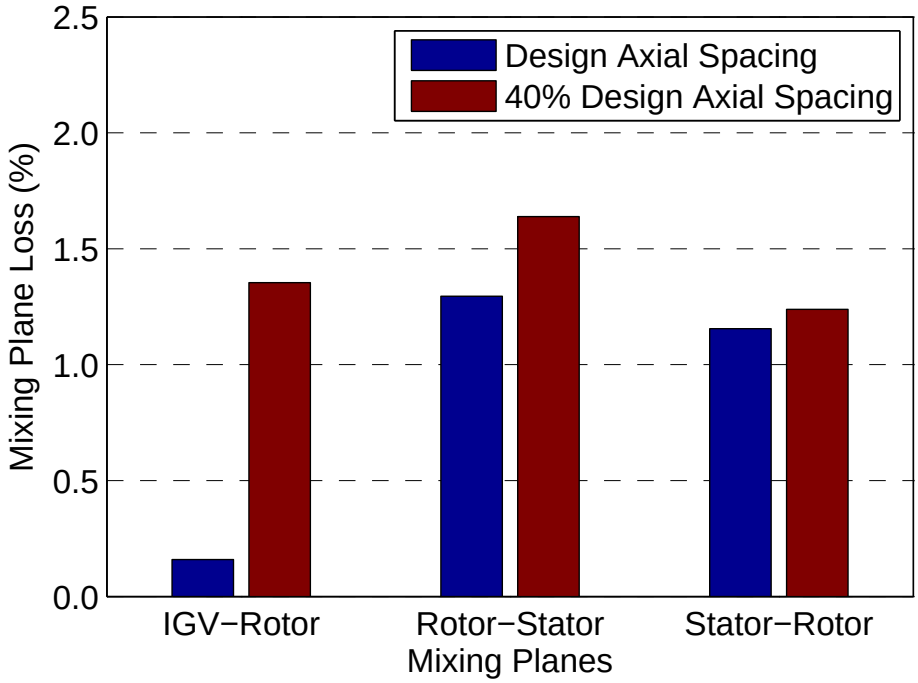

Fig. 5.21 Loss across different mixing planes for design axial spacing and 40% design axial spacing at a stage 1 pressure ratio of approximately 1.6

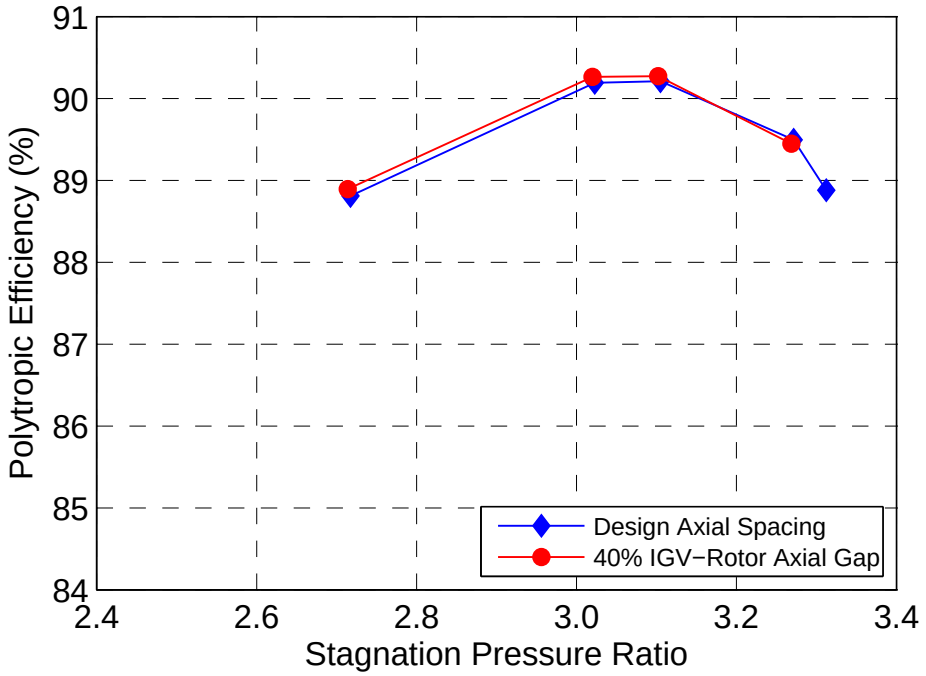

Fig. 5.22 3-stage efficiency for design and 40% IGV-Rotor axial spacing from unsteady simulations

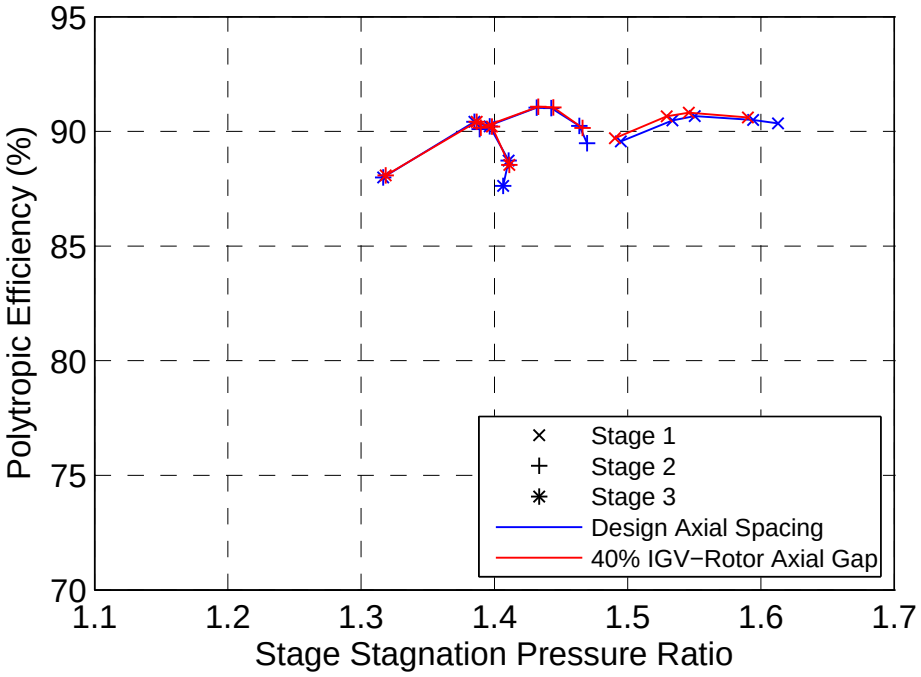

Fig. 5.23 Individual stage efficiencies for design and 40% IGV-Rotor axial spacing unsteady simulations

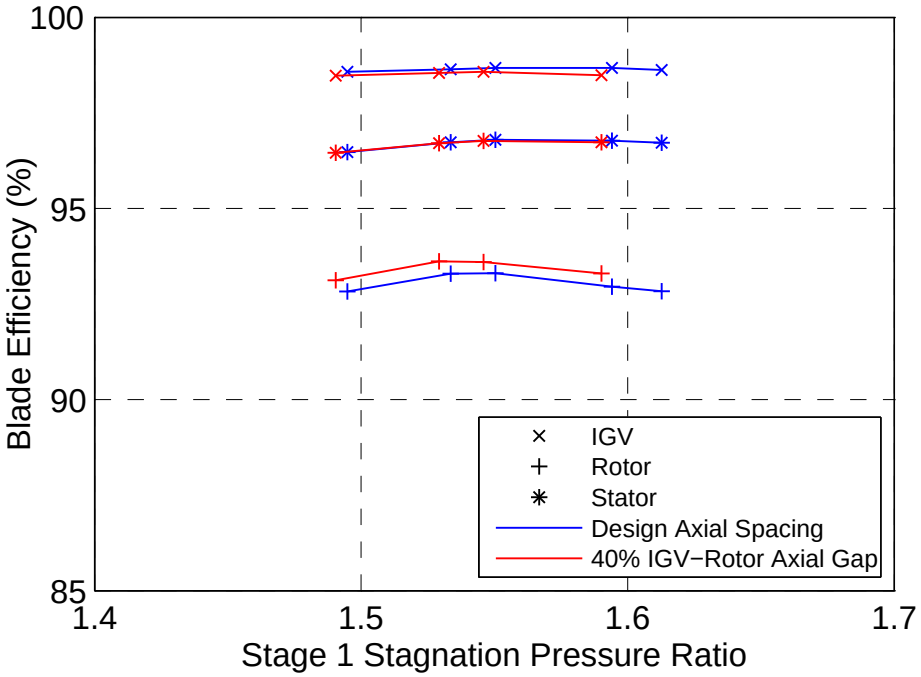

Fig. 5.24 3-stage compressor efficiency for design and 40% IGV-Rotor axial spacing unsteady simulations

In order to overcome the uncertainty around the mixing plane, and to capture the effects of blade row interaction at closer separations, the compressor is characterised with the design and 40% IGV-Rotor spacings using quarter annulus unsteady simulations. The overall compressor efficiency predictions for these simulations are presented in Fig. 5.22. Over the majority of the range there is a small efficiency improvement of about 0.1% for the configuration with a smaller axial gap between the IGV and the rotor. This efficiency improvement drops off at higher pressure ratios and at a pressure ratio of 3.27 the efficiency is below the efficiency of the design axial spacing configuration by 0.05%. The data in Fig. 5.23 shows that the overall efficiency improvement, seen in Fig. 5.22, has occurred due to an efficiency improvement in stage 1 as a result of reducing the IGV-Rotor spacing. (The stage 1 efficiency is not seen to reduce at high pressure ratio for the smaller axial spacing configuration as was seen in the steady simulation results (Fig. 5.20)). It can also be seen that a very slight change has occurred in the stage matching. This change in stage matching has led to a lower pressure rise in stage 1 and a slightly higher pressure ratio in stage 2 and 3 for any given operating point. The stage efficiency characteristics for stages 2 and 3 have remained unchanged so, at lower overall pressure ratios, the slightly higher pressure ratios in stage 2 and 3 have led to a slight increase in efficiency for these stages as the operating points are pushed up the characteristics. At high overall pressure ratios, stage 1 still has a slightly higher efficiency, when the IGV-Rotor Gap is 40% of design spacing, however the re-distributed stage matching means that at high pressure ratios the increased pressure ratio in stage 2 and 3 pushes these stages to a slightly lower efficiency. The drop in stage 2 and 3 efficiencies is what causes the drop in overall efficiency at higher pressure ratios. Unlike stages 2 and 3, the stage one characteristic has changed and has a higher efficiency across its entire range. Looking at Fig. 5.24 it can be seen that the efficiency increase in stage 1 has come from an improvement in the rotor efficiency as defined in Eqn. (4.2). It can also be seen in Fig. 5.24 that the IGV efficiency is lower for the 40% configuration and the difference grows at higher pressure ratios. This is due to the greater disturbance of the IGV flow by the rotor leading edge shock wave when the IGV-Rotor gap is reduced.

The improvement in the rotor efficiency was investigated further by looking at the entropy increase through the rotor and it is shown in Fig. 5.25 for the design pressure ratio simulations of both axial spacing configurations. It can be seen that there is a reduction in the entropy increase through the rotor from 5% to 80% span for the 40% IGV-Rotor axial spacing configuration. One reason for this is that the reduced axial gap simulation has a lower peak suction surface Mach number. The isentropic surface Mach number is plotted in Fig. 5.26 for 50% span. The instantaneous results are plotted for each time step through a full revolution of the domain (quarter annulus) in order to show the variation of the results through a number

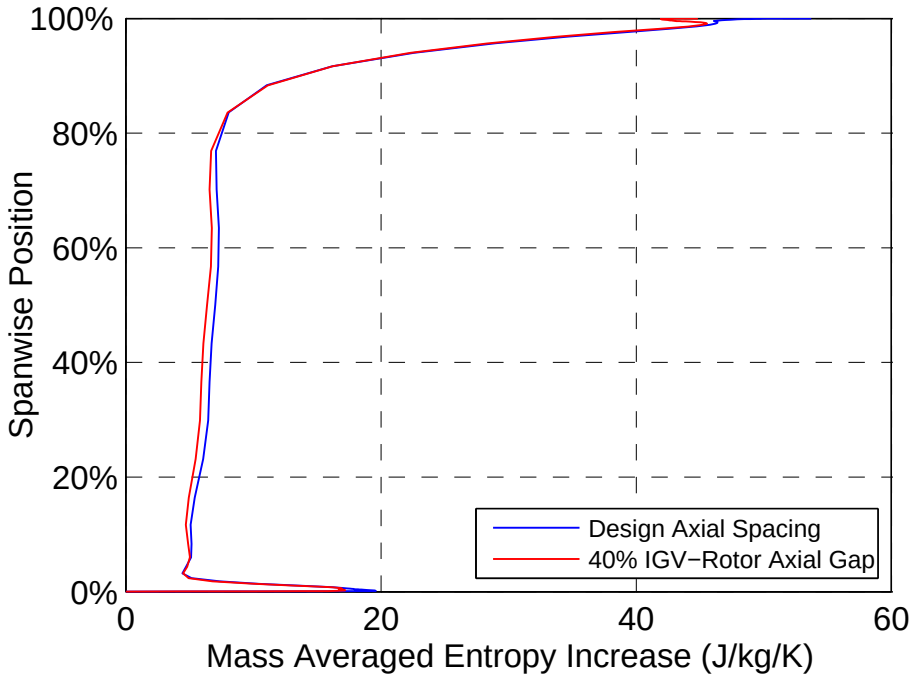

Fig. 5.25 Entropy increase through rotor 1 for design and 40% IGV-Rotor axial spacings from time averaged unsteady simulations at design pressure ratio

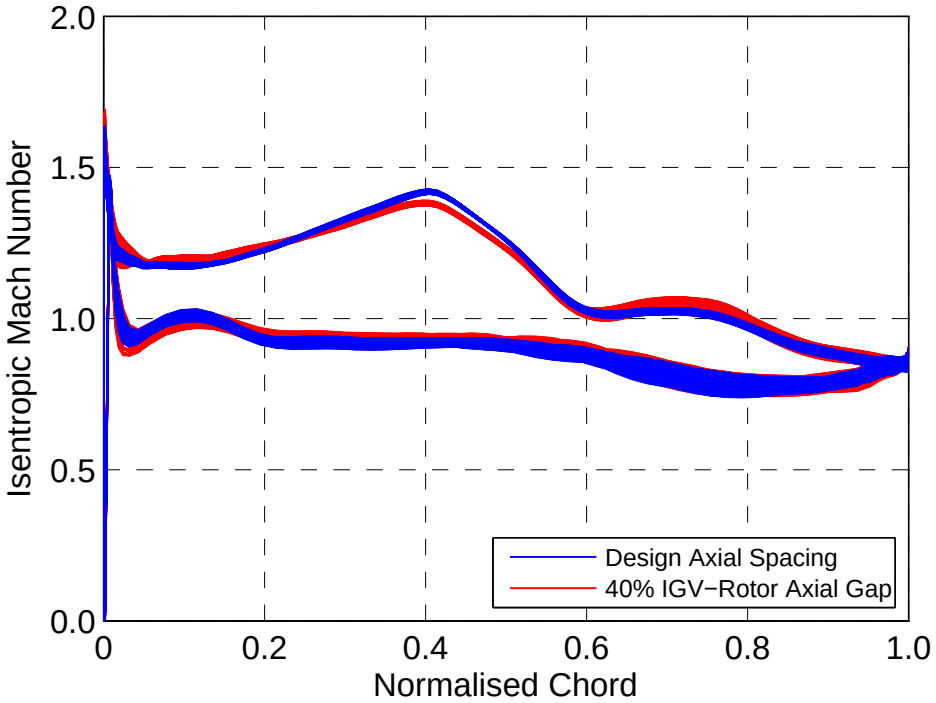

Fig. 5.26 Rotor 1 isentropic surface Mach number at 50% span for design and 40% IGV-Rotor axial spacings from unsteady simulations at design pressure ratio

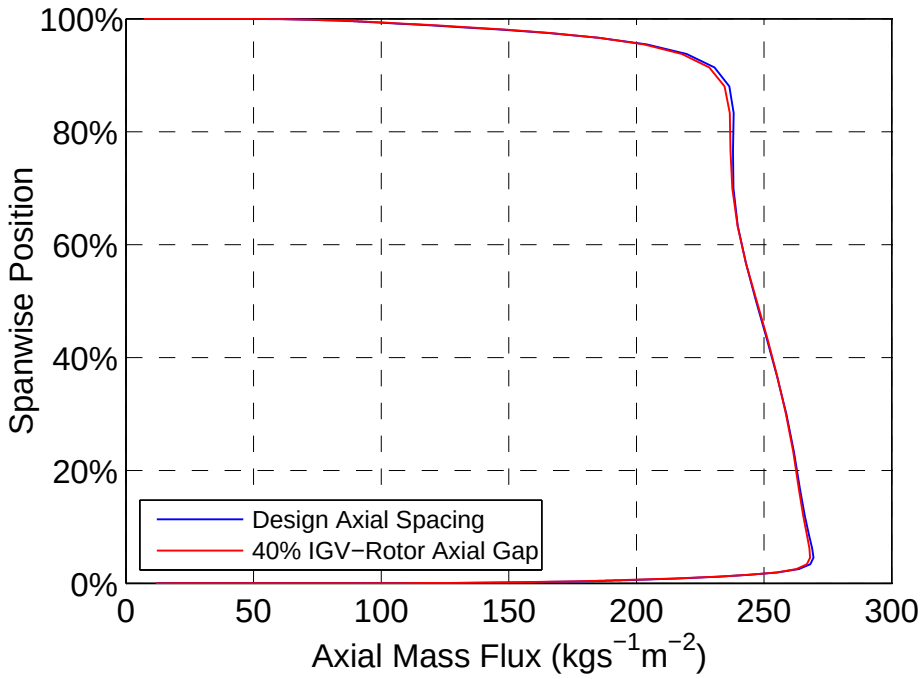

Fig. 5.27 Mass flux distribution downstream of rotor 1 for design and 40% IGV-Rotor axial spacings from time averaged unsteady simulations at design pressure ratio

of blade passings. It can be clearly seen that the peak Mach number at 40% of chord is lower at all points in time for the configuration with the reduced axial gap.

A final comparison of the time averaged, quarter annulus, unsteady results is made of the mass flow distribution across the span downstream of the rotor 1 blade row. The axial mass flux is plotted in Fig. 5.27 for both the design and 40% IGV-Rotor axial spacing. It can be seen that the different axial spacings have only a very small effect on the radial mass flow distribution. There is a very slight reduction in the mass flow around 90% and 5% span, however there is no significant re-distribution of flow.

5.4 Blade Loading Analysis of Smaller Axial Spacing

The differences in blade loadings are analysed in this section at design operating conditions for the design and 40% IGV-Rotor axial spacings in order to gain a better understanding of the mechanical implications of reducing the axial spacing. The analysis is performed using results from full annulus unsteady simulations in order to capture the correct frequencies of the blade row interactions. The analysis will focus on the dynamic tangential blade loadings as it was found earlier in this chapter that both the axial and tangential forces exhibited similar frequencies. Furthermore, the changes in the dynamic tangential forces, as the geometry

Table 5.5 IGV time averaged tangential blade loading comparison

	Mean time average blade loading (N)	Change from design
Design spacing	43.5	0.0%
40% spacing	45.4	+4.4%

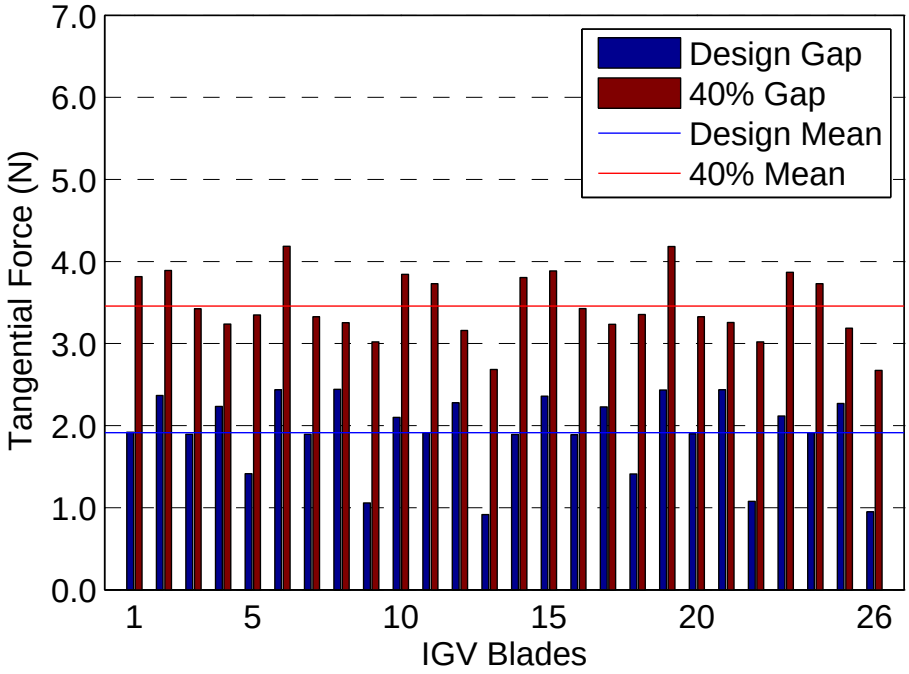

Fig. 5.28 Fourier transform values at EO21 for each IGV blade comparing both axial spacings

changes, are greater than the changes in the dynamic axial forces so focusing on the tangential forces will give a clearer indication of the effect of altering the axial spacing. In order to make comparisons, that take into consideration the differences in blade loadings that occur between blades in the same blade row, results will be presented in bar charts as introduced earlier in this chapter. This allows the magnitude of the dynamic tangential loading at a significant frequency (i.e. relative blade passing frequencies) to be compared between IGV-Rotor gap configurations for all blades in a given blade row.

Altering the axial spacing between the IGV and rotor blade rows affects both the time averaged loading and the dynamic loading of the blade rows. Table 5.5 shows the mean of the time averaged loading across all of the IGV blades for the design and reduced IGV-Rotor axial spacing. The mean blade loading has increased by 4.4% and this increase is distributed fairly uniformly across the individual blades. There is also an increase in the dynamic tangential loading on the IGVs which is shown for EO21 and EO42 in Figs. 5.28 and 5.29.

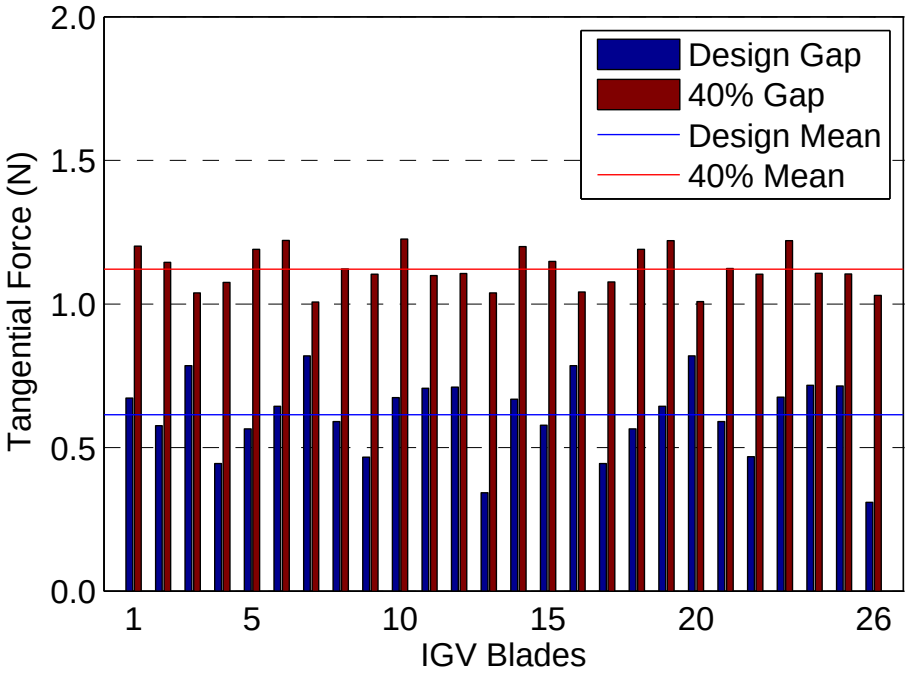

Fig. 5.29 Fourier transform values at EO42 for each IGV blade comparing both axial spacings

Table 5.6 Rotor time averaged tangential blade loading comparison

	Mean time average blade loading (N)	Change from design
Design spacing	157.8	0.0%
40% spacing	155.8	-1.3%

At both of these frequencies, there is an increase in the dynamic tangential loading by a factor of 1.8. The reduced spacing has also caused the variation in dynamic tangential loading between IGVs to reduce so that at EO21 the dynamic tangential loading in the 40% spacing configuration varies between 77% and 122% of the mean value (compared to 48% and 128% at design spacing).

The time averaged loading for the rotor 1 blades has decreased by 1.3% (Tab. 5.6) however the dynamic tangential loading has increased. Figure 5.30 shows that the mean dynamic tangential loading for the frequency component at EO26 (IGV relative blade passing frequency) has increased by a factor of 6.5. This increase has occurred because the IGV wakes are less mixed out when they interact with the rotor blade due to the axial spacing being smaller. (For comparison the dynamic axial loading increases only by a factor of 1.3.) Despite the large ratio for the increase in dynamic tangential loading, the absolute values for the dynamic tangential loading remain small and the magnitude of the component of

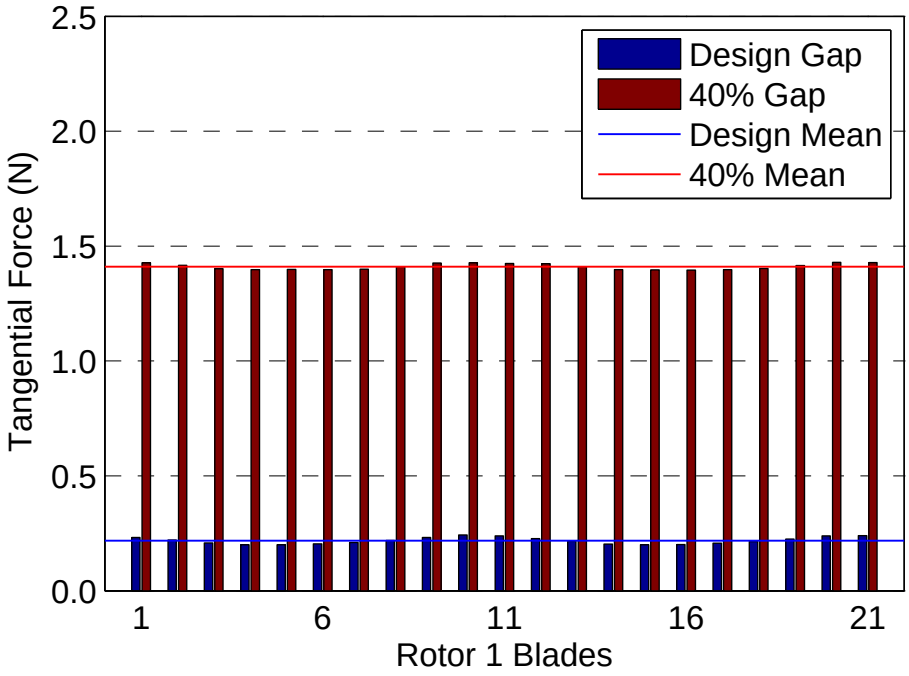

Fig. 5.30 Fourier transform values at EO26 for each rotor 1 blade comparing both axial spacings

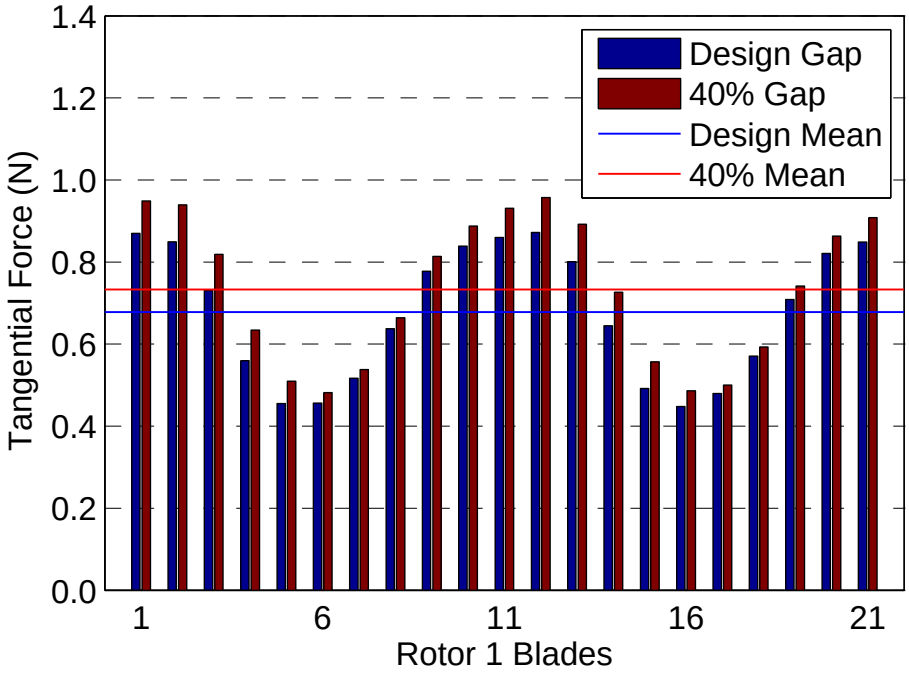

Fig. 5.31 Fourier transform values at EO32 for each rotor 1 blade comparing both axial spacings

dynamic tangential loading at the frequency corresponding to EO26 is only 0.9% of the mean time averaged blade loading of 155.8 N. The component of dynamic tangential loading corresponding to the 2nd harmonic of the IGV relative blade passing frequency (EO52) is affected in a similar way, although the ratio of the increase in the mean dynamic tangential loading at this frequency is only 1.4. At EO32 (corresponding to the relative stator blade passing frequency), the mean dynamic tangential loading increases by a factor of 1.1 and the blade to blade variation is maintained between both spacing configurations, as shown in Fig. 5.31. The increase in the dynamic tangential loading component at EO32 is unexpected because there has been no change in the geometry between the rotor and the stator, however it is thought that the increase could be attributed to the increase in the stator time averaged loading shown in Tab. 5.7. Although the increase is small, the increased loading would cause it to influence the loading of adjacent blade rows (i.e. the rotor) more.

As already mentioned, the mean stator time averaged loading has increase slightly (0.4%) as a consequence of reducing the IGV-Rotor spacing. The dynamic tangential loading has been affected more noticeably, as shown in Fig. 5.32, however the change in the mean value across all the stator blades for the component of dynamic tangential loading at EO21 (rotor blade passing frequency) is very small. Although the mean value is very similar, there is significant variation in the dynamic tangential loading for individual blades. This is very similar to a clocking effect between the IGV and stator blades. Although neither the IGV nor stator have been clocked (changed physical circumferential location), the reduction of the gap between the IGV and the rotor mean that the IGVs and stators are also closer to each other in the axial direction. The closer spacing means that the IGV wakes, which have a tangential component to their velocity, have less axial distance to travel before interacting with the stator blades and therefore travel less tangential distance as well. This means that a given IGV wake interacts with the stator blade row at a different tangential location, in a manner similar to if the IGV had been clocked, and this is the cause of the change in the blade to blade variation of the dynamic tangential loading seen in Fig. 5.32.

One of the reasons for performing the IGV-Rotor axial spacing investigation in a multi-stage simulation was to investigate the effect that the change in spacing has on the downstream

Table 5.7 Stator time averaged tangential blade loading comparison

	Mean time average blade loading (N)	Change from design
Design spacing	90.1	0.0%
40% spacing	90.4	0.4%

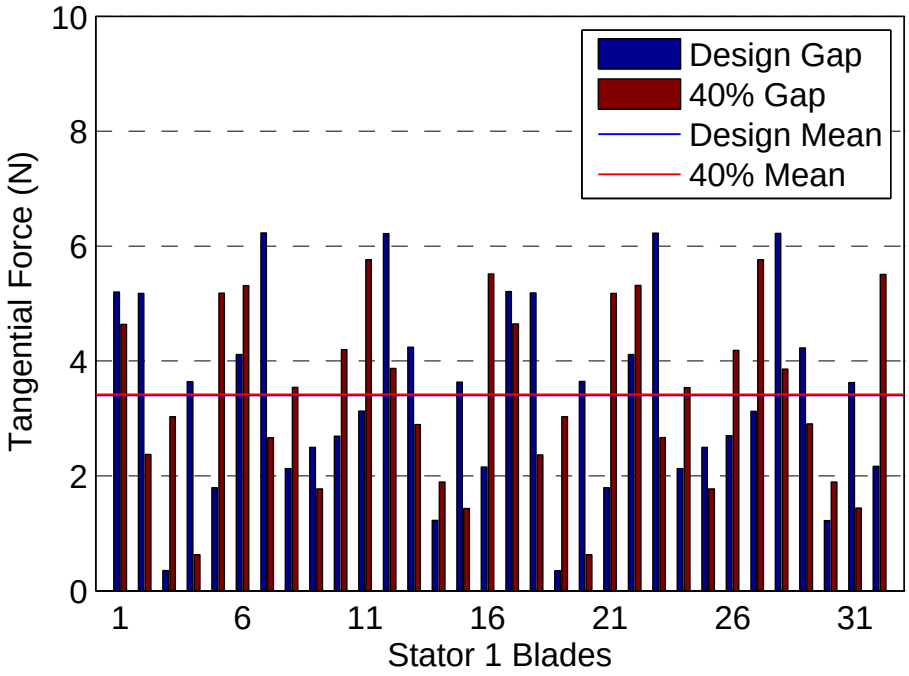

Fig. 5.32 Fourier transform values at EO21 for each stator 1 blade comparing both axial spacings

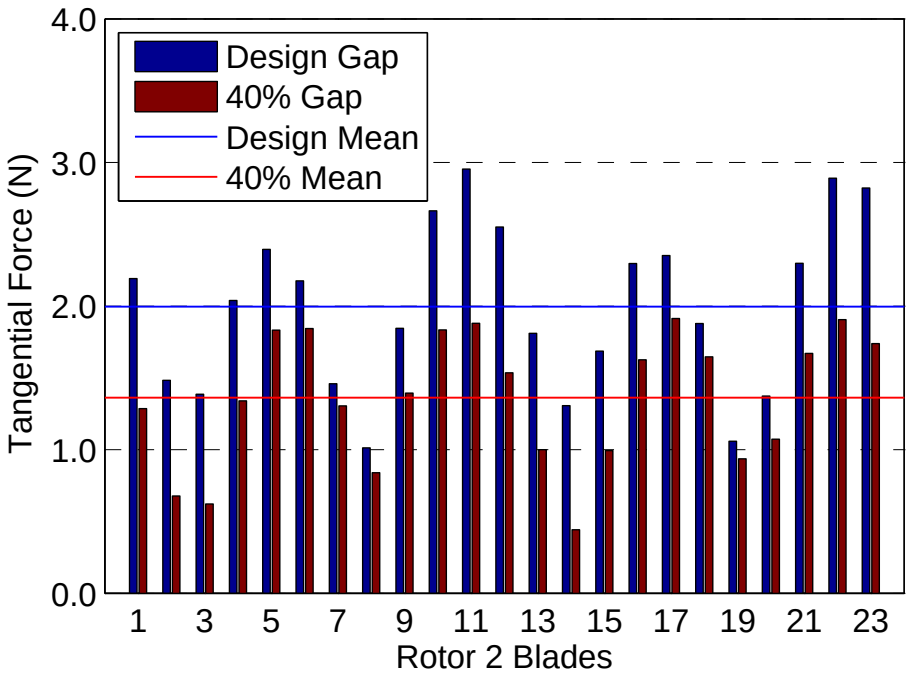

Fig. 5.33 Fourier transform values at EO26 for each rotor 2 blade comparing both axial spacings

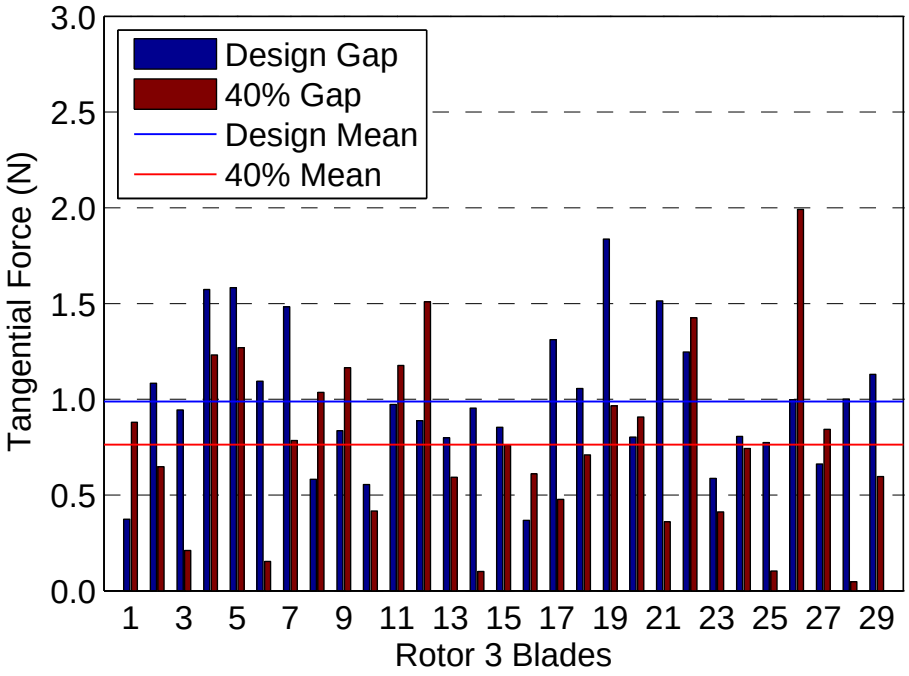

Fig. 5.34 Fourier transform values at EO26 for each rotor 3 blade comparing both axial spacings

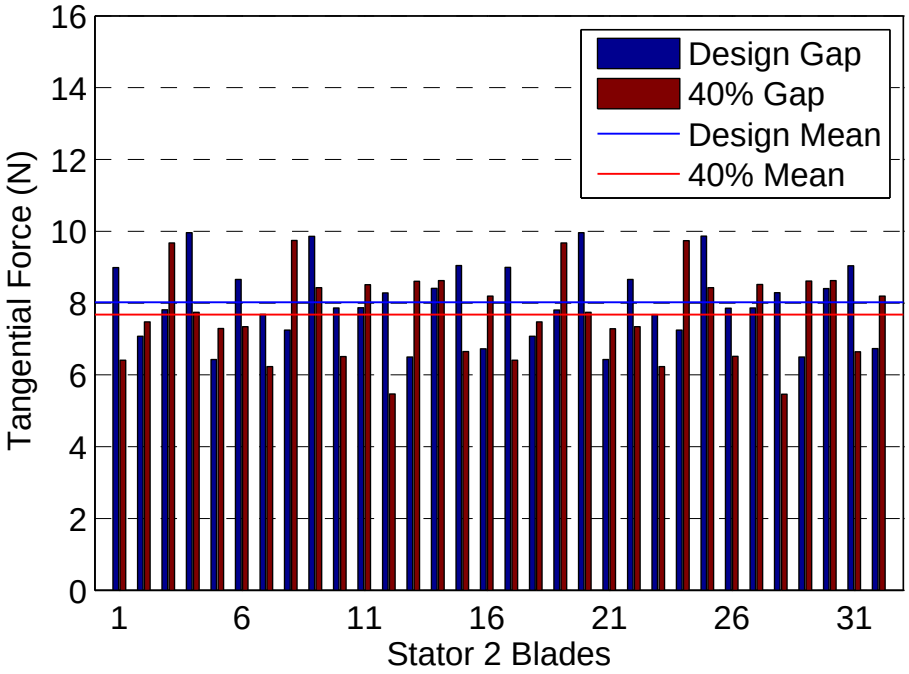

Fig. 5.35 Fourier transform values at EO21 for each stator 2 blade comparing both axial spacings

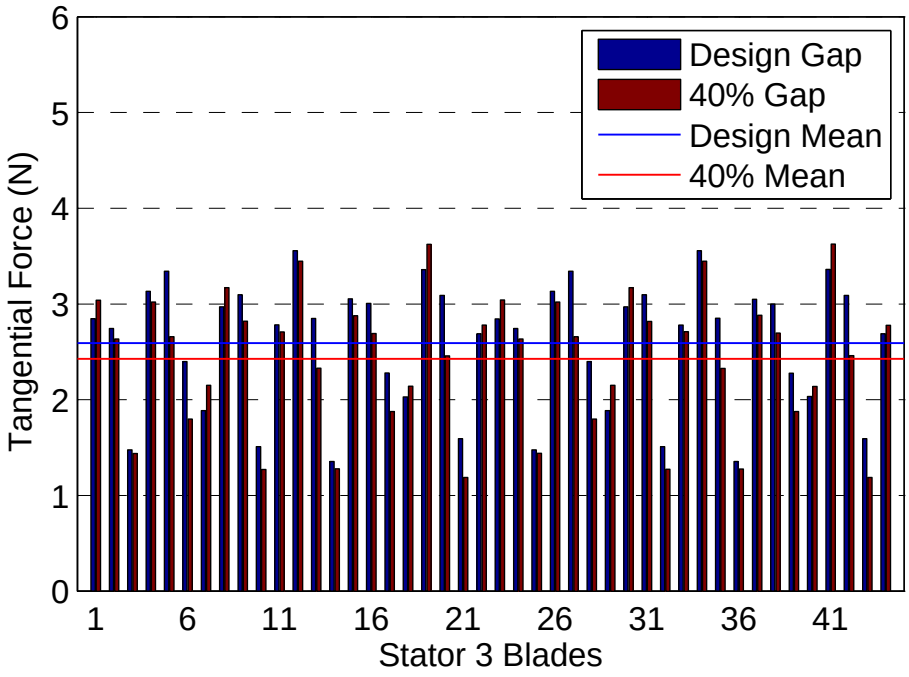

Fig. 5.36 Fourier transform values at EO21 for each stator 3 blade comparing both axial spacings

stages. The stage 2 and stage 3 blade rows experience very little change in the time averaged blade loadings between the two IGV-Rotor spacing configurations with the mean value changing just 0.1% in all four blade rows. The dynamic tangential loading is affected in these 4 blade rows and it can be attributed directly to the IGV-Rotor spacing by just looking at the frequency components of the dynamic tangential loading that are caused by the IGV blade passing (EO26) and the rotor 1 blade passing (EO21).

The component of the dynamic tangential blade loadings at EO26 is shown in Figs. 5.33 and 5.34 for the rotor 2 and rotor 3 blade rows. In the rotor 2 blade row, there is a reduction in the dynamic tangential loading for every rotor blade, with the mean value dropping to 0.68 of the design spacing mean value. In rotor 3, the mean value still drops, this time to 0.77 of the design mean value, however there is not a reduction in the loading for each rotor blade. Most notably the dynamic tangential loading on rotor blade 26 has doubled and has a greater magnitude than any blade from the design axial spacing.

The component of the dynamic tangential blade loadings at EO21 for the stator 2 and stator 3 blade rows is shown in Figs. 5.35 and 5.36. The effect of changing the IGV-Rotor spacing on the stator blade rows is much smaller than the effect on the rotor blade rows. The mean dynamic tangential loading, at EO21, has reduced to 0.96 of the design spacing mean value for the stator 2 blade row and to 0.94 for the stator 3 blade row. Although the

mean value has reduced for both stator blade rows the dynamic loading for a number of the individual stator blades has increased.

Performing this analysis in a multistage environment has shown that changing the IGV-Rotor spacing affects the dynamic loading of the blade rows at least 2 stages downstream. The effect has been greater on the downstream rotor rows (than the stator rows) because changing the IGV-Rotor gap has a direct effect on the IGV wakes so their downstream propagation is altered and this change is detected in the rotor dynamic tangential loadings. In contrast the rotor 1 wakes, which affect the downstream stator loadings, are not directly affected by changing the IGV-Rotor gap but are only affected by the change in loading on rotor 1 (which is in turn affected by the IGV-Rotor spacing) and therefore the effect on the downstream stators is smaller than the effect on the downstream rotors.

5.5 Modal Force Analysis of Rotor 1

The previous section contained a comparison of the aerodynamic forces that are exerted on the blades, in different blade rows, when the IGV-Rotor axial spacing is reduced. In this section, a brief modal force comparison will be used to support the previous findings and provide more context for linking the aerodynamic comparison, already presented, to the effect that this will have on the mechanical vibrations of the blades. This is an important step, because ultimately it is the mechanical vibration that will determine the lifetime of a blade before it fails due to fatigue. A modal force analysis gives an understanding of the way in which a blade is likely to fail and also allows the designer to analyse a single vibration shape that may be of particular concern for the structural integrity of the blade, such as the impact of the pressure forces on the dynamic bending or torsional stresses experienced by the blade. The analysis in this section is focused only on rotor 1 and is performed using a modal force calculation and a prediction of the relevant mode shape provided by Siemens Turbomachinery Ltd. The modal force is analysed for mode 14 EO26 which corresponds to the IGV passing frequency. The mode shape is shown in Fig. 5.37 and it can be seen that the mode is particularly excited near the tip at the leading and trailing edges. The modal force is calculated for a nodal diameter (ND) of 5 (calculated as the difference between the IGV and rotor 1 blade counts) using the mode shape and the rotor surface pressure forces from full annulus unsteady simulations performed at 100% and 40% of the IGV-Rotor design axial spacing.

The results for both axial spacing configurations are presented in the frequency domain by taking the Fourier transform of the modal force signal, and are shown in Fig. 5.38. The results for the design axial (Fig. 5.38a) spacing show a spike at EO26, corresponding to IGV

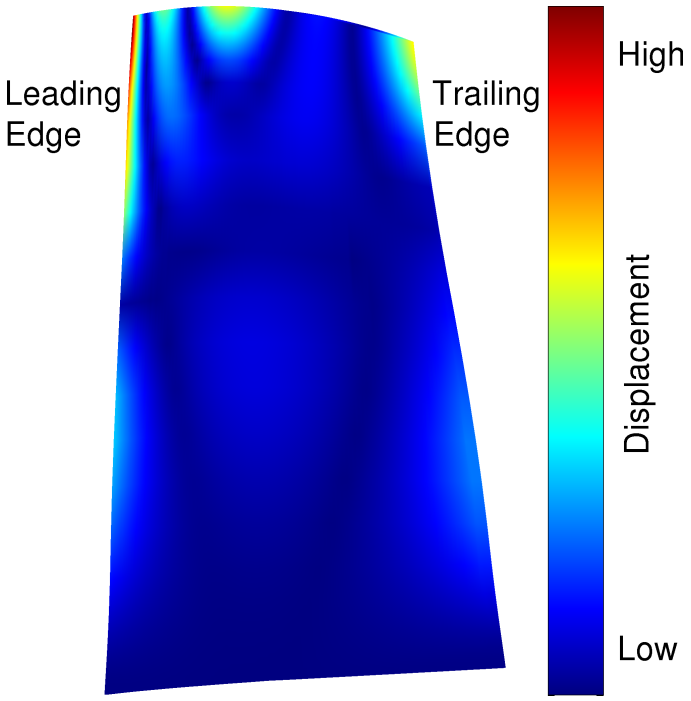

Fig. 5.37 Mode shape for rotor 1 mode 14 EO26

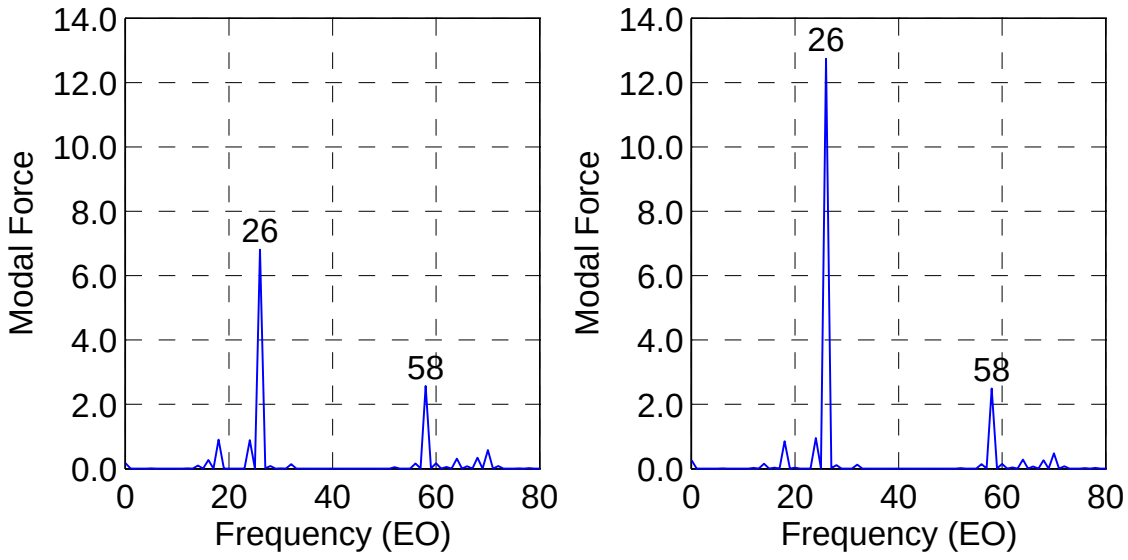

(a) Design IGV-Rotor 1 axial spacing

(b) 40% IGV-Rotor 1 axial spacing

Fig. 5.38 Fourier transform of model force on rotor 1 for mode 14 EO26 with ND 5

blade passing, and a lower spike at EO58. The spike at EO58 corresponds to the combined blade passing frequency of the IGV (EO26) and the stator 1 (EO32) blade rows. At 40% IGV-Rotor spacing the results show a stronger spike at EO26 with the spike at EO58 not noticeably altered (Fig. 5.38b). The EO26 peak increases by a factor of 1.9 which represents a significant increase in the modal forcing of the rotor as a result of the IGV wakes, however it is not as great an increase as was seen in the dynamic tangential pressure loading at EO26, although it is larger than the increase in the dynamic axial pressure loading. The EO26 component of the dynamic tangential pressure loading increased by a factor of 6.5 when the IGV-Rotor was reduced from 100% to 40% of the design spacing as shown in Fig. 5.30 and the dynamic axial pressure loading by a factor of 1.3.

The modal force analysis presented here has shown the limitations of making aerodynamic force comparisons, when attempting to predict the effect that the dynamic pressure loading will have on the mechanical integrity of a blade. It has shown that for this blade, and this mode shape, the effect of reducing the IGV-Rotor axial spacing is less severe than indicated by the tangential pressure force analysis but more severe than indicated by the axial pressure force. The pressure force analysis does predict the correct trends and a change in the dynamic pressure forces will always be indicative of a change in the dynamic modal forcing, and as such is still a useful method to compare different blade configurations.

5.6 Conclusions

In this chapter, a comparison has been made of two different axial spacings between the IGV and rotor 1 blade rows in a 3-stage transonic compressor by using unsteady CFD simulations. The aim of this analysis has been to provide information to the compressor designer about how this design decision affects the compressor performance and the mechanical integrity within a multistage machine.

The efficiency of the compressor in the two different configurations has been compared using quarter annulus unsteady simulations. It is found that reducing the IGV-Rotor axial spacing increases the stage 1 efficiency by 0.2%, and the overall efficiency by 0.1%, at the design pressure ratio. A similar efficiency gain is found at pressure ratios lower than the design pressure ratio, however, at higher pressure ratios the reduced axial spacing affects the stage matching. The change in matching leads to a drop in the overall efficiency, despite a small improvement in the stage 1 efficiency, because stages 2 and 3 operate at a higher pressure ratio and with a lower efficiency. The higher efficiency in stage 1 is associated with a lower Mach number on the rotor suction surface and therefore a weaker shock system. It is also found that steady simulations cannot accurately predict the compressor efficiency

for the configuration with the smaller IGV-Rotor spacing as they showed a reduction in the stage 1 efficiency, when the axial spacing was reduced, that wasn't present in the unsteady simulations.

The dynamic blade loading was compared using full annulus unsteady simulations in order to capture the blade row interactions at the correct frequencies. The dynamic tangential loading was compared across all the blades in a given row by looking at the relative magnitudes of specific frequency components of the dynamic tangential loading and the frequencies investigated were chosen to match the blade passing frequencies of the blade rows of interest. Dynamic tangential loading was presented in preference to dynamic axial loading because the changes in dynamic axial loading (between the two axial spacings) are smaller for all blade rows. When the axial spacing is reduced, the dynamic tangential loading increases in the IGVs by a factor of 1.8 and in the Rotor 1 blades by a factor of 6.5 (which is indicative of increased stress in the blades) while changes in the time-averaged loading are comparatively small at 4.4% and -1.3% respectively. The change in mean dynamic tangential loading in the stator 1 blades is very small, however there is an obvious change in the blade to blade dynamic loading because the reduced axial spacing has changed the locations of the interactions between the IGV wakes and the stators. Performing this analysis in a multistage simulation allowed the effect on the dynamic loading in the downstream stages to be analysed. It is found that the mean dynamic tangential loading (attributed to the IGV and rotor 1 blade passings) in the stage 2 and 3 blade rows decreased as a result of reducing the IGV-Rotor axial spacing. This effect is greater in the rotor blade rows because they interact with the IGV wakes which have been affected more than the rotor 1 wakes by changing the IGV-Rotor spacing.

It has been found that the dynamic loadings, at a certain frequency, for a blade row can increase many times over as a result of reducing the IGV-Rotor axial spacing. However, in most of the cases considered, the absolute magnitude of the forcing is fairly weak. For example, the dynamic tangential loading of rotor 1, attributed to the IGV wakes, increases by a factor of 6.5 but the absolute amplitude of the tangential forcing is only 1.4 N, on a static loading of over 150 N. A small attempt to gain a better mechanical interpretation of the results has been performed by analysing the modal force on the rotor, however, given the absolute values are so small, it remains important to perform further mechanical analysis in order to gain a better understanding of how the increased dynamic pressure loading translates to blade vibration and ultimately blade life before failure.

Chapter 6

Trends and Benefits of Rescheduling in a Multistage Transonic Compressor

6.1 Introduction

Variable Guide Vanes (VGVs) are commonly used to help achieve good compressor performance over a large range of operating conditions by rescheduling them in order to alter the stage matching. VGV schedules are usually derived through expensive and time consuming rig testing although low order modelling, such as stage stacking or streamline curvature, is also used to try and predict the appropriate scheduling.

One of the uses of VGVs is at part speed operating conditions experienced during start up and part load. At these low speed conditions, large VGV angle changes in many blade rows are required in order to make the compressor operation stable. In these situations the flow is very different to the flow at design conditions and large portions of the span may have separated flow with negative axial velocity. This makes the overall performance of the compressor very hard for low order models to predict, as they are not able to simulate the regions of separated flow.

Another use of VGVs is to correct any stage mis-matching that has occurred as a result of original design uncertainties, or to improve the stage matching in order to improve the overall compressor performance. This requires smaller and more localised changes to the vane schedules. It is this use of VGVs that is the focus of the work in this chapter. CFD simulations are used to model the effects of vane rescheduling in order to gain a more detailed insight into the behaviour of the flow and to attempt to accurately predict the changes in performance. If CFD can be found to accurately predict the performance of a rescheduled compressor close to the design speed, then further work could be performed to investigate

the ability of CFD to accurately predict the compressor performance at lower speeds where large scale separations exist. If CFD can accurately predict the performance for either of these conditions then it could be used to significantly reduce the cost of optimising VGV schedules in rig tests. Furthermore a greater understanding of how rescheduling alters the flow could lead to improved stator designs that provide better performance when rescheduled without significantly effecting on-design performance.

In this chapter results are presented from rescheduling the IGVs and the 3 stator blade rows. Initially a systematic investigation is presented of the effects of rescheduling a single blade row. The knowledge gained from this is then used to analyse the original geometry [56] and seek an improvement in the design speed efficiency. Next the optimised geometry [90] is compared to the rescheduled baseline geometry to compare the different methods that lead to an improvement in the overall efficiency. Finally the optimised geometry is rescheduled at off-design speed in order to show how rescheduling can be used to improve the off-design efficiency and stall margin. In addition it is shown how rescheduling affects the 3D flow field and how this leads to a change in the location of the flow separation that leads to stall.

All results presented in this chapter are from steady simulations using the real blade counts. All the efficiency and pressure ratio data has been calculated using the discrete spanwise locations detailed in the numerical method in order to allow a fair comparison to the available rig data. As with the other simulations in this thesis, the rotor tip gaps and stator hub gaps have been modelled, as detailed in the numerical methods, however the penny gaps on the VGVs have not been included in the simulations. As the vane angle changes simulated in this chapter are relatively small (up to 11 degrees) it is assumed that the losses generated by the penny gaps will not vary significantly and therefore the trends observed will not be affected by not including them in the simulations.

6.2 Examine Changes to Performance Trends Caused by Vane Rescheduling

The effects of rescheduling stator 1 and stator 2 are investigated in the original geometry by sweeping the stagger angle of each stator individually from 0 degrees (design) to 10 degrees closed (in increments of 1 degree) while keeping the overall pressure ratio close to the design pressure ratio of 3. The results for sweeping stator 1 (red) are shown in the stage characteristics plotted in Fig. 6.1 along with the design characteristic for the compressor operating with design vane scheduling over a range of pressure ratios (blue). As stator 1 is closed the flow angle into rotor 2 is reduced which causes it to do less work and it can be

seen to be dropping below its design characteristic. This has the effect of throttling stage 1 which pushes it up its design characteristic line, forcing it to do more work. Stage 3 can be seen to change its operating point slightly. As stator 1 closes to around 5 degrees there is very little change in the stage 3 operating point however as stator 1 closes further to 10 degrees, stage 3 starts to move up its operating line slightly.

Rescheduling stator 1 has clearly affected the stage matching and it is useful to look at how the individual stage pressure ratios change, plotted against the overall compressor pressure ratio, when the stators are rescheduled. This way of plotting the data clearly shows the trade off in pressure ratios between the stages and makes it easier to understand how this affects the stage efficiencies when that is investigated later in this chapter. The stage pressure ratios for the stator 1 sweep are shown in Fig. 6.2 along with the stage pressure ratios for the design speed and design schedule characteristic. Figure 6.2 clearly shows the transfer of pressure ratio from stage 2 to stage 1 as stator 1 is closed. Closing stator 1 has reduced the mass flow rate of the compressor, as shown in Fig. 6.3.

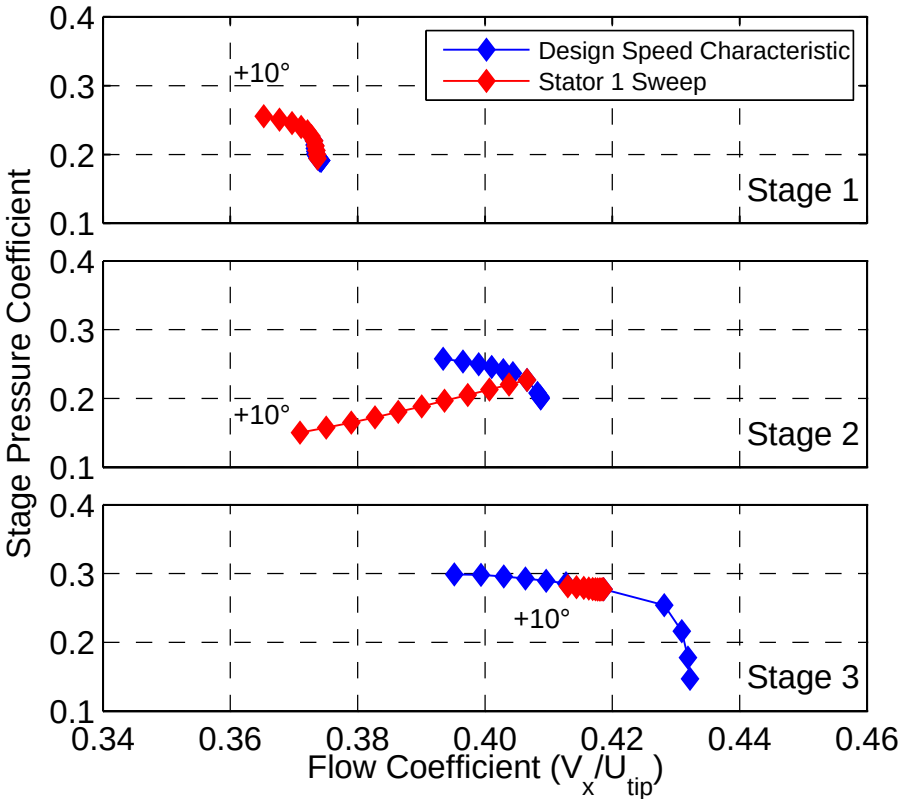

Fig. 6.1 Individual stage characteristics for design speed line and stator 1 rescheduling at design point

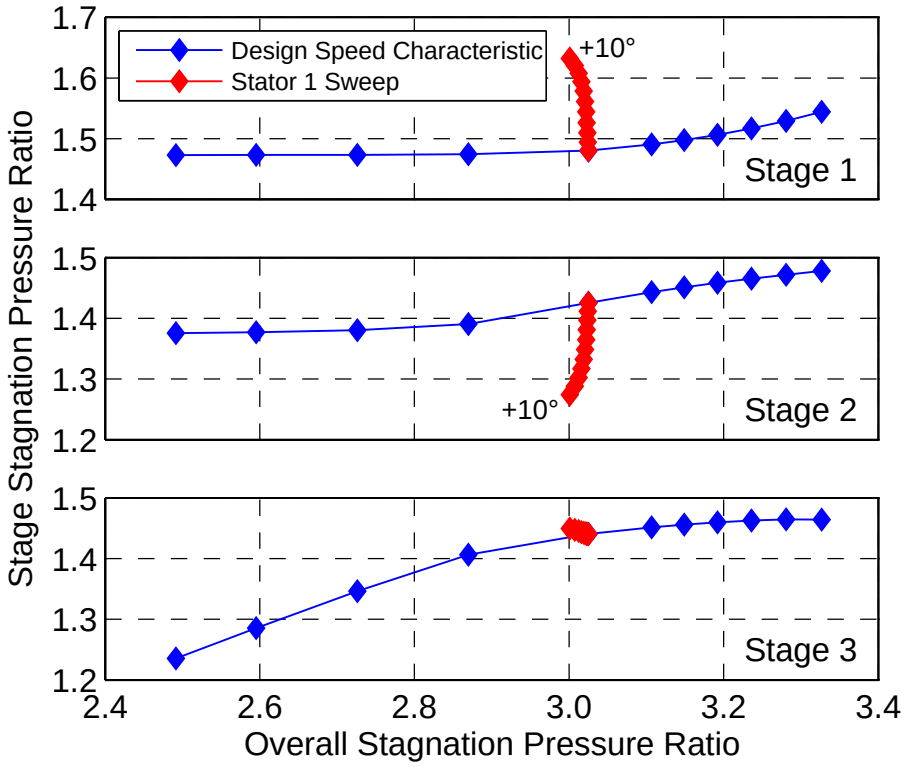

Fig. 6.2 Individual stage pressure ratios for design speed line and stator 1 rescheduling at design point

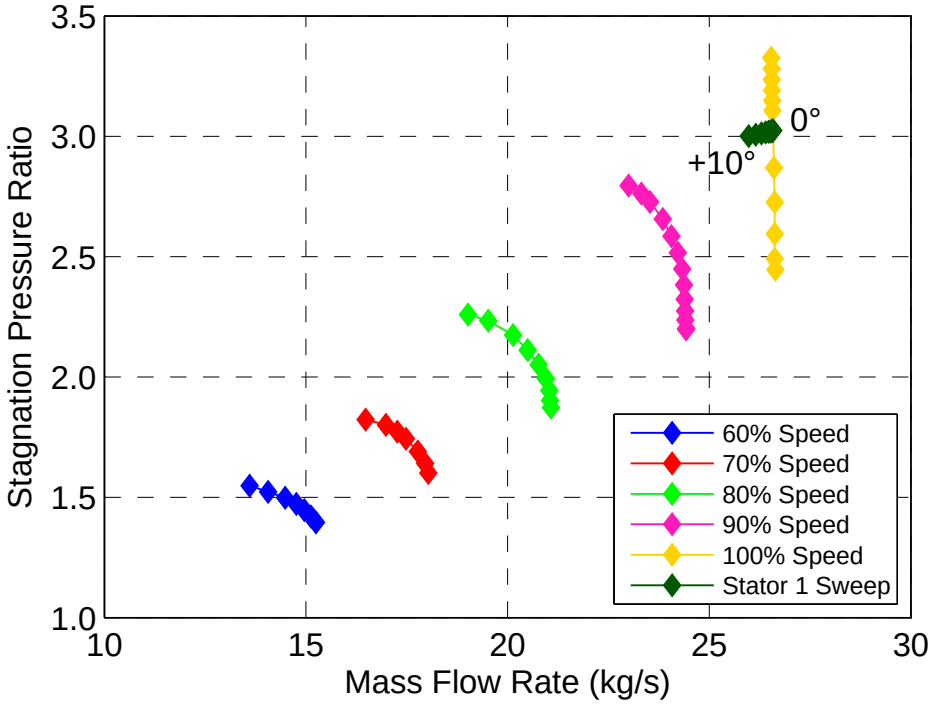

Fig. 6.3 Compressor operating map with change in mass flow rate for stator 1 rescheduling

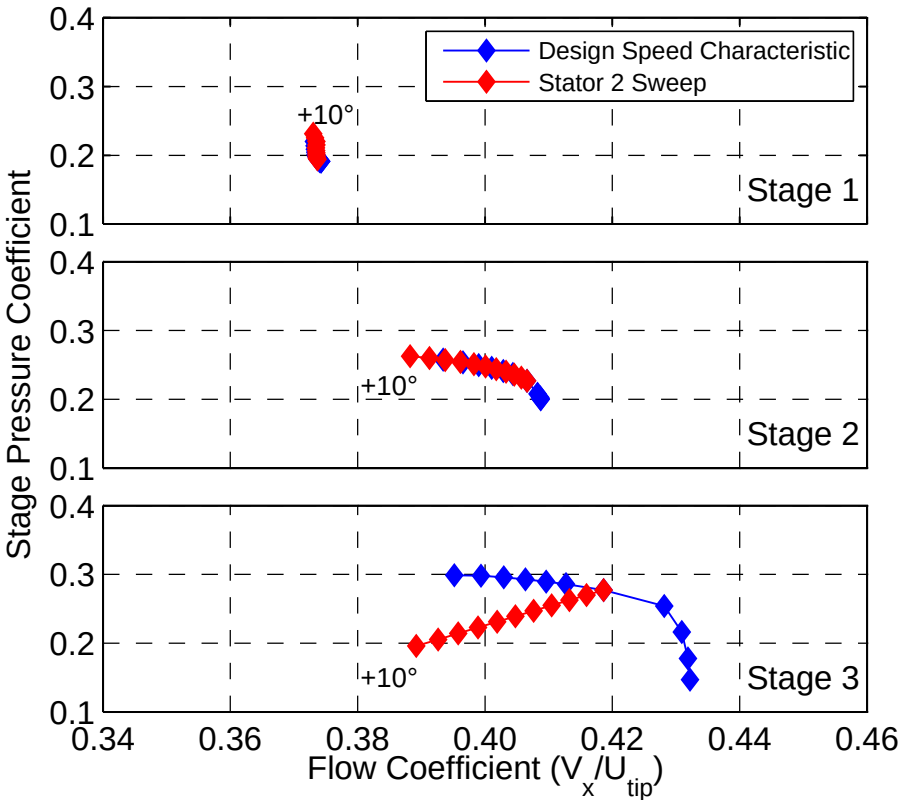

Fig. 6.4 Individual stage characteristics for design speed line and stator 2 rescheduling at design point

Figures 6.4 and 6.5 show that closing stator 2 has a similar effect of throttling the upstream stages and increasing their pressure ratios, however, in this case the pressure ratio increases in both stage 1 and stage 2. Initially the pressure ratio increases mostly in stage 2 then at higher stagger angles the extra pressure ratio is mostly picked up in stage 1. This reflects the way the pressure ratio increase is split between these two stages as the overall pressure ratio increases along the design speed line at the design stator scheduling. This is shown in Fig. 6.5 as the design speed characteristic for stage 2 has a higher gradient than the stage 1 characteristic around the design pressure ratio of 3. When stator 2 is closed the mass flow rate, shown in Fig. 6.6, remains unchanged.

Having established how the stage matching is affected by rescheduling, the effect that this has on the stage efficiencies is now presented. Fig. 6.7 shows the efficiency for the individual stages of the compressor. Results are shown for the design speed characteristic and the stator 2 sweep, where the overall pressure ratio was held close to 3. As the stator angle increases, and the stage 1 pressure ratio increases, the stage 1 efficiency increases and matches well with the stage 1 design speed characteristic. This is to be expected as there is no change to the stage geometry or to the inlet flow angle. The stage 2 efficiency also matches the design

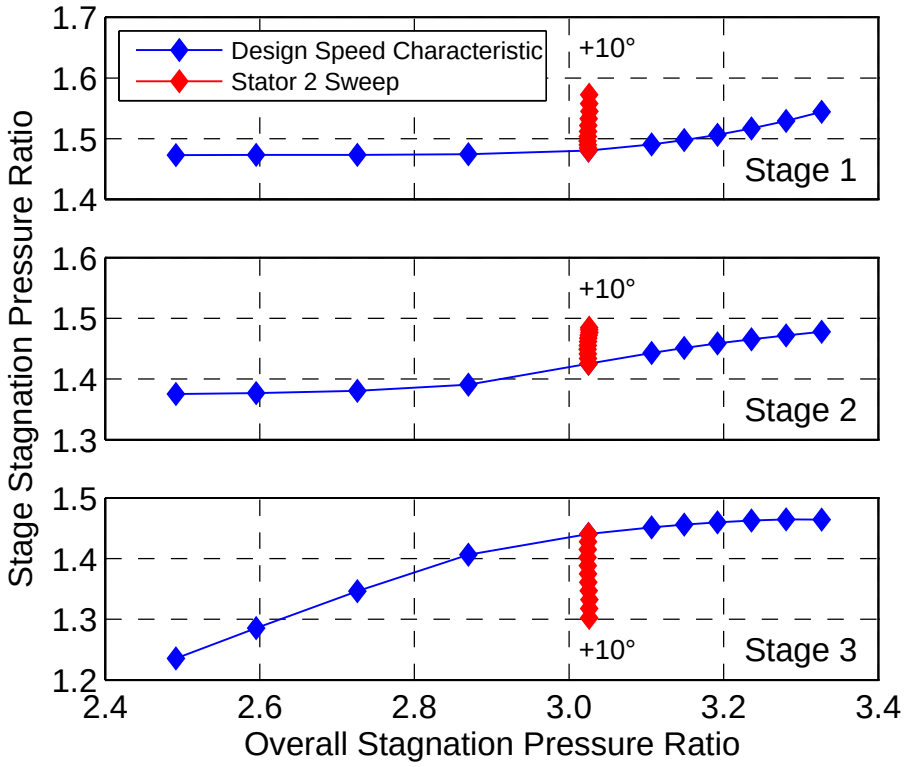

Fig. 6.5 Individual stage pressure ratios for design speed line and stator 2 rescheduling at design point

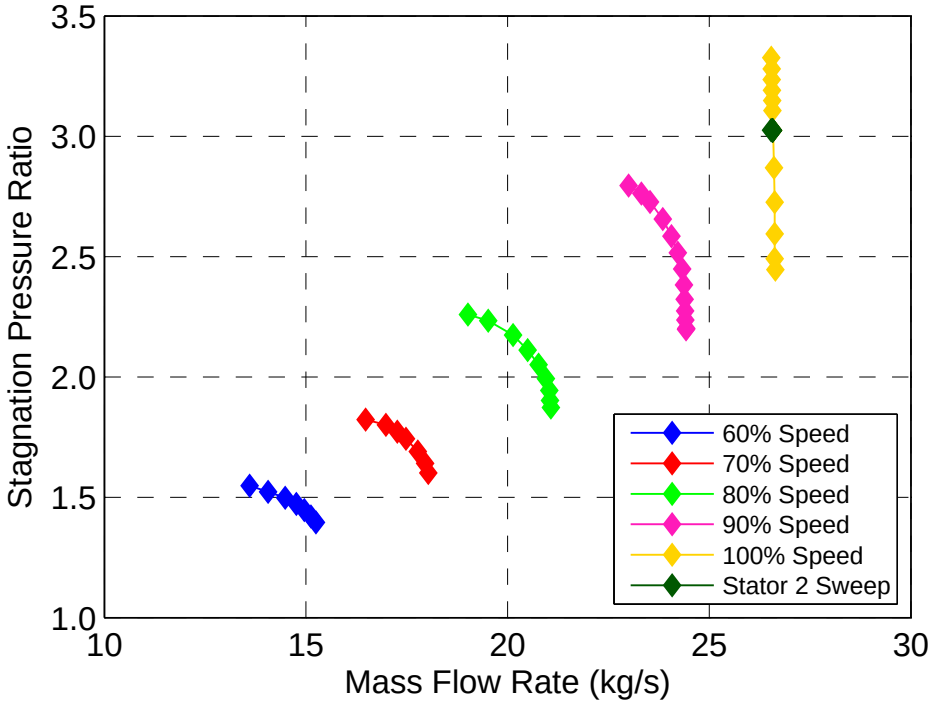

Fig. 6.6 Compressor operating map with change in mass flow rate for stator 2 rescheduling

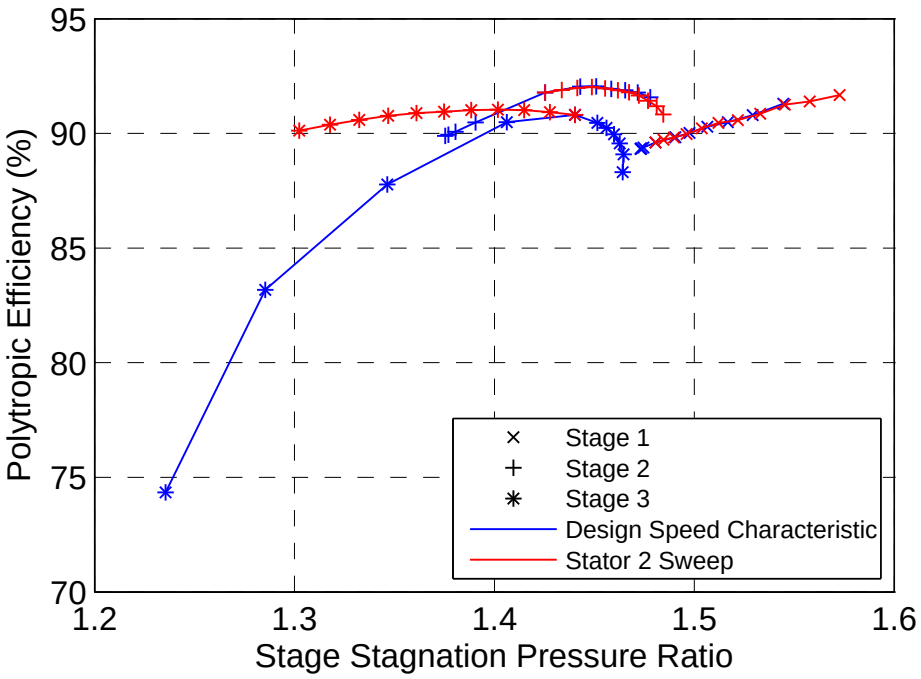

Fig. 6.7 Stage efficiencies for design speed line and stator 2 rescheduling at design point

speed characteristic well despite the stage geometry changing as the stator is rescheduled, however, a small deviation starts to appear at high stagger angles as the geometry changes are most significant.

The stage 3 efficiency does not follow the design speed characteristic as stator 2 is closed and the stage pressure ratio drops. Instead the stage 3 efficiency gradually increases and then decreases as the stator is rescheduled. To investigate this, the radial relative flow angle and Mach number distributions upstream of rotor 3 are plotted in Figures 6.8 and 6.9 for design VGV schedule at design and low pressure ratios, and for stator 2 rescheduled to 10 degrees at design pressure ratio. The low pressure ratio (2.6) is selected because the stage 3 pressure ratio is similar between the design schedule low pressure ratio case and the rescheduled, design pressure ratio case. Figure 6.8 clearly shows the flow angle onto rotor 2 reducing as stator 2 is closed, when compared to design schedule and design pressure ratio, which is to be expected. Similarly the relative flow angle reduces as the pressure ratio reduces to 2.6 from design pressure ratio of 3.0, however, the change is greater nearer the tip for the rescheduled case and greater nearer the hub for the low pressure ratio case. Despite comparable changes in flow angle between the low pressure ratio and rescheduled case, Fig. 6.9 shows significant differences in the inlet Mach number to rotor 3. Whereas the low pressure case has an increase in relative inlet Mach number compared to design, the rescheduled case has a significantly lower relative inlet Mach number. The lower inlet Mach

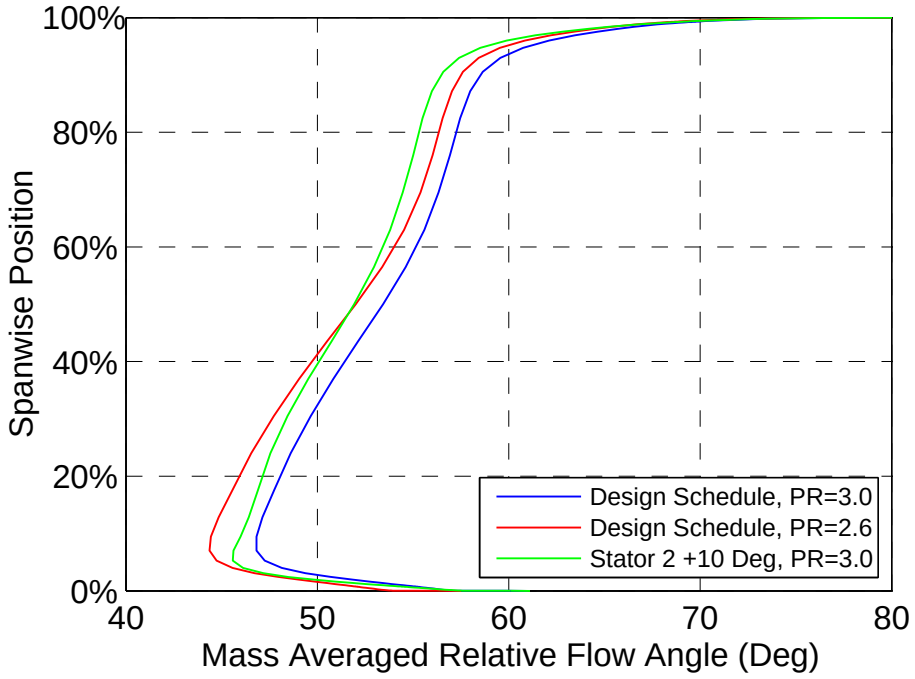

Fig. 6.8 Radial relative flow angle distribution upstream rotor 3

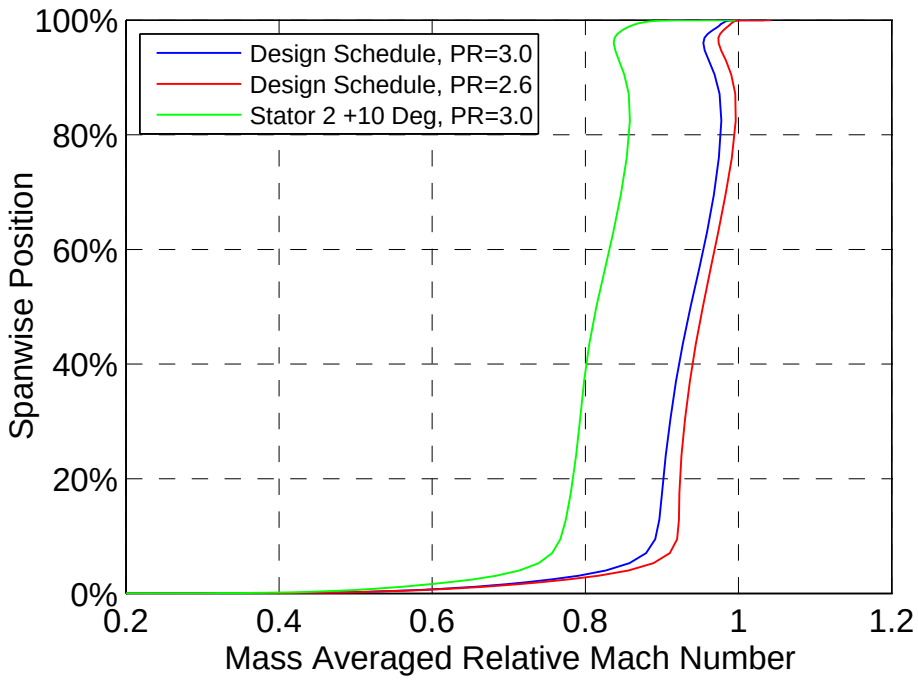

Fig. 6.9 Radial relative Mach number distribution upstream rotor 3

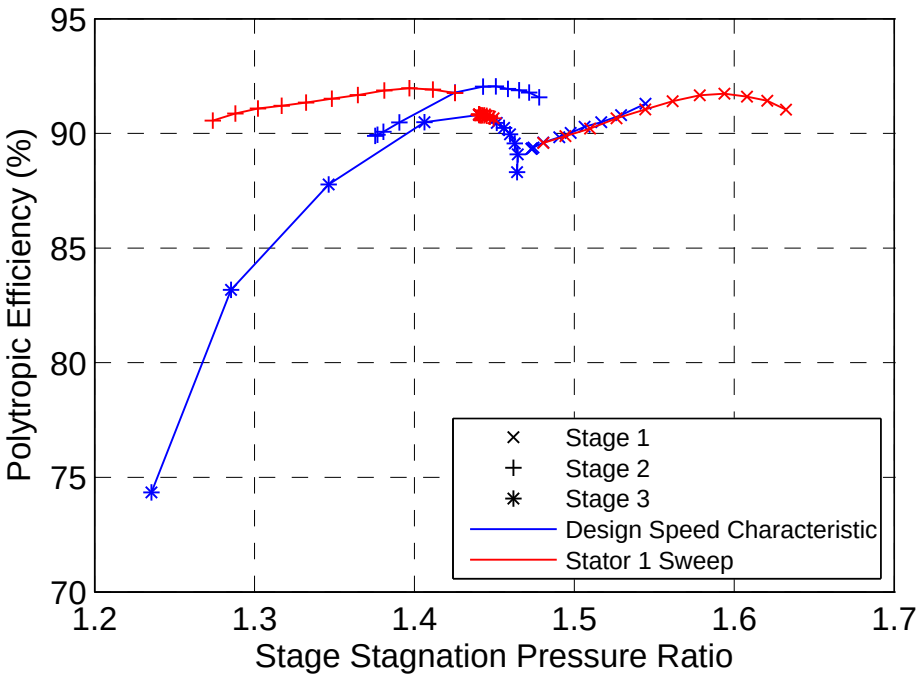

Fig. 6.10 Stage efficiencies for design speed line and stator 1 rescheduling at design point

number prevents strong shock waves forming in stage 3 (that are present in the low pressure ratio case) and thus gives the higher efficiency that is seen in Fig. 6.7.

When stator 1 is rescheduled instead of stator 2, it is reasonable to expect that the efficiencies of the stages immediately upstream and downstream of stator 1 will change in a similar way to the stages upstream and downstream of stator 2 when it was rescheduled. The results in Fig. 6.10 show that this is indeed what happens. The stage 1 efficiency follows the design scheduling characteristic with a small deviation due to the stator geometry change and the stage 2 efficiency deviates significantly and remains much more level than the design schedule characteristic. The stage 3 efficiency is unchanged because the stage pressure ratio remains fairly constant.

6.3 Rescheduling of Original Geometry to Improve Design Efficiency

The previous section has shown that it is possible to change the stage matching by rescheduling the stators. This section seeks to use this fact to improve the stage matching in order to achieve a greater overall (3-stage) efficiency at design. The potential improvement that this could have is highlighted by the plot in Fig. 6.11 which shows the individual stage

efficiencies from the 3-stage design speed simulations alongside the stage 1 efficiency from the single stage simulations of the first stage. The green markers show the operating point of the 3 individual stages at the design pressure ratio of 3. At design, stages 2 and 3 can be seen to be operating very close to their maximum efficiency, however, stage 1 is not operating close to its maximum efficiency and is actually operating close to choke. At design, stage 1 is operating with an efficiency of 89.6% while the single stage simulations show that stage 1 is able to achieve a maximum efficiency of 92.4%. This highlights the potential efficiency gain that could be achieved.

Having established that there is potential to increase the overall efficiency the rest of this section will present the work done in order to achieve this. The approach taken will be outlined first. Although the work done here is performed on a 3-stage compressor, it is the intention that any work done on this rig would have the potential to be universal and transferred to a much wider range of compressors with more stages. As the 3-stage rig represents the first 3 stages of a larger compressor, it is necessary to make sure that the 3-stage compressor remains matched to the downstream stages. This means that after the optimisation of the VGVs, the mass flow rate and the 3-stage exit flow angles must remain as close as possible to the original design values. In order to achieve this, stator 3 will not be rescheduled so that the exit flow angles are not unnecessarily changed and the IGV will be

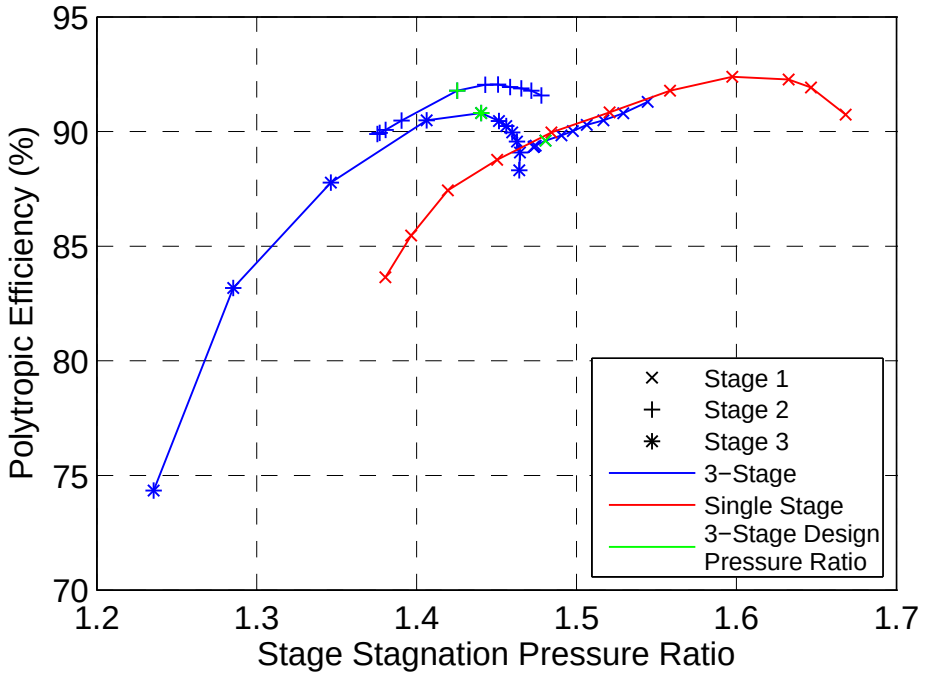

Fig. 6.11 Individual stage efficiencies for 3-stage and 1-stage design speed simulation with design operating points shown in green

Table 6.1 Vane schedules and difference in overall efficiency at design point

	Vane Schedule			η_{design}	$\Delta\eta_{design}$
	IGV	Stator 1	Stator 2		
Design	0	0	0	90.3%	-
Stator 1 Optimised	-1	+7	0	90.8%	0.5%
Stator 1 & 2 Optimised	-1	+6	+6	91.2%	0.9%

used to correct the mass flow as rescheduling the IGVs has the greatest effect on the mass flow rate. This leaves stators 1 and 2 that can be optimised in order to improve the design efficiency.

It was shown in the previous section that rescheduling stator 1 effected the stage 1 pressure ratio more than stator 2 so this blade row was optimised first before going on to optimise stators 1 and 2 together. The process for optimising stator 1 was to sweep the angle of stator 1 at design to find the maximum overall efficiency and then reschedule the IGV in order to correct the mass flow rate. This was done by rescheduling blades at increments of 1 degree and the optimised vane settings are shown in Table 6.1. Optimising stator 1 gives an increase in overall efficiency of 0.5 percentage points at the design pressure ratio.

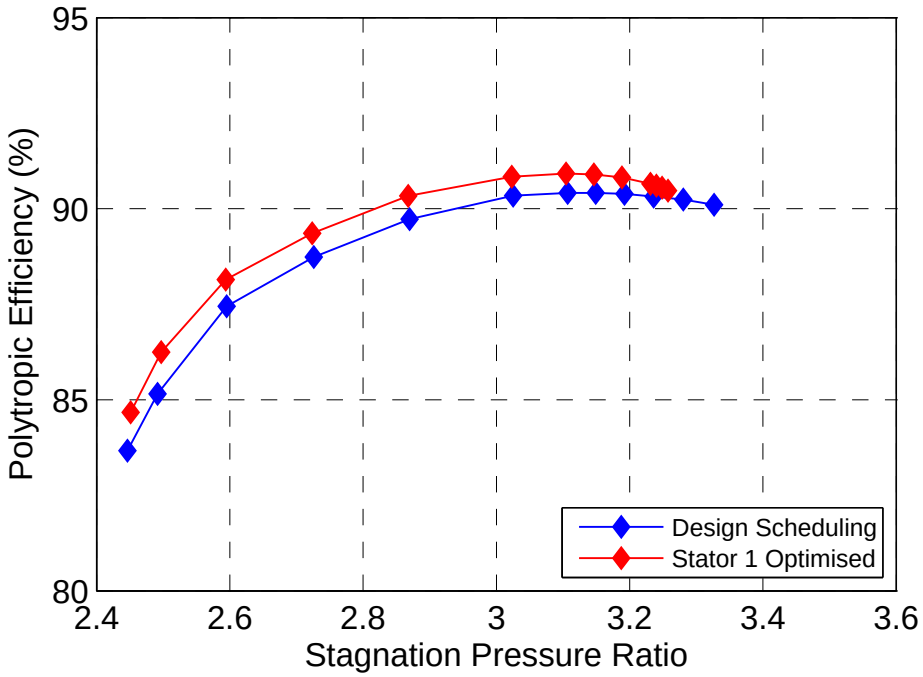

Fig. 6.12 Overall efficiency for design scheduling and stator 1 optimised scheduling with varying back pressure to give design speed characteristic

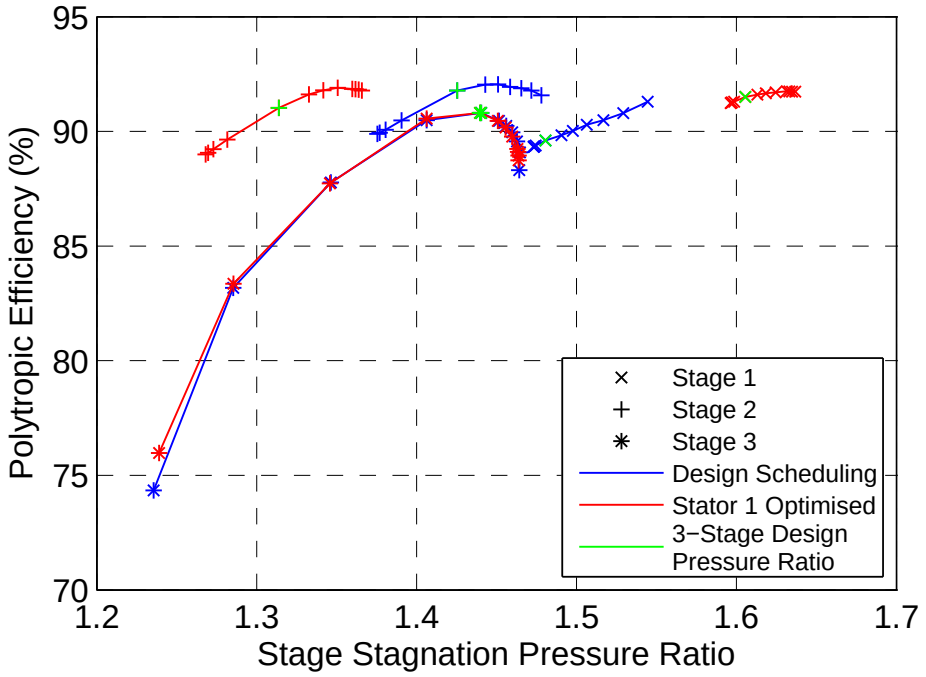

Fig. 6.13 Individual stage efficiencies for design scheduling and stator 1 optimised scheduling

Figure 6.12 shows the overall efficiency for the design speed line, obtained by varying the back pressure, and shows that optimising stator 1 at the design point has led to an increase in efficiency across the whole range. In order to understand how this efficiency increase has occurred, the individual stage efficiencies are presented in Fig. 6.13 for the design and optimised stator 1 scheduling. As expected, rescheduling stator 1 has increased the pressure ratio of stage 1 and this has led to a significant improvement in the stage 1 efficiency for the whole range of the embedded stage. To balance the increased pressure ratio in stage 1, stage 2 has dropped in pressure ratio which has led to a small drop in the stage efficiency at the design operating point. Stage 3 is unaffected by the rescheduling of stator 1 as was shown in the previous section. While the overall efficiency has improved, rescheduling stator 1 has indicated a reduction in the stall margin from the design scheduling. The highest pressure ratios plotted in Fig. 6.12 show the last stable steady operating point for both design and optimised scheduling before separation occurs in the stator 2 blade row and the calculation fails to converge well. Although the steady simulations cannot simulate stall, the occurrence of this separation is very likely to be the onset of a stalling blade row and therefore there is a high degree of confidence in saying the optimised schedule will stall at a lower pressure ratio than the design schedule. This is supported further by looking at the mass flow rate for the last stable operating point in Fig. 6.14 where it can be seen that the optimised scheduling causes the compressor to operate at a mass flow rate 0.7% lower than the design scheduling.

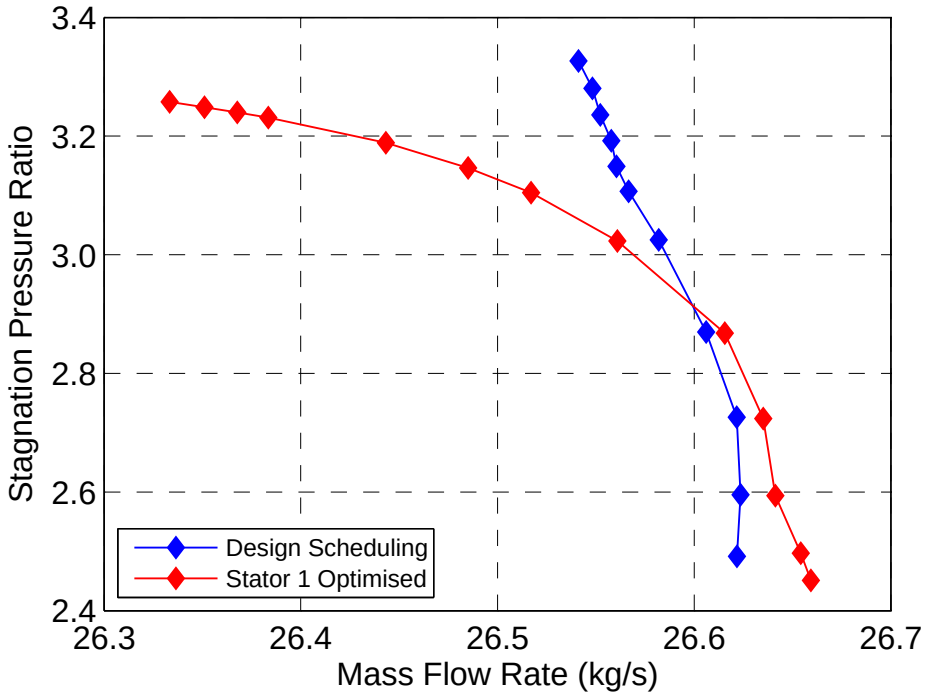

Fig. 6.14 Overall stagnation pressure ratio and mass flow rate for design scheduling and stator 1 optimised scheduling

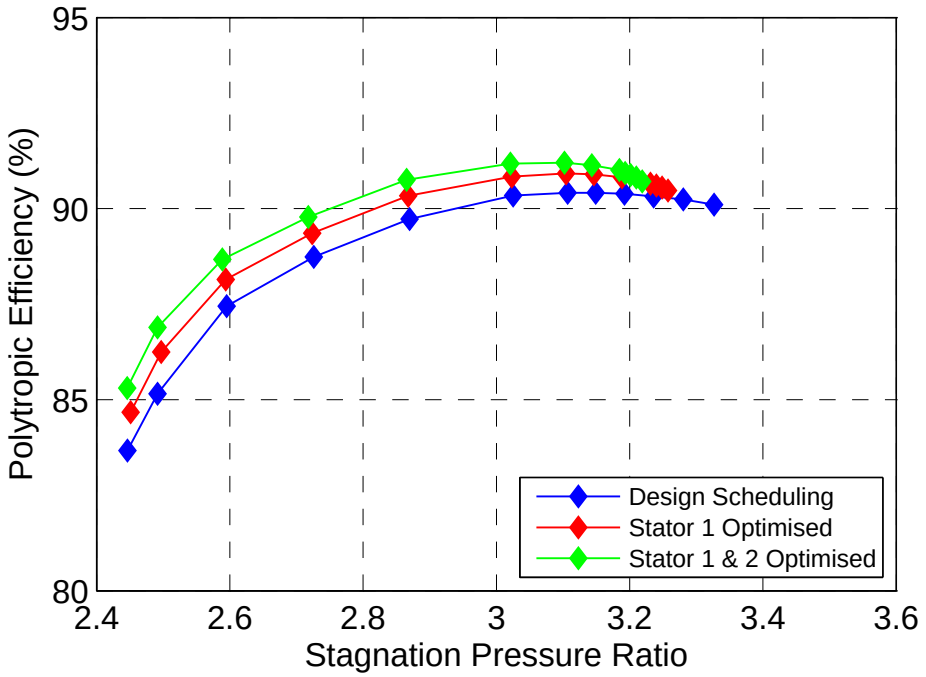

Fig. 6.15 Overall efficiency for design, stator 1 optimised and stator 1 & 2 optimised scheduling

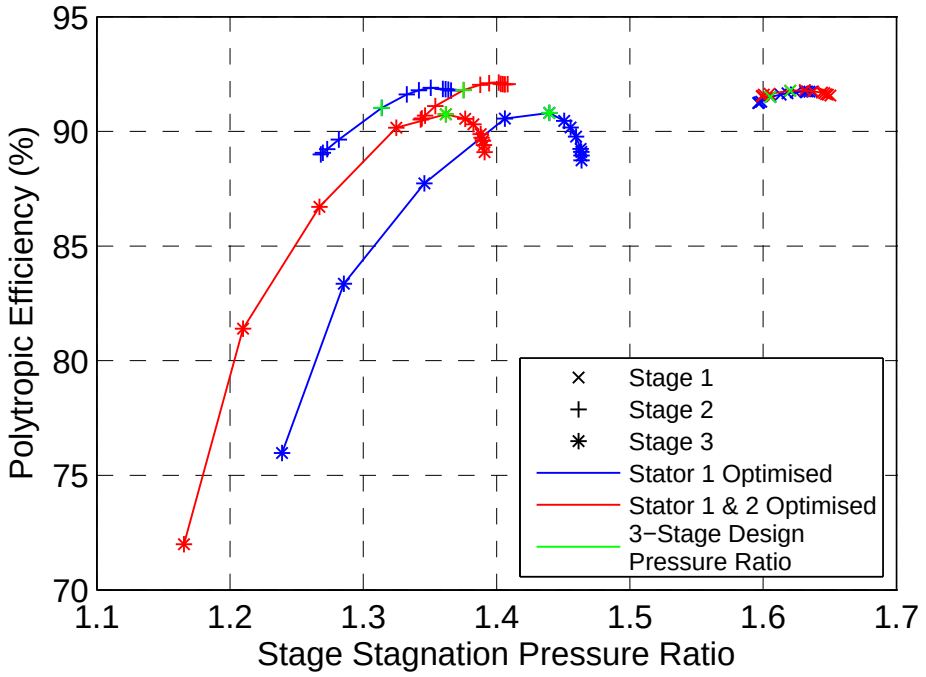

Fig. 6.16 Individual stage efficiencies for stator 1 optimised and stator 1 & 2 optimised scheduling

Figure 6.13 showed that the stage 2 efficiency dropped when the stage pressure ratio dropped as a result of rescheduling stator 1 so stator 2 was rescheduled as well in order to increase the stage 2 efficiency and achieve the maximum overall efficiency. To optimise stator 1 and stator 2, both stator rows were rescheduled one at a time until the maximum overall efficiency was achieved to within a stagger angle of one degree. The IGV was then rescheduled in order to maintain the design mass flow rate. The optimised vane schedule is shown in Table 6.1 and it can be seen that a further 0.4 percentage points of efficiency was gained at the design pressure ratio, giving a total increase in efficiency of 0.9 percentage points from the design vane schedule. Figure. 6.15 shows that a similar efficiency increase is maintained across the whole speed line except at high pressure ratios. At high pressure ratios the efficiency for the two stator optimisation converges with the single stator optimisation and the two stator optimisation indicates stall (through stator separation and non-convergence of the simulation) at a lower pressure ratio than the single stator optimisation or the design scheduling. Figure 6.16 shows that the desired effect of increasing the stage 2 pressure ratio and efficiency has been achieved when compared to the optimised stator 1 speed line. In addition the stage 1 efficiency has increased slightly at design and the stage 3 efficiency has stayed constant.

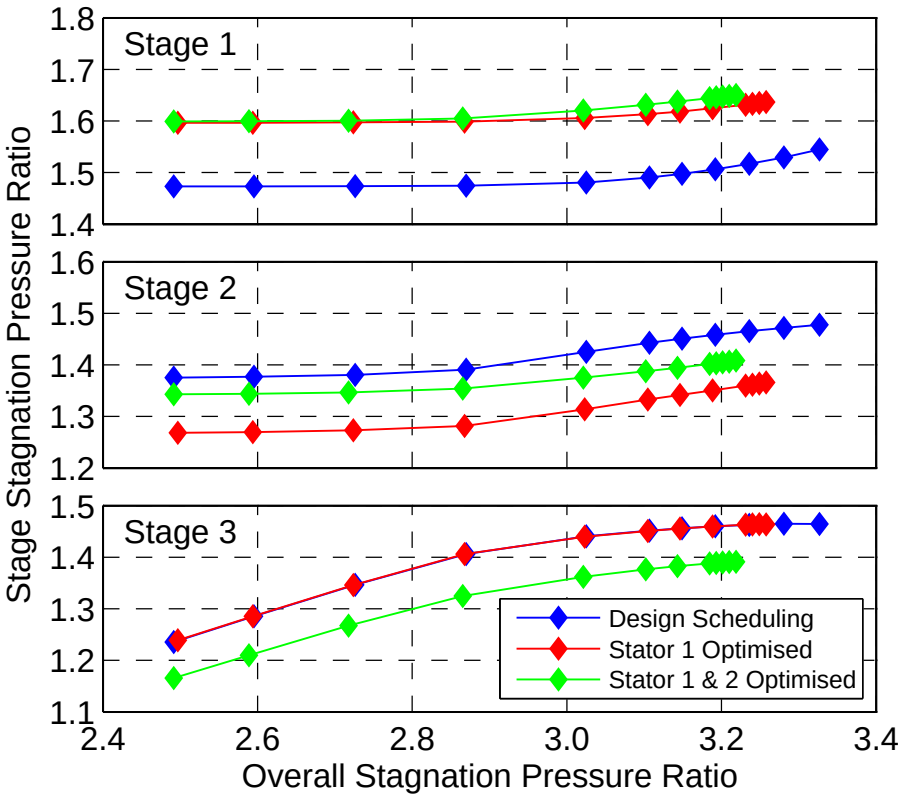

Fig. 6.17 Individual stage pressure ratios for design, stator 1 optimised and stator 1 & 2 optimised scheduling

It has been shown that it is possible to increase the overall compressor efficiency from 90.3% to 91.2% by rescheduling stators 1 & 2 in order to improve the stage matching. The change in the stage matching can be most easily seen by looking at the individual stage pressure ratios shown in Fig. 6.17. Stage 1 shows the largest change, increasing its pressure ratio significantly to 1.6 at the design operating point when stator 1 was optimised and then increased slightly further still when stators 1 & 2 were optimised. The stage 2 pressure ratio decreased when stator 1 was optimised but this effect was smaller when both stators where optimised. Stage 3 is unaffected when only stator 1 is optimised but its stage pressure ratio reduces when stator 2 is rescheduled, however this did not significantly affect the stage's efficiency (Fig. 6.16).

It was a requirement of the VGV optimisation that the 3-stage machine would still be well matched to the downstream stages by making sure that the mass flow rate and exit flow angles were not significantly affected. The mass flow rate was matched in the optimisation process by rescheduling the IGVs however this does not provide direct control over the mass flow distribution across the span which is also important. The mass flux downstream of stator 3 is shown in Fig. 6.18 for the design scheduling and the optimised scheduling (stator

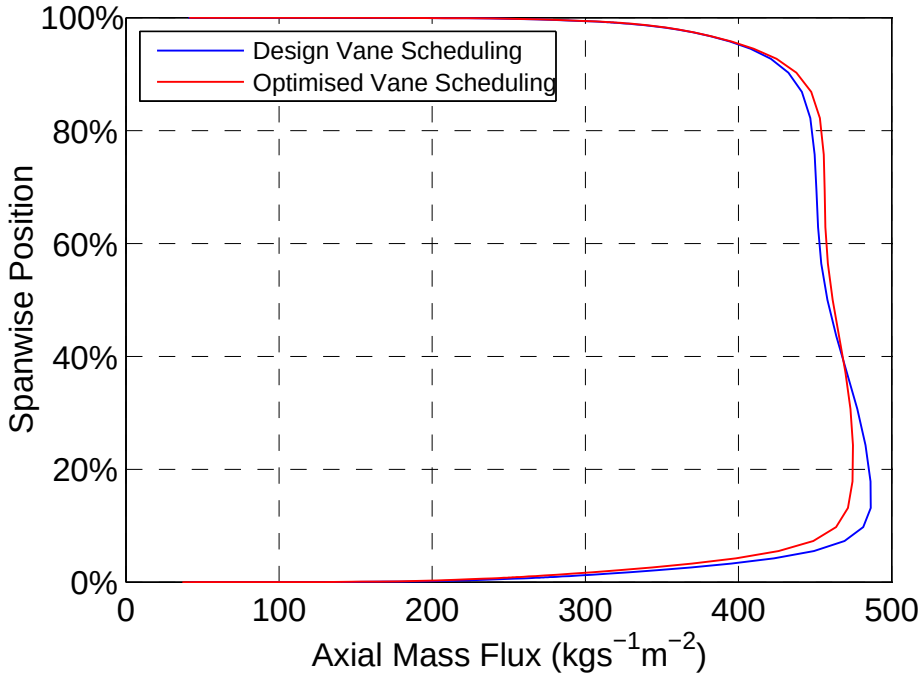

Fig. 6.18 Exit mass flow distribution for design and optimised scheduling

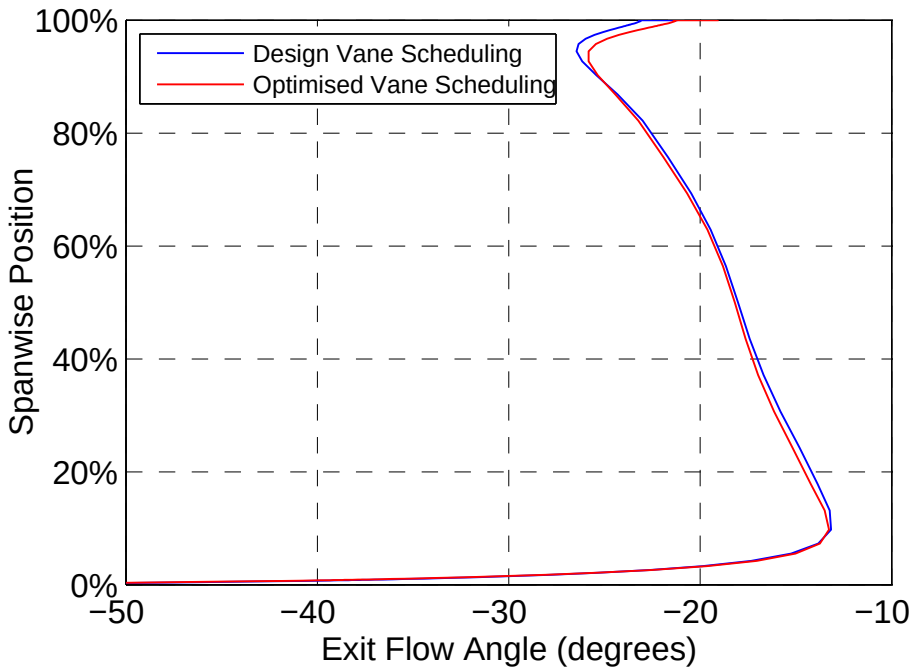

Fig. 6.19 Exit flow angle distribution for design and optimised scheduling

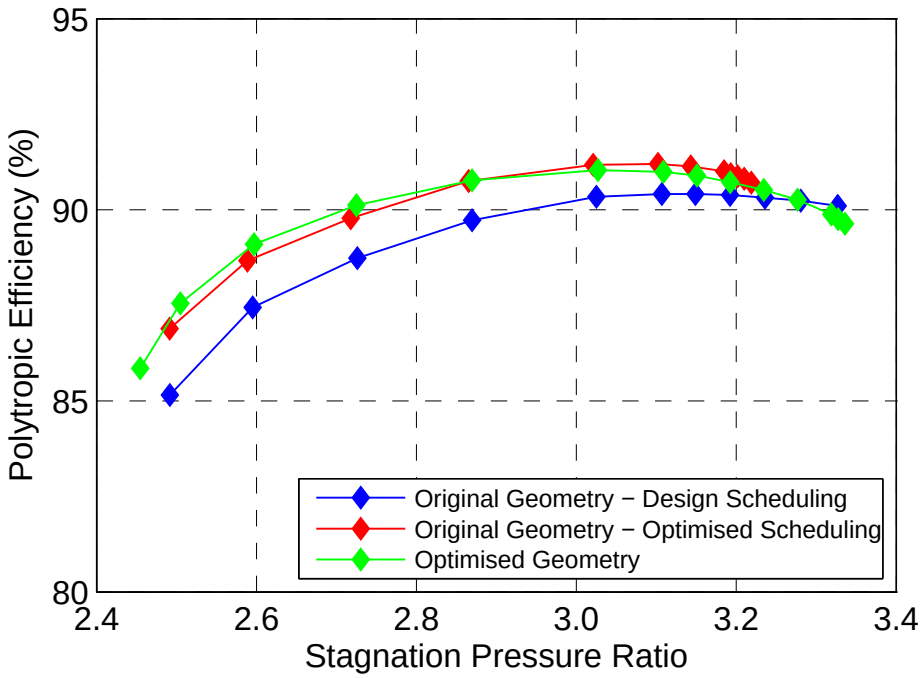

Fig. 6.20 Overall efficiency for original geometry with design and optimised scheduling and optimised geometry

1 and stator 2 optimised) at the design pressure ratio. It can be seen that the rescheduling has caused a small shift in mass flow rate from near the hub to near the casing. The greatest change at about 10% of span is less than 4% of the mass flux however this may explain why the stator hub flow separates at a lower pressure ratio for the optimised VGV schedule. The exit flow angle for the design pressure ratio is plotted in Fig. 6.19 and there is very little change in the exit flow angle between the design and optimised vane schedules. Across the majority of the span the difference in the exit flow angle is similar and within 0.3 degrees. There is a slightly greater difference in the top 10% of the span however it is still less than 1 degree. A good matching of the mass flow rate and the exit flow angle to the original scheduling gives a high degree of confidence that the optimised vane schedule would perform well when used as embedded stages within the larger multistage compressor.

6.4 Comparing Original and Optimised Geometries

It has been shown that rescheduling the VGVs can improve the design efficiency of the original blade geometry by improving the stage matching. Achieving an improved design efficiency was also the motivation for the redesign of the blade geometry that produced the optimised geometry [90]. The overall efficiency for the two geometries and the optimised

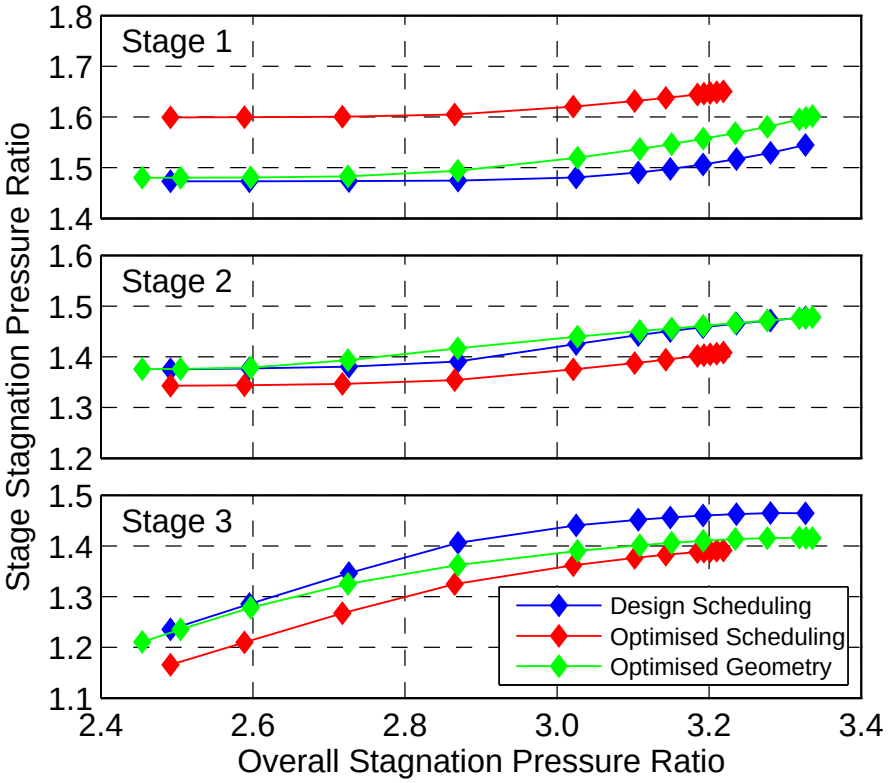

Fig. 6.21 Individual stage pressure ratios for original geometry with design and optimised scheduling and optimised geometry

scheduling of the original geometry is shown in Fig. 6.20. It is noticeable that the optimised geometry gives a similar increase in efficiency as the optimised vane schedule of the original geometry does, across the whole range. The optimised geometry has a larger stall margin than the rescheduled original geometry and is able to reach a slightly higher pressure ratio than the original geometry with design scheduling. It can been seen in Fig. 6.21, that the optimised geometry altered the stage matching and some of the trends are similar to the effect caused by rescheduling the original geometry. At low pressure ratios the matching is unchanged, however at medium to high pressure ratios the stage 1 pressure ratio is greater and the stage 3 pressure ratio is lower. This is the same trend as for the rescheduled original geometry however the change is smaller as the optimised blade geometry has allowed for the stages to perform better at the design pressure ratios. The stage 2 pressure ratio has remained mostly unchanged.

At the design operating point the greatest efficiency increase has come from stage 1 which, as shown in Fig. 6.22, is now operating with an efficiency of 91.1%—up from 89.6%. There is also a small efficiency increase in stage 2 but stage 3 remains virtually constant. The optimisation has made the individual stages operate at, or near to, their peak efficiency when

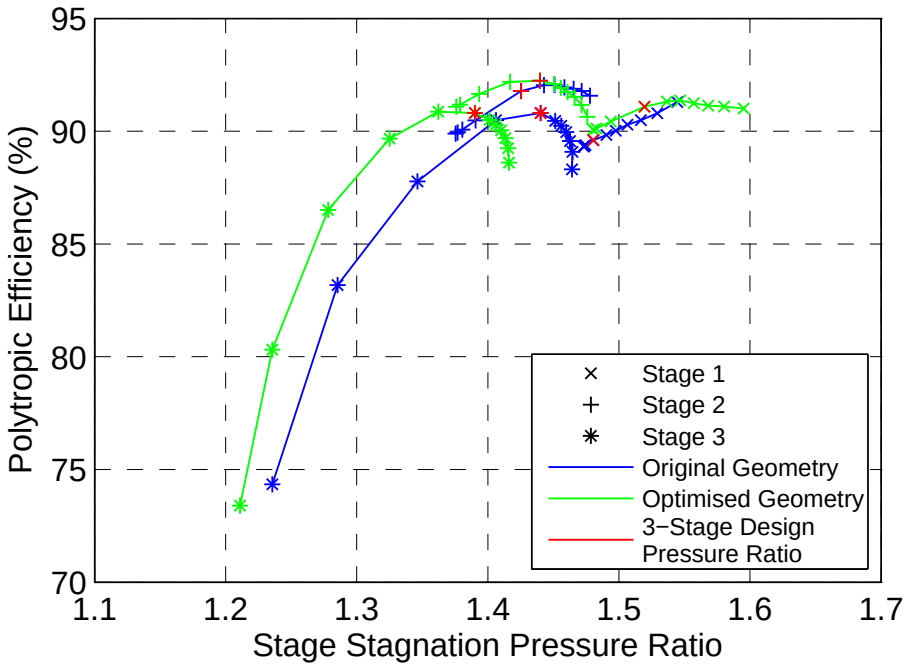

Fig. 6.22 Individual stage efficiency for original geometry with design and optimised scheduling and optimised geometry

operating at the overall design point. In particular the range of stage 1, when embedded in the 3-stage compressor, is no longer restricted to deep choke (and low efficiency) for the majority of the 3-stage design speed characteristic. Given that each stage is already operating close to its peak efficiency there is no significant improvement to be had by rescheduling the VGVs at the design operating point.

6.5 Rescheduling of Optimised Geometry to Improve Off-Design Performance

It has been shown that the optimised geometry has improved the stage matching and has led to all 3 stages operating close to their maximum efficiency when the compressor is operating at the design pressure ratio. The primary reason for the improved efficiency is that stage 1 is now operating near peak efficiency instead of in deep choke. When a multistage compressor operates at off-design speeds the front stage is the most sensitive to changes in operating condition so the altered stage 1 design operating conditions will have a large effect on the off-design speed performance. This is very clear by looking at the compressor efficiency operating map presented in Fig. 6.23. Efficiency results are shown for the original and optimised blade geometries with design vane scheduling at a number of operating speeds

below and above the design speed. Despite the optimised geometry having a higher efficiency at the design speed, the original blades have a higher efficiency at 90% speed and below.

This can be understood by the change in stage 1 operating point. As the compressor operates at lower speeds, the front stage is pushed towards stall, even when operating on the compressor working line. In the optimised geometry at the design pressure ratio, stage 1 is operating near peak efficiency (compared to near choke in the original geometry) so it is already closer to stall before the compressor even starts to run at part speed. As the compressor operates at lower speed stage 1 will be pushed to stall much quicker in the optimised geometry and will therefore operate near stall and with a lower efficiency. In contrast stage 1 in the original geometry first has to get out of choke when the speed drops which will initially move the stage towards peak efficiency (for that speed) and therefore the 3-stage efficiency is higher in the original geometry at speeds lower than the design speed. A similar argument, in reverse, can be made for the optimised geometry operating at a higher efficiency than the original geometry at over-speed. At over-speed the front stage is pushed more towards choke. In the original geometry stage 1 is already near choke at design so its efficiency will drop quickly as it is forced into deeper choke. However in the optimised geometry stage 1 is still pushed towards choke but it is starting from a higher pressure ratio, and efficiency, so the efficiency does not drop off so quickly.

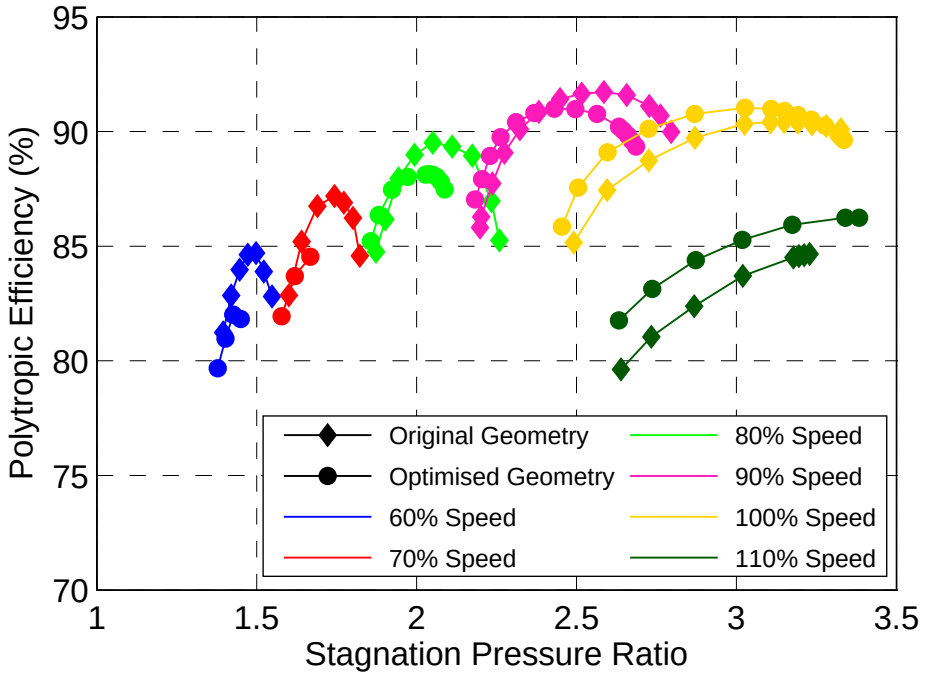

Fig. 6.23 Compressor efficiency map for original and optimised geometries

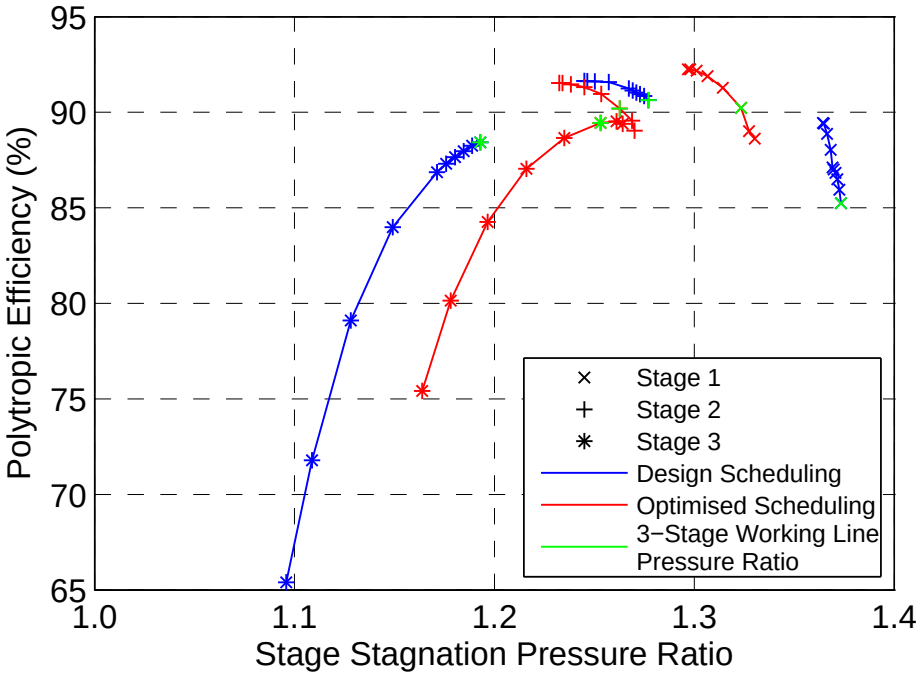

Fig. 6.24 Individual stage efficiencies for design and optimised scheduling at 80% speed

6.5.1 Part-Speed Vane Optimisation

At part speed, the mismatching of the stages provides the potential to improve the efficiency by re-staggering the VGVs. The mismatching of the stages for the design scheduling can be seen, in blue, from the embedded stage efficiencies in Fig. 6.24. Over the 3-stage range, at 80% speed, stage 3 operates at pressure ratios lower than peak efficiency while stage 1 and 2 operate at pressure ratios above peak efficiency. Stage 1 in particular can be seen to be operating on a line with a steep gradient that shows no sign of rounding off to a peak efficiency. This indicates it is operating close to stall and on the nominal 3-stage working line the stage is only operating with an efficiency of 85%.

Optimisation of the VGVs followed the same method as the optimisation for the original geometry at design: Stators 1 and 2 were optimised for maximum efficiency at the nominal working line operating point for the given speed and then the IGV was re-scheduled to match the mass flow rate of the design scheduling at the same nominal working line operating condition. Stator 3 was not re-scheduled in order to maximise integration potential to the downstream stages in the larger multistage compressor.

The VGV optimisation offers an improvement in the stage matching and it can be seen in Fig. 6.24 that the stage 1 efficiency increases from 85% to 90%, when operating on the nominal working line. Rescheduling also leads to an improvement in the overall efficiency across the entire range as shown in Fig. 6.25. The improvement has been gained by using the

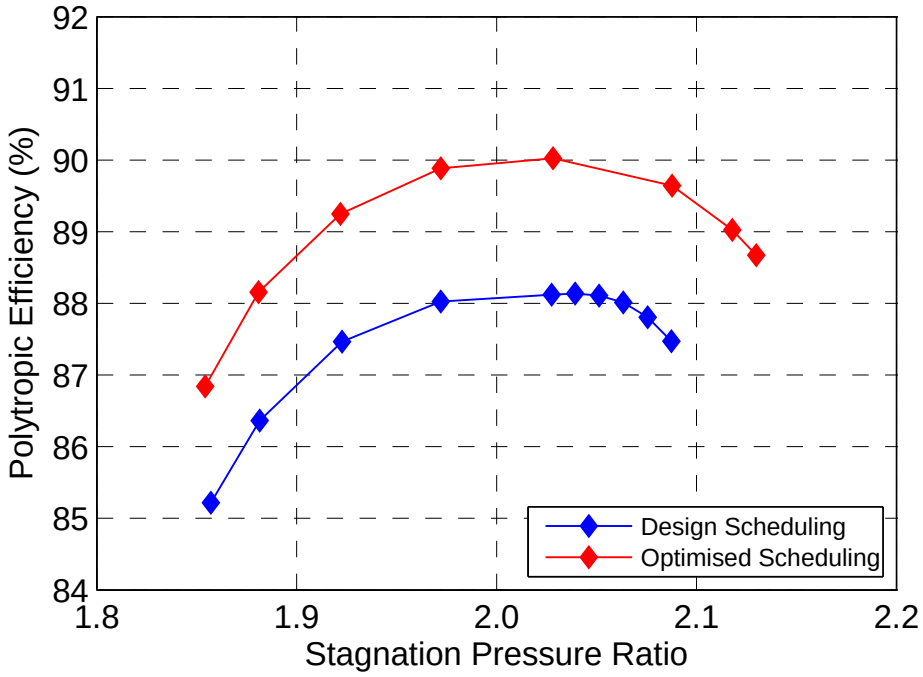

Fig. 6.25 Overall efficiency for design and optimised scheduling at 80% speed

Table 6.2 Vane schedules and difference in overall efficiency for 80% speed

	Vane Schedule			η_{nwl}	$\Delta\eta_{nwl}$
	IGV	Stator 1	Stator 2		
Design	0	0	0	87.5%	-
Optimised	+7	-1	-7	89.6%	2.1%

vane schedule shown in Table 6.2. By opening stator 1 and 2, stage 3 performs more work which relieves stage 1 and pushes it away from its near stall operating point. This trade in stage pressure ratios can be seen in Fig. 6.24. In addition to the efficiency increase, achieved by rescheduling, there is also an increase in the maximum overall pressure ratio that can be achieved, from 2.09 to 2.13, because relieving the stage 1 loading has meant the stage stalls at a higher overall pressure ratio.

6.5.2 Over-Speed Vane Optimisation

At 110% speed the overall efficiency quickly drops off from the efficiency at the design speed as seen in Fig. 6.23. Although the optimised geometry has a higher efficiency than the original geometry at 110% speed, there is still potential for increased efficiency by rescheduling. The optimised VGV schedule is shown in Table 6.3 and the effect on the stage

Table 6.3 Vane schedules and difference in overall efficiency for 110% speed

	Vane Schedule				η_{nwl}	$\Delta\eta_{nwl}$
	IGV	Stator 1	Stator 2	Stator 3		
Design	0	0	0	0	85.9%	-
Optimised	0	+10	+11	0	88.3%	2.4%
Stator 3 Rescheduled	0	+10	+11	+3	88.5%	2.6%

pressure ratios and stage efficiencies is shown in Fig. 6.26. The stage matching has shifted in a very similar way to the shift that happened when the original geometry was optimised at design speed earlier in this chapter. The rescheduling has increased the pressure ratio of stage 1 which has pushed it away from deep choke and increased its efficiency from 83.0% to 87.4%. A smaller efficiency gain is also seen in stage 2 while the stage 3 efficiency does not significantly change on the nominal working line, however there is a reduction in the pressure ratio. The increased stage efficiencies have led to an increase in the overall efficiency by 2.4% on the nominal working line and a similar increase in efficiency across the entire 110% speed line is seen in Fig. 6.27

The optimised scheduling at 110% has increased the overall efficiency, however the highest stable operating pressure ratio has reduced very slightly from 3.38 to 3.37. The

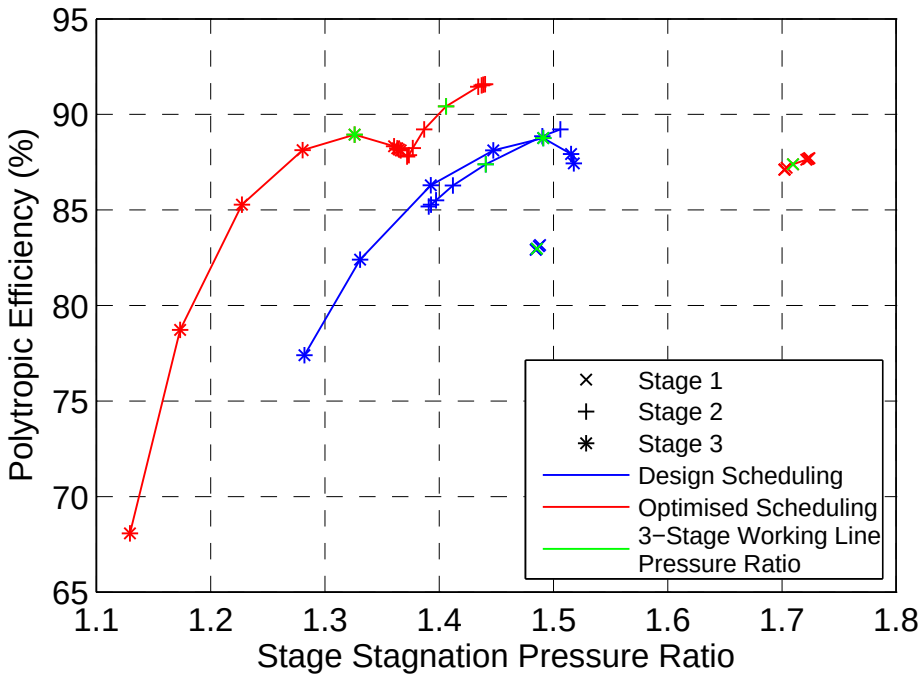

Fig. 6.26 Individual stage efficiencies for design and optimised scheduling at 110% speed

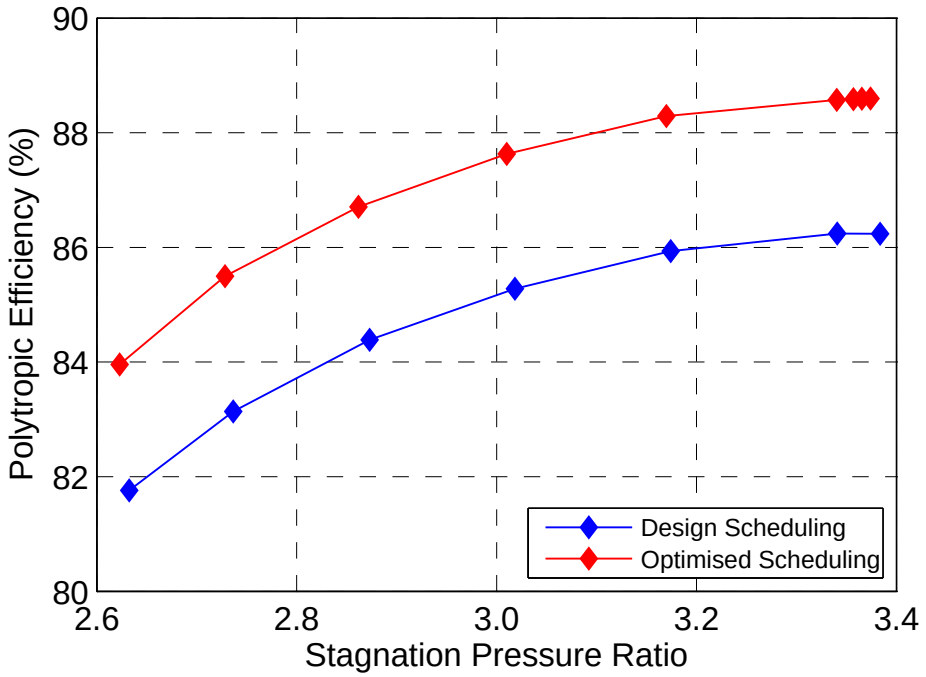

Fig. 6.27 Overall efficiency for design and optimised scheduling at 110% speed

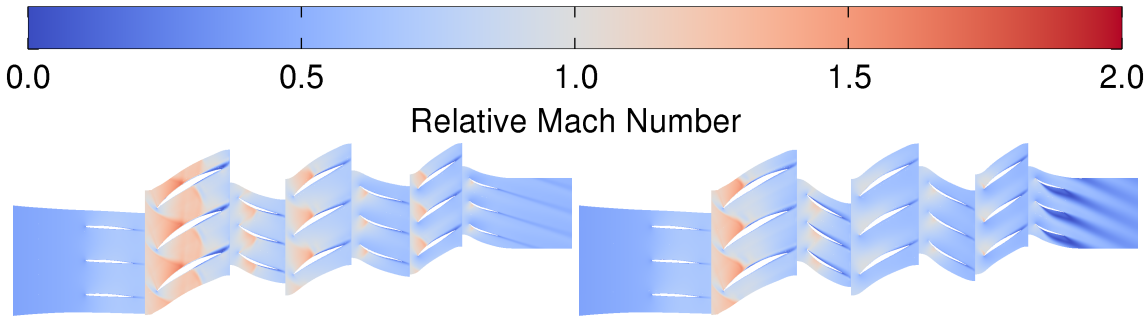

(a) Design schedule 20% span

(b) Optimised schedule 20% span

(c) Design schedule 80% span

(d) Optimised schedule 80% span

Fig. 6.28 Relative Mach number plots for 110% speed at the onset of stator 3 separation

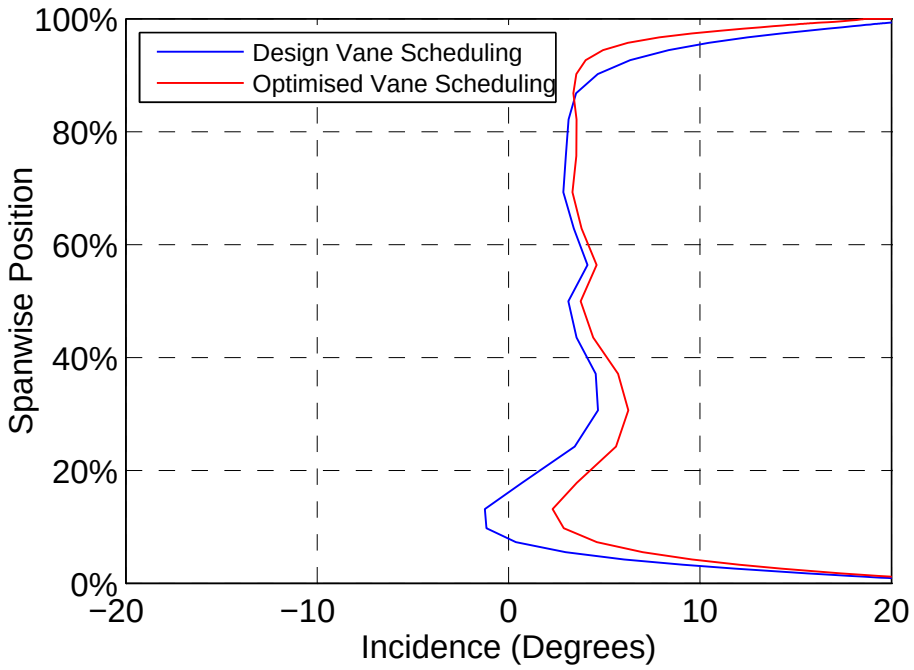

Fig. 6.29 Stator 3 incidence just before separation occurs in design and optimised scheduling

design scheduling and optimised scheduling both fail at higher pressure ratios because of a separation that occurs in stator 3, but the location of the separation changes between the two vane schedules. Figure 6.28 shows relative Mach number plots for the design and optimised vane schedules at a pressure ratio just high enough to cause separation in the stator 3 blade row. Results are plotted at 20% and 80% of span. It can be seen that the separation in stator 3 changes from near the casing in the design scheduling (Fig. 6.28c) to near the hub in the optimised scheduling (Fig. 6.28b). This change of separation location on stator 3 has occurred as a result of rescheduling only stator 1 and stator 2 and is a clear sign that rescheduling upstream stages affects the flow exiting rotor 3. The flow incidence onto stator 3 is shown in Fig. 6.29. There is not much change of incidence in the upper half of the span, however the lower half of the span shows an increased incidence onto the stator for the optimised vane scheduling which is 3 degrees higher at 10% span. The higher incidence near the hub causes the separation to develop at the hub before it occurs at the casing. At the same time the lower incidence in the upper 15% of span suppresses the casing separation. The change in incidence has been caused by a redistribution of the loading along the span of rotor 3.

An attempt to suppress the stator separation was made by rescheduling stator 3 to reduce the incidence of the flow onto it. It was decided to reschedule stator 3 by 3 degrees in order to try to return the incidence at 10% of span back to the value in the design scheduling

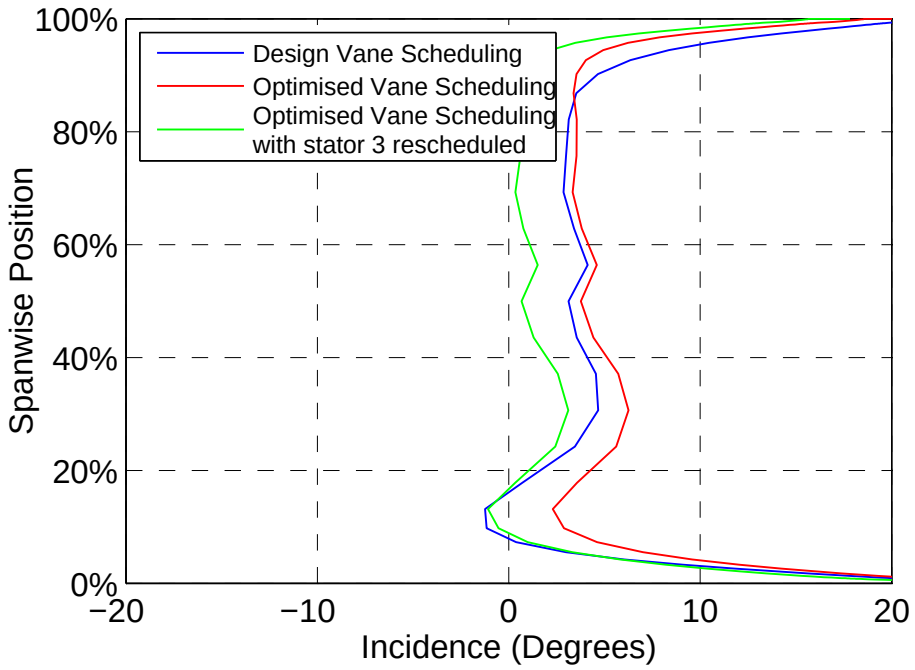

Fig. 6.30 Stator 3 incidence just before separation occurs in design, optimised and optimised with stator 3 rescheduling

simulation. The result of this is shown in Fig. 6.30 and it can be seen that the incidence at 10% of span has been successfully matched with the incidence for the design scheduling however the uniform re-staggering of the entire blade means that the incidence is now lower across the rest of the span. Reducing the incidence has successfully suppressed the separation and has allowed higher pressure ratios to be achieved, as shown in Fig. 6.31. In addition there is also a small increase in the overall efficiency on the nominal working line, as noted in Table 6.3, although at lower pressure ratios the efficiency is reduced as can be seen in Fig. 6.31.

6.5.3 Part-Speed Stall Margin

The work so far has focussed on using vane rescheduling to maximum the efficiency. The rest of the chapter will look at the use of vane rescheduling to improve the stall margin at part-speed. It was chosen to perform this investigation at 94.5% speed as rig tests have established that a pinch point in the stall margin exists at this speed. It has already been demonstrated that, at 80% speed, rescheduling to improve the efficiency also led to an increase in the stall margin. This happened because, at 80% speed, stage 1 was the first stage to stall so relieving the loading on stage 1 both improved the efficiency and caused the compressor to stall at a higher overall pressure ratio. At 94.5% however, stage 1 is not the first stage to fail so

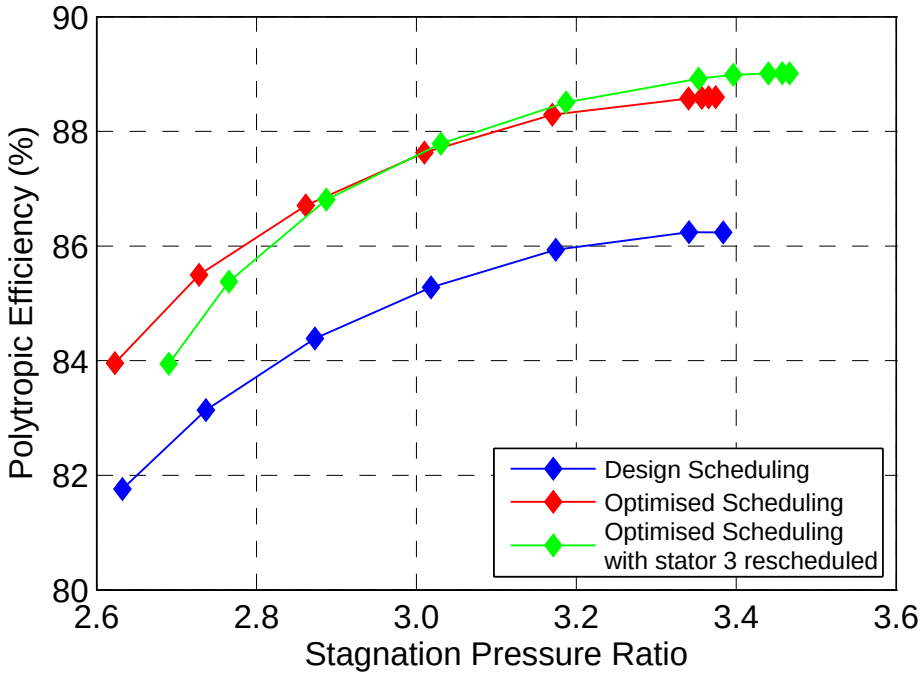

Fig. 6.31 Overall efficiency for design, optimised and optimised with stator 3 rescheduling

Table 6.4 Vane schedules and difference in overall efficiency and stalling mass flow rate for 94.5% speed

	Vane Schedule			η_{nwl}	$\Delta\eta_{nwl}$	Stalling Mass Flow Rate (kg/s)
	IGV	Stator 1	Stator 2			
Design	0	0	0	91.2%	-	24.2
Rescheduled	-2	+2	+2	90.9%	-0.3%	23.8

this would not work. Instead stators 1 & 2 are closed, to the values shown in Table 6.4. As seen in Fig 6.32 this has increased the stage 1 pressure ratio but it has reduced the stage 2 & 3 pressure ratios. This has led to an increase in the stall margin as shown in Fig. 6.33 and Table 6.4. The stalling mass flow rate, in Table 6.4, is defined as the mass flow rate of the last stable operating point. It is known that multistage compressors can support front stages that would otherwise have stalled at part speed. This vane schedule takes advantage of this fact by pushing stage 1 closer to stall in order relieve stages 2 & 3.

Although this vane schedule has led to an increase in the stall margin, it has led to a reduction in the overall efficiency on the nominal working line of 0.3% and across the whole speed line as shown in Fig. 6.34. This trade-off between stall margin and efficiency gives the designer flexibility to change the vane settings depending on what is required for the overall operation of the gas turbine.

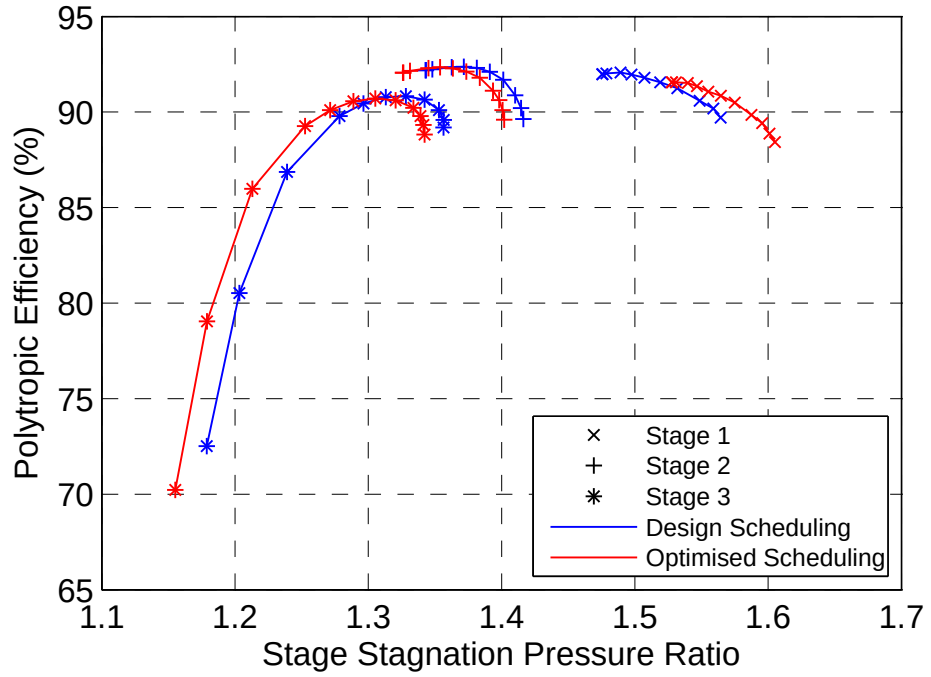

Fig. 6.32 Individual stage efficiency for 94.5% speed with design and rescheduled vanes settings

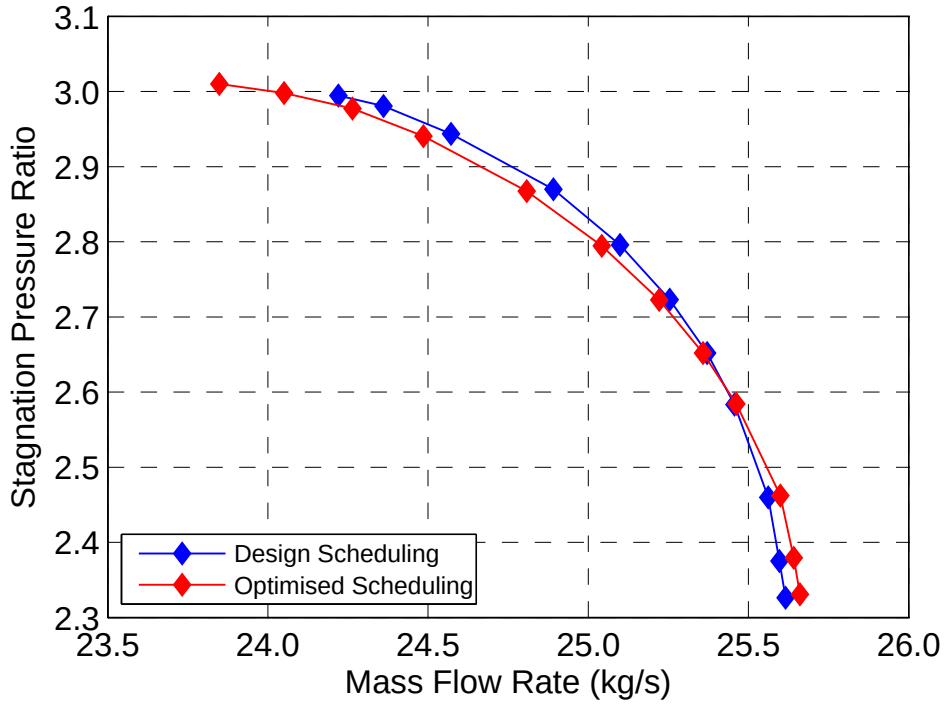

Fig. 6.33 Characteristic for 94.5% speed showing increased range for rescheduled vanes

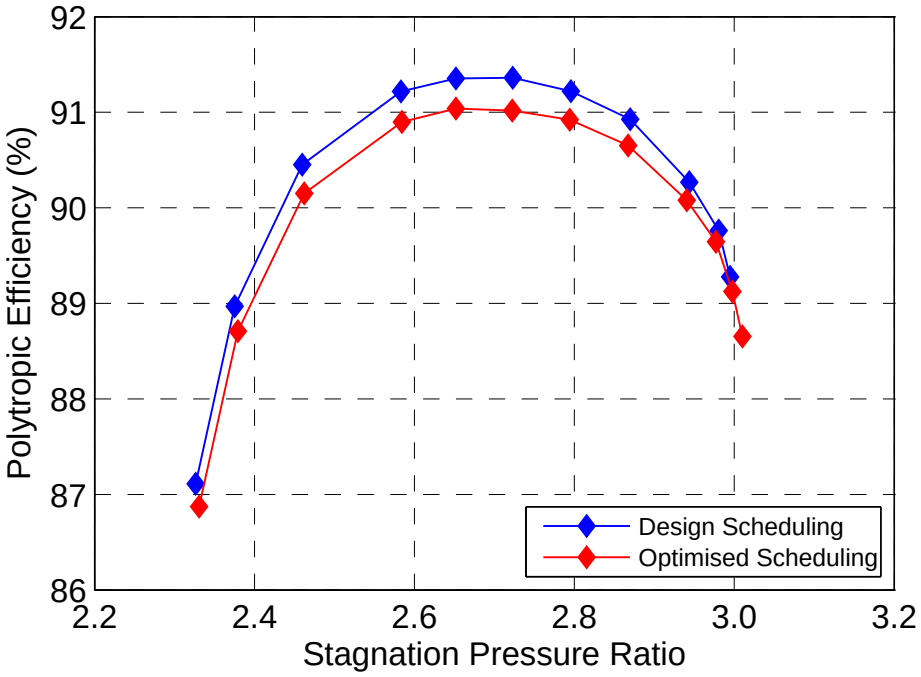

Fig. 6.34 Overall efficiency for 94.5% speed with design and rescheduled vanes settings

6.5.4 Rig Test Results

In order to provide validation for the results presented in this chapter some of results of the investigations where examined on the test rig by Siemens Industrial Turbomachinery Ltd. Optimised off-design vane schedules for 80% and 110% have already been discussed earlier in this chapter and formed the basis for the investigation on the test rig. The optimised vane schedule, as predicted by the CFD, for 80% speed has been tested on the test rig. In addition, a vane schedule for 105% was also tested. Although the results and proposed vane schedule for 105% speed have not been discussed in this chapter, the results for the optimised vanes are similar to those for 110% speed, with reduced rescheduling required at 105% to achieve the largest efficiency improvement.

The vane schedules tested, and the changes in overall efficiency, are given in Table 6.5. Due to the test data available the comparison presented is the difference in the peak efficiency points between the design schedule and optimised schedule. This is in contrast to the results presented in Table 6.2 where the efficiency delta was compared at the point on the nominal working line and not at peak efficiency point for the given speed. Table 6.5 shows that at 80% speed the CFD predicted a 1.9 percentage point increase in efficiency while the test rig gave a 1.7 percentage point increase in efficiency, when using the optimised vane schedule. At 105% speed the CFD predicted a 1.3 percentage point increase while the test rig gave a 1.0 percentage point increase. At both speeds the test rig did not achieve quite as much

Table 6.5 Off-design vane rescheduling peak efficiency improvements

	Vane Schedule			Increase in Peak Efficiency	
	IGV	Stator 1	Stator 2	CFD	Test Rig
80% Speed	+7	-1	-7	1.9%	1.7%
105% Speed	-1	+7	+9	1.3%	1.0%

of an efficiency increase as the CFD had predicted. However the tests at both speeds prove that efficiency gains can be made by making adjustments to the vane schedule at off-design speeds and that these schedules can be predicted by CFD with reasonable success.

6.6 Conclusions

The investigations in this chapter have explored the effects of rescheduling VGVs in a 3-stage transonic compressor. It was shown that a knowledge of the trends can be used to reschedule the compressor in order to increase efficiency and stall margin at speeds close to the design speed. Using 3D CFD has provided detailed information about the flow field that it is not possible to acquire with low order models. For the compressor speeds analysed in this study the CFD results do not show any very large scale separations in the flow. (Part span separations were shown in Fig. 6.28 for ratio pressures beyond the scope of this study in order to highlight the different stall locations however in general no large scale separations have been investigated as part of this study.) The overall trends in the performance predictions agree with the available experimental data, so it is likely that 3D CFD will be able to calculate more accurate vane scheduling predictions than lower order models at speeds close to the design speeds, and if this is successful, then also at lower operating speeds where very high angle settings are required.

The vane schedule for the original geometry was optimised at the design operating condition in order to achieve an increase in the overall efficiency of 0.9%. Rescheduling led to an improvement in the stage matching and allowed the individual stages to operate closer to their peak stage efficiency. It was found that the overall efficiency improvement gained by improving the stage matching was greater than the efficiency improvement gained by the optimised blade profiles for the design pressure ratio. This suggests that optimising the matching between the stages, and within each stage, is more important than optimising the blade profiles when trying to achieve the best overall efficiency. This means that future optimisations of multistage compressors could focus on the stage matching instead of the optimisation of the blade profiles thus significantly reducing the control parameters for the

optimisation and allowing a greater focus on improving the matching along the blade span for each blade row.

New schedules were also found for the optimised blade geometry that gave a 2.1% efficiency increase at 80% speed and a 2.4% increase at 110% speed. This has been supported by similar trends in test rig experiments at 80% and 105% speeds. Rescheduling the vanes in the counter intuitive direction (making the stage matching worse) was used at 94.5% speed in order to successfully increase the stall margin, although this occurred at a small cost to the efficiency of 0.3%. The trade-off between stall margin and efficiency gives a compressor designer great flexibility to tune the VGV schedule in order to best meet the compressor characteristics required for a given operation.

At 110% speed it was found that rescheduling stators 1 & 2 had a significant effect on the flow field entering stator 3, which led to a change in the separation location from near the casing to near the hub. This insight provides useful information for the stator design as taking this into consideration could lead to improved stator designs that are more resilient to upstream re-staggering and thus improve the off-design operation range.

Chapter 7

Conclusions and Recommendations

7.1 Introduction

The work presented in this thesis has aimed to provide useful information for compressor designers in the development cycle of transonic compressors. In order to seek further improvements in compressor efficiency it is necessary to continue to gain a better understanding of the flow within transonic compressors and to know how best to use the design tools available. The work has focused on three main areas of research:

- The differences in results between steady and unsteady simulations (which can be used to quantify the modelling uncertainties in the steady simulations),
- Investigating IGV-Rotor interaction with a focus on aerodynamic and mechanical implications of reducing the IGV-Rotor spacing,
- How vane rescheduling can be used for improving stage matching, thus improving compressor performance.

Each of these areas of research provides information to the designer on different aspects of the design that need to be considered during the design cycle. In the rest of this chapter the main conclusions from each section of work will be discussed and a suggestion of further work is given that would provide even greater understanding of the flow in transonic multistage compressors.

7.2 Steady and Unsteady Simulation Comparison

7.2.1 Summary of Conclusions

The first chapter of results investigated the differences between the results for steady and unsteady simulations of a multistage industrial transonic compressor. Unsteady simulations model more of the physical flow features than steady simulations and are therefore able to provide a greater insight into the flow, and to predict the losses and operating performance more accurately. Steady simulations intentionally make the assumption that the flow is steady and only the mixed out flow properties are passed between the blade rows through the use of mixing planes. In contrast, unsteady simulations allow the full transfer of the wakes and unsteady pressure fields between the blade rows. Unsteady simulations, despite being more accurate, have not yet replaced steady simulations as the backbone of CFD simulations during the design process because they are significantly more expensive to perform.

Given that it is not always possible to perform unsteady simulations, it is very useful for the designer to have an appreciation of how the assumptions involved in steady simulations affect the results, when compared to unsteady simulations. This also gives the designer a greater understanding of when it might be necessary to perform unsteady simulations in order to accurately predict the compressor performance. In order to investigate the differences between steady and unsteady simulations, the comparison was first performed using steady and unsteady simulations of the front 1.5 stages of a 3.5 stage industrial transonic compressor. The comparison was made between the two simulation methods for a range of operating conditions at different speeds in order to investigate how the discrepancies between the steady and unsteady simulations vary. The aim of performing this study was to provide new information about how the steady modelling assumptions affect the prediction of the compressor performance (when compared to unsteady simulations) and to do this in more detail than has previously been reported.

The steady simulations always give a higher predicted efficiency with a maximum efficiency delta of 1.05 percentage points on the design speed line at high pressure ratios. The efficiency delta at peak efficiency for a given speed is larger at faster speeds, varying from 0.54 percentage points at 90% speed to 0.98 percentage points at 110% speed. The overall stage efficiency is broken down into individual blade row isentropic efficiencies in order to gain a greater understanding of how each blade row performs. For the steady simulations, the mixing loss occurring at the mixing plane immediately upstream of a given blade row is included when calculating that blade row's efficiency because the majority of that mixing loss would occur in that blade row as the wakes mix out. Having done this it is found that the small stage efficiency delta that exists at low pressure ratios (<0.2 percentage points) is only

small because the efficiency deltas in the rotor and stator blade rows show opposite trends and cancel each other out. This is an important observation because it means that a small shift in either the rotor or stator efficiency curve would lead to a different stage efficiency delta. This would easily explain why some previous researchers have found that steady simulations over predict single stage efficiency while others have found them to under predict the efficiency.

The steady simulations always give a higher rotor efficiency due to a weaker passage shock wave which leads to a weaker interaction between the shock wave and the rotor boundary layer. The location of the passage shock wave in the steady simulations is located further downstream than in the unsteady simulations, due to less blockage near the rotor tip. The IGV efficiency is also higher for the steady simulations, mostly at high pressure ratios, because the interaction between the IGV and the rotor leading edge shock wave is not captured by the steady simulations. This interaction gets stronger at higher pressure ratios and at lower speeds, as the shock structure in the rotor is pushed further upstream and reduces the efficiency (when modelled in unsteady simulations).

For the stator blade row, a lower efficiency is observed in the steady simulations. To understand this, the two main sources of loss have been analysed—the rotor wake mixing loss and, for the unsteady simulations, the interaction between the rotor wakes and the stator blades. When the rotor wake interacts with the stator boundary layer, it creates a negative jet effect on the suction surface boundary layer, and on the pressure surface the rotor wake is seen to stretch. As the rotor wake interacts with the leading edge of the stator blade a large amount of loss is generated. This loss, caused by the interaction of the rotor wake and the stator blades, is not present in the steady simulations, so the greater stator efficiency in the steady simulation must be due to a lower mixing loss from the mixing out of the rotor wakes. There are two reasons for the change in mixing loss between the steady and unsteady simulations. Firstly, the steady simulations assume that the rotor wakes will fully mix out to a pitch-wise uniform flow and this is imposed at the rotor-stator mixing plane. In reality, and as happens in the unsteady simulations, the rotor wakes are not fully mixed out even by the time they exit the stator passage. This means that some of the rotor wake mixing loss is occurring further downstream in the unsteady simulation and so is incorrectly attributed to the loss in the stator blade row for the steady simulations. Another reason that gives the steady simulations a lower efficiency than the unsteady simulations, is that the rotor wakes recover some of the stagnation pressure loss due to mixing as they are chopped up by the stator blades and travel through the stator passage. This recovery process is not modelled by the steady simulations and contributes to the lower stator efficiency in the steady simulations.

Investigation of the unsteady flow over a complete cycle reveals that the magnitude of the shock wave oscillation on the rotor blade surface is small for this compressor rotor. At

80% rotor span, across a range of operating conditions at the design speed, the passage shock wave was found to oscillate no more than 1% of the rotor chord despite the upstream and downstream pressure influences from adjacent blade rows. The size of the oscillation means that the non-linear effects of the unsteady flow are negligible and the unsteady shock could be simply modelled as linear perturbations.

In order to gain understanding of the effects that the downstream stages have on the unsteady efficiency characteristic of the upstream stage, the front 1.5 stages (previously modelled in isolation), were also modelled embedded within the 3.5 stage machine. When the first stage is embedded within the 3-stage compressor, the downstream stages do not significantly affect the efficiency characteristic prediction of the first stage. This suggests that the effect of the pressure potential fields from the downstream stages has a minimal effect on the first stage. This is an important finding as it means the designer does not need to give great consideration to the unsteady interaction effects of the downstream stages when designing the first compressor stage.

All the conclusions discussed in this section have been shown to be consistent across a range of speeds. The isolated and embedded compressor stage was analysed at 90%, 100% and 110% of design speed with the only difference between the speeds being small changes in the magnitudes of the efficiency deltas between steady and unsteady simulations.

In addition these results have been shown to be consistent for both the baseline [56] and optimised [90] geometries at the design speed. This suggests that the results presented here can be applied to other transonic compressor geometries.

7.2.2 Recommendations for Further Work

The findings relating to the differences between steady and unsteady simulations were found to be consistent for two different blade geometries, which gives a suggestion that the findings may be applicable to a wider range of different transonic compressor geometries operating at similar speeds. In order to test this hypothesis a similar comparison of steady and unsteady simulations would need to be performed on a range of different geometries. Ideally these would encompass a range of different stage loadings and rotor inlet Mach numbers. If the results were found to be consistent with the findings given in this thesis, the designer would have a strong indication of how the efficiency prediction from a steady simulation would differ from an unsteady simulation without necessarily needing to perform the unsteady simulation. This could be particularly useful for obtaining a better prediction of efficiency earlier in the design cycle.

The investigation presented in this thesis has focused on the front stage of the compressor where the propagation of unsteady effects from upstream is minimal. Performing a similar

investigation on a central stage would provide new information on how the presence of an upstream stage would affect the unsteady performance.

7.3 IGV-Rotor interaction and Axial Spacing

7.3.1 Summary of Conclusions

The second results chapter contained the results of studying the IGV-Rotor interaction effects by primarily investigating the effect the interactions had on the unsteady loading of the blades. This investigation was aided with a comparison of two different axial spacings of the IGV and rotor 1 blade rows, so that differences in the interaction could be analysed when the axial spacing, and therefore the strength of interaction, varied. Varying the IGV-Rotor axial spacing also allowed analysis of the effect this had on the compressor efficiency. This study was performed in a 3.5 stage transonic compressor using unsteady CFD simulations. The aim of this analysis was to provide information to the compressor designer about the IGV-Rotor interaction, how the IGV-Rotor axial spacing affects this interaction and what this means in terms of efficiency and unsteady blade loading variation. Unlike previous studies [2, 6, 32, 35, 36, 57, 71, 72, 89], this work was performed in a multistage environment in order to assess the impact of the IGV-Rotor interaction on the downstream stages. Analysing the dynamic blade forcing also gave an indication of the effect on the mechanical integrity of the blade when the blade row spacing is altered. Knowing how the IGV-Rotor spacing affects the compressor performance and the mechanical integrity within a multistage machine, will help designers make decisions about the best size for the IGV-Rotor axial spacing.

The efficiency of the compressor in the two different configurations was compared using quarter annulus unsteady simulations at the design speed. It is found that reducing the IGV-Rotor axial spacing increases the stage 1 efficiency by 0.2 percentage points and the overall efficiency by 0.1 percentage points at the design pressure ratio. A similar efficiency gain is found at pressure ratios lower than the design pressure ratio, however at higher pressure ratios the overall efficiency is reduced. This is due to the reduced axial spacing affecting the stage matching. This leads to a drop in the overall efficiency, despite a small improvement in the stage 1 efficiency, because stages 2 and 3 operate at a higher pressure ratio and with a lower efficiency. The higher efficiency in stage 1 is associated with a lower Mach number on the rotor suction surface and therefore a weaker shock system. It is also found that steady simulations cannot accurately predict the compressor efficiency for the configuration with the smaller IGV-Rotor spacing because a significant discrepancy in the predicted efficiency occurred between the unsteady and steady CFD simulations.

The dynamic blade loading was compared using full annulus unsteady simulations in order to capture the blade row interactions at the correct frequencies. The dynamic loading was compared across all the blades in a given row by looking at the relative magnitudes of specific frequency components of the dynamic loading and the frequencies investigated were chosen to match the blade passing frequencies for the blade rows of interest. When the axial spacing is reduced, the dynamic loading increases in the IGVs by a factor of 1.8 and in the rotor 1 blades by a factor of 6.5, while changes in the time-averaged loadings are comparatively small at 4.4% and -1.3% respectively. The change in mean dynamic loading in the stator 1 blades is very small, however, there is an obvious change in the blade to blade dynamic loading because the reduced axial spacing has changed the locations of the interactions between the IGV wakes and the stators. Performing this analysis in a multistage simulation allowed the effect on the dynamic loading in the downstream stages to be analysed. It is found that the mean dynamic loading (attributed to the IGV and rotor 1 blade passing frequencies) in the stage 2 and 3 blade rows has decreased as a result of reducing the IGV-Rotor axial spacing. This effect is greater in the rotor blade rows because they interact with the IGV wakes and these have been affected more than the rotor 1 wakes by changing the IGV-Rotor spacing.

It has been found that the dynamic loadings (at a certain frequency) for a blade row can increase many times over as a result of reducing the IGV-Rotor axial spacing. However, in most of the cases considered, the absolute magnitude of the forcing is fairly weak. For example the dynamic loading of rotor 1, attributed to the interaction with the IGVs, increased by a factor of 6.5 but the absolute amplitude of the forcing is only 1.4 N, on a static loading of over 150 N. An attempt to gain a better mechanical interpretation of the results has been attempted by analysing the modal force on the rotor, however it remains important to perform further mechanical analysis in order to gain a better understanding of how the increased dynamic pressure loading translates to blade vibration and ultimately blade life before failure.

The studies undertaken suggest that reducing the IGV-Rotor axial spacing would increase the efficiency, for the 3.5 stage compressor investigated, by 0.1 percentage points over the majority of the operating range at design speed. Doing so, however, will increase the unsteady pressure loading on the blades and this must be investigated further to see if it will significantly affect the mechanical integrity of the blades. Performing the study in a multistage compressor has shown that the IGV-Rotor interaction has an effect on the blade rows in the downstream stages and this has not previously been shown.

7.3.2 Recommendations for Further Work

While it has been found that reducing the axial spacing increased the efficiency for the design pressure ratio and below, it was found to be detrimental to the efficiency at high pressure ratios due to a change in the stage matching. Combining the reduced axial spacing with a small rescheduling of the stator blades could improve the stage matching and allow the efficiency gain at high pressure ratios to be realised and this would be of value to investigate.

If the efficiency can be shown to be improved for some pressure ratios at design speed then it would be useful to establish if similar efficiency improvements can be obtained at off-design speeds. In addition, investigating a greater number of axial spacings would reveal if further efficiency improvements can be found by making the gap even smaller or if there is an optimal spacing to be found for this compressor, as has been found by others for different machines.

The main unanswered question from this investigation is the significance of the changes in dynamic pressure loading for the mechanical integrity of the blades. It has been shown that reducing the axial spacing affects the dynamic loading on the blades therefore it is necessary to understand the real effect that this would have in terms of blade life. This knowledge is necessary in order to give the designer the information needed to decide on the best trade-off between efficiency and mechanical integrity.

7.4 Vane Rescheduling

7.4.1 Summary of Conclusions

The chapter on vane rescheduling presented results from rescheduling IGV and stator vanes in a 3.5 stage transonic compressor using 3D steady CFD. Previous rescheduling investigations on transonic compressors have mainly focused on using low fidelity methods to predict optimal vane schedules for off-design speeds. However there is uncertainty about the ability of such low fidelity methods to successfully do this, especially at low speed where large vane angle adjustments are required and large regions of separated flow are present. Therefore there is an interest in investigating the suitability of using 3D CFD in order to accurately predict the vane schedules at these low speeds. The work presented in this thesis contributes to this goal by using 3D CFD to predict vane schedules for correcting errors in the stage matching at design speed that have occurred due to design uncertainties. In addition vane schedules were calculated for off-design speeds, close to the design speed, in order to improve the efficiency and operating range at these conditions. At these speeds relatively small changes in vane angles are required and it is believed that if CFD can accurately predict

the optimal vane schedules for these conditions then further work to investigate the ability of CFD to accurately predict optimal vane schedules at lower speeds should be performed. Ultimately it is hoped that accurate 3D CFD predictions of vane schedules at low speed will give a cheaper method to develop vane schedules than rig testing and a more accurate method than low fidelity models. In addition 3D CFD also provides additional information about how the flow field is affected when vanes are rescheduled and this information can be used to develop better stator designs that can perform well at a range of different setting angles.

Results have been presented that establish the trends that occur in the stage matching and efficiency as a result of rescheduling individual blade rows. The lessons learnt from this were then used to seek improvements in the efficiency and stall margin by optimising the vane schedules at different speeds.

The vane schedule for the original geometry [56] was optimised at the design operating condition in order to correct errors in the stage matching that occurred as a result of design uncertainties. The proposed vane schedule achieved an increase in the predicted overall efficiency of 0.9 percentage points. Rescheduling led to an improvement in the stage matching and allowed the individual stages to operate closer to their peak stage efficiency. Similarly, new schedules were found that gave a 2.1 percentage point efficiency increase at 80% speed and a 2.4 percentage point increase at 110% speed for the optimised compressor blade geometry [90]. Optimised off-design vane schedules, as calculated by CFD, for 80% and 105% speeds were tested in the test rig and the test rig results were found to support the efficiency improvements predicted by the CFD although the efficiency gains realised in the test rig were slightly smaller than those predicted by CFD. Rescheduling the vanes in the counter intuitive direction (making the stage matching worse) was used at 94.5% speed in order to successfully increase the stall margin although this occurred at a small cost to the efficiency of 0.3 percentage points. The trade-off between stall margin and efficiency gives a compressor designer great flexibility to tune the VGV schedule in order to best meet the compressor characteristics required for a given operation.

As well as predicting performance more accurately, 3D CFD gives the opportunity to investigate the changes in the internal flow field as the vane schedule is altered. It was found that the rescheduling has a radially non-uniform effect on the flow field in the downstream stages. At 110% speed it was found that rescheduling stators 1 & 2 had a significant effect on the flow field entering stator 3. This led to a change in the separation location from near the casing to near the hub. This highlights the impact that a relatively small amount of vane setting angle change has on the radial equilibrium of the compressor which causes the spanwise flow redistribution in the stages.

7.4.2 Recommendations for Further Work

The vane rescheduling investigation has been performed using steady CFD simulations and has been partially verified by a small number of experimental results. In order to further verify the results and in turn the efficiency improvements predicted, the work needs to be compared to more experimental results. This is necessary in order to give confidence in steady CFD as a means to generate optimised vane schedules at the compressor speeds investigated. If verified, steady CFD would give a much cheaper and quicker way to develop vane schedules earlier in the design process than rig tests. Furthermore a range of different designs could be analysed for off-design performance with vane schedules customised for each design. In particular, investigations need to be performed at low compressor speeds in order to investigate the ability of 3D CFD to accurately predict optimal vane schedules when large vane setting angles are required and large regions of separated flow are likely to be present.

Now that optimised schedules have been proposed using results from steady simulations, an unsteady analysis could be conducted in order to evaluate the significance of the unsteady effects on the losses and the radial redistribution of the flow. The different stator stagger angles will alter the interaction between the rotor wakes and the stators. However it is not known what the impact of this will be.

It has been found that rescheduling the upstream stator blades can have an effect on the flow field entering the downstream stator blade row. Further work should be done to investigate this further and learn if it is possible to balance hub and casing separations elsewhere in the compressor through this method in order to maximise the stall margin. This also opens up a range of possibilities for optimising the downstream stator row in order to take account of variations in the inlet flow field. Redesigning the downstream stator row to appropriately balance the hub and casing separation could lead to an increased stall margin, however, it should be noted that doing this could prove detrimental to the compressor efficiency at design scheduling. Despite this, it provides another method to trade efficiency for stall margin in order to achieve the operation performance required.

References

[1] Adamczyk, J. J. (1996). Wake Mixing in Axial Flow Compressors. ASME Paper No. 96-GT-029.

[2] Arnone, A. and Pacciani, R. (1998). IGV-Rotor Interaction Analysis in a Transonic Compressor Using the Navier-Stokes Equations. *Journal of Turbomachinery*, 120(1):147–155.

[3] Barbosa, J. R., Silva, F., Tomita, J. T., and Bringhenti, C. (2011). Influence of Variable Geometry Transients on the Gas Turbine Performance. ASME Paper No. GT2011-46565.

[4] Benini, E. and Biollo, R. (2007). Aerodynamics of Swept and Leaned Transonic Compressor-Rotors. *Applied Energy*, 84(10):1012–1027.

[5] Bergner, J., Kablitz, S., Hennecke, D. K., Passrucker, H., and Steinhardt, E. (2005). Influence of Sweep on the 3D Shock Structure in an Axial Transonic Compressor. ASME Paper No. GT2005-68835.

[6] Biela, C., Brandstetter, C., Holzinger, F., and Schiffer, H. P. (2011). Influence of Inlet Guide Vane Wakes on Performance and Stability of a Transonic Compressor. ISABE Paper No. 2011-1209.

[7] Biesinger, T., Cornelius, C., Nürnberger, D., and Rube, C. (2012). Speed Line Computation of a Transonic Compressor Stage With Unsteady CFD Methods. ASME Paper No. GT2012-68029.

[8] Biollo, R. and Benini, E. (2012). Recent Advances in Transonic Axial Compressor Aerodynamics. *Progress in Aerospace Sciences*, 56:1–18.

[9] Bloch, G. S., Copenhaver, W. W., and O'Brien, W. F. (1999). A Shock Loss Model for Supersonic Compressor Cascades. *Journal of Turbomachinery*, 121(1):28.

[10] Brandvik, T. and Pullan, G. (2010). An Accelerated 3D Navier Stokes-Solver for Flows in Turbomachines. *Journal of Turbomachinery*, 133(2):021025.

[11] Broichhausen, K.-D. and Harster, P. (1990). Aerodynamic Analysis of a Two Stage Transonic Compressor With Variable Stator Vanes. ASME Paper No. 90-GT-073.

[12] Broichhausen, K. D. and Ziegler, K. U. (2005). Supersonic and Transonic Compressors: Past, Status and Technology Trends. ASME Paper No. GT2005-69067.

[13] Bruce, P. and Babinsky, H. (2010). An Experimental Study of Transonic Shock/Boundary Layer Interactions Subject to Downstream Pressure Perturbations. *Aerospace Science and Technology*, 14(2):134–142.

[14] Burger, G. D. and Keenan, M. J. (1975). Two-Stage Fan. 4: Performance Data for Stator Setting Angle Optimization. NASA CR-134717.

[15] Burguburu, S., Toussaint, C., Bonhomme, C., and Leroy, G. (2004). Numerical Optimization of Turbomachinery Bladings. *Journal of Turbomachinery*, 126(1):91.

[16] Calvert, W. J., Emmerson, P. R., and Moore, J. M. (2003). Design, Test and Analysis of a High-Pressure-Ratio Transonic Fan. ASME Paper No. GT2003-38302.

[17] Calvert, W. J. and Ginder, R. B. (1999). Transonic fan and compressor design. *Proceedings of the Institution of Mechanical Engineers, Part C: Journal of Mechanical Engineering Science*, 213(5):419–436.

[18] Chen, J., Hathaway, M. D., and Herrick, G. P. (2008). Prestall Behavior of a Transonic Axial Compressor Stage via Time-Accurate Numerical Simulation. *Journal of Turbomachinery*, 130(4):041014.

[19] Choi, J. and Choi, T. (2015). Investigation of Axial Spacing and Effect of Interface Location in a 1.5 Stage Transonic Axial Compressor. ASME Paper No. GT2015-44020.

[20] Copenhaver, W. W., Mayhew, E. R., Hah, C., and Wadia, A. R. (1996). The Effect of Tip Clearance on a Swept Transonic Compressor Rotor. *Journal of Turbomachinery*, 118(2):230.

[21] Copenhaver, W. W., Puterbaugh, S. L., and Hah, C. (1997). Unsteady Flow and Shock Motion in a Transonic Compressor Rotor. *Journal of Propulsion and Power*, 13(1):17–23.

[22] Cumpsty, N. A. (2003). *Jet Propulsion : A Simple Guide to the Aerodynamics and Thermodynamic Design and Performance of Jet Engines*. Cambridge University Press, second edition.

[23] Cyrus, V. (1994). Separated Flows in Axial Flow Compressor With Variable Stator Vanes at Positive Incidence Angles. ASME Paper No. 94-GT-480.

[24] Delery, J. M. (1985). Shock Wave/Turbulent Boundary Layer Interaction and its Control. *Progress in Aerospace Sciences*, 22(4):209–280.

[25] Denton, J. D. (1983). An Improved Time-Marching Method for Turbomachinery Flow Calculation. *Journal of Engineering for Power*, 105(3):514–521.

[26] Denton, J. D. (1992). The Calculation of Three-Dimensional Viscous Flow Through Multistage Turbomachines. *Journal of Turbomachinery*, 114(1):18–26.

[27] Denton, J. D. (1993). The 1993 IGTI Scholar Lecture: Loss Mechanisms in Turbomachines. *Journal of Turbomachinery*, 115(4):621–656.

[28] Dodds, J. and Vahdati, M. (2014a). Rotating Stall Observations in a High Speed Compressor: Part 1 — Experimental Study. ASME Paper No. GT2014-25634.

[29] Dodds, J. and Vahdati, M. (2014b). Rotating Stall Observations in a High Speed Compressor: Part 2 — Numerical Study. ASME Paper No. GT2014-25635.

[30] Dong, Y., Mansour, M., Hingorani, S., and Hayes, J. (2001). A New Multistage Axial Compressor Designed With the APNASA Multistage CFD Code: Part 2 — Application to a New Compressor Design. ASME Paper No. 2001-GT-0350.

[31] Dorney, D. J. and Sharma, O. P. (1996). Evaluation of Flow Field Approximations for Transonic Compressor Stages. ASME Paper No. 96-GT-371.

[32] Estevadeordal, J., Gorrell, S. E., and Copenhaver, W. W. (2007). PIV Study of Wake-Rotor Interactions in a Transonic Compressor at Various Operating Conditions. *Journal of Propulsion and Power*, 23(1):235–242.

[33] Gallar, L., Arias, M., Pachidis, V., and Singh, R. (2011). Stochastic Axial Compressor Variable Geometry Schedule Optimisation. *Aerospace Science and Technology*, 15(5):366–374.

[34] Giles, M. B. (1988). Calculation of Unsteady Wake/Rotor Interaction. *Journal of Propulsion and Power*, 4(4):356–362.

[35] Gorrell, S. E., Car, D., Puterbaugh, S. L., Estevadeordal, J., and Okiishi, T. H. (2006). An Investigation of Wake-Shock Interactions in a Transonic Compressor With Digital Particle Image Velocimetry and Time-Accurate Computational Fluid Dynamics. *Journal of Turbomachinery*, 128(4):616–626.

[36] Gorrell, S. E., Okiishi, T. H., and Copenhaver, W. W. (2003). Stator-Rotor Interactions in a Transonic Compressor— Part 1: Effect of Blade-Row Spacing on Performance. *Journal of Turbomachinery*, 125(2):328.

[37] Gourdain, N., Wlassow, F., and Ottavy, X. (2012). Effect of Tip Clearance Dimensions and Control of Unsteady Flows in a Multi-Stage High-Pressure Compressor. *Journal of Turbomachinery*, 134(5):051005.

[38] Hah, C. (2015). Effects of Unsteady Flow Interactions on the Performance of a Highly-Loaded Transonic Compressor Stage. ASME Paper No. GT2015-43389.

[39] Hah, C., Puterbaugh, S. L., and Copenhaver, W. W. (1997). Unsteady Aerodynamic Flow Phenomena in a Transonic Compressor Stage. *Journal of Propulsion and Power*, 13(3):329–333.

[40] Hah, C., Puterbaugh, S. L., and Wadia, A. R. (1998). Control of Shock Structure and Secondary Flow Field Inside Transonic Compressor Rotors Through Aerodynamic Sweep. ASME Paper No. 98-GT-561.

[41] Hah, C., Rabe, D. C., and Wadia, A. R. (2004). Role of Tip-Leakage Vortices and Passage Shock in Stall Inception in a Swept Transonic Compressor Rotor. ASME Paper No. GT2004-53867.

[42] Hanoca, P. and Shobhavathy, M. T. (2011). CFD Analysis to Investigate the Effect of Axial Spacing in a Single Stage Transonic Axial Flow Compressor. *Symposium on Applied Aerodynamics and Design of Aerospace Vehicle 2011*, 1:430–438.

[43] Herrick, G., Hathaway, M., and Chen, J. (2009). Unsteady Full Annulus Simulations of a Transonic Axial Compressor Stage. AIAA Paper No. 2009-1059.

[44] Ikeguchi, T., Matsuoka, A., Sakai, Y., Yoshiura, K., and Sakano, Y. (2012). Design and Development of a 14-Stage Axial Compressor for Industrial Gas Turbine. ASME Paper No. GT2012-68524.

[45] Jameson, A. (1991). Time Dependent Calculations Using Multigrid, With Applications to Unsteady Flows Past Airfoils and Wings. AIAA Paper No. 91-1596.

[46] Kemp, N. H. (1953). Aerodynamic Interference Between Moving Blade Rows. *Journal of the Aeronautical Sciences*, 20(9):585–597.

[47] Kemp, N. H. (1955). The Unsteady Forces Due to Viscous Wakes in Turbomachines. *Journal of the Aeronautical Sciences*, 22(7):478–483.

[48] Kerrebrock, J. L. (1981). Flow in Transonic Compressors. *AIAA Journal*, 19(1):4–19.

[49] Key, N. L. (2014). Influence of Upstream and Downstream Compressor Stators on Rotor Exit Flow Field. *International Journal of Rotating Machinery*, 2014:392352.

[50] Kim, S., Kim, D., Son, C., Kim, K., Kim, M., and Min, S. (2015). A Full Engine Cycle Analysis of a Turbofan Engine for Optimum Scheduling of Variable Guide Vanes. *Aerospace Science and Technology*, 47:21–30.

[51] Kim, S., Son, C., and Kim, K. (2017). Combining Effect of Optimized Axial Compressor Variable Guide Vanes and Bleed Air on the Thermodynamic Performance of Aircraft Engine System. *Energy*, 119:199–210.

[52] Lee, B. H. K. (1990). Oscillatory Shock Motion Caused by Transonic Shock Boundary-Layer Interaction. *AIAA Journal*, 28(5):942–944.

[53] Leichtfuss, S., Biela, C., Schiffer, H., and Heinichen, F. (2012). Influence of Inlet Guide Vane Wakes on the Passage Flow in a Transonic Axial Compressor. ASME Paper No. GT2012-69485.

[54] Li, B., Gu, C., Li, X., and Liu, T. (2016). Numerical Optimization for Stator Vane Settings of Multi-Stage Compressors Based on Neural Networks and Genetic Algorithms. *Aerospace Science and Technology*, 52(52):81–94.

[55] Li, Y. and Sayma, A. (2014). Numerical Investigation of VSVs Mal-Schedule Effects in a Three-Stage Axial Compressor. ASME Paper No. GT2014-25145.

[56] Li, Y. S. and Wells, R. G. (1999). The Three-Dimensional Aerodynamic Design and Test of a Three-Stage Transonic Compressor. ASME Paper No. 99-GT-068.

[57] List, M. G., Gorrell, S. E., and Turner, M. G. (2010). Investigation of Loss Generation in an Embedded Transonic Fan Stage at Several Gaps Using High-Fidelity, Time-Accurate Computational Fluid Dynamics. *Journal of Turbomachinery*, 132(1):011014.

[58] McDevitt, J. B., Levy Jr., L. L., and Deiwert, G. S. (1976). Transonic Flow about a Thick Circular-Arc Airfoil. *AIAA Journal*, 14(5):606–613.

[59] Miller, G. R. and Hartmann, M. J. (1958). Experimental Shock Configurations and Shock Losses in a Transonic-Compressor Rotor at Design Speed. NACA-RM-E58A14b.

[60] Miller, G. R., Lewis, G. W., and Hartmann, M. J. (1961). Shock Losses in Transonic Compressor Blade Rows. *Journal of Engineering for Power*, 83(3):235.

[61] Neshat, M., Akhlaghi, M., Fathi, A., and Khaledi, H. (2015). Investigating the Effect of Blade Sweep and Lean in One Stage of an Industrial Gas Turbine's Transonic Compressor. *Propulsion and Power Research*, 4(4):221–229.

[62] Osborne, C. (1973). Compressible Unsteady Interactions Between Blade Rows. *AIAA Journal*, 11(3):340–346.

[63] Ottavy, X., Courtiade, N., and Gourdain, N. (2012). Experimental and Computational Methods for Flow Investigation in High-Speed Multistage Compressor. *Journal of Propulsion and Power*, 28(6):1141–1155.

[64] Oyama, A., Liou, M., and Obayashi, S. (2004). Transonic Axial-Flow Blade Optimization: Evolutionary Algorithms/Three-Dimensional Navier-Stokes Solver. *Journal of Propulsion and Power*, 20(4):612–619.

[65] Passrucker, H., Engber, M., Kablitz, S., and Hennecke, D. K. (2003). Effect of Forward Sweep in a Transonic Compressor Rotor. *Proceedings of the Institution of Mechanical Engineers, Part A: Journal of Power and Energy*, 217(4):357–365.

[66] Perkins, S. C. T. and Henderson, A. D. (2012). The Effect of Reduced Frequency on Transition and Separation at the Leading Edge of a Compressor Stator. ASME Paper No. GTINDIA2012-9684.

[67] Prasad, A. (2003). Evolution of Upstream Propagating Shock Waves From a Transonic Compressor Rotor. *Journal of Turbomachinery*, 125(1):133–140.

[68] Probasco, D. P., Leger, T. J., Wolff, J. M., Copenhaver, W. W., and Chriss, R. M. (2000). Variations in Upstream Vane Loading With Changes in Back Pressure in a Transonic Compressor. *Journal of Turbomachinery*, 122(3):433–441.

[69] Reising, S. (2010). *Steady and Unsteady Performance of a Transonic Compressor Stage with Non-Axisymmetric End Walls*. PhD Thesis, Technische Universität Darmstadt, Darmstadt, Germany.

[70] Reitenbach, S., Schnös, M., Becker, R.-G., and Otten, T. (2015). Optimization of Compressor Variable Geometry Settings Using Multi-Fidelity Simulation. ASME Paper No. GT2015-42832.

[71] Sadek, J. (2015). *Effect of Axial Gap Distance on Transonic Compressor Performance*. Master's Thesis, Royal Institute of Technology, Sweden.

[72] Sanders, A. J. and Fleeter, S. (2000). Experimental Investigation of Rotor-Inlet Guide Vane Interactions in Transonic Axial-Flow Compressor. *Journal of Propulsion and Power*, 16(3):421–430.

[73] Schobeiri, M. T. (1998). Shock-Loss Model for Transonic and Supersonic Axial Compressors with Curved Blades. *Journal of Propulsion and Power*, 14(4):470–478.

[74] Schobeiri, M. T. and T., M. (1997). Advanced Compressor Loss Correlations, Part I: Theoretical Aspects. *International Journal of Rotating Machinery*, 3(3):163–177.

[75] Schwenk, F. C., Lewis, G. W., and Hartmann, M. J. (1957). A Preliminary Analysis of the Magnitude of Shock Losses in Transonic Compressors. NACA-RM-E57A30.

[76] Shadaram, A., Fathi, A., and Azizi, R. (2009). Optimization of Variable Stator's Angle for Off Design Compression System Using Streamline Curvature Method. ASME Paper No. GT2009-59772.

[77] Smith, L. H. (1966). Wake Dispersion in Turbomachines. *Journal of Basic Engineering*, 88(3):688.

[78] Smith, L. H. (1970). Casing Boundary Layers in Multistage Axial Flow Compressors. *Flow Research in Blading*, pages 275–306.

[79] Sohoni, N., Hall, T., Brandvik, T., and Parry, A. (2015). Prediction and Measurement of Unsteady Blade Surface Pressures On An Open Rotor. ASME Paper No. GT2015-42334.

[80] Spalart, P. R. and Allmaras, S. R. (1994). A One-Equation Turbulence Model for Aerodynamic Flows. *La Recherche Aerospatiale*, 1:5–21.

[81] Suder, K. L. and Celestina, M. L. (1994). Experimental and Computational Investigation of the Tip Clearance Flow in a Transonic Axial Compressor Rotor. ASME Paper No. 94-GT-365.

[82] Sun, Y., Ren, Y., Fu, S., and Wadia, A. R. (2008). The Unsteady Loss in One-Stage Transonic Compressor Under Peak Efficiency and Near Stall Conditions. ASME Paper No. GT2008-51019.

[83] Tomita, J. T. and Barbosa, J. R. (2003). A model for numerical simulation of variable stator axial flow compressors. 17th International Congress of Mechanical Engineering Paper No. COBEM2003-0239.

[84] Valkov, T. V. and Tan, C. S. (1999). Effect of Upstream Rotor Vortical Disturbances on the Time-Averaged Performance of Axial Compressor Stators: Part 2—Rotor Tip Vortex/Streamwise Vortex–Stator Blade Interactions. *Journal of Turbomachinery*, 121(3):387.

[85] van de Wall, A. G., Kadambi, J. R., and Adamczyk, J. J. (2000). A Transport Model for the Deterministic Stresses Associated With Turbomachinery Blade Row Interactions. *Journal of Turbomachinery*, 122(4):593.

[86] Wadia, A. R. and Copenhaver, W. W. (1996). An Investigation of the Effect of Cascade Area Ratios on Transonic Compressor Performance. *Journal of Turbomachinery*, 118(4):760.

[87] Wadia, A. R. and Law, C. H. (1993). Low Aspect Ratio Transonic Rotors: Part 2—Influence of Location of Maximum Thickness on Transonic Compressor Performance. *Journal of Turbomachinery*, 115(2):226.

[88] Wadia, A. R., Szucs, P. N., and Crall, D. W. (1998). Inner Workings of Aerodynamic Sweep. *Journal of Turbomachinery*, 120(4):671.

[89] Walker, G. J., Hughes, J. D., Köhler, I., and Solomon, W. J. (1998). The Influence of Wake-Wake Interactions on Loss Fluctuations of a Downstream Axial Compressor Blade Row. *Journal of Turbomachinery*, 120(4):695.

[90] Wang, D. X., He, L., Li, Y. S., Wells, R. G., and Chen, T. (2008). Adjoint Aerodynamic Design Optimization for Blades in Multi-Stage Turbomachines: Part II—Validation and Application. ASME Paper No. GT2008-50209.

[91] Wheeler, A. P. S. and Miller, R. J. (2008). Compressor Wake/Leading-Edge Interactions at Off Design Incidences. ASME Paper No. GT2008-50177.

[92] Wheeler, A. P. S., Miller, R. J., and Hodson, H. P. (2007). The Effect of Wake Induced Structures on Compressor Boundary-Layers. *Journal of Turbomachinery*, 129(4):705.

[93] Wheeler, A. P. S., Sofia, A., and Miller, R. J. (2009). The Effect of Leading-Edge Geometry on Wake Interactions in Compressors. *Journal of Turbomachinery*, 131(4):041013.

[94] Wu, L., Huang, F., Liu, F., and Wang, Y. (1985). Investigation and Experiment on Optimizing Angles of Variable Stator of Axial Flow Compressor. ASME Paper No. 85-IGT-32.

[95] Yamada, K., Furukawa, M., Inoue, M., and Funazaki, K. (2003). Numerical Analysis of Tip Leakage Flow Field in a Transonic Axial Compressor Rotor. IGTC2003 Tokyo TS-030.

[96] Yamagami, M., Kodama, H., Kato, D., Tsuchiya, N., Horiguchi, Y., and Kazawa, J. (2009). Unsteady Flow Effects in a High-Speed Multistage Axial Compressor. ASME Paper No. GT2009-59583.

[97] Yamagami, M., Kodama, H., Kato, D., Tsuchiya, N., Horiguchi, Y., and Kazawa, J. (2011). CFD Modeling Effects on Unsteady Multistage Simulation for a Transonic Axial Compressor. ASME Paper No. GT2011-46198.